



**This electronic thesis or dissertation has been
downloaded from Explore Bristol Research,
<http://research-information.bristol.ac.uk>**

Author:
Durstun, Nick

Title:
Quantifying the flight stability of free-gliding birds of prey

General rights

Access to the thesis is subject to the Creative Commons Attribution - NonCommercial-No Derivatives 4.0 International Public License. A copy of this may be found at <https://creativecommons.org/licenses/by-nc-nd/4.0/legalcode>. This license sets out your rights and the restrictions that apply to your access to the thesis so it is important you read this before proceeding.

Take down policy

Some pages of this thesis may have been removed for copyright restrictions prior to having it been deposited in Explore Bristol Research. However, if you have discovered material within the thesis that you consider to be unlawful e.g. breaches of copyright (either yours or that of a third party) or any other law, including but not limited to those relating to patent, trademark, confidentiality, data protection, obscenity, defamation, libel, then please contact collections-metadata@bristol.ac.uk and include the following information in your message:

- Your contact details
- Bibliographic details for the item, including a URL
- An outline nature of the complaint

Your claim will be investigated and, where appropriate, the item in question will be removed from public view as soon as possible.

Quantifying the flight stability of free-gliding birds of prey



Nicholas E. Durston

A dissertation submitted to the University of Bristol in accordance
with the requirements for award of the degree of DOCTOR OF
PHILOSOPHY in the Faculty of Engineering.

School of Civil, Aerospace & Mechanical Engineering

June 2019

Word count: 63,000

ABSTRACT

By morphing their wings and tail, birds manoeuvre around obstacles and mitigate the effects of atmospheric turbulence with apparent ease. However, the stability and control of bird flight is poorly understood due to difficulty obtaining the relevant data. In this project, linear flight dynamics models of gliding birds were created based on rigid body assumptions and small perturbations from trim. These represent the first flight dynamics models of birds based on shapes and mass properties closely matching those in free-flight.

A novel multi-stereo approach was used to reconstruct the surfaces of a free-gliding barn owl (*Tyto alba*) and peregrine falcon (*Falco peregrinus*) at a single instant in time during steady gliding flight. The surface reconstructions were used to create vortex lattice models for three flights per bird. These models were integrated with centre of mass and moment of inertia estimates from calibrated X-ray computed tomography scans of barn owl and peregrine cadavers.

Linear flight dynamics models based on these datasets revealed a high degree of longitudinal instability in both birds. The time to double of the pitch divergence was typically below 50 ms, which is three times faster than the highly unstable X-29 experimental aircraft. Lateral-directional dynamic stability varied between flights and species, particularly the dutch roll and spiral modes.

Current understanding of avian physiology suggests that neural feedback may be too slow to stabilise these animals. This implies a potential role for passive stabilisation through structural compliance, a mechanism that could increase the time available for neural feedback. Overall, this project revealed new insights into the flight stability of gliding birds, largely through the novel application of the imaging methods used. These findings could inspire stabilisation mechanisms for future designs of unmanned air vehicles of similar size.

To my beautiful wife Abigail

*There be three things which are too wonderful for me,
yea, four which I know not:
the way of an eagle in the air;
the way of a serpent upon a rock;
the way of a ship in the midst of the sea;
and the way of a man with a maid.*

Proverbs 30:18-19 (AV)

— *Soli Deo Gloria* —

ACKNOWLEDGEMENTS

This PhD could not have been completed without the incredible support of so many friends and colleagues. I would therefore like to offer my sincere thanks to:

My supervisor, Dr Shane Windsor, whose technical expertise, support and enthusiasm has guided my thoughts and decisions throughout this project. Thank you for letting me work on this fascinating project.

Patrick Metcalfe, who assisted during long hours in the field and oversaw the design and manufacture of the 3D printed barn owl (chapter 5) and related hardware.

Lloyd and Rose Buck and their amazing birds, without whom this project could not have been completed.

Professor Mark Lowenberg, Professor Christian Allen, Dr Thomas Rendall and Dr Richard Bomphrey for their advice and feedback at many important stages throughout the project.

Dr Yusuf Mahadik and James Shelton, for their assistance with the experimental work presented in chapter 4.

Carys Davies, for her support during use of the Veterinary School laboratory.

Ed Drewitt, for his expertise and assistance identifying the sex of the bird cadavers used in chapter 4.

Dayton Taylor at Digital Air, for provision of camera synchronisation equipment.

Bel Deering at the Royal Society for the Protection of Animals (RSPCA), Steve Hopper at South Hams Hawks and Owls and Simon Allen at the Gower Bird Hospital for their provision of naturally deceased bird cadavers.

Dr Ty Hedrick and Dr Simon Walker for their provision of photogrammetry code..

Lee Winter and Russ Eyre, for their assistance during wind tunnel testing.

Dr Jorn Cheney and Dr Jonathan Stevenson, for their advice and encouragement throughout.

Hywel and Gill Williams, for the use of their house as a quiet place to write.

Dave Williams for his mentoring, friendship and advice.

All members of the bio-inspired flight laboratory, for making our workplace such a friendly place to work.

Everyone in the University of Bristol workshop, for their support during manufacturing of various items of hardware.

The Engineering and Physical Sciences Research Council (EPSRC), for funding the project.

Our au pair, Bethan Joyce, for providing essential support at home.

My children, Anna, Joey and Eliana who have waited so patiently for me to finish during several months of long days in the office.

And above all, my wife Abigail, for her truly tireless and unwavering support.

DECLARATION

I declare that the work in this dissertation was carried out in accordance with the requirements of the University's Regulations and Code of Practice for Research Degree Programmes and that it has not been submitted for any other academic award. Except where indicated by specific reference in the text, the work is the candidate's own work. Work done in collaboration with, or with the assistance of, others, is indicated as such. Any views expressed in the dissertation are those of the author.

SIGNED:.....

DATE:.....

Nicholas E. Durston

June 2019

TABLE OF CONTENTS

Table of contents	xi
List of figures	xvii
List of tables	xxi
1 Introduction	1
1.1 Chapter summary	1
1.2 Chapter structure	1
1.3 Background	2
1.4 The bird as a complete system	6
1.5 Literature review: Avian flight dynamics	10
1.5.1 Key concepts	10
1.5.2 Longitudinal static stability	12
1.5.3 Lateral-directional static stability	14
1.5.4 Dynamic Stability	16
1.5.5 Control	19
1.5.6 Summary	21
1.6 Research questions, aims and objectives	21
1.7 Conclusions	23
2 High-resolution surface reconstruction of free-gliding birds of prey	25
2.1 Chapter summary	25
2.2 Chapter structure	25
2.3 Introduction	26
2.4 Experimental animals	27
2.5 Experimental setup	28
2.6 Experimental procedure	31
2.6.1 Overview	31
2.6.2 Basic principle of stereo reconstruction	31
2.6.3 Stereo reconstruction	33
2.6.3.1 Disparity estimation	33

Table of contents

2.6.3.2	Stereo calibration and reconstruction	35
2.6.3.3	Stereo alignment	35
2.6.4	Edge reconstruction	36
2.6.5	Wing-body coordinate system	38
2.7	Accuracy assessment	40
2.8	Bird reconstructions	42
2.9	Conclusions and recommendations	45
3	Quantifying the geometry of free-gliding birds of prey and implications for longitudinal stability	47
3.1	Chapter summary	47
3.2	Chapter structure	47
3.3	Introduction	48
3.4	Material and methods	55
3.4.1	Geometry evaluation	55
3.4.2	Estimation of flight conditions	61
3.5	Results	64
3.5.1	Flight conditions	64
3.5.2	Spline fitting	67
3.5.3	Wing shapes	72
3.6	Discussion	77
3.6.1	Summary of results	77
3.6.2	Longitudinal static stability	77
3.6.3	Flight control	79
3.7	Conclusions and recommendations	81
4	How wing and tail configuration influence the centre of mass and moments of inertia of free-gliding birds of prey	83
4.1	Chapter summary	83
4.2	Chapter structure	84
4.3	Introduction	84
4.4	Material and methods	88
4.4.1	Bird cadavers and preparation	88
4.4.2	CT scanner and calibration	89
4.4.3	Estimation of inertial properties	90
4.4.4	Method validation summary	98

4.4.5	Trifilar pendulum overview	98
4.4.6	Trifilar pendulum accuracy assessment	100
4.4.7	Trifilar pendulum bird MoI estimation	101
4.5	Results	102
4.5.1	Method validation	102
4.5.2	Cadaver CoM and MoI	105
4.5.3	Free-flight centre of mass and moment of inertia	112
4.6	Discussion	117
4.6.1	Method	117
4.6.2	Flight dynamics and inertia	119
4.7	Conclusions and recommendations	122
5	Flight stability analysis of free-gliding birds of prey	125
5.1	Chapter summary	125
5.2	Chapter structure	126
5.3	Introduction	126
5.4	Material and Methods	130
5.4.1	Geometry refinement	130
5.4.1.1	Overview	130
5.4.1.2	Section categorisation	130
5.4.1.3	Arm wing	132
5.4.1.4	Hand wing	134
5.4.1.5	Body	136
5.4.1.6	Partly tail	138
5.4.1.7	Wing and tail tips	138
5.4.1.8	Section visualisations	139
5.4.1.9	Meshing	141
5.4.2	Wind tunnel testing	144
5.4.2.1	Experimental setup	144
5.4.2.2	Model deformation	147
5.4.2.3	Transducer calibration checks	149
5.4.2.4	Post-processing	152
5.4.3	Flight dynamics modelling	153
5.4.3.1	Overview	153
5.4.3.2	Dynamic model	154

Table of contents

5.4.3.3	Aerodynamic modelling in AVL	157
5.4.3.4	Wind tunnel derivative estimation	162
5.5	Results	163
5.5.1	Validation	163
5.5.2	Longitudinal static stability and control effectiveness	172
5.5.3	Longitudinal dynamic modes	177
5.5.4	Lateral-directional stability	182
5.5.5	Sensitivity studies	188
5.6	Discussion	190
5.6.1	Summary of results	190
5.6.2	Methods	190
5.6.3	Longitudinal stability	192
5.6.4	Lateral-directional stability	193
5.6.5	Flight stabilisation	195
5.6.6	Ecological implications of instability	201
5.7	Conclusions and recommendations	202
6	Summary and Conclusions	205
	Appendix A Flight videos	213
	Appendix B Principle axes and components of inertia	215
B.1	Visualisation of principle axes of inertia	215
B.2	Inertia tensor data	217
B.2.1	Reference tables	217
B.2.2	Tensors - table B.1	218
B.2.3	Tensors - Table B.2	219
B.2.4	Tensors - Table B.3	220
	Appendix C Consistent cadaver alignment	223
	Appendix D AVL concise derivative check	229
D.1	Summary	229
D.2	Calculation procedure	229
D.3	Results	230
D.4	Equations	232
D.5	Tables	234

Appendix E	Additional flight dynamics data	237
E.1	Root locus plots	237
E.2	Time histories	239
E.3	Reduced order model results	243
E.4	State matrices, eigenvalues and eigenvectors	244
E.4.1	Flight O1	244
E.4.2	Flight O2	245
E.4.3	Flight O3	246
E.4.4	Flight P1	247
E.4.5	Flight P2	248
E.4.6	Flight P3	249
E.5	Sensitivity studies	250
E.5.1	Lift coefficient	250
E.5.2	Anteroposterior centre of mass position	250
E.5.3	Inertia tensor	251
References		253

LIST OF FIGURES

1.1	Pigeon wing morphing in the first tilting wind tunnel.	3
1.2	The ‘Great flight diagram’.	5
1.3	The bird as a complete system.	8
1.4	Estimates of longitudinal static stability with bird cadavers.	13
1.5	How tail drag contributes towards directional stability.	15
1.6	The effect of distal wing sweep on directional stability.	17
2.1	Photogrammetry experimental setup.	28
2.2	Example images from each camera pair for barn owl flight O1.	30
2.3	Surface reconstruction process flowchart.	31
2.4	The basic principle of stereophotogrammetry.	32
2.5	Shape carving example.	37
2.6	The ‘wing-body’ coordinate system.	38
2.7	Method to spline the edge of the bird.	39
2.8	Photogrammetry error analysis.	41
2.9	Textured reconstruction of barn owl flight O1.	43
2.10	Textured reconstruction of peregrine flight P1.	43
2.11	Spanwise sections through all flights (raw data points).	45
3.1	Static and dynamic stability.	49
3.2	Pitching moment slopes for stable and unstable configurations.	50
3.3	Stability and trim of an isolated lifting surface.	52
3.4	The contribution of geometric features to zero-lift pitching moment. . .	54
3.5	Example mean camber, dorsal and ventral spline fitting.	56
3.6	The use of splines and polynomials for section fitting.	59
3.7	Definitions of camber, thickness, angle of twist and angle of attack. . .	61
3.8	Method for estimating true air speed, angle of attack and angle of sideslip.	63
3.9	Time histories of velocity, angle of attack and angle of sideslip during each flight.	64
3.10	Visual comparison between the raw points and fitted splines/polynomials for barn owl flight O1.	68

List of figures

3.11	Visual comparison between the raw points and fitted splines/polynomials for peregrine flight P1.	70
3.12	Assessment of the accuracy of the stereo reconstructions by comparing with a high accuracy laser scan of a fibreglass gull model.	71
3.13	Wing camber heatmaps.	73
3.14	Spanwise angle of attack, sweep and dihedral.	75
3.15	Wing thickness heatmaps.	76
4.1	Bird cadaver preparation.	89
4.2	Example CT image through peregrine cadaver, pfl	90
4.3	CT calibrations of grey value vs. absolute density.	91
4.4	Example 3D CT data and thresholding.	93
4.5	Example histogram of voxel densities.	94
4.6	Virtually dissected appendages.	95
4.7	Alignment of CT data to photogrammetry data.	97
4.8	Planview of trifilar pendulum.	99
4.9	Estimating the misalignment of the bird's centre of mass on the trifilar pendulum.	103
4.10	Pie chart comparison between physically and virtually dissected appendage masses.	104
4.11	Wing moment of inertia about the humeral head compared with previous research.	105
4.12	The impact of emaciation on appendage masses.	106
4.13	The impact of emaciation on inertia.	107
4.14	Projected mass and inertia distributions.	109
4.15	Pie charts comparing appendage contributions to total mass and moments of inertia.	110
4.16	Spanwise inertia distributions.	112
4.17	Changes in centre of mass position with flight configuration.	114
4.18	Changes in the principal components of inertia with flight configuration.	115
4.19	How moments of inertia may vary between the cadavers and live birds from chapters 2 and 3	116
5.1	Section categorisation prior to fitting.	131
5.2	Arm wing thickness distribution fitting.	133
5.3	Example arm wing aerofoil fits.	134

5.4	Example hand wing aerofoil fits.	136
5.5	Example body closed-loop fits.	138
5.6	Comparison between the raw points and close-loop section fits (coarse spanwise distribution).	140
5.7	Comparison between the raw points and close-loop section fits (fine spanwise distribution).	141
5.8	Watertight, error free surface mesh of barn owl flight O1.	143
5.9	Lateral view of wind tunnel experimental setup.	145
5.10	Images of wind tunnel experimental setup.	146
5.11	Comparison between the 3D printed model and original mesh for flight O1 after manufacture and after wind tunnel testing.	148
5.12	Calibration checks (force-torque transducer).	150
5.13	Calibration checks (overhead balance).	151
5.14	Drag correction used for the overhead balance.	151
5.15	Estimation of the pitching moment about the centre of mass.	153
5.16	Mean camber lines for the wing and tail of flight O1.	159
5.17	Wind tunnel lift, drag and pitching moment vs. angle of attack and Reynolds number for flight O1.	165
5.18	Wind tunnel lift to drag ratio vs. angle of attack and Reynolds number for flight O1.	166
5.19	Estimates of AVL lattice independence for lift, drag and pitching moment estimates using Richardson's extrapolation for flight O1.	168
5.20	AVL vs. wind tunnel estimates of lift, drag and pitching moment vs. angle of attack.	170
5.21	AVL estimates of the static margin for all flights.	175
5.22	AVL estimates of spanwise loading for all flights.	176
5.23	AVL estimates of pitch control effectiveness using tail elevation, wing camber, sweep and twist.	177
5.24	Root locus plot of the longitudinal dynamic modes.	179
5.25	Time history of the pitch divergence mode of flight O1.	180
5.26	Time history of the third oscillatory mode of flight P1.	181
5.27	Root locus plot of the lateral-directional dynamic modes.	184
5.28	Time history of the spiral mode of flights P2 and P3.	186
5.29	Time history of the spiral mode of flight P1.	187
5.30	Time history of the dutch roll mode of flights P2 and P3.	187

List of figures

5.31	Time history of the unstable roll yaw sideslip modes of flights O1 and O3.	188
5.32	How primary feather compliance could affect lateral-directional stability.	199
5.33	How chordwise compliance could influence longitudinal stability.	200
6.1	The flight dynamics of birds is the result of numerous, complex interacting phenomena. PNS = peripheral nervous system, CNS = central nervous system.	209
B.1	Visualisations of the prinipal axes of inertia.	216
C.1	Part 1 of cadaver alignment to photogrammetry data: Slave to master cadaver alignment.	224
C.2	Part 2 of cadaver alignment to photogrammetry data: Intra-flight alignment.	225
C.3	Part 3 of cadaver alignment to photogrammetry data: Inter-flight alignment.	227
C.4	Cadavers bo1, bo2, pf1, pf2 and pf4 aligned to all flights.	228
E.1	Root locus plot of the longitudinal dynamic modes based on the original AVL derivative estimates.	237
E.2	Root locus plot of the lateral-directional dynamic modes without a thick central torso.	238
E.3	Time histories of the pitch divergence mode (all flights).	239
E.4	Time histories of the third oscillatory mode (O1-O3).	239
E.5	Time histories of the third oscillatory mode (P1-P3).	240
E.6	Time histories of the roll subsidence mode (all flights).	240
E.7	Time histories of the spiral mode (O1-O3).	241
E.8	Time histories of the roll yaw sideslip 1 mode (O1-O3)	241
E.9	Time histories of the roll yaw sideslip 4 mode (P1)	242
E.10	Time histories of the roll subsidence 2 mode (P1)	242

LIST OF TABLES

2.1	Comaprison of approaches for the surface reconstruction of free-gliding birds.	42
3.1	Flight conditions data.	66
3.2	Comparison between the raw points and fitted splines/polynomials. . .	67
3.3	Estimates of longitudinal dihedral.	78
4.1	Bird cadavder maturity, sex, mass, span, emaciation and mass loss. . .	88
4.2	Trifilar pendulum validation with nylon blocks.	101
4.3	Trifilar pendulum vs. CT estimates of dorsoventral moment of inertia. .	105
4.4	Variation in anteroposterior centre of mass position between cadavers and flights (barn owl).	113
4.5	Variation in anteroposterior centre of mass position between cadavers and flights (peregrine).	113
4.6	Comparison between bird and aircraft moments of inertia.	119
5.1	Body to wind axes conversion formulae.	161
5.2	Formulae for North American aerodynamic derivatives in wind axes. . .	162
5.3	Inputs used to analytically estimate C_{Z_q} and C_{M_q}	163
5.4	AVL vs. wind tunnel estimates of longitudinal aerodynamic derivatives in wind axes.	171
5.5	AVL vs. analytical estimates of C_{X_q} , C_{Z_q} and C_{M_q}	172
5.6	AVL estimates of the static margin for all flights.	175
5.7	Planform based estimates of CoM and wing aerodynamic centre for flights O1, P1 and P3	176
5.8	The natural frequency and damping of the third oscillatory mode vs. reduced order model estimates of the phugoid mode for all flights. . . .	179
5.9	Example eigenvectors for the pitch divergence mode and third oscillatory mode of flight P1.	181
5.10	AVL estimated lateral-directional derivatives.	183
5.11	Lateral-directional mode breakdown between flights.	185

List of tables

B.1	References for the ‘as scanned’ inertia tensors.	217
B.2	References for the consistently aligned inertia tensors.	217
B.3	References for the inertia tensors used in flight dynamics analysis. . . .	217
D.1	Results of the AVL conversion to concise derivatives vs. textbook formulae.	231
D.2	North American to British non-dimensional derivative comparison. . .	234
D.3	British conversions between dimensional and non-dimensional derivatives.	235
D.4	Formulae for the conversion of British dimensional aerodynamic derivatives to concise form.	236
E.1	AVL vs. reduced order model time constant estimates of the roll subsidence mode.	243
E.2	AVL vs. reduced order model time constant estimates of the spiral mode.	243
E.3	AVL vs. reduced order model natural frequency and damping estimates of the dutch roll mode (P2 and P3).	243
E.4	Sensitivity of the third oscillatory mode to the trim lift coefficient. . . .	250
E.5	Sensitivity of the dutch roll mode to the trim lift coefficient.	250
E.6	Sensitivity of the pitch divergence mode to the centre of mass.	250
E.7	Sensitivity of the pitch divergence mode to the inertia tensor.	251
E.8	Sensitivity of the roll subsidence mode to the inertia tensor.	251
E.9	Sensitivity of the roll yaw sideslip 1, 2 and 4 modes to the inertia tensor.	251
E.10	Sensitivity of the dutch roll mode to the inertia tensor.	251



Fig. 1 Samual Langley (1834-1906), a pioneer in aerospace engineering, studying birds from the roof of the arts and industries building of the Smithsonian Institution, ca. 1901-02, with what appear to be a pair of synchronised cameras. From Smithsonian Institution Archives. Image MAH-21444. Used with permission.

INTRODUCTION

1.1 Chapter summary

The recent growth of the unmanned air vehicle (UAV) market has revived an interest in bird flight among engineers and biologists. Unlike conventional fixed wing UAVs, birds demonstrate exceptional control during flight, especially in adverse turbulent conditions. A better understanding of the mechanisms employed by birds for stability and control could inspire the future development of ‘agile autonomous’ UAVs. However, understanding the flight dynamics of gliding birds represents a significant technical challenge. This is due to the complexity of the various elements influencing the system dynamics, in addition to the challenge of integrating these into a complete system. Currently, little is known even about the static stability of gliding birds, let alone their dynamic modes and flight control system. Here, the concept of the ‘bird as an integrated system’ is introduced, in conjunction with project objectives involving the accurate quantification of the rigid body linear dynamics of gliding birds, based on measurements of their shape and inertial properties (i.e. centre of mass and moments of inertia) representative of free-flight. Quantifying the flight stability of free-gliding birds could represent the foundation for a longer-term research effort in which the various complex elements of the bird and its environment are modelled in increasing detail.

1.2 Chapter structure

This chapter begins with a brief history of bird flight research and the engineering motivation for studying avian flight dynamics. The challenges associated with flight dynamics modelling of gliding birds are described, and the concept of ‘the bird as an integrated system’ is introduced. A review of avian flight dynamics literature is carried out, and critiqued in light of the previously introduced integrated system approach. The project objectives are then summarised, followed by a brief conclusion.

1.3 Background

The flight of birds has fascinated human beings for millennia, yet current understanding is still limited [1]. Observations of avian wing shapes influenced the thin aerofoil designs of famous pioneers such as Cayley, Lilienthal, Langley and the Wright brothers [2, 3]. Eventually it was found that bird-like aerofoils were suboptimal at the higher Reynolds numbers associated with powered flight, and aerospace science progressed without regard for birds [4]. Biologists continued to study bird flight through the first half of the 20th century based on careful observation, combining insights from evolutionary theory and aerodynamics to develop understanding [5–10]. During the second-half of the 20th century, researchers began to apply more sophisticated and controlled techniques to the study birds. The idea of training a bird to glide in a tilting wind tunnel [2] proved to be a defining moment, and was first achieved with a pigeon at the University of Bristol [11]. This led to the first accurate estimates of lift and drag coefficient, in addition to the first systematic description of wing configuration changes with air speed and glide angle (figure 1.1). Previous attempts to measure lift-to-drag ratio and airspeed were made by flying a glider alongside black vultures (*Coragyps atratus*), but these estimates were uncertain due to wind and thermals, despite efforts to make corrections [2, 12].

Around this time, researchers in Germany developed techniques to measure the surface profiles of narcotised birds [13] and also trained a house sparrow (*Passer domesticus*) to flap in a wind tunnel. They combined stereophotogrammetry with their wind tunnel technique to reconstruct the dorsal surface profiles of the sparrow’s wings at low spatial resolution (approximately 100 points) at different stages through the wing-beat cycle [14, 15]. Wind tunnels were also used to estimate the lift, drag and pitching moment of ‘prepared’ wings from bird cadavers [16, 17], a technique that is still used [4, 18–20] despite being unrepresentative of the wing geometry and aerodynamics of free-flying birds [21–23].

More recently, interest in bird flight has increased due to the growth of the unmanned air vehicle (UAV) market [24–26]. Demand for UAVs of similar size to birds is steadily rising due to their relatively low cost and utility for ‘dirty, dangerous and dull’ missions that would be undesirable or dangerous for humans. UAV missions might include traffic management, visual inspection of difficult-to-access machinery (i.e. offshore wind turbines, oil rigs), disaster relief, crime prevention, scientific data collection and surveillance. It is essential that these activities are carried out safely, despite

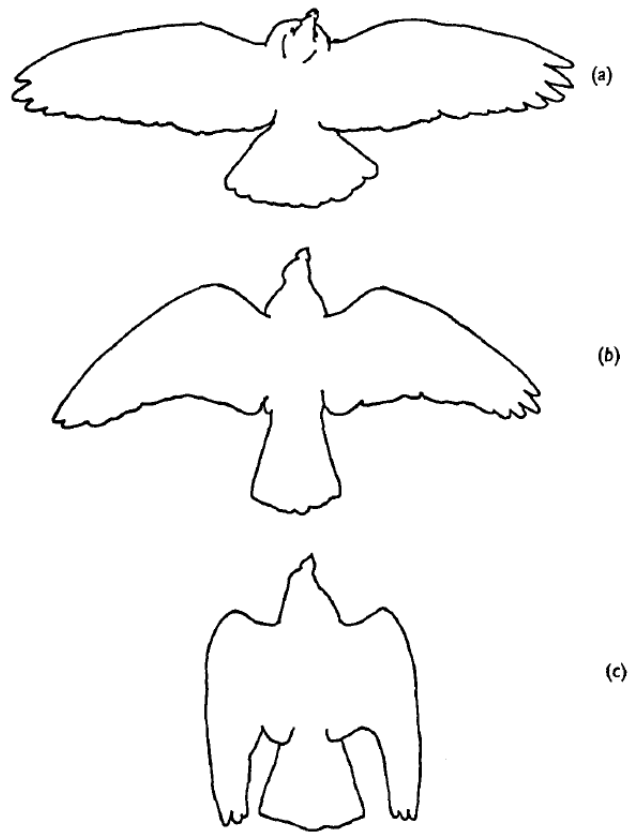


Fig. 7. Outlines traced from overhead photographs of a pigeon gliding steadily at various speeds: (a) 8.6 m./sec., span 65 cm.; (b) 12.4 m./sec., span 57 cm.; (c) 22.1 m./sec., span 25 cm.

Fig. 1.1 The first tilting wind tunnel for birds showed how a pigeon's wing and tail planform changed with airspeed and glide angle. From Pennycuik [11]. Used with permission.

the challenges of (i) atmospheric turbulence and (ii) autonomous navigation/control through cluttered environments.

Challenge (i), atmospheric turbulence, is a particular challenge for small UAVs due to their low size and mass (figure 1.2). Roll acceleration, α_{roll} , scales with mass, m , according to [27, 28]

$$\alpha_{roll} \propto m^{-\frac{1}{3}}. \quad (1.1)$$

Equation (1.1) is based on the ratio between aerodynamic moments and mass moment of inertia (Newton’s second law for rotation motion) and provides insight into the sensitivity of smaller UAVs to gusts and turbulence compared with larger aircraft¹. This increased sensitivity occurs in conjunction with low-altitude flight, where atmospheric turbulence is high. For example, cobra probe arrays mounted above a car at a height of 2-3.9 m, with spacings of only 14 mm, revealed significant spatial and temporal variations in flow velocity and angle during tests in several different locations [29–31]. Furthermore, the Reynolds numbers at which bird-sized UAVs operate ($20\text{--}200 \times 10^3$) can result in undesirable flow phenomena such as laminar separation bubbles [32, 33]. These issues represent a significant challenge for the controllability of conventionally designed, fixed wing configurations [32, 34, 35].

Challenge (ii), navigation through cluttered environments, has been referred to as ‘agile autonomy’ [37]. This refers to the ability of a UAV to navigate autonomously in environments that present a formidable (if not impossible) challenge to current control systems. These include forests, dynamic urban environments (i.e. movement of people, cars, machinery) and canyons. Unlike current conventional fixed-wing UAVs, birds of prey exploit these high-turbulence, cluttered environments with apparent ease. This provides a strong incentive to understand the stability and control mechanisms employed by birds so that the insight gained may be used to improve the robustness of engineered systems. Within this context, ‘stability’ is concerned with the open loop or passive system dynamics, in the hypothetical scenario that the bird rigidly fixed its wings in place. In this sense, the stability of the bird would be quantified by treating it as a rigid body, as is the case for most conventional aircraft [38]. It is this definition that is used throughout this study in terms of quantifying the flight stability of free-gliding birds. However, the flight feathers of birds are much more flexible than most conventional aircraft structures, so the definition of stability could be extended to include the passive influence of structural flexibility (see chapter 5 section 5.6). Flight

¹And also the increase in agility gained by reduction in size.

‘control’ is concerned with the muscle activations used to maintain a desired trajectory. In conventional aircraft, these are equivalent to actuations of the control surfaces (i.e. ailerons, elevator, rudder, flaps etc.) by the pilot or flight computer. Defined this way, control inputs could be used (i) to provide corrective forces and moments to maintain equilibrium (i.e. constant velocity) flight (ii) to execute and maintain or adjust trajectory during manoeuvres. In comparison with conventional aircraft, the concepts of stability and control are particularly intertwined for birds. The definitions described above, analogous to those used for aircraft, are not necessarily as clear for gliding birds [39]. For example, birds are unlikely to be truly ‘passive’, even during steady gliding flight, because muscles must be constantly activated to maintain pose. Contraction of the pectoralis muscles for instance, is required to counteract the lift forces acting on the wings [40, 41]. The concepts of stability and control in bird flight therefore have more overlap than conventional aircraft. Understanding the stability and control of bird flight is therefore a challenging task, requiring the integration of numerous individual system elements that are each difficult to measure. Both stability and control fall under the general topic of flight dynamics, a discipline concerned with understanding the forces, moments and kinematics of aircraft motion.

1.4 The bird as a complete system

Accurately quantifying the flight dynamics of birds represents a significant technical challenge due to the sheer complexity of the various elements that must be considered (figure 1.3). Unlike conventional, relatively rigid aircraft with simple hinged control surfaces, birds undergo dynamic shape changes during flight due to the structural compliance of their musculoskeletal system and feathers. The shape/position of the wings, head, legs and tail can all change during flight, through passive (flow acting on bird) or active (bird acting on flow) mechanisms. Unlike conventional aircraft, passive mechanisms do not necessarily imply a lack of muscle/actuator involvement or neural feedback, because even with the most static glide shape, a bird still has to brace its musculature to balance the aerodynamic forces [39, 41]. This suggests that the ‘passive/active’ distinction, so useful in engineering, may be unhelpful for describing biological systems [39]. Morphological changes may include feather flexing and isometric (constant length) contraction of muscles for viscoelastic damping in response to time-varying aerodynamic loads [39, 42], flight stabilisation through reflex-based neural feedback mechanisms [43, 44] and reaction-based correctional-control,

such as large changes in wing sweep [11]. The last of these involves the use of muscles as actuators, whose motion is controlled through innervation by motor neurons which themselves are controlled either via the brain (i.e. reactions) or just the peripheral nervous system (i.e. reflexes).

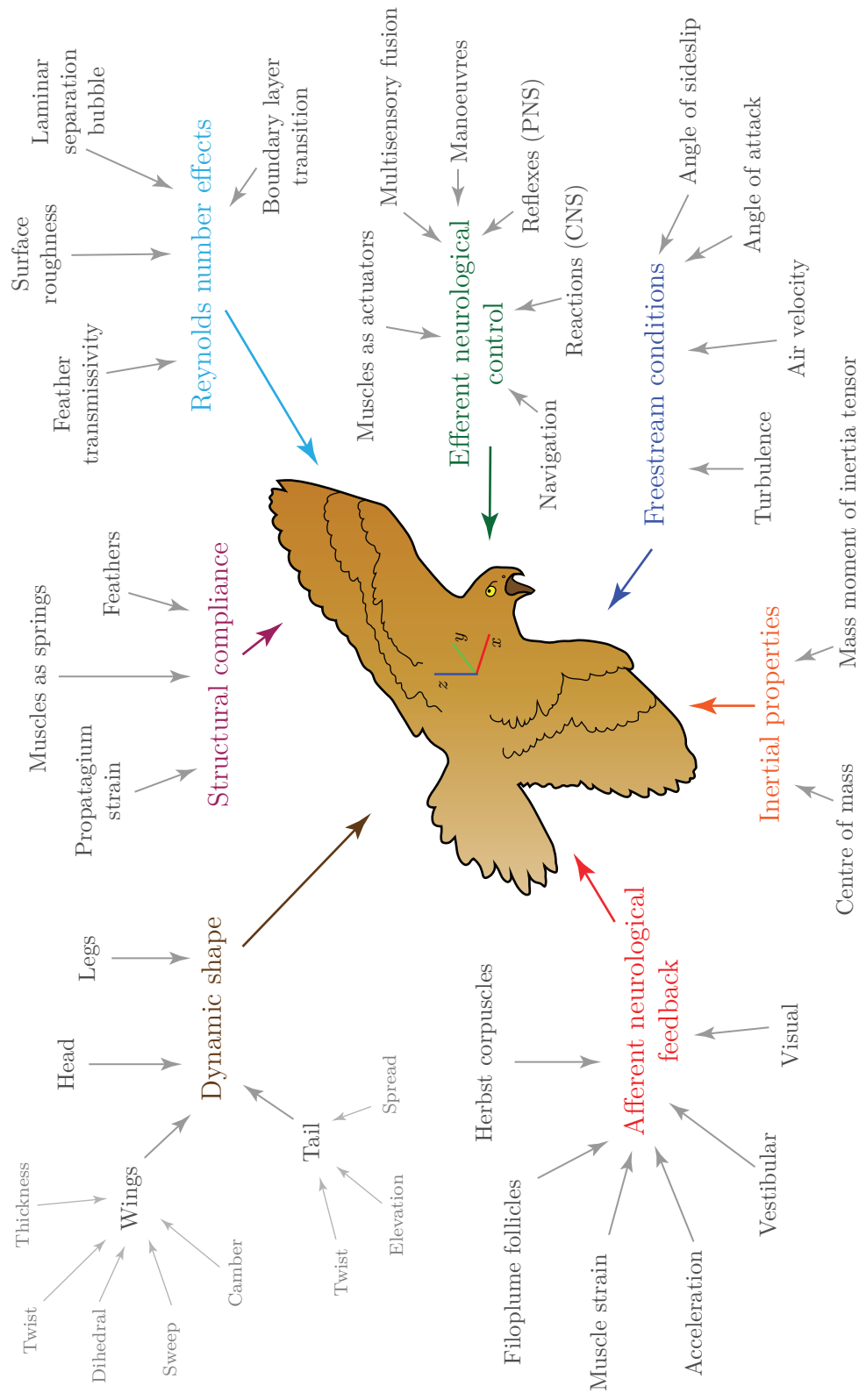


Fig. 1.3 The flight dynamics of birds is the result of numerous, complex interacting phenomena. PNS = peripheral nervous system, CNS = central nervous system.

Muscle control is informed by afferent neurological signals from the bird’s suite of sensory systems [45]. These include the visual and vestibular (inner ear/balance) systems, in addition to mechanosensors such as Herbst corpuscles, filoplume follicles and muscle spindles [46]. Herbst corpuscles are sensitive to high-frequency vibrations between 100-1000 Hz and are found in high concentration on the leading edge of the alula feather, implying a possible role in flight control [47]. Rapidly and slowly adapting mechanoreceptors in the skin, located at the base of filoplume follicles, may provide information on airspeed and stall angle [48, 49]. Muscle spindles could be used for the control of tension in skeletal muscles [50], and those in the mesenteries (tissues connecting internal organs to abdomen wall) may provide acceleration information [43]. Birds receive a range of sensory information during flight, but significant further research is required to understand how it is processed and used for flight control [45].

The flow conditions experienced by birds are more complex than those of conventional aircraft cruising in the tropopause. As mentioned previously (section 1.3), the aerodynamics of bird flight is complex due to high atmospheric turbulence near the ground and the Reynolds numbers at which birds fly. The roughness and porosity of feathers add even more complexity. Laminar-turbulent transition and separation bubbles have been observed on model owl wings with and without hairy surfaces [51–54]. Compared with the original smooth surface, these hairy materials (similar to the soft surface of owl feathers) reduced the extent of the separation bubble and influenced transition. Interestingly, the application of these surfaces resulted in increased drag [55], since the increase in skin friction was greater than the reduction in pressure drag [56]. Not all surface types yield the same result however. Experiments with starling models in a wind tunnel showed that sandpapered surfaces delay the onset of stall, with significant differences in the drag polar above 10° [57, 58]. Measurements of transition over prepared swift wings using a stethoscope showed that although the protruding shafts of their primaries feathers trigger boundary layer transition, laminar flow is obtained over the majority of the wing because the chord is similar to the distance travelled by the air after transition initiation [59]. The outer vanes of both primary and secondary flight feathers allow air to pass through, which may influence the flow in the boundary layer [60].

These numerous and complex structural, physiological and aerodynamic factors interact with one another, resulting in the dynamic shape changes observed in free-gliding birds. Wing shape can be described using spanwise camber, geometric twist, sweep, dihedral and thickness [4, 61], all of which may exhibit asymmetry between

the wings. Interspecific tail shapes vary considerably [62, 63] and can be twisted, elevated, spread and yawed about the pygostyle bone (fused caudal vertebrae)² [64–67]. Birds also use their legs to control rate of descent by reducing their lift-to-drag ratio [68, 69]. For example, African white-backed vultures (*Gyps africanus*) use this technique to increase their descent rate onto carcasses [70]. Birds also move their heads during flight, both for looking around and to stabilise their visual field with head saccades during turns [64]. The shape and flight dynamics of birds is further complicated by the different flight styles adopted, such as flapping, soaring, hovering, bounding and stooping (i.e. the wings tucked attacking dive of some falcons). All of these dynamic shape changes affect the bird’s mass distribution, further complicating the flight dynamics [39].

In summary, the flight dynamics of gliding birds is a challenging research area, requiring appreciation of aerodynamics, mechanics, physiology, structures, dynamics and control. Studying each individual element is important, but ultimately a bird must be understood as an integrated system [39]. Current progress towards this goal is limited, even with respect to the individual elements described above from figure 1.3.

In the following section, we will review existing literature on the flight dynamics of birds, with a particular focus on gliding flight. This flight style is simpler to analyse than flapping, and was therefore considered a more appropriate place to begin, given the complexity of this subject. Furthermore, the motivation for this research was based on fixed-wing UAVs (section 1.3) for which flapping has limited relevance. The review will provide a framework within which to formulate the research objectives for the current project, which are described in section 1.6.

1.5 Literature review: Avian flight dynamics

1.5.1 Key concepts

Research into the flight dynamics of birds may be categorised into three distinct subject areas: (i) static stability (ii) dynamic stability and (iii) control. In flight dynamics, ‘stability’ is defined as the tendency of an aircraft to return to its original equilibrium condition following a disturbance such as a gust of wind. Studies in aircraft stability are often ‘decoupled’ into two three-degree-of-freedom dynamic models that

²Tail twist: rotation about the anteroposterior axis of the tail. Tail elevation: pitching motion relative to the body. Tail spread: fanning out of the tail feathers. Tail yaw: rotation approximately parallel to the dorsoventral axis.

describe longitudinal (rotational: pitch, rectilinear: anteroposterior and dorsoventral) and lateral-directional (rotational: roll, yaw, rectilinear: mediolateral) motion. After a disturbance, static stability refers to the system tending towards equilibrium, while static instability refers to a divergence away from equilibrium. Dynamic stability is concerned with the damping of oscillations over time. These concepts are described in more detail in chapter 3 section 3.3. When stability is achieved solely through the aerodynamic and inertial properties (i.e. mass distribution), an aircraft is said to be ‘inherently’ or ‘passively’ stable [38], and many conventional subsonic aircraft are designed as such. Inherently unstable aircraft require some form of feedback control to avoid loss of control, which is usually achieved through a ‘stability augmentation system’ (SAS) [38, 71]. This system feeds back parameters such as angle of attack³ and pitch rate from on-board sensors to a computer, which then issues commands to the control surfaces that stabilise flight⁴. This ‘feedback loop’ lies at the heart of a SAS, and is often referred to as ‘inner loop’ control [38]. A human pilot could theoretically provide the inner loop control using their own visual and vestibular feedback, but depending on the degree of instability, this would likely lead to pilot fatigue or loss of control. The advantage of an inherently unstable aircraft is high manoeuvrability, due to its tendency to depart from equilibrium flight. This is why high-performance combat aircraft are inherently unstable, and would crash in the event of total failure of the SAS [72–75]. However, even stable aircraft may utilise a SAS to improve ‘handling qualities’⁵ if, for example, low damping results in pilot fatigue [38]. By analogy, the inherent stability of a gliding bird has significant implications for the function of its biological equivalent of a SAS, if it possesses one at all. Clearly, the inherent static and dynamic stability of a bird or aircraft has significant implications for flight control.

Aircraft may also be referred to as having ‘outer loop’ control, which is concerned with manoeuvring and course control. This could be provided by a pilot or autopilot, and also requires some form of feedback signal that is compared with a reference condition such as a compass bearing, altitude or climb rate. Birds utilise a combination of visual and vestibular feedback for manoeuvres, while magnetoreception, and possibly baroreception, play a role during migration [45].

³The angle between the freestream and some reference line on the aircraft (such as chord line).

⁴In this instance, an inherently unstable aircraft is stabilised by its SAS.

⁵These define how easy or difficult most pilots find it to fly an aircraft

1.5.2 Longitudinal static stability

The longitudinal static stability of 15 species of birds was estimated by comparing the anteroposterior positions of their centre of mass and wing aerodynamic centre⁶ (figure 1.4) [76]. Dead birds were arranged in an approximate glide configuration, with the wings swept as far forwards as possible while fully protracted. A plumb-line was hung from three different positions on each bird and used to estimate the centre of mass. The aerodynamic centre of the wing was assumed to act at the quarter-chord, based on thin aerofoil theory [3]. The relative positions of the centre of mass and aerodynamic centre suggested that 11 of the 15 species were longitudinally statically stable during gliding flight. In these measurements, the wing aerodynamic centre was used as a proxy for the neutral point⁷ of the bird. This finding agreed with observation-based indications of longitudinal stability, including aft-sweep and washout of the wings [77] and pendulum stability⁸ from a high-wing/low-body [78]. Experiments with very simplified bird-like configurations showed that the removal of the tail resulted in a change from longitudinal stability to instability, leading to the conclusion that birds are probably statically stable in pitch [79]. These conclusions were opposed by the notion of a gradual transition from longitudinally stable to unstable flight based on fossil evidence that the tails of birds have shortened over time [67], that extant birds can fly without a tail and that natural selection should favour increased manoeuvrability in the ‘arms race’ between predator and prey [8, 9, 68]. This idea finds support from wind tunnel experiments with models of extinct flying animals [80], however, the strength of these conclusions depends on whether fossils can be used to accurately determine in-flight geometry and centre of mass position.

The findings of Thomas & Taylor [76] were based on the assumption that the configurations they used represented the least stable planform configuration, based on full protraction and forward sweep of the wings. However, this is uncertain and may also be species dependent. For example, observations and planform measurements of a Harris’ hawk (*Parabuteo unicinctus*) gliding in a tilting wind tunnel suggested that the centre of pressure for protracted wings was further forward than for retracted wings [81]. In contrast, observations of a Steppe eagle (*Aquila nipalensis*) showed that wing retraction moved the centre of pressure forwards, and was used to pitch up during

⁶The aerodynamic centre is the fore-aft point on a wing about which the pitching moment is constant with angle of attack.

⁷The neutral point is the aerodynamic centre of the wing, body and tail.

⁸For small perturbations from trim, wing lift due to pitch rotation about a low (ventral) centre of mass is stabilising, assuming the centre of mass is closely aligned to the centre of lift.

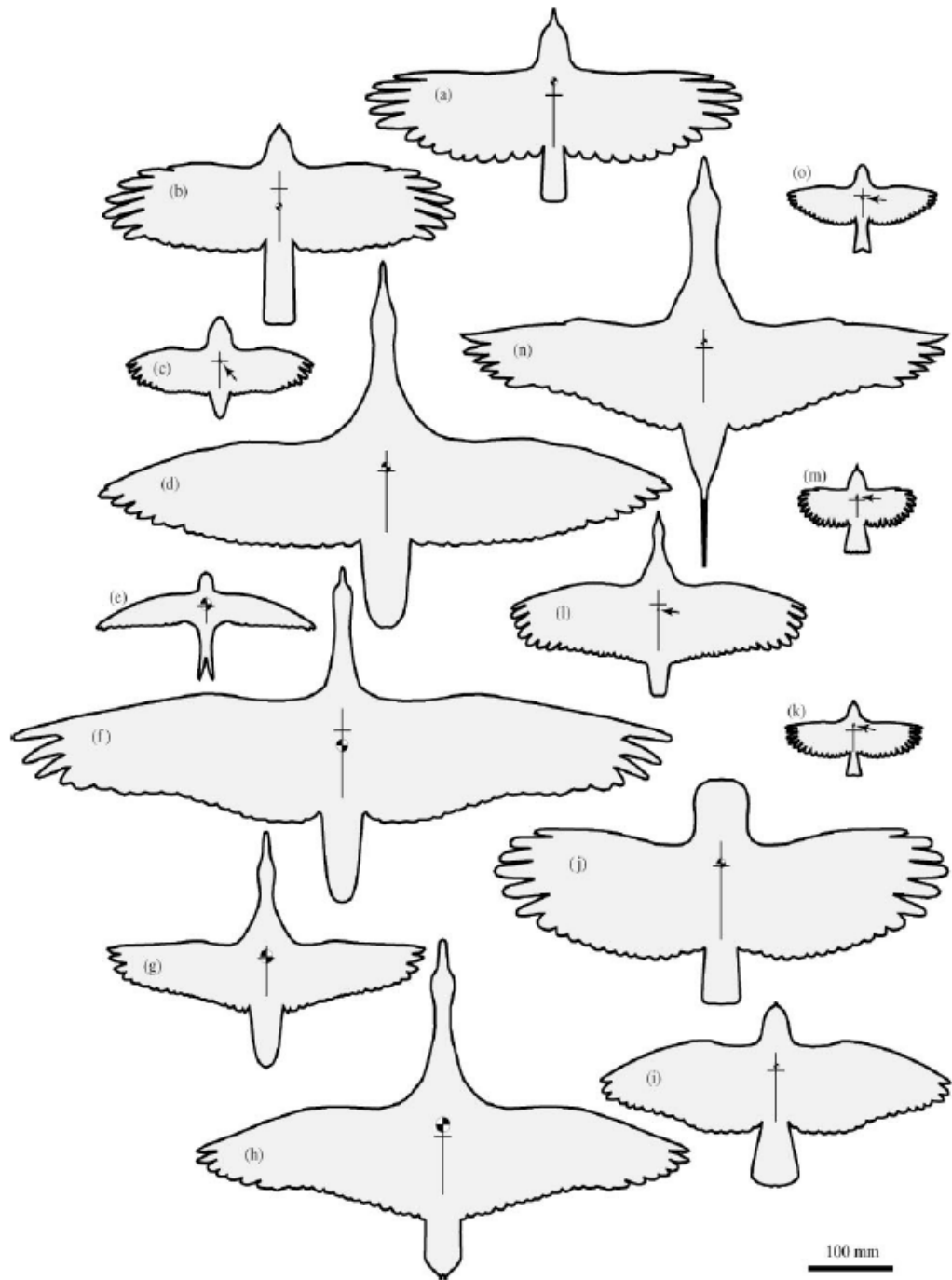


Fig. 1.4 Estimates of longitudinal static stability using dead birds. The centre of mass is indicated by the black and white circular targets, while the wing aerodynamic centre is marked using cross-hairs. From Thomas & Taylor [76]. Used with permission.

perching [82, 83]. These examples illustrate the limitations of using dead birds to estimate longitudinal static stability. In the only study with a live bird in which pitch stability was explored [81], forward movement of the centre of pressure⁹ was combined with the lowering and spreading of the tail to maintain equilibrium, suggesting that the wing was destabilising¹⁰. In summary, different species likely possess differing degrees of longitudinal static stability, but this has not yet been conclusively quantified for any bird [63, 84].

1.5.3 Lateral-directional static stability

Hypotheses about the lateral-directional static stability of birds have mostly concentrated on the implications of not having a vertical tail fin [85–89]. This feature is used on conventional aircraft to provide directional, or ‘weathercock’, stability by overcoming the destabilising contribution of the fuselage. The lack of a vertical tail has led to the suggestion that birds may be directionally unstable [68, 76]. However, scaling between aerodynamic moments and mass moment of inertia (mentioned previously in section 1.3, equation (1.1)) might imply that stabilising moments from the wing or tail are sufficient for directional stability [85, 86]. Inviscid computational fluid dynamics (CFD) estimates of the yaw stiffness derivative (change in yawing moment with sideslip angle) based on very approximate ‘bird-like’ shapes [90] at a range of lift coefficients, showed that asymmetry in induced drag due to distal aft sweep of the wings is sufficient for yaw stability [85, 86]. These computational models were used to investigate emarginated (i.e. separated) wing tip feathers with and without aft-sweep [87], variation in dihedral angle [91, 92] and the addition of a horizontal tail [89]. Aft-sweep of the emarginated wing tips increased the directional stability, as did the addition of a horizontal tail due its induced drag moment about the centre of mass.

Lift-to-drag ratio reduced non-linearly between dihedral angles of 0°, 22.5° and 45°. The effect of wing dihedral on weathercock and roll stability was unclear from these studies, due to contradictory results both in sign and magnitude between the conference paper and journal paper for C_{l_β} (rolling moment coefficient vs. sideslip angle) based on exactly the same wing model and flow conditions[91, 92]. These studies revealed the high degree of sensitivity between the bird’s geometry and several critical lateral-directional aerodynamic derivatives. Although the simulations were inviscid,

⁹The position of action of the net aerodynamic force.

¹⁰Note that this did not prove static stability or instability.

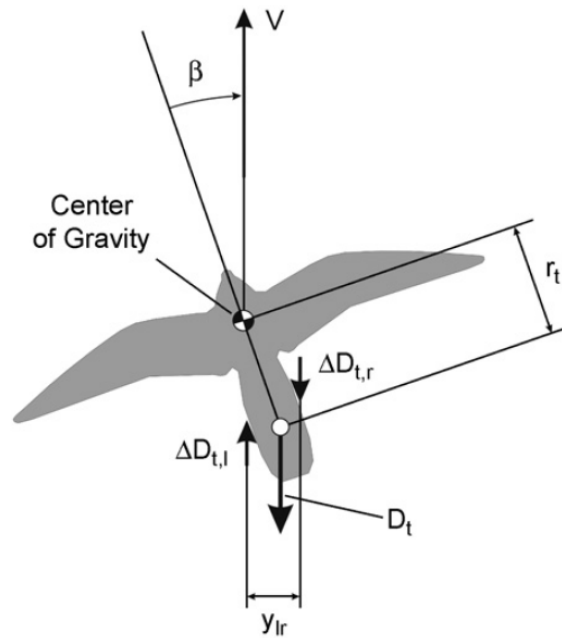


Fig. 8. Effect of ΔD_{tl} , ΔD_{tr} and D_t on the yawing moment: (a) The asymmetrical induced-drag changes ΔD_{Ll} and ΔD_{Lr} which are caused by the sideslip angle β form a couple if they are of the same magnitude. This couple yields a stabilizing yawing moment given by $N_{lr} = \Delta D_{t,l} y_{lr}$. (b) The force D_t represents the overall tail drag which is not changed by ΔD_{tr} and ΔD . It produces also a stabilizing yawing moment given by $N_{t2} = D_t r_t \sin \beta$.

Fig. 1.5 How drag on the horizontal tail in birds may contribute towards directional static stability. From Sachs [88]. Used with permission.

later wind tunnel testing of identical shapes provided evidence that these results were reasonably accurate [93]. However, the bird geometry was not representative of real animals, so the results may only be used to provide general indications about stability in birds that could easily change with the use of different morphologies. Furthermore, wind tunnel tests with similar bird-like shapes, showed that adding a tail does not increase yaw stability if it is unloaded [79]. In these experiments it was necessary to twist the tail in order for it to increase stability, suggesting that birds may use transient morphing of their tails to modulate their directional stability [76, 79].

Roll stability is usually associated with wing dihedral and aft sweep [38], and simple observation of these has been used to draw tentative conclusions about the roll stability of birds [76, 94]. However the complex coupling between roll and yaw means that inferring lateral-directional stability from morphology is ill-advised [65, 76]. Lateral-directional stability has also been explored using bird-like radio-controlled gliders [95]. Experience with these was consistent with the previously mentioned CFD models of ‘bird-like’ shapes [85, 86, 89] in that the wing and tail appeared to provide a small degree of stability.

In summary, a few studies have been conducted in which several important lateral-directional stability derivatives were quantified against changes in lift coefficient. However, these studies used highly-simplified bird geometries or gross approximations of real birds, without regard for centre of mass position. These findings are therefore useful for a general appreciation of how bird-like geometric features may affect stability, but cannot be used to infer anything about real birds, whose shapes are significantly more complex.

1.5.4 Dynamic Stability

Most conventional aircraft exhibit five distinct dynamic modes¹¹ named the ‘phugoid’, ‘short period’ (longitudinal modes) ‘roll subsidence’, ‘spiral’ and ‘dutch roll’ (lateral-directional modes). Full descriptions of these may be found in introductory flight dynamics texts [38, 96]. These modes have not been quantified for any bird, although some helpful general principles have been explored.

The phugoid mode may be reasonably described using a reduced order model that is a function of air speed and lift-to-drag ratio [38]. It is almost certainly present in gliding birds [39], and probably has a higher natural frequency compared with large

¹¹These are convergent or divergent oscillatory or exponential motions that are initiated by certain control inputs or external disturbances.

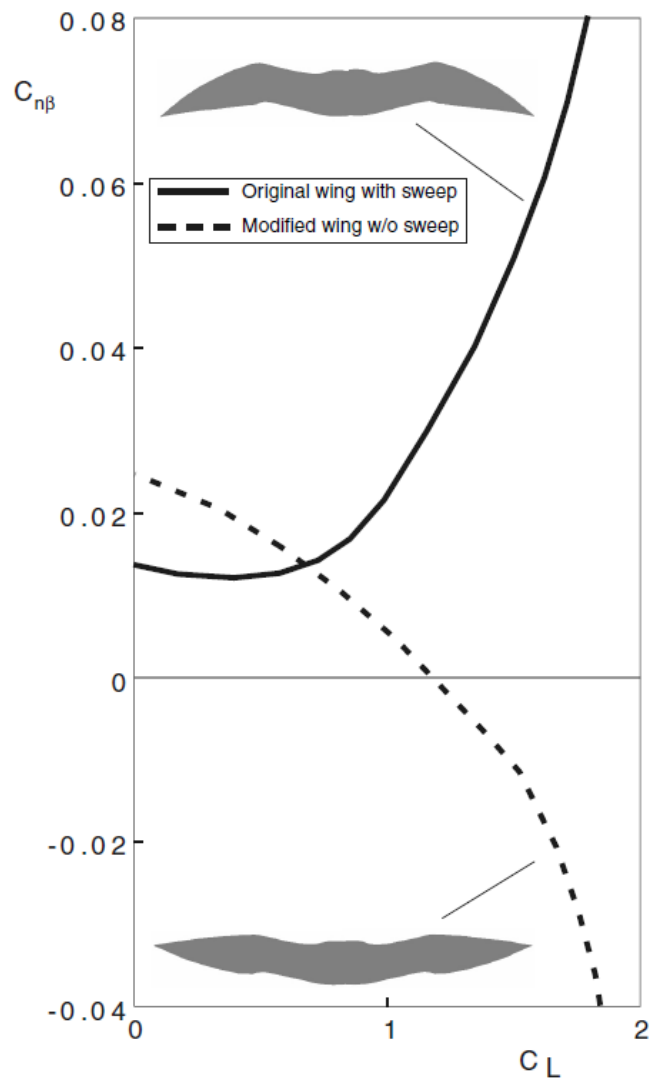


Fig. 7 Yawing moment due to sideslip of wing with sweep.

Fig. 1.6 How subtle changes in distal wing sweep may affect directional stability in birds. From Sachs [88]. Used with permission.

conventional aircraft due to the lower airspeeds involved. The short period mode depends on the degree of longitudinal static stability, which has not been quantified in birds (section 1.5.2). In conventional aircraft, short period damping is provided through the horizontal stabiliser which acts like a paddle during pitch oscillations [38]. The short moment arm in the tail of birds might imply lower damping of this mode, compared with conventional aircraft, due both aerodynamic and inertial effects (i.e. reduced paddle damping and mass moment of inertia about the pitch axis).

The lateral-directional modes of gliding birds have also not yet been quantified. Sachs [28, 88, 97] used flight handling qualities requirements [98] for human-piloted aircraft to assess the minimum required yaw stiffness and damping derivatives for acceptable dutch roll dynamics. This was based on the assumption that what is acceptable for humans must be acceptable to birds. This revealed that, similar to the static case, the wings and horizontal tail were sufficient to produce acceptable handling due to the relative scaling between aerodynamic moments and mass moment of inertia (see section 1.3). This scaling principle means that birds have a high degree of roll manoeuvrability, which has been measured in some instances to be over $1000^\circ/\text{s}$ [28, 99]. The wing and tail motions observed with a camera on-board a Steppe eagle (*Aquila nipalensis*) during banked turns, combined with accelerometer and gyroscope data, suggested that the bird may have mild spiral instability [65]. In conventional aircraft, spiral instability is acceptable if the time to double¹² is at least 4s (FHQ level 3) [98]. A stable dutch roll mode was observed in the bird-like radio controlled gliders mentioned previously [95] that was sensitive to the inertia tensor. This does not however, reveal anything about the dynamics of real birds because their shape and inertia were probably not the same as the model gliders.

In summary, neither the longitudinal nor lateral-directional dynamic stability of birds has been quantified. Models of (very approximate) bird-like shapes indicated that a vertical tail may not be required for acceptable handling qualities (assuming a human pilot), due to the scaling relationship between aerodynamic moments and moments of inertia. Current understanding of avian flight dynamics is mainly based on observations and quantitative analyses with highly approximately shapes and inertial properties that likely represent significant differences with real birds.

¹²For modes exhibiting exponential divergence, the time to double is the time taken for the motion variable of interest (i.e. forward velocity, pitch rate etc.) to double in magnitude.

1.5.5 Control

Current understanding of avian flight control is also limited, which is unsurprising given the lack of knowledge regarding flight stability (sections 1.5.2 to 1.5.4). Basic observation clearly reveals that birds change their wing planform and dihedral as well as spreading, elevating and twisting their tails [5]. By changing wing sweep, a gliding bird may achieve pitch control by adjusting the position of the centre of pressure relative to its centre of mass [77, 78, 95]. Tail elevation can also be adjusted, similar to an aircraft’s elevator, for trim and pitch control [27, 95]. The control effectiveness of the tail is probably dependent on its shape, with forked and spread tails generating more lift than rectangular tails [79]. Wing sweep, tail elevation and spread may be used in combination to achieve equilibrium during gliding [81]. Lateral-directional control during gliding may be achieved through asymmetry in wing twist and/or sweep [27, 49, 88, 100], however experimental verification of these suggested mechanisms is limited.

The role of the tail for stability and control continues to elicit debate [101, 102]. Early models treated the tail as an isolated lifting surface, and used delta wing theory to predict aerodynamic forces and tail morphing for power minimisation [62, 63, 103]. However, the validity of this approach was questionable due to the lack of interference effects due to the body and wings [104–106]. Wind tunnel force and flow visualisations with a frozen European starling (*Sturnus vulgaris*) tail and body combination (without wings) showed that leading edge vortex, slender wing and lifting line models were poor predictors of lift coefficient variation with tail spread angle, suggesting that the addition of the body had a significant effect on the aerodynamics [104]. The authors of this study suggested that the tail acts as a drag reducing splitter flap [105]. Correlation between tail spread angle and air velocity in barn swallows flying in a wind tunnel also showed that delta-wing theory did not closely predict the behaviour of the birds [106]. However, further wind tunnel testing with a frozen wood pigeon (*Columba livia*), starling (*Sturnus vulgaris*) and house sparrow (*Passer domesticus*), including the wings, showed that delta wing theory did provide reasonable predictions of lift coefficient at tail spread angles below 60° and angle of attack below 20° [107]. These experiments show the importance of modelling the bird as a complete system (figure 1.3), even when considering only aerodynamic phenomenon. The avian tail could be used for stability and control, lift augmentation during landing and turning and drag reduction, in addition to mating and display [63, 104]. Observations of

soaring birds appears to show that their tails generate lift, based on correlation between the direction of twist and wing bank angle during turning [95].

The avian wing is controlled by at least 20 muscles, yet most research has focussed only on the activity of the major flight muscle, the pectoralis and supracoracoideus, during flapping flight [45]. Electromyography (EMG) has been successfully used to measure motor impulses supplied to these muscles, in conjunction with wing kinematic data [108]. EMG recordings were obtained from an American kestrel (*Falco sparverius*) during gliding flight in a wind tunnel, revealing continuous activity from various regions of the pectoralis, supracoracoideus, biceps brachii and triceps humeralis [40] that might be suggestive of correctional control. The muscles of birds consist of at least five different fibre types that can be categorised as slow tonic and twitch types [109]. Slow tonic and slow twitch muscles are adapted for high levels of endurance during isometric (constant length) contraction, and have been found in the deep layer of the pectoralis in Laysan and Black-footed albatrosses (*Diomedea immutabilis* and *D. nigripes*) [110]. These fibre types are therefore associated with maintaining the relatively rigid pose required for soaring flight. Several groups of fast twitch fibres include 'fast oxidative' and 'fast oxidative glycolytic' [111] and are found in the pectoralis muscles of most birds [112]. These muscle fibres have fast contraction speeds required for flapping flight, but fatigue more rapidly [111]. Surprisingly, some soaring birds do not have high proportions of slow tonic or slow twitch fibres, which might imply their function in fast corrective control actuations [113].

There is some evidence that birds utilise neurological feedback for flight stabilisation, analogous to the inner loop SAS used in many aircraft. This control system is 'state dependent', and is activated when both the legs are unloaded and air flows over the breast feathers [43, 44, 114]. Applying rotations to either a pigeon's head or body results in corrective control movements from the wings and tail in pitch and roll that occur even when visual stimuli are absent (i.e. in darkness) [44]. This implies the use of vestibular feedback in flight control that may be connected to the vestibulo-ocular (ear stabilises head) reflex. However, corrective control responses were still observed in birds after their spinal chord was severed between the wings and legs, which might suggest that flight control can be achieved solely through the peripheral nervous system [43, 45, 115, 116]. The advantage of this would include reduced control system lag since the brain is by-passed. Significant further research is required to firmly establish the neurophysiological aspects of avian flight control, especially the involvement of the brain [45].

1.5.6 Summary

Comparison between figure 1.3 and current understanding of flight dynamics and control in gliding birds, shows that only limited progress has been made in each of the key areas identified, with almost no progress towards integrated models of the complete system. While understanding of individual sub-systems is important, it must always be remembered that the bird and its environment behave as a complete system, and that the different elements may interact. Understanding of these interactions may therefore result in different conclusions to those drawn from models of each individual element. Due to the complexity of this system, an integrated flight dynamics model of a gliding bird that takes all the elements of figure 1.3 into account is not likely to be a near-term prospect [39]. However, efforts towards a greater understanding of avian flight dynamics should certainly strive towards such an integrated approach.

1.6 Research questions, aims and objectives

The overall aim of this project was to quantify, for the first time, the inherent static and dynamic stability of the configurations adopted by free-gliding birds. Gliding was chosen in contrast to flapping because it represented a simpler mode of flight to measure, but still represented a significant challenge. In support of this overarching objective, the following more specific research questions were formulated:

1. Are birds longitudinally statically stable or unstable and to what degree?
2. Can birds modulate their longitudinal static stability by altering their configuration (i.e. changing wing sweep, lowering their legs, spreading their tail etc.)? Is this achieved through changes to aerodynamic forces and moments or through changes in mass distribution or both?
3. Do the glide configurations of birds possess the same dynamic modes as conventional aircraft configurations (i.e. phugoid, short-period, roll-subsidence, spiral and dutch roll), and are these stable or unstable and to what degree?
4. How do changes in configuration affect the dynamic modes of gliding birds and to what degree?
5. Can birds modulate their dynamic stability by altering their configuration? Is this achieved through changes to aerodynamic forces and moments or through

changes in mass distribution or both?

6. If birds are unstable, how do they maintain smooth trajectories during flight?

Predicting the answers to these questions is not straightforward due to the limited quantity and accuracy of previous research. Prior work on the longitudinal static stability of birds suggests that it is likely species dependent [76], and that many species may in fact be longitudinally statically stable. From an evolutionary perspective, it makes sense that the need to attack prey, avoid predators and flight in cluttered environments could provide selective pressure towards instability [9]. It seems likely that changing wing sweep and tail spread would alter both the centre of mass, mass moments of inertia and neutral point position, allowing birds to modulate their longitudinal stability. Perhaps predatory birds utilise more unstable configurations while attacking prey to increase their manoeuvrability? Regarding the dynamic modes, gliding birds probably do possess a phugoid mode [39] and may also possess a spiral mode [65]. As the spiral mode is affected by wing sweep and dihedral, it seems reasonable to suggest that birds can modulate this mode to alter their manoeuvrability. The roll-subsidence mode is almost certainly stable, due to the restorative asymmetry in angle of attack during roll. The dutch roll mode is more difficult to predict, however the lack of vertical tail might suggest this is absent in birds [38]. Given instability, birds can morph their wings and tail with multiple degrees of freedom to provide corrective control. However, the precise nature of control for stabilisation will depend on the degree of instability. Highly unstable modes will require a corresponding high response time for corrective control actions. Since these are limited by the speed of the birds' control system (i.e. nerve conduction velocity, muscle contraction rates etc.), it seems reasonable to suggest that any instability will not exceed a threshold that would make it impossible to control flight. Overall, some of the questions are more difficult to predict than others, and limited current understanding of avian flight makes most of these suggestions highly speculative. To enable these questions to be answered, the following project milestones were defined:

1. Obtain high resolution surface reconstructions of *free-gliding* birds and describe their wing and tail geometry (chapters 2 and 3).
2. Develop an approach capable of estimating the centre of mass and mass moment of inertia tensor of free-gliding birds (chapter 4).

3. Combine the surface geometry and inertial models into linear flight dynamics models of free-gliding birds to enable estimation of their inherent static and dynamic stability (chapter 5).

These objectives represent an attempt an initial step towards modelling the bird as a complete system (figure 1.3), by combining shape measurements from free-gliding flight with inertial properties (based on flights conducted outdoors in natural freestream conditions) into a linear flight dynamics model. Clearly, these three elements of ‘dynamic shape’, ‘inertial properties’ and ‘freestream conditions’ from figure 1.3 did not include all the elements of the integrated system. Moreover, the last of these three elements was incorporated only to the extent that the shape measurements of free-gliding birds were obtained outdoors in turbulent freestream conditions. However, this approach represented a significant step forwards compared with previous research involving dead birds, bird-like shapes and a lack of inertial data. It was hoped that future research would build on this foundation by incorporating the additional elements, or through the development of improved models based on the same goal.

1.7 Conclusions

Although interest in bird flight waned following the first successful powered flight by the Wright brothers in 1903, the recent growth in demand for UAV technology as sparked renewed interest from both biologists and engineers. One of the critical requirements of future UAVs is ‘agile autonomy’, yet conventional fixed-wing designs are far from this goal. This is partly due to their low mass and inertia resulting in susceptibility to atmospheric turbulence, which is particularly high in UAV operating environments. Birds however, fly through these environments with ease, continuously morphing their wings and tail for control. Understanding how birds achieve stability and control could unlock principles that can be used in the development of agile autonomous UAVs, yet current understanding of avian flight dynamics is very limited. This is because the problem is highly complex (figure 1.3) and requires the integration of numerous related phenomena such as transitional Reynolds number flows, neurophysiological control mechanisms and dynamic shape/morphological changes. A series of project objectives were formulated involving the development of a simple ‘bird as an integrated system’, combining ‘dynamic shape’, ‘inertial properties’ and ‘freestream conditions’ in linear flight dynamics models. The research was not only concerned

with quantifying the stability of free-gliding birds of prey, but also about laying the foundation for better modelling of avian flight dynamics in the future.

HIGH-RESOLUTION SURFACE RECONSTRUCTION OF FREE-GLIDING BIRDS OF PREY

2.1 Chapter summary

Birds control their flight by shaping their wings and tail, but the exact geometry during flight is difficult to quantify. Many aerodynamic studies in bird flight are based on highly approximated ‘bird-like’ shapes or cadavers that have been laser scanned or placed in wind tunnels, yet these are unrepresentative of free-gliding birds. Here, a method is presented for multi-stereo surface reconstruction of the wings, tail and body of a bird at high spatial resolution (~ 1 point per mm^2) during free-flight outdoors. The method utilised four synchronised stereo camera pairs, with sub-pixel matching between images using phase correlation. The experiment was conducted outdoors and was minimally intrusive, utilising only the naturally occurring texture patterns of the birds’ feathers for stereo surface-reconstructions of single instants in time for three flights per bird. The accuracy of this method was estimated to be $0.10 \pm 1.58 \text{ mm}$ (mean \pm s.d.). If this method were developed for use with high-speed video, it would represent a powerful new tool for dynamic wing morphing studies in flying animals.

2.2 Chapter structure

This chapter begins with a brief review of published methods for surface reconstruction of free-flying birds. A new multi-stereo approach, capable of reconstructing the wings, body and tail of free-gliding birds is then presented in detail. The main output from the method is presented and discussed, along with the benefits and limitations of the method.

2.3 Introduction

Birds manipulate the aerodynamic forces and moments governing their motion by changing the shape of their wings and tail. The difficulty of measuring the shape of freely flying birds means that little is known about the precise morphologies adopted for flight control. Wing models based on measurements of narcotised or dead birds [4, 13, 16–18, 20, 52, 54, 90, 117, 118] may not accurately represent the wing geometry in flight, due to the subjectivity of manually positioning the wings and the lack response by the bird to aerodynamic loading and flow conditions [119]. Comparison between the measured wing cross-sections of a pigeon (*Columba livia*) when freely flying and narcotised, showed significant differences in aerofoil shape [21]. These geometric differences resulted in significantly different aerodynamic drag polars [23]. This has motivated the development of methods for directly measuring the wing shapes of freely flying birds.

Stereo-photogrammetry with manual point matching has been used in a number of previous studies to measure the wing geometry of flying birds. The dorsal wing surface of a house sparrow (*Passer domesticus l.*) was reconstructed from ~ 100 points measured during flight in a wind tunnel [14, 15, 120]. This approach was later combined with wing thickness measurements from narcotised birds to enable reconstruction of ten aerofoil sections from a gliding pigeon (*Columba livia*) [21, 22]. The dorsal and ventral surfaces of a starling (*Sturnus vulgaris*) gliding in a wind tunnel have been measured using several stereo camera pairs, revealing distinct differences in wing geometry at different flow velocities [121]. A cross-section through the arm wing of a perching steppe eagle (*Aquila nipalensis*) was estimated based on ~ 250 points measured using multi-station photogrammetry and manual point matching [119]. More recently, two approaches with significantly higher spatial resolution ($\sim 10^4$ points) have been developed. In the first, a moving, multi-camera stereo arrangement along with a projected random dot pattern was used with automated point matching based on normalized cross-correlation. This approach allowed the reconstruction of a single wing of a barn owl (*Tyto alba*) at 1 kHz temporal resolution, revealing the complex variation in wing camber, twist and thickness during a complete flap cycle [61]. In the second, the deformation of a structured light pattern filmed by a single camera was used to automatically reconstruct the dorsal surface of both wings of a pacific parrotlet (*Forpus coelestis*) in flapping flight at 3.2 kHz [122].

In this chapter, a method is presented for high spatial resolution (1 point per

mm²) photogrammetric reconstructions of the surface of freely gliding birds outdoors at a single instant in time. The approach is minimally intrusive to the bird, can be used outdoors and is relatively low cost (\sim £10k), with a ‘measurement volume’ approximately 3 m long \times 2 m wide \times 3 m high. Details of the measurement method and accuracy are presented with example reconstructions of a free-gliding barn owl (*Tyto alba*) and peregrine falcon (*Falco peregrinus*). The benefits and limitations of the method are discussed in the context of existing methods for imaging birds in flight.

2.4 Experimental animals

A one-year-old adult female barn owl (*Tyto alba*) and three-year-old adult male peregrine (*Falco peregrinus*), familiar with performing flights on cue in front of cameras, were flown in an open field to facilitate the most natural flying conditions. The two bird trainers iteratively adjusted their positions so that each bird glided in front of the cameras (see section 2.5) prior to initiation of the perch manoeuvre. Flights took place in summer during dry weather and light winds (\sim Beaufort scale < 3) to maximise light levels and minimise potential camera vibration. The barn owl flew between the gloves of two bird trainers spaced approximately 18 m apart, and would naturally glide for several metres prior to initiating its perch sequence. The peregrine would only glide given a significantly longer flight path of approximately 60 m, with an elevated take-off position situated on a small grassy mound about 3 m high. Rather than landing on a glove, the peregrine flew to a lure placed on a table where it landed at relatively high speed compared with the barn owl. A 1.2 m fence was erected prior to the measurement volume to prevent the birds flying in ground effect, and to facilitate photographs of their ventral surfaces. The fence did not represent a challenging obstacle to natural gliding flight and ensured the birds were more than a wingspan in height above the ground [123]. After one day of training, the barn owl reliably glided past the camera setup. In contrast, the peregrine’s speed and trajectory varied between flights, even though it consistently flew on demand. All data were then collected during a second day in which the barn owl completed ten flights while the peregrine completed twenty-four flights. Since the barn owl flew very consistently, three representative flights with the highest image quality were selected for analysis. Only three of the twenty-four peregrine flights were suitable for analysis due to variation in its position and reduced image exposure later in the day. All work was approved by the University of Bristol Animal Welfare and Ethical Review Body (UIN UB/14/049).

2.5 Experimental setup

The experimental setup consisted of eight digital single lens reflex (70D, Canon, Tokyo, Japan) cameras arranged in pairs above and below the expected flight path (figure 2.1). Two camera pairs were mounted on a 4.7 m mobile access tower to image the bird's dorsal surface, while the other two pairs were placed level with the ground looking up at the bird's ventral surface. Each camera pair had a baseline of approximately 230 mm, with the bird at a range of 2-3 metres.

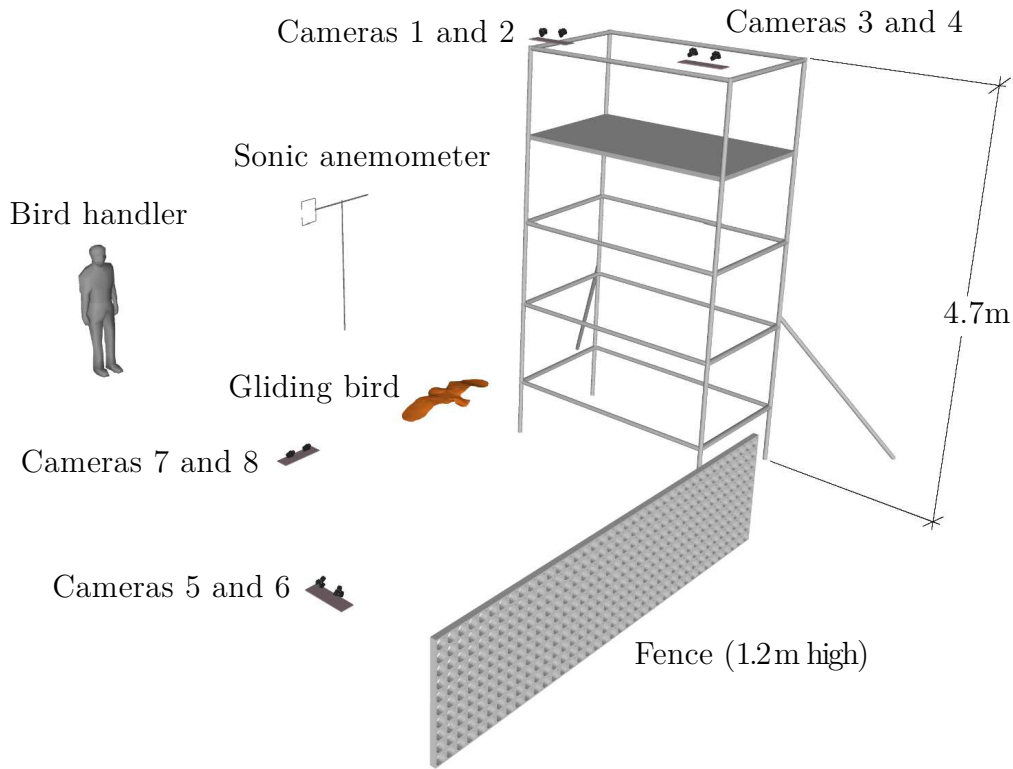


Fig. 2.1 Scale view of experimental setup. Cameras 1-4 were mounted on a mobile access tower, while cameras 5-8 were mounted on custom made supports recessed into the ground to maximise the field of view.

Variable focal length lenses (17-50 mm f2.8 XR Di II VC, Tamron, Tokyo, Japan) allowed the field of view to be adjusted depending on the consistency of the flight paths. The focal lengths used were approximately 30 mm for cameras 1-4 (dorsal view) and 17 mm for cameras 5-8 (ventral view) with the bird taking up approximately 0.2 megapixels of the 20 megapixel sensor area (figure 2.2). This small area

provided a spatial resolution of approximately 1 point per mm^2 and allowed the exposure to be increased without introducing motion blur, as well as keeping the bird close to the centre of the image where lens distortion was minimised. A maximum ISO 200 was used to minimise noise in the images. Shutter speeds of $1/2500\text{ s}$ and $1/4000\text{ s}$ were required for the barn owl and peregrine respectively to avoid motion blur. Increasing the focal lengths (i.e. zooming in) would have increased the resolution, but would have reduced the size of the measurement volume. An even faster shutter speed would also have been required to minimise motion blur, reducing exposure. There was therefore a trade-off between resolution and exposure. The cameras were electronically synchronised to within $\sim 1\text{ ms}$ using a commercially available system (Time ControlTM/Camera ControlTM digital systems, Digital Air, Geneva), ensuring any change in the bird's shape was negligible between the images. The mis-synchronisation was likely due to subtle variations in the mechanics of the cameras rather than the electronic synchronisation signal. To avoid the need for recalibration, it was necessary to position equipment such that the flight path was into the prevailing wind and for the ventral view cameras to be pointing away from the sun for as much of the day as possible. The cameras were triggered manually as this reliably captured the bird at the centre of the image. The distance between the centre of the measurement volume and the landing point was approximately 4 m for the barn owl and 9 m for the peregrine.



Fig. 2.2 Example images from cameras 1, 3, 5 and 7 used to reconstruct barn owl flight O1.

Video cameras (Lumix DFZ400, Panasonic, Osaka, Japan and GoPro Hero 3+, GoPro Inc., San Mateo, CA, USA) running at 100 fps with resolutions of 1280 x 720 pixels and 1280 x 960 pixels respectively, were positioned either side of the flight path. The GoPro camera was placed on the scaffold tower with the wide-angle lens providing video footage of each flight from a range of approximately 2 m. This is referred to as the 'tower' video camera from here on. The Lumix camera located in the field was oriented towards the camera setup and captured flight behaviour several metres before and after the measurement volume. This is referred to as the 'field' video camera from here on. The footage was used for the qualitative assessment of each flight and estimation of the bird's ground velocity. A 3-axis sonic anemometer (HS-50, Gill, Lymington, UK) sampling at 4 Hz was placed approximately 6 m from the centre of the measurement volume, and was used to measure the local wind velocity during each flight.

2.6 Experimental procedure

2.6.1 Overview

Figure 2.3 shows the main steps used to generate surface reconstructions of the free-gliding birds from the original images. Firstly, stereo reconstructions of the dorsal and ventral surfaces of the bird were generated independently using each camera pair (i.e. $\times 2$ dorsal, $\times 2$ ventral). The stereo reconstructions were then aligned to form the complete bird. Reduced measurement quality near the edges of each stereo reconstruction meant that these were removed, and an alternative approach was used to reconstruct the edge position. Finally, the aligned stereo reconstructions and the edge reconstruction were transformed to a coordinate system amenable to flight mechanics analysis. Each part of this process is now described in more detail.

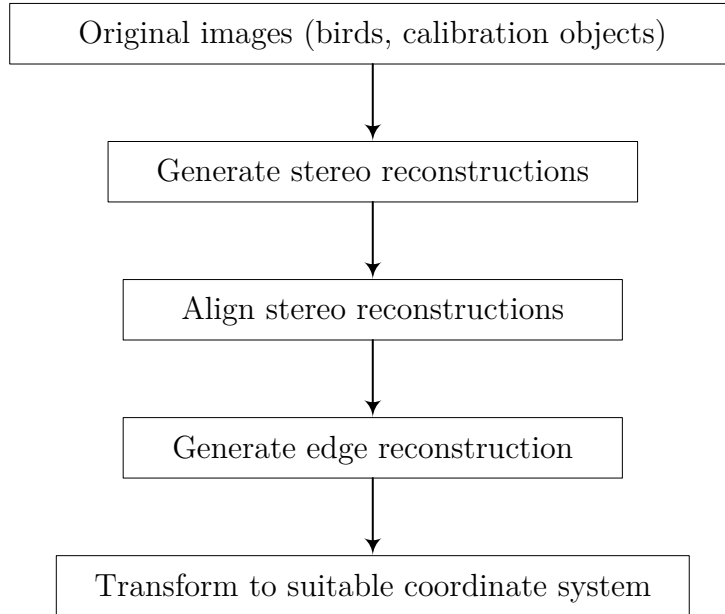


Fig. 2.3 High-level overview of the surface reconstruction process.

2.6.2 Basic principle of stereo reconstruction

Stereophotogrammetry is a well-established technique for three-dimensional reconstruction of points in a scene [124]. The ideal case represented in figure 2.4 shows two

rectilinear camera sensors, s_1 and s_2 , with their respective centres of projection, c_1 and c_2 , triangulating a point, P , in a scene. Using similar triangles, the depth Z can be estimated using

$$Z = f \frac{B}{x_1 - x_2}, \quad (2.1)$$

where f is focal length and B is the ‘baseline’.

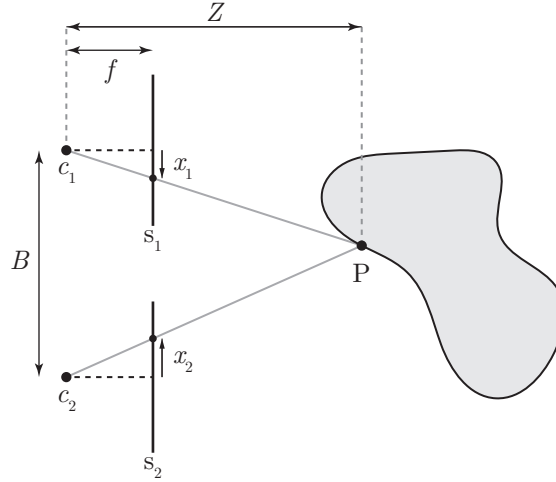


Fig. 2.4 The basic principle of stereo 3D reconstruction.

The ‘disparity’, $x_1 - x_2$, is the horizontal distance between matching points in the two images. To estimate the depth, Z , in equation (2.1) it is necessary to know the positions and orientations of the two cameras relative to one another (i.e. B), their internal geometry (i.e. f) and the image coordinates of matching points in the scene (i.e. $x_1 - x_2$). Most real applications of stereo-photogrammetry are more complex than the ideal case described by figure 2.4 and equation (2.1), and require estimation of lens distortion coefficients, principal points (intrinsic) and the translation and rotation of two cameras relative to one another in six-degrees-of-freedom (extrinsic) [124]. The role of camera calibration is to provide accurate estimates for these geometric descriptors of the cameras.

To reconstruct large numbers of points, disparity estimation can be automated through a process known as ‘image matching’. When large numbers of matched points are identified, a ‘disparity map’ is generated from which it is possible to generate high-resolution, reconstructions of the surfaces of objects in a scene.

2.6.3 Stereo reconstruction

2.6.3.1 Disparity estimation

To maximise regions of the bird's surface visible to both cameras, a relatively low baseline-to-object-distance ratio ($B/Z \sim 0.1$) was used. While this was beneficial for maximising surface coverage, smaller B/Z could potentially reduce accuracy because the triangulation process becomes more sensitive to matching errors. It was therefore important to estimate the disparity to high accuracy.

Disparity estimation may be broadly categorised into feature and area-based methods [125]. Feature-based methods match distinctive objects in the images such as edges and corners, while area-based methods utilise a small window (usually square) that scans the images and finds the best match for every unique window position. If the image texture is sufficiently unique for each window position, this can achieve very high-resolution 3D reconstructions because every pixel in the reference image is matched to a corresponding position in the target image. As a result, area-based methods tend to yield higher resolution than feature-based methods simply because a match is sought for every pixel.

One particular area-based approach is phase-correlation, which utilises the Fourier shift theorem

$$h(x, y) = g(x - a, y - b), \quad (2.2)$$

$$H(u, v) = G(u, v) \exp \{ -i(ua + vb) \}, \quad (2.3)$$

where g and h are two images with a relative translational shift, (a, b) , with $G(u, v)$ and $H(u, v)$ denoting their Fourier transforms. Calculation of the normalised cross power spectrum, $Q(u, v)$, (also termed the phase correlation matrix) isolates the phase difference between the two images, as shown in equation 2.4 where \star indicates the complex conjugate:

$$Q(u, v) = \frac{G(u, v)H(u, v)^\star}{|G(u, v)H(u, v)^\star|} = \exp \{ -i(au + bv) \}. \quad (2.4)$$

Several approaches have been developed to obtain a and b from equation 2.4 [126–129]. A common approach is via the inverse Fourier transform of $Q(u, v)$ and subsequent identification of the function peak, which can be obtained to sub-pixel accuracy by curve fitting [130, 131]. A more accurate, but slightly slower approach is to fit a

plane to the 2π unwrapped phase shift data (r.h.s. equation 2.4) in order to yield the translations, a and b . These approaches can be extended to account for rotation and scale differences in the spatial domain by representing the Fourier transforms in polar and logarithmic coordinates respectively [132, 133].

To generate 3D reconstructions of the gliding birds, the Phase Correlation based Image Analysis System (PCIAS) software was used [134]. PCIAS implements recently developed phase-correlation-based algorithms that can achieve accuracies of up to 1/50th pixel, significantly outperforming most commonly used matching techniques such as normalised cross-correlation [135]. PCIAS computes pixel-to-pixel disparity maps for image pairs via a scanning window that refines the disparities using a coarse-to-fine, multi-resolution pyramid, after an initial whole image registration step, also carried out using phase correlation [136]. At each pyramid level but the last, the faster but less accurate curve fitting approach is used. Then for the final, full resolution pyramid level, the more accurate 2D-fitting approach is used. The advantage of the pyramidal approach is that large disparities in the full resolution images can be estimated using a small scanning window (usually 16×16 or 32×32 pixels). The susceptibility of pyramidal approaches to error propagation is mitigated through the use of adaptive size median filtering at coarse pyramid levels and median-shift-propagation filtering at the full resolution level [137].

PCIAS was developed to generate digital elevation models used, for example, to measure changes in the earth's surface after an earthquake [138]. It also works effectively in the context of close-range photogrammetry and was therefore used to compute disparity maps for each camera pair. One challenge however, was the parallax between the bird, camera pair and background, which meant that the scene information around the edges of the bird was very different between the two images. Furthermore, the image area occupied by the background was much greater than that occupied by the bird and resulted in the initial registration step aligning the background rather than the bird. These challenges were largely overcome by manually masking the background. Masking around the edges of the bird, however, tended to increase the matching errors in this region due to the sudden loss of image data. A more effective approach was to offset the mask by a half-window size from the edge of the bird. Even with this approach however, the parallax still caused unrealistic 'edge artefacts' in the 3D reconstructions. These included span and chord-wise waviness, or sudden divergence of the otherwise smooth surface likely due to the median filter smoothing matched points at the edges of the bird with matched background

points. These errors were typically observed up to around a half window size inside the edge of the bird, so the reconstructions of these pixels were not used. A window size of 32×32 pixels was used for all reconstructions except the dorsal surfaces of the peregrine for flights P2 and P3 where a 16×16 window size generated slightly more accurate disparity maps. A median-shift-propagation filter size of 15×15 pixels was used to smooth the full-resolution disparity map.

2.6.3.2 Stereo calibration and reconstruction

Each camera pair was calibrated using the MATLAB computer vision system toolbox [139] with a 300 mm square planar array of 196 circular reference points whose spatial distribution was known precisely. The calibration routine used bundle adjustment to optimise the first two radial lens distortion coefficients only, as testing showed negligible difference in taking additional distortion coefficients into account. A minimum of 40 images was obtained for each pair, from locations covering the full extent of the measurement volume. Images with high mean reprojection error ($\text{MRE} > 1$ pixel) were removed, resulting in a MRE across all the stereo calibrations of less than 0.7 pixels. The image coordinates of the grid points were calculated semi-automatically using Calibration Toolbox v1.3.2 [140], and then used with Matlab’s ‘estimateStereoParameters’ function to compute the calibration. The images were undistorted prior to estimating the disparity map using PCIAS. The surface reconstructions were then generated using the MATLAB ‘triangulate’ function for each camera pair’s disparity map and calibration [139].

2.6.3.3 Stereo alignment

To align the stereo reconstructions, an additional calibration was carried out using cameras 1, 3, 5 and 7, referred to here as the ‘global calibration’. This was done using EasyWand5, a wand calibration algorithm utilising sparse bundle adjustment [141]. Around 40 images were obtained of a custom-made wand with two 50 mm diameter spheres whose centres were spaced 529.2 mm apart, distributed evenly around the measurement volume. The image coordinates of the wand were estimated manually by carefully drawing an ellipse around each sphere. When calculating the calibration, the initial values for the intrinsics were provided from the stereo calibrations, and were then further optimised by EasyWand5. The mean reprojection error across all cameras was 0.33 pixels for the global calibration.

Fixed-scale Helmert transformations were calculated [142] between the 3D wand points measured by each camera pair and those measured by the global calibration to obtain four spatial similarity transformations used to align the stereo-reconstructions in the coordinate system of the global calibration. The alignment was effective for stationary objects (see section 2.7) for which camera mis-synchronisation had negligible impact. For the birds in motion however, the camera mis-synchronisation (~ 1 ms) resulted in alignment errors that required some correction. This was achieved by applying iterative closest point alignment to the overlapping regions of the point clouds using CloudCompare v2.8.1 [143]. Importantly, the shape of the bird is unlikely to have changed significantly due to the mis-synchronisation between images, given their relatively low ground velocity of 6-11 m/s (see chapter 3 table 3.1).

2.6.4 Edge reconstruction

A shape-carving approach adapted from Walker et al [144] was used to estimate the 3D outline (i.e. edge) of the bird. Shape-carving works by retaining 3D points in the measurement volume that reproject onto silhouette images of the object of interest, for a set of calibrated cameras. To obtain the 3D outline, erosion and dilation were applied to silhouettes of the bird based on reprojections of the aligned stereo-reconstructions, leaving only the edge of the bird in each image as shown in figure 2.5. The shape-carving process then retained only points in the measurement volume that reprojected onto these ‘edge’ silhouettes, resulting in an approximately dorsoventral outline of the bird that generally followed the leading and trailing edges of the wings.

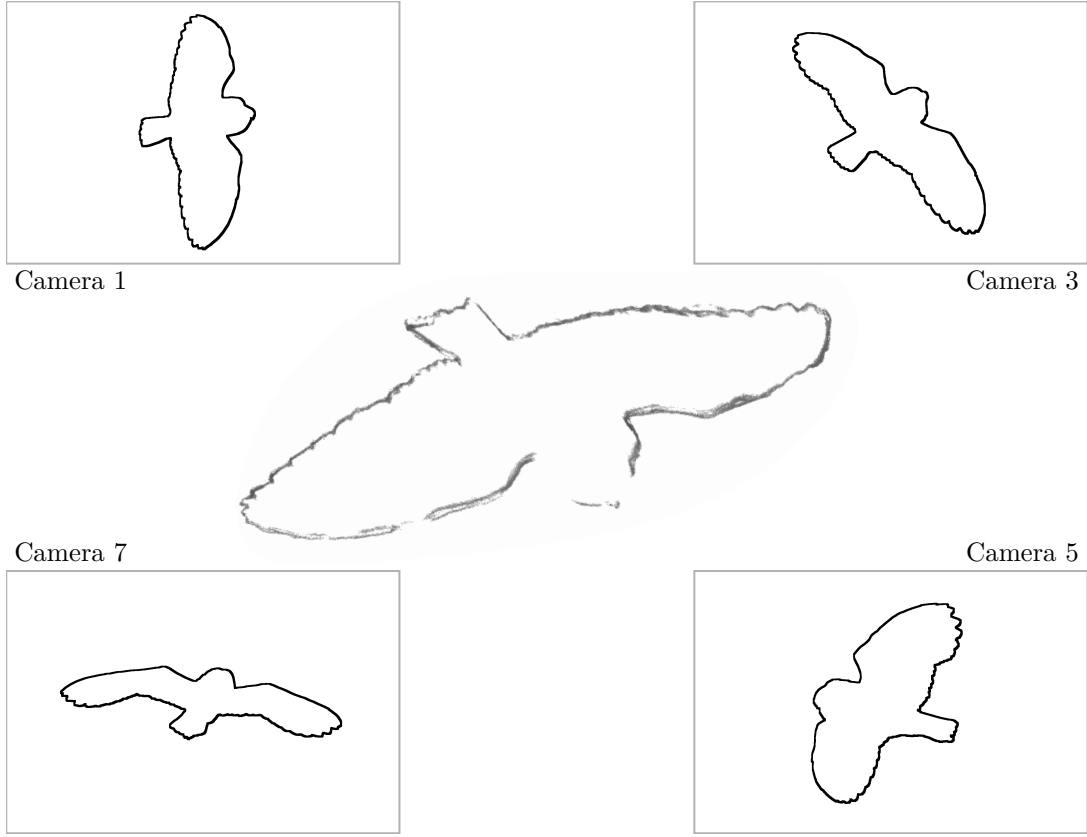


Fig. 2.5 Example edge silhouettes for barn owl flight O1 (one per camera pair) and the raw shape carved raw points (centre).

Using all the globally calibrated cameras for the shape-carving process resulted in an accurate but sparse and unevenly distributed set of points. To increase the sampling density, multiple carving operations were carried out using all possible two-camera combinations from the global calibration. This significantly increased the number of points around the edge of the bird, but also introduced a large number of spurious points. These were removed in CloudCompare v2.8.1 [143] using a distance threshold of 2mm relative to the stereo-based surface reconstructions of the bird, leaving a continuous band of points around the edge of the bird (example shown in figure 2.5).

Spline-fitting was used to recover the clean, closed-loop outline of the bird. This required the points to be sorted into a suitable order representative of a closed-loop around the edge. A bespoke algorithm was developed to do this, whose basic principle is described in figure 2.7. The raw shape-carved data were first projected onto the xy -plane. An initial point, P_i , was then chosen based on the centroid of points within a window, k_i , of size, r , located randomly on the point set (figure 2.7A). The algorithm

then resampled the edge in a closed loop by continuously searching for, and following, the edge direction. The local direction of travel was estimated using the peak spatial density in a sector swept from 0 to 360 degrees (figure 2.7B). At each iteration, the points from the previous iteration were ignored to avoid reversals in direction. Where gaps in the data existed (i.e. to the left of P_i in A), a nearest neighbour search was conducted ignoring all the points from previous iterations. A cubic interpolating spline was then fitted to the resampled points, referred to from here on as the ‘edge spline’.

2.6.5 Wing-body coordinate system

To enable the geometry of the wing to be described in an aerodynamically meaningful way (see chapter 3), the reconstructed points were transformed from the coordinates of the global calibration to a ‘wing-body’ fitted coordinate system using the method described in figure 2.6.

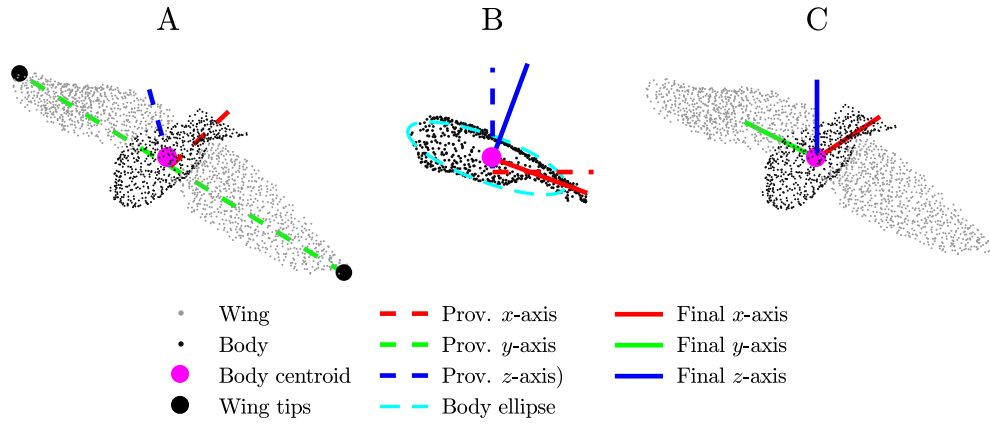


Fig. 2.6 Fitting a coordinate system to the wings and body of the bird. A) Evenly re-sampled points in the global coordinate system were segmented manually into body and wings. (The wing and body points have been further re-sampled here to improve visualisation). The origin was calculated using the centroid of the body and tail, with the two points on each wing furthest from the origin defining a provisional y -axis. A provisional z -axis was then calculated as the line coincident with the origin and perpendicular to the provisional y -axis. The cross-product of the provisional y - and provisional z - axes resulted in the provisional x -axis. B) The final anteroposterior (x) and ventrodorsal (z) axes were defined respectively by the major and minor axes of an ellipse fitted to the body and tail data projected onto the sagittal plane defined by the provisional x - and z - axes. C) The final wing-body fitted coordinate system in which the final y -axis is parallel to the provisional y -axis and coincident with the origin.

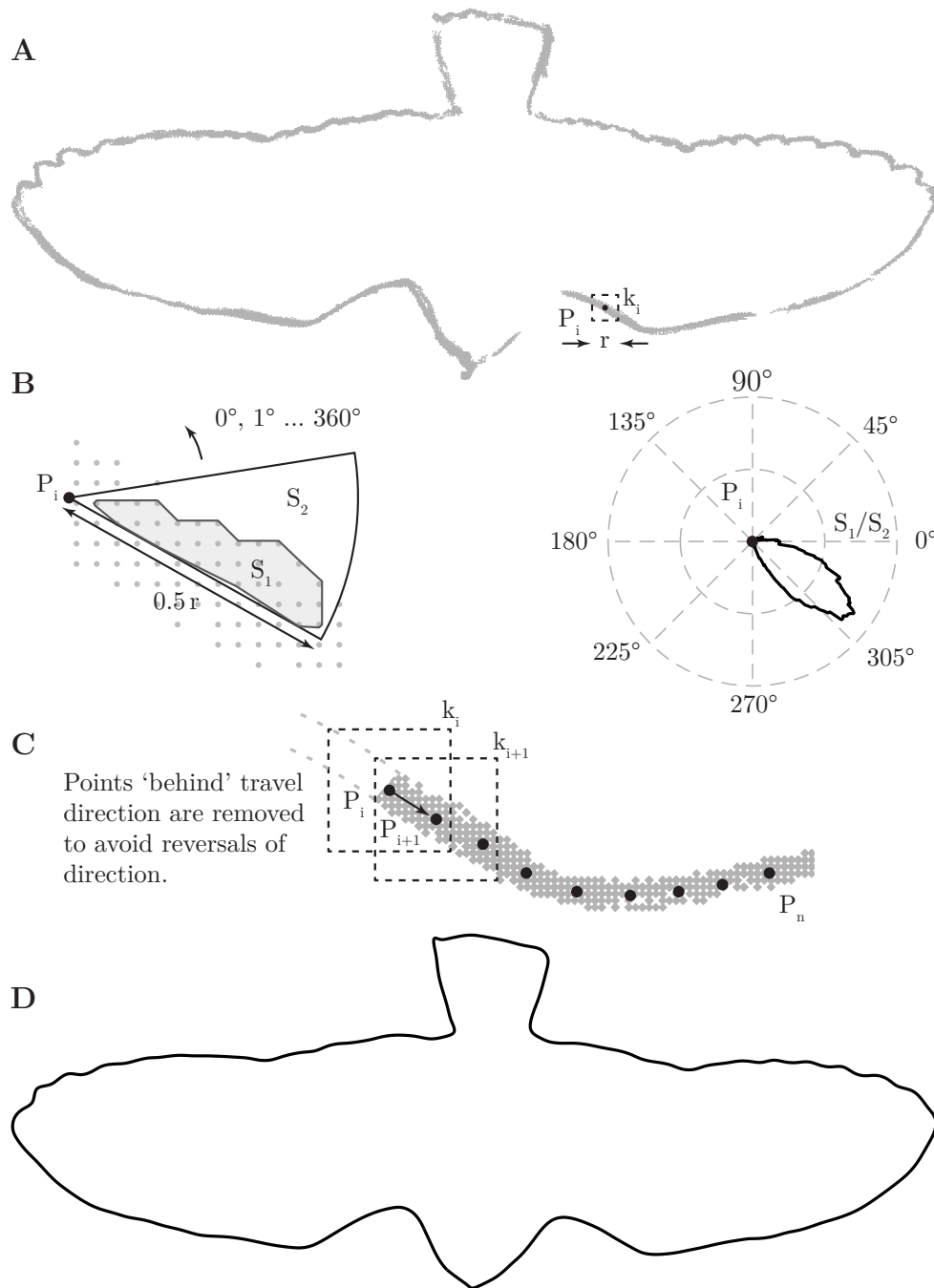


Fig. 2.7 Method developed to represent the edge of the bird. To enable parametric spline fitting (D), it was essential to correctly order the points around the edge (A-C). This was done by marching around the edge in small steps in an iterative manner. The direction of travel was determined by sampling the spatial density of the points in polar coordinates at each iteration.

2.7 Accuracy assessment

A rigid fibreglass model gull of loosely similar size, shape and texture to a living bird was laser scanned to high accuracy (Romer Absolute Arm, RA-7525-SI, accuracy 0.063 mm) and used to validate the method¹ (figure 2.8F). The stereo-reconstructions (with edges retained) were individually aligned to the laser scan using iterative closest point alignment in CloudCompare v2.8.1 [143]. The distances between the individual stereo reconstructions (one per camera pair) and the meshed laser scan were then calculated (figure 2.8A-D). Alignment was also carried out for all the stereo reconstructions (i.e. merged into a single point cloud), again with the edges retained, and is referred to here as ‘collective alignment’. Comparison of the error between individual and collective alignment of the stereo reconstructions with the edges removed is shown in figure 2.8E. Retaining the edges increased the standard deviation by approximately 0.2 mm which confirms the lower precision reconstruction in this region. Figure 2.8E shows only a small increase in standard deviation of the error for the collectively aligned points, which shows that using the reconstructed wand points for alignment is effective for well synchronised images. It is likely that a comparable error increase would be introduced by iterative-closest-point alignment of dorsal and ventral surfaces using the thin primary feathers, which was necessary for the real birds due to camera mis-synchronisation (section 2.6.3.3).

To understand the contribution of this method to the field of animal flight, its accuracy was compared with the small number of alternative approaches used to reconstruct free-flying birds (table 2.1). Due to the different error estimation approaches used, comparisons should be made with care. The error of low resolution arm wing profile measurements from a Steppe Eagle (*Aquila nipalensis*) [119] was estimated using the strongly correlated linear relationship between mean re-projection error and 3D reconstruction error to estimate the mean error [140]. No indication of the distribution of the error was given however. The mean error of 4.31 mm was based on the absolute rather than signed estimates, and is therefore not easily comparable with the present results. The 3D reconstruction error from surface measurements of the single wing of a flapping barn owl were based on the assumption that the disparity error did not exceed 0.1 pixels [61]. No attempt was made to quantify the error of the reconstructed points against an object of known shape, although visualisations of the bird

¹This validation applied to a static object, and did not assess any inaccuracies arising from the effects of camera mis-synchronisation.

appeared to be of high accuracy. In contrast, the reconstruction error of a flapping pacific parrotlet (*Forpus coelestis*) was estimated using a sphere whose diameter was known to high accuracy [122]. Comparison between the measured and nominal surface (similar to the approach presented here) enabled the mean and standard deviation of the error to be averaged over 400 frames. This approach was therefore reasonably comparable with the present results.

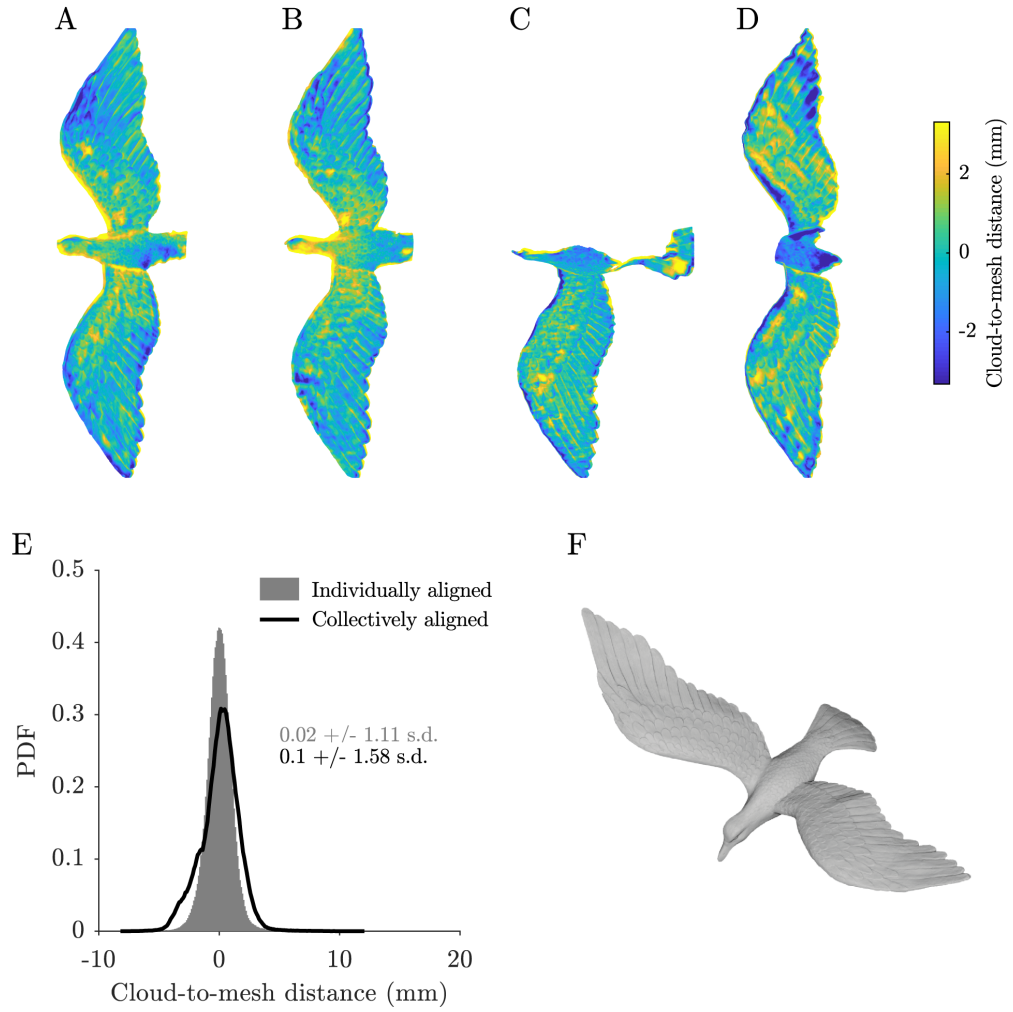


Fig. 2.8 Assessing the accuracy of the stereo reconstructions by comparison with a high accuracy laser scan. A-D) Planform views of the stereo reconstruction errors (edges retained) following individual alignment to the laser scan. The occluded regions were due either to lack of visibility from the camera view or the region around the tail where the model was held. View A corresponds to cameras 1 and 2, view B to cameras 3 and 4, view C to cameras 5 and 6 and view D to cameras 7 and 8. E) Probability density functions (PDF) of the stereo reconstructions (edges removed) both individually and collectively aligned to the laser scan. F) The laser scanned gull model.

Reference	Stated error (μ , mean, σ , s.d.)	Resolution
Butz et al [22]	range: ± 0.3 mm at distance 800 mm	Low
Carruthers et al [119]	absolute $\mu = 4.31$ mm	Low
Wolf and Konrath [61]	$\sigma < 0.3$ mm at distance 1400 mm*	High
Deetjen et al [122]	$\mu = 0.31$ mm, $\sigma = 1.03$ mm	High
Present results	$\mu = -0.016$ mm, $\sigma = 1.31$ mm	High

Table 2.1 Stated error for surface measurements of flying birds obtained from other methods. The error for the present results is based on individually aligned reconstructions without the edges removed as this was most similar to the other methods. *Error inferred from disparity estimation error rather than measured directly.

2.8 Bird reconstructions

Figures 2.9 and 2.10 show surface reconstructions of flights O1 and P1 respectively from dorsoventral, posteroanterior and lateral viewpoints. Videos of these point clouds are also available (Appendix A). The reconstructions are shown with their edges removed and have a spatial densities of approximately ~ 1 point per mm^2 (hence why individual points cannot be distinguished). Each individual point was generated based on the disparity estimate for a single pixel in the reference image, and was assigned its red-green-blue (RGB) value. The texture was not, therefore, projected onto the measured surface post-reconstruction and therefore provides a qualitative indication of the accuracy of the disparity map. The dorsoventral view also includes the edge spline and shows that removal of the edges did not result in a significant reduction in surface coverage.

Figure 2.11 shows cross-sections taken every 10% span for all flights, from the same view relative to the wing-body coordinate system, with distinct colours applied to the dorsal and ventral points. The barn owl and peregrine flights are labelled with the prefixes ‘O’ and ‘P’ respectively, which is the case for all remaining chapters. The aerofoil geometry changed markedly across the span, with increased thickness proximally towards the leading edge where the bones and muscles of the arm wing are located. The camber also reduced distally, where the sections comprise entirely of feathers. The edge spline is also plotted and shows that the tail was widely spread and twisted to the right (posteroanterior view) in P1.

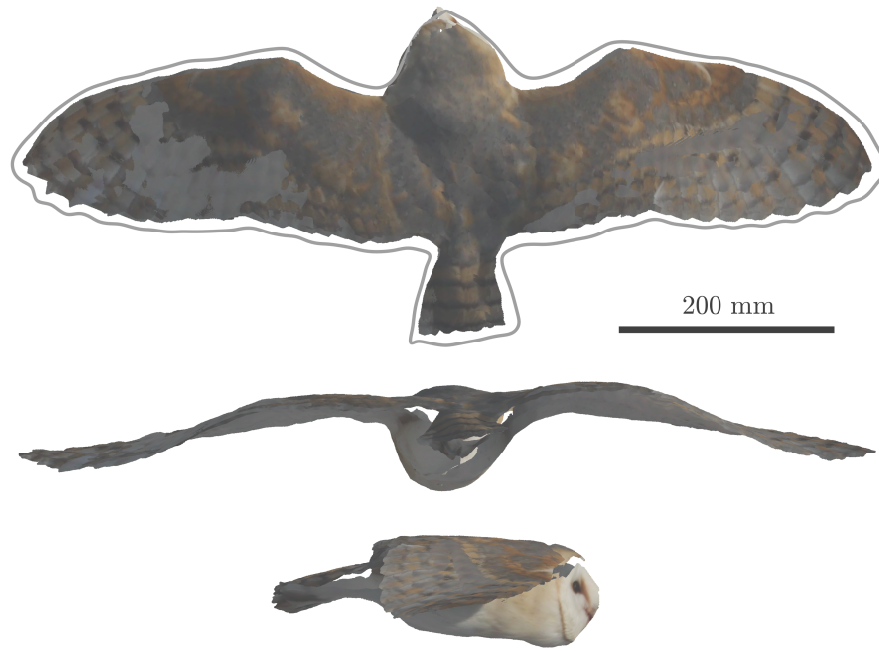


Fig. 2.9 High-resolution surface reconstruction of barn owl flight O1 showing the dorsal surface (top), posteroanterior view (centre) and lateral view (bottom).

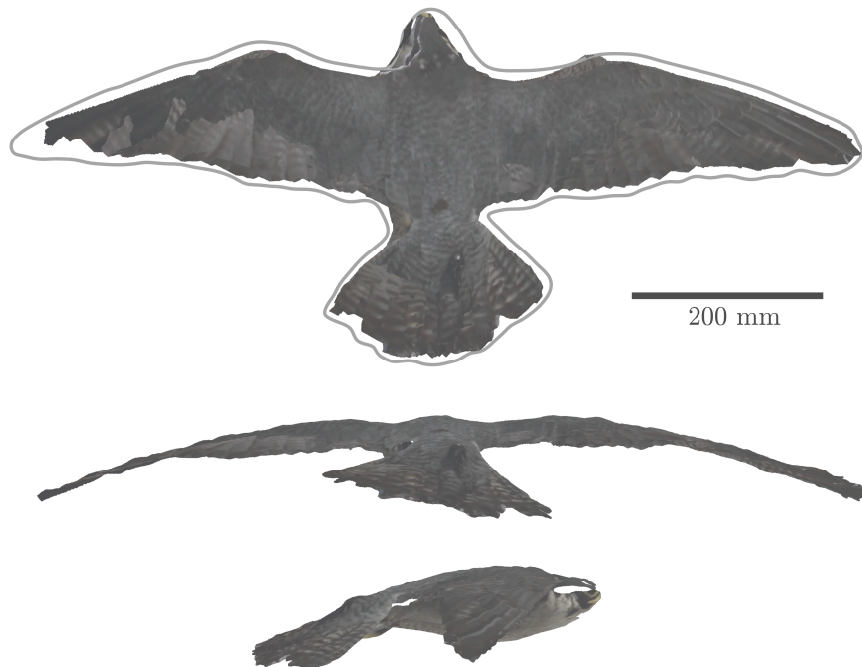


Fig. 2.10 High-resolution surface reconstruction of peregrine flight P1 showing the dorsal surface (top), posteroanterior view (centre) and lateral view (bottom).

Figure 2.11 also shows that it was not possible to reconstruct the entire dorsal surface of the left wing in flights P2 and P3, due to the locally poor exposure. The dark colouration of the peregrine's dorsal surface made it more challenging obtain well exposed images with negligible motion blur. The images were therefore sensitive to any reduction in natural light level that may have occurred (i.e. due to a passing cloud).

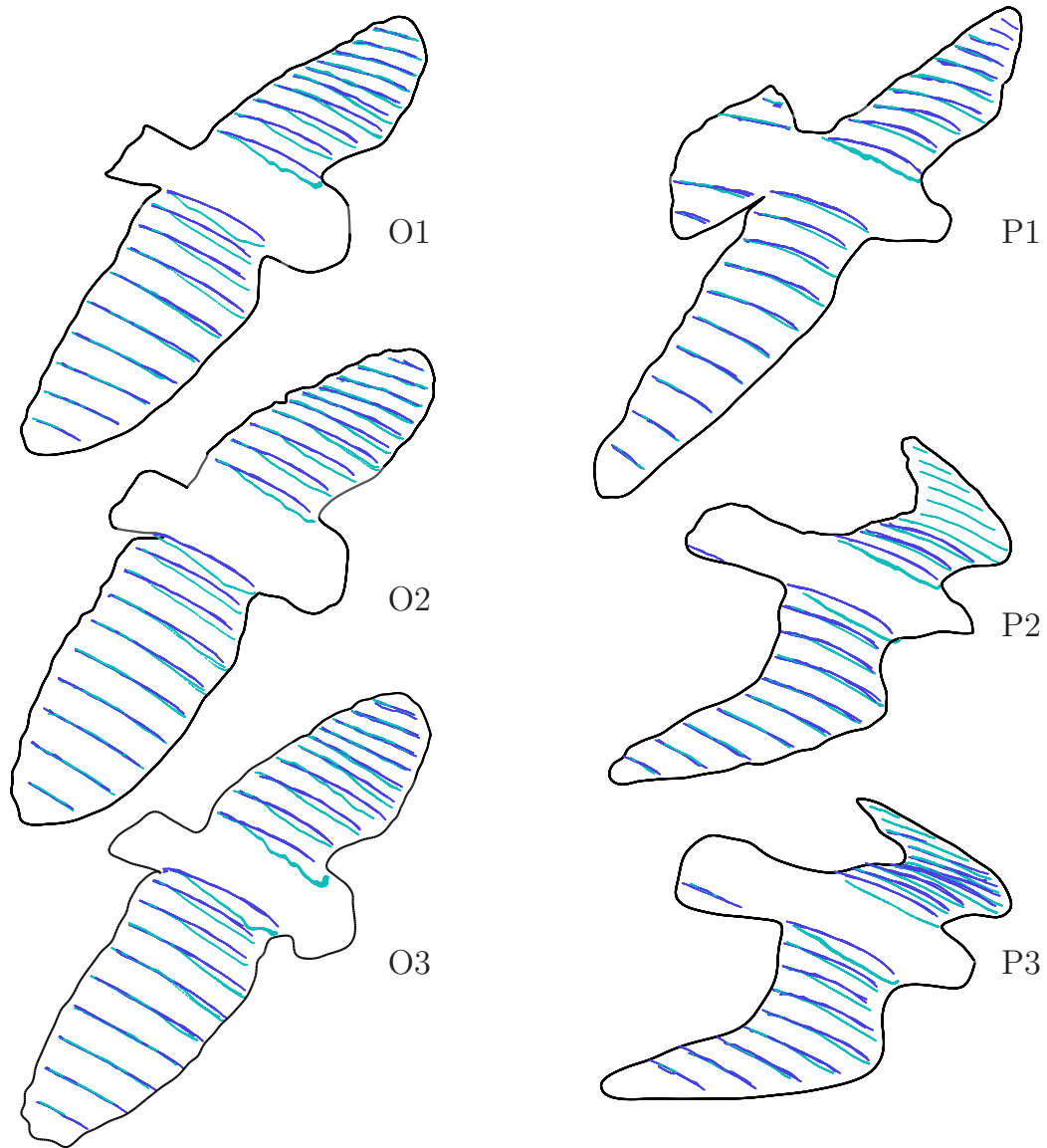


Fig. 2.11 Surface reconstruction of the wing sections every 10% span for the barn owl (O1-O3) and peregrine (P1-P3) flights including the edge spline. The dorsal surface is darker than the ventral surface to improve visualisation. The waviness apparent proximally in both wings is due to sectioning at the wing-body interface where the surface becomes almost vertical, amplifying the appearance of local noise.

2.9 Conclusions and recommendations

In this chapter, the methods used to obtain high-resolution surface and edge reconstructions of free-gliding birds of prey were described. The method represents a new combination of existing photogrammetric techniques, combining multi-view stereopho-

togrammetry with a phase-correlation-based image matching algorithm to obtain surface measurements of the almost complete surface of free-gliding birds of prey. The method demonstrates similar order of accuracy and resolution compared with published methods for reconstructing free-flying birds. It also has the advantage of being minimally intrusive to the birds, requiring only natural light for illumination of the scene, with measurements possible across a relatively large measurement volume. The equipment can be used outdoors, was assembled in several hours and was relatively low cost (\sim £10k).

The limitations of the method included the need to remove poorly matched points around the wing edges and the additional steps required to correct for misalignment due to camera synchronisation errors. The use of shape-carving to improve definition around the edges significantly improved the efficacy of the reconstructions, enabling them to be further processed into aerodynamically useful datasets (see chapters 3 and 5). However, future development of this method should still focus on obtaining high-quality stereo reconstruction data close to the edges, due to its increased surface coverage compared with the edge spline. With an increased budget, high-speed cameras could be used to overcome the mis-synchronisation issues, or alternatively a powerful strobe with a long camera exposure could be used with DSLRs. The process of masking the background could be automated if the image backgrounds were controlled.

Despite several limitations, this method yields data of sufficient accuracy to quantify the spanwise camber, twist, sweep, dihedral and thickness of a bird's wing (chapter 3) and to create geometric models for aerodynamic and flight stability analysis (chapter 5).

CHAPTER 3

QUANTIFYING THE GEOMETRY OF FREE-GLIDING BIRDS OF PREY AND IMPLICATIONS FOR LONGITUDINAL STABILITY

3.1 Chapter summary

Birds adopt a wide variety of geometric configurations in flight to suit different flight conditions, but the effect of such configuration changes on stability is not well understood. In this chapter, high-resolution surface reconstructions of a free-gliding barn owl (*Tyto alba*) and peregrine falcon (*Falco peregrinus*) obtained in chapter 2 are used to quantify wing camber, twist, sweep, dihedral and thickness in addition to tail twist and angle of attack. These measurements are used to draw conclusions about the longitudinal static stability of the glide configurations based on existing flight dynamics theory. The barn owl geometry was consistent between flights and exhibited geometric features indicative of longitudinal static instability. The peregrine adopted different configurations between flights that did not point conclusively to static stability or instability. Video footage and subtle asymmetries in the measured glide geometries showed that the birds appeared to correct for wind fluctuations that occurred during the flights. Overall this approach provides a way of accurately quantifying the geometry of free flying birds based on photogrammetric measurements, and has the potential to enable detailed studies of wing morphing in birds.

3.2 Chapter structure

This chapter introduces the concepts relating to stability within a flight dynamics context. A method is presented by which certain geometric features of a birds' wings and tail may be used to infer longitudinal static stability or instability, without prior knowledge of the centre of mass and neutral point. Methods to quantify camber, twist, sweep, dihedral and thickness from photogrammetric surface measurements of

the free-gliding barn owl and peregrine are described, in addition to the approach used to estimate flight conditions such as air velocity and angle of attack. The bird geometry, flight conditions and video data are presented and used to discuss the likely longitudinal static stability for each flight. Correctional control is also explored based on the video footage and subtle asymmetries measured between the wings.

3.3 Introduction

Birds adopt a variety of wing and tail configurations during gliding flight, yet relatively few data exist describing the complexity of avian surface geometry measured during free-flight (see chapter 2 section 2.3) where both passive (flow acting on bird) and active (bird acting on flow) influences affect the overall morphology. In this chapter, the geometry discussed in chapter 2 is described in terms of wing camber, twist, sweep, dihedral and thickness in addition to tail elevation, spread and twisting. The measured glide shapes are then used to explore whether the barn owl and peregrine flights are likely to be longitudinally statically stable or unstable.

A dynamic system is stable if it returns to equilibrium following a disturbance. Equilibrium is the condition in which the forces and moments sum to zero, and in flight dynamics is often referred to as ‘trim’ or ‘balance’. A disturbance may be a gust of wind or a control input that upsets the balance of forces and moments leading to a departure from equilibrium. An *inherently* stable system will eventually return to equilibrium following a disturbance without the need for correctional control. Inherently unstable systems diverge from equilibrium unless some form of control is used for stabilisation.

In describing the response of a dynamic system to a disturbance, it is important to distinguish between static and dynamic stability. Static stability refers to the direction of the initial response following disturbance, while dynamic stability is the tendency for oscillations to dampen out over time (figure 3.1).

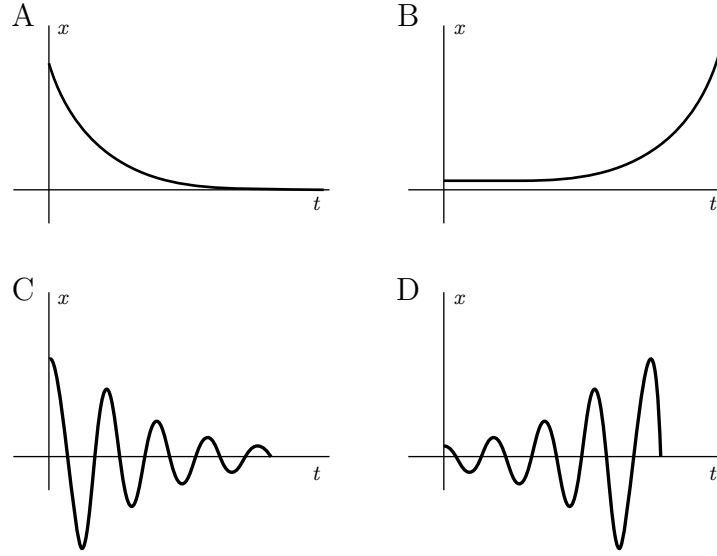


Fig. 3.1 The concepts of static and dynamic stability illustrated using plots of a system's displacement (x) vs. time (t) following disturbance from equilibrium. A) Non-oscillatory statically stable response B) Non-oscillatory statically unstable response C) statically and dynamically stable response D) statically stable, dynamically unstable response.

In flight dynamics, aircraft are often treated as rigid bodies with three rectilinear (forward, lateral, vertical) and three rotational (roll, pitch, yaw) degrees-of-freedom [38]. Longitudinal (forward, vertical, pitch) and lateral-directional (lateral, roll, yaw) motion are sometimes modelled separately, since coupling between these degrees-of-freedom is usually small. In chapters 4 and 5, the stability of each flight is quantified by solving the fully coupled equations of motion, based on estimation of the aerodynamic and inertial properties of each glide configuration. However, prior to this process, it was informative to describe the wing and tail geometry in detail and explore whether longitudinal static stability may be inferred solely from the morphology of each flight.

A bird or aircraft is longitudinally statically stable when its pitching 'moment slope' is negative

$$\frac{\partial M}{\partial \alpha} < 0, \quad (3.1)$$

where M is pitching moment and α is angle of attack. This condition is shown in figure 3.2A and shows that a nose up disturbance in angle of attack, α , results in a restorative nose-down pitching moment and vice versa. The equivalent case for an unstable system is shown in figure 3.2B, where a pitch disturbance is perpetuated by the positive moment slope. The moment slope is dependent on the relative positions of the centre of mass and neutral point [38]. The neutral point is the position at which

the moment slope is zero, and corresponds to a configuration that is neither stable nor unstable¹. In this chapter, it is argued that, given the assumption of a linear moment slope, certain combinations of geometric features might allow longitudinal static stability to be inferred without the need to estimate the centre of mass and neutral point.

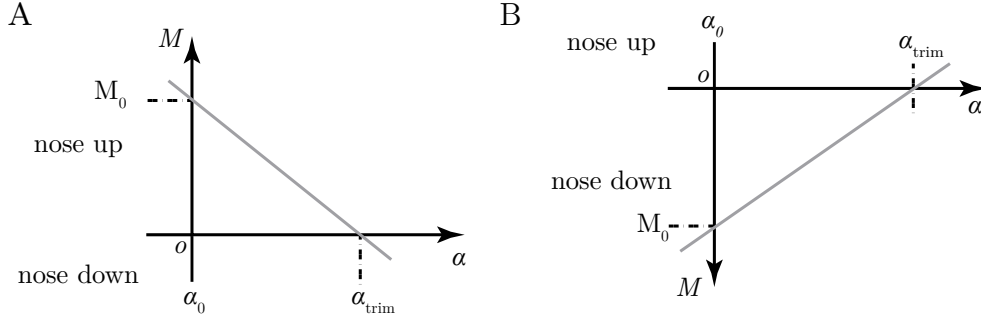


Fig. 3.2 The relationship between pitching moment, M , and angle of attack, α (referenced to the zero lift angle, α_0), for longitudinally statically A) stable and B) unstable configurations. A linear relationship between pitching moment and angle of attack is assumed.

In order to fly steadily, there must exist some angle of attack, α_{trim} , at which both forces and moments sum to zero (i.e. equilibrium). If the moment slopes in figure 3.2 were translated to the left, so that their intersection with the horizontal axis became negative, trim would be impossible. This is because there would be no angle of attack at which positive lift could be produced *and* for zero pitching moment - it would be impossible to balance both forces and moments simultaneously. Assuming a linear moment slope, it is therefore necessary that for a stable, trimmed flight that,

$$M_0 > 0, \quad (3.2)$$

where M_0 is the zero-lift pitching moment. Since the opposite applies to an unstable configuration (i.e. $M_0 < 0$), a qualitative assessment of longitudinal static stability might be possible, based not on the position of the centre of mass (as is traditionally done for aircraft [96]) but on the combined contributions of various geometric features to the zero-lift pitching moment. Thomas and Taylor [76] used this reasoning to predict the geometric features that might be observed in longitudinally statically stable gliding birds and these predictions will be used here to explore whether stability may be inferred from the morphologies measured in flight.

¹This is referred to as ‘neutral’ stability.

Figure 3.3 illustrates these concepts in more detail for an isolated two-dimensional lifting surface. In figure 3.3A, a symmetric (zero camber) aerofoil is shown with its corresponding pitching moment slope. The configuration is clearly stable in pitch because any rotation about the centre of mass would be counteracted by the lift force acting on the aerofoil at the aerodynamic centre². To trim this configuration, it would be necessary to zero the pitching moment, however this would also result in zero lift, making it impossible to balance the lift and weight. So although this configuration is stable, it cannot be trimmed. In figure 3.3B, the unstable equivalent of figure 3.3A is shown, for which it is also impossible to balance lift with weight at zero pitching moment. Therefore, this configuration is unstable and cannot be trimmed. In figure 3.3C, a stable, positively cambered aerofoil is shown. A positively cambered aerofoil generates a nose-down pitching moment which can be considered to act at approximately 25% chord and is constant with changes in angle of attack [3]. The positive camber results in a nose-down pitching moment at zero lift, which in turn means negative lift production at zero pitching moment. Similar to figure 3.3A, this configuration is stable but cannot be trimmed. Figure 3.3D shows a positively cambered aerofoil with the centre of mass aft of the aerofoil, leading to a positive, unstable pitching moment slope. The positive camber yields a nose-down zero-lift pitching moment similar to figure 3.3C. In contrast to figure 3.3C however, the positive moment slope means that there exists some positive C_L when the pitching moment is zero. So although this configuration is unstable, it can be trimmed³. Figure 3.3E shows a negatively cambered aerofoil with a forward (stable) centre of mass position and correspondingly negative moment slope. The negative camber generates a positive zero-lift pitching moment, such that this stable configuration can also be trimmed: zero pitching moment is accompanied by some positive value of lift coefficient. In conventional aircraft, negative camber is almost never used because it is aerodynamically inefficient (i.e. large lift-to-drag penalty). However, on tailless aircraft, symmetric or reflex cambered aerofoils are sometimes used to reduce the magnitude of the nose-down zero-lift pitching moment due to camber [145]. Finally, figure 3.3F shows a negatively cambered aerofoil with an aft (unstable) centre of mass position. For all the reasons already explained, this configuration is both unstable and cannot be trimmed.

²The aerodynamic centre is the neutral point of an aerofoil, i.e. the point about which the pitching moment is constant with angle of attack[3].

³This would require some sort of control system to maintain steady flight and avoid rapid divergence from equilibrium.

In summary, assuming a linear pitching moment slope⁴, to trim a stable configuration requires a positive, nose-up, zero-lift pitching moment, while to trim an unstable configuration requires a negative, nose-down, zero-lift pitching moment [76].

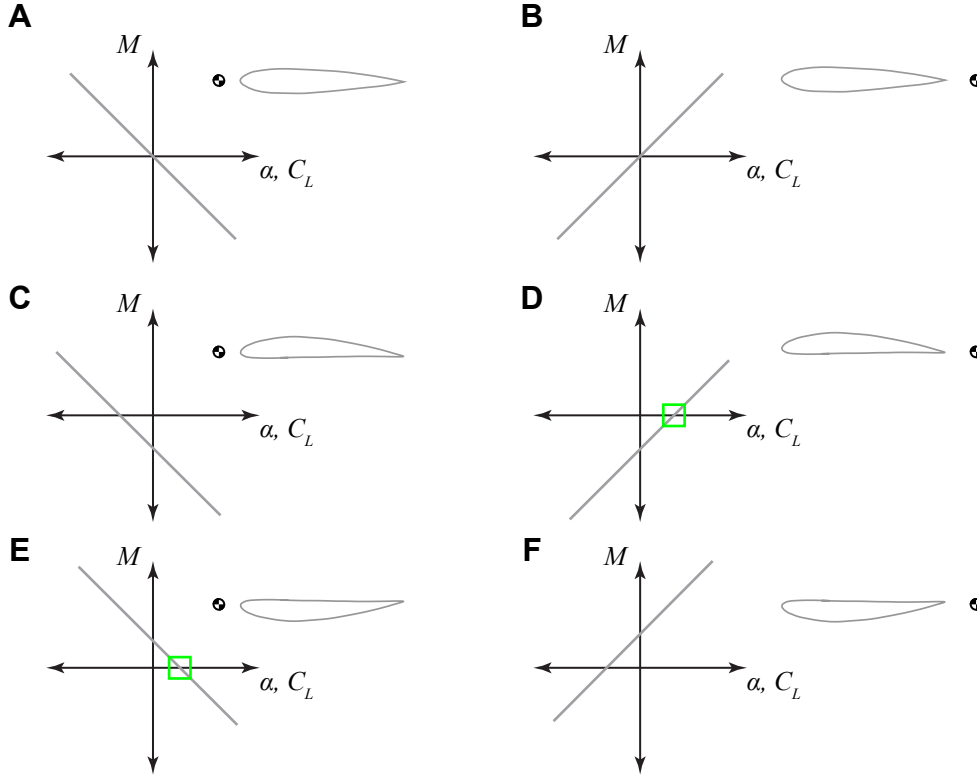


Fig. 3.3 Stability and trim of an isolated, two-dimensional lifting surface with A-B) zero camber C-D) positive camber and E-F) negative camber. When the centre of mass is forward of the aerodynamic centre, the aerofoil is stable in pitch (A,C,E). The aerofoil is unstable in pitch when the centre of mass is aft of the aerodynamic centre (B,D,F). As shown with green boxes, trimming a two-dimensional lifting surface requires positive C_L at zero pitching moment to enable balance between lift and weight.

Figure 3.4 shows additional geometric features that generate positive (figure 3.4A,C,E) or negative (figure 3.4B,D,F) zero-lift pitching moments. These geometric features, in addition to wing camber (figure 3.3) can therefore be considered as indicators of longitudinal static stability or instability if their collective contribution to the zero-lift pitching moment is clear. The drag of the wing (D) contributes towards the zero-lift pitching moment depending on the relative vertical positions of the centre of drag and the centre of mass. With a high wing configuration, wing drag contributes a nose-up

⁴Or equally valid, a monotonic moment slope.

zero-lift pitching moment (figure 3.4C) and vice versa for a low wing (figure 3.4D). Combining aft sweep with wash-out (twisting the wing to reduce incidence along the span) generates a nose-up zero-lift pitching moment (figure 3.4E), and is often used in tailless aircraft [145]. Forward sweep and wash-in (twisting the wing to increase incidence along the span) would also achieve the same effect (not shown). Aft-sweep and wash-in generates a nose-down zero-lift pitching moment (figure 3.4F), and again, forward sweep with wash-out would have the same effect (not shown). A horizontal tail plane is commonly used in conventional aircraft to generate the nose-up zero-lift pitching moment required for a stable configuration (figure 3.4G). In this case the zero-lift angle of attack of the tail is negative relative to the zero-lift angle of attack of the wing, which is known as longitudinal dihedral [96]. Unstable configurations may require the opposite, referred to here as longitudinal anhedral (figure 3.4H). Note that having longitudinal dihedral does not necessarily imply that the tail generates negative lift at the trim angle of attack. Overall the features shown only provide a clear indication of longitudinal static stability if their combined contribution to zero-lift pitching moment is clearly positive or negative. For example, a combination of aft sweep, washout and longitudinal dihedral would be a strong indicator of stability. Conversely, aft sweep, wash in and longitudinal anhedral would represent a strong indicator of instability. If the geometric indicators are mixed⁵, then longitudinal static stability cannot be easily inferred with this approach and further aerodynamic analysis would be required. This geometric assessment of longitudinal static stability is based around the assumption of a linear moment slope and does not require any knowledge of the anteroposterior (fore-aft) position of the centre of mass, as is used in the traditional analysis of aircraft longitudinal stability [96]. The zero-lift pitching moment is a pure couple and as such does not change with the anteroposterior position of the centre of mass, as can be appreciated by considering the effect of its position on the configurations shown in figure 3.4. The assumption of a linear pitching moment slope is a reasonable one for subsonic aircraft operating below stall [38], but this analysis still holds if this assumption is relaxed to the more general assumption that the pitching moment slope does not change sign over the range α_0 to α_{trim} . The pitching moment of a flying bird has not been directly measured, but measurements on an isolated birds wing showed the positive linear pitching moment slope expected for a positively cambered wing when measured about a point posterior to the quarter

⁵Such that some features would generate a nose-up and some a nose-down zero-lift pitching moment.

chord [17]. In this analysis it is also assumed that the bird is a rigid body, meaning that the geometry could be rotated to a different angle of attack without changing shape. This analysis does not assume that birds remain in the same rigid shape when flying at lower angles of attack, just that the geometry measured at equilibrium could conceptually be rotated to an angle where zero-lift would be produced. The stability characteristics of the system for small perturbations about the equilibrium condition are then inferred. These assumptions are the same as those used in standard linear flight dynamics analysis [38]. Overall, this analysis does not require knowledge of the location of the centre of mass, which is difficult to determine for a flying bird, and allows directional inferences about longitudinal static stability to be made based on measured in-flight geometry.

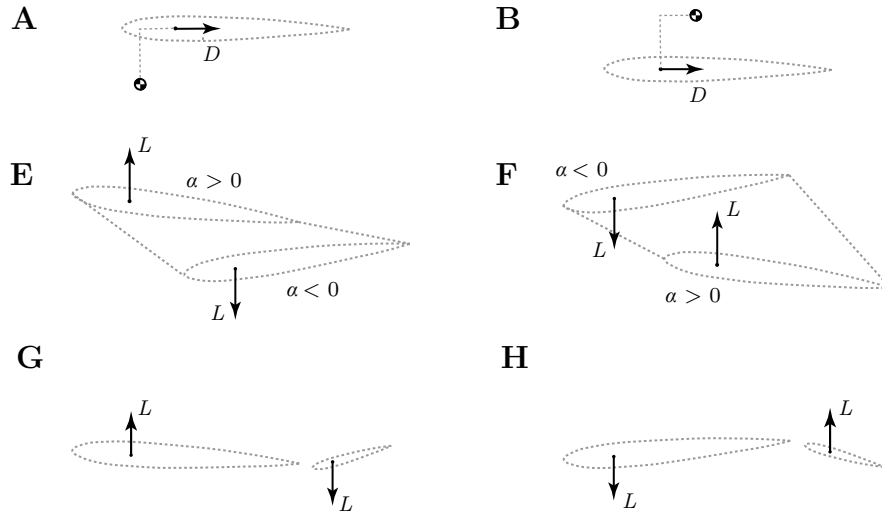


Fig. 3.4 Assuming a linear moment slope, to trim a stable configuration requires a positive (nose-up) zero-lift pitching moment (A,C,E), while unstable configurations require a negative (nose-down) zero-lift pitching moment (B,D,F). Vertical wing position relative to centre of mass (A,B), combinations of wing sweep and twist (C,D) and longitudinal dihedral/anedral (E,F) can all generate both positive and negative zero-lift pitching moments depending on their configuration. Each configuration is shown for zero net lift. Drag is not shown where its contribution is negligible. Each element within this figure represents only how a given geometric feature, in isolation, contributes towards the zero-lift pitching moment.

The following sections describe the methods used to quantify wing camber, twist, sweep, dihedral and thickness along with tail elevation, spread and twist for the three barn owl and three peregrine flights of chapter 2 figure 2.11. The implications of these features for longitudinal static stability are then discussed. The flight conditions are also described based on estimates of air velocity, angle of attack and sideslip estimated

using video footage and anemometer data. The video footage and glide geometries are also used to discuss correctional control during gliding flight.

3.4 Material and methods

3.4.1 Geometry evaluation

Quantifying camber, twist, sweep, dihedral and thickness from the raw point clouds described in chapter 2 was challenging due to,

1. A lack of data at the leading and trailing edges (although the chordwise distance was available via the edge spline (see chapter 2 figure 2.7)).
2. Multiple datasets representing each physical surface (see chapter 2 figure 2.1) that did not always agree due to noise and alignment error.
3. Variation in spatial resolution between stereo reconstructions of the same surface due to differences in camera angle.
4. Differences in chordwise distance between datasets representing the same surface.
5. The morphological challenge of a long thin trailing edge where datasets for the dorsal and ventral surfaces intersected.

A processing strategy was formulated in which the manually segmented wing data were first divided into spanwise sections taken every 2 mm along the y -axis of the wing-body coordinate system (see chapter 2 figure 2.6). In each section, mean camber, dorsal and ventral splines were fitted to the raw points as shown in figure 3.5. Firstly, smoothing splines (sp1,2, sp3,4, sp5,6, and sp7,8 in figure 3.5B) were fitted to the section data from each stereo pair (c1,2, c3,4, c5,6 and c7,8 in figure 3.5A). The smoothing parameter for each spline was optimised using a k-fold cross validation approach based on Breaz [146]. The ‘dorsal spline’ (spD in figure 3.5C) was then calculated based on the sampled mean of sp1,2 and sp3,4. This process was repeated using sp5,6 and sp7,8 to obtain the ventral spline (spV in figure 3.5C). The sampled mean of the dorsal and ventral splines was then itself splined and quadratically extrapolated to the anterior and posterior x -coordinates of the edge spline (spEa and spEp) to generate the completed mean camber spline (spMcI in figure 3.5C). The chord was defined as the straight line joining the end-points of the mean camber spline (not the

edge spline points, spEa and spEp, due to their variable accuracy in the z -direction). The dorsal and ventral splines were used to quantify the section thickness distribution in the direction perpendicular to the chord line (figure 3.7). First and second order polynomial fitting was applied to sections in which one or more datasets (i.e. c1,2, c3,4, c5,6 or c7,8 in figure 3.5a) covered less than 50% of the chord (figure 3.6). When the z -coordinates of either the dorsal (c1,2 and c3,4) or ventral (c5,6 and c7,8) points disagreed by more than 4% chord, the data were not used for generating the resulting splines (sp1,2, sp3,4, sp5,6 and sp7,8). This ensured the splines were based on measurements of the bird's surface where reasonable agreement was found between two stereo reconstructions of the same physical surface. Measurements of spanwise camber, angle of twist, thickness, dihedral and sweep were obtained using the mean, dorsal and ventral splines as illustrated in figure 3.7.

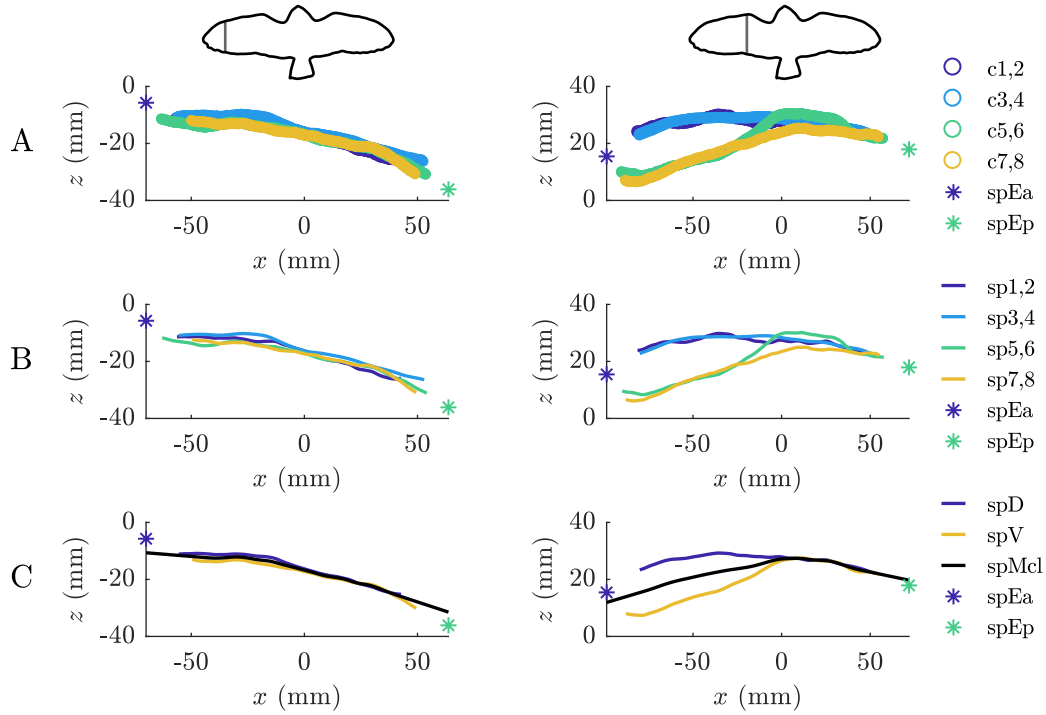


Fig. 3.5 Generation of the dorsal, ventral and mean camber splines, illustrated using representative sections from the arm wing (left) and hand wing (right) of flight O1. The z -axis is slightly stretched for clarity. The edge spline anterior and posterior positions (spEa, spEp) are shown in each plot. A) The raw data from each stereo pair (c1,2, c3,4, c5,6 and c7,8) for the section. B) Smoothing spline fits to each dataset (sp1,2, sp3,4, sp5,6 and sp7,8). C) The resulting dorsal (spD), ventral (spV) and mean camber line splines (spMcl) used to measure camber, twist, thickness and dihedral based on averaging the splines generated in B. The mean camber spline required extrapolation to the x -coordinates of the anterior and posterior edge spline data points, spEa and spEp.

In several instances, the default spline-fitting approach required adaptation to enable estimation of the dorsal and ventral splines. This was due to low ‘data coverage’ in a section from one or more stereo datasets, and occurred either ventrally and proximally on the wing due to occlusion by the body, or distally due to the reduced number of pixels in the chordwise direction due to reduced disparity estimation accuracy. ‘Data coverage’ was calculated firstly by dividing the section data into small segments. The number of segments, N_{segs} , used in each section was defined using

$$N_{segs} = \frac{N_{points}}{N_{datasets} \times N_{min}}, \quad (3.3)$$

where N_{points} is the number of points in the section, N_{min} was a desirable minimum number of points for a segment (assuming relatively uniform spatial density) and $N_{datasets}$ was the number of stereo reconstructions represented in the section⁶. Coverage was then defined as the number of segments containing at least one data point divided by the total number of segments. The approaches used to quantify the geometry of these low coverage sections are shown in figure 3.6 and are described below:

1. ‘Default’. As previously described, smoothing splines were fitted to all four datasets in the section, represented by the four stereo reconstructions. Dorsal and ventral splines were then generated based on the sampled means of the two dorsal and two ventral reconstructions (figure 3.5).
2. ‘Low coverage - spline’. Proximally, the view of the ventral wing surface was occluded from either cameras 5 and 6 or cameras 7 and 8. The ventral spline used for the thickness distribution and mean camber line estimation was therefore based on a spline-fit to the data from the non-occluded camera pair. In other words, the ventral spline-fit was dependent on data from just one stereo reconstruction rather than being based on the mean of two stereo reconstructions for the section.
3. ‘Low coverage - linear’ and ‘Low coverage - quadratic’. Low data coverage (defined as <50%) from one or more dorsal or ventral view camera pairs led to spurious extrapolations of the mean camber line using the default approach. Fitting a spline across the complete range of both datasets (to extend chordwise distance and reduce extrapolation distance) led to kinking⁷ at the domain bound-

⁶This was set to 4 for all sections, but could have been lower for sections where some camera pairs had occluded views.

⁷i.e. sudden changes in direction or spikes in the second derivative.

ary of the smaller dataset, because their chordwise distances did not match. To obtain fits to the complete range without kinking, linear or quadratic polynomials were used, rather than splines. If the data points clearly showed camber, a quadratic polynomial was fitted, otherwise a linear fit was used. Selecting the fit-type based on a visual assessment of camber avoided mis-representation of camber where it was clearly negligible.

4. ‘Fit to all - linear’ and ‘Fit to all - quadratic’. For some sections comprising of only feathers, low data coverage from both dorsal or ventral view camera pairs meant that the ‘Low coverage - linear’ and ‘Low coverage - quadratic’ approaches led to spurious extrapolations of the mean camber line. Linear or quadratic polynomials were therefore fitted to all the available data in the section in order to obtain either the chord line (linear fitting) or mean camber line (quadratic fitting). Again, if the data points clearly showed camber, a quadratic polynomial was fitted, otherwise a linear fit was used.
5. ‘No fit’. At the wing tips of both birds, the quality of the data points was insufficient for accurate fitting with any method. No attempt was made to represent the geometry of these sections.

In all instances except ‘no fit’, the dorsal and ventral splines or polynomials were used to obtain the thickness distribution, mean camber line and chord line. If the dorsal and ventral fits were both linear, the section had zero camber and featured only the chord line. Visual inspection was applied to every single section to ensure that the mean, dorsal and ventral splines were representative of the raw points.

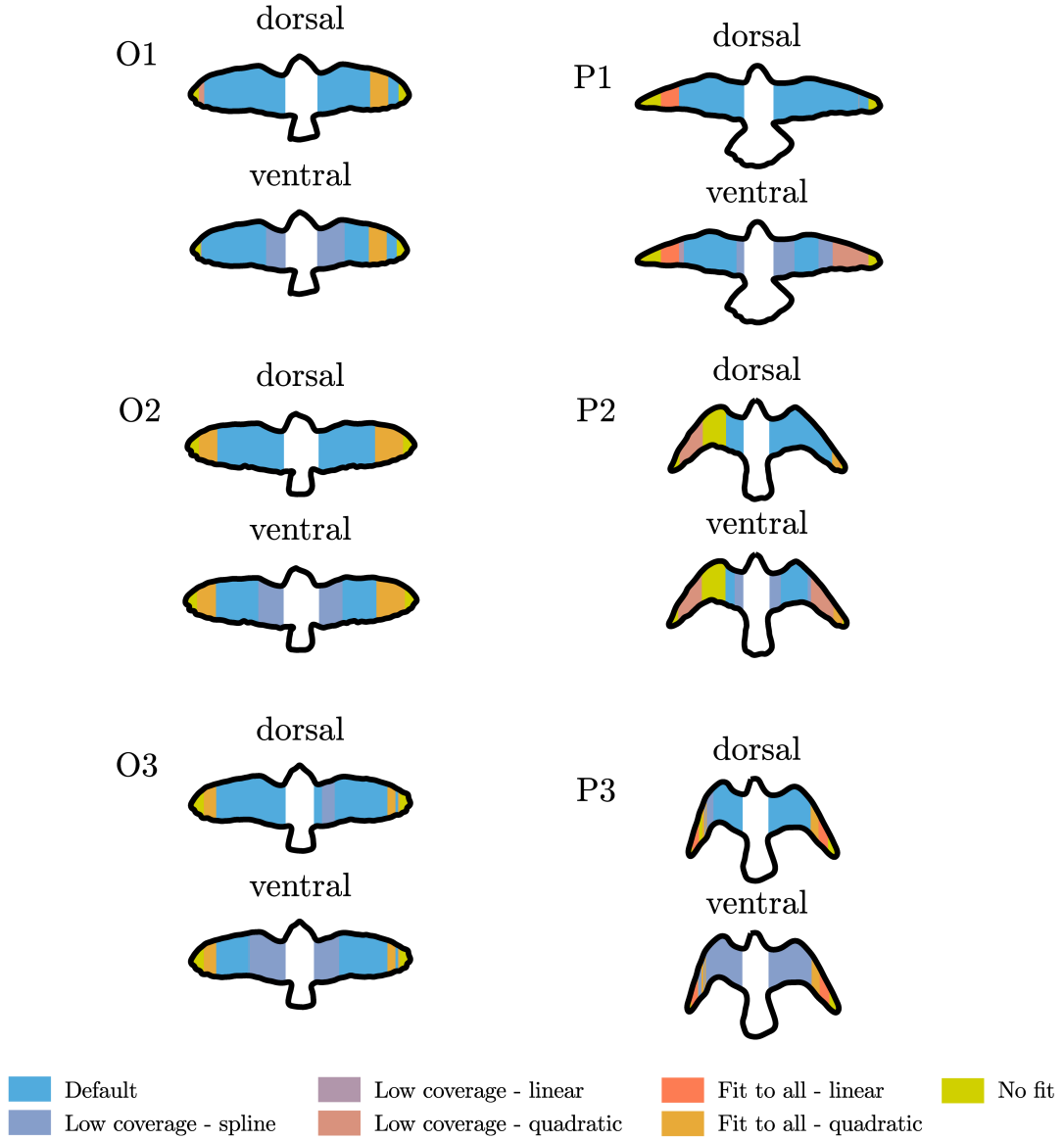


Fig. 3.6 Dorsoventral views of the barn owl (O1-O3) and peregrine (P1-P3) flights, showing where the default fitting approach was adapted to allow estimation of the dorsal, ventral and mean camber splines. No fit was attempted to the mid-region of the left wing of P2 due to difficulty reconstructing the poorly exposed dorsal surface.

The mean camber, dorsal and ventral splines were used to quantify the distribution of camber, angle of twist, sweep, dihedral and thickness across the span, as defined in figure 3.7. The dorsal and ventral splines commonly intersected in the very thin feather-only regions of the wing, so the absolute thickness was always used to avoid negative values. Wing span, mean aerodynamic chord and planform area were

calculated based on Pennycuick [147] using the edge spline (see chapter 2 figure 2.7). This approach is equivalent to that conventionally used in aircraft, where the planform area of the wing box⁸ is included in the wing area.

Aspect ratio was calculated using

$$A = \frac{b^2}{S}, \quad (3.4)$$

where b was wing span and S was wing planform area (including wing box). The lift coefficient was estimated using

$$C_L = \frac{2W}{\rho V^2 S}, \quad (3.5)$$

where W was the bird's weight measured during data collection, ρ was air density (calculated using the local air temperature and relative humidity [148] to be 1.16 kg/m^3), V was true air speed and S was the wing planform area (including wing box). Pitch and roll attitude were estimated using the known gravity vector from the global calibration (see chapter 2 section 2.6.3.3). Tail twist⁹ and elevation were estimated using the partial derivatives of a plane fitted to manually segmented raw points from the dorsal reconstructions of the rectrices.

⁸This was the spanwise distance between the wing root sections multiplied by the mean chord of both wing root sections.

⁹Tail twisting refers to the rigid transformation of a 2D plane.

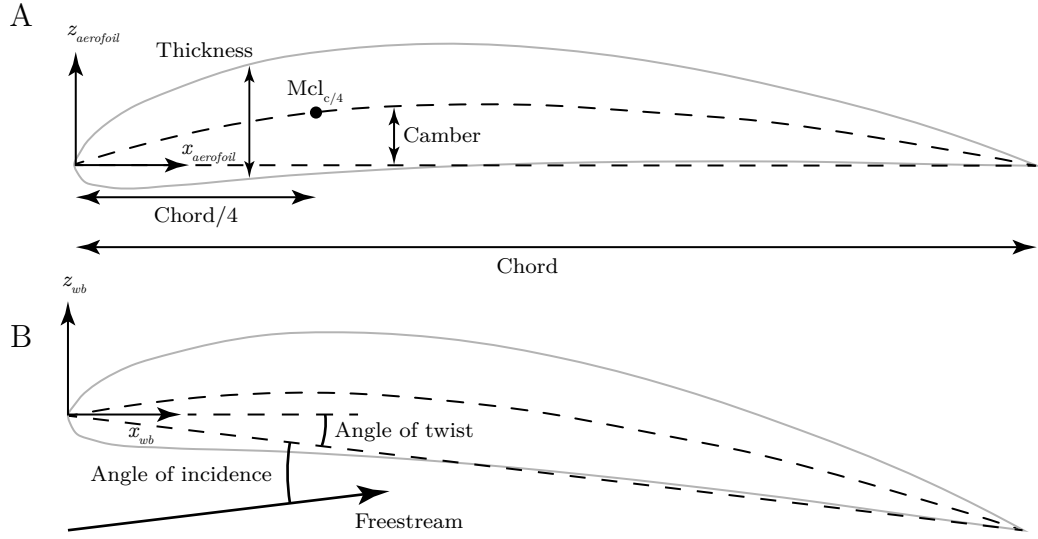


Fig. 3.7 Conventions used to define the spanwise geometry of the wing. A) To quantify camber and thickness each section was transformed so that the chord was parallel to the x -axis. Following transformation, camber was defined as the vertical distance between the mean camber line and chord line. Thickness was defined as the vertical distance between the dorsal and ventral splines. The quarter-chord evaluation of the mean camber line, $Mcl_{c/4}$, was transformed back to wing-body coordinates and used to visualise sweep and dihedral. B) Angle of attack was defined as the angle between the chord and freestream, while angle of twist defined only the geometric angle of each section relative to the x -axis of the wing-body coordinate system.

3.4.2 Estimation of flight conditions

To estimate the air velocity, angle of attack and sideslip of the bird, a three-dimensional geometric model of the experimental setup, gliding bird and wind velocity was created (figure 3.8). The relative positions of the bird, cameras, access tower and anemometer (chapter 2 figure 2.1) were obtained using the global calibration (see chapter 2 section 2.6.3.3), and the known position and orientation of the anemometer relative to the tower. The pitch and roll attitude of the bird were also estimated because the global calibration was aligned with gravity using images of a plumb line. The ground velocity of the bird was estimated using the field video camera (see section 2.5), with the horizontal distance travelled based on frames where the bird's head was aligned with the edges of the mobile access tower. The wind and ground velocity vectors were transformed into the wing-body coordinate system of the bird (see section 2.6.5) and combined to obtain the air velocity vector. The 'mean wing angle of attack', $\bar{\alpha}_{wing}$

(table 3.1), was calculated using

$$\begin{aligned}\bar{\alpha}_{wing} &= \alpha_{wb} + \bar{\alpha}_{twist}, \\ \alpha_{wb} &= \tan^{-1} \left(\frac{W}{U} \right),\end{aligned}\tag{3.6}$$

where W and U are the magnitudes of the vertical and horizontal components of the air velocity vector in wing-body coordinates and $\bar{\alpha}_{twist}$ is the mean geometric twist angle of both wings in wing-body coordinates. Sideslip angle, β , was calculated using

$$\beta = \sin^{-1} \left(\frac{V}{|\mathbf{V}|} \right),\tag{3.7}$$

where V is the magnitude of the lateral component of the air velocity vector in wing-body coordinates and \mathbf{V} is the air velocity vector [38]. The mean and standard deviation of the wind velocity (sampled at 4 Hz) were based on ± 2.5 s data obtained either side of the moment at which the cameras were triggered (20 samples per flight). Error in ground velocity was based on ± 1 frame. Estimates of the lift coefficient assumed steady flight, with the errors based on the total error in true air speed. Variation estimates for α and β were based on the standard deviation of wind velocity. Roll attitude depended on the accuracy of the plumb line based gravity estimate which could have a small standard error of several degrees. Altitude was based on combining photogrammetric calibration extrinsics for cameras 1 to 4 with tape measure estimates of their height above the ground, and could have a standard error of ± 50 mm. The altitude loss and glide angle were based on the displacements of the bird's head obtained using the field camera footage.

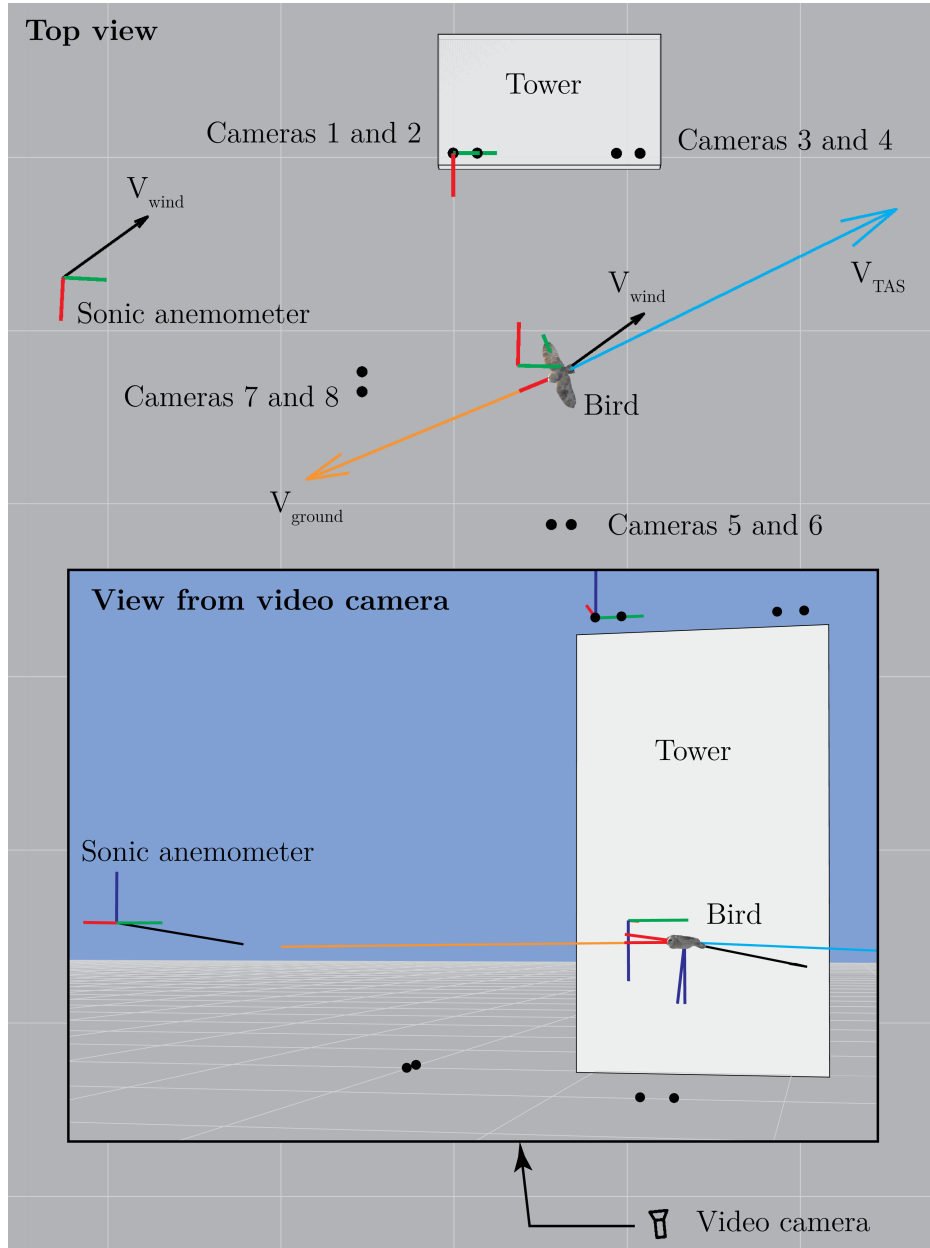


Fig. 3.8 Estimation of the bird's true air speed, geometric angle of attack and angle of sideslip were estimated by subtracting the wind velocity (averaged over ± 2.5 s from the moment of reconstruction) from the ground velocity (averaged across the front face of the tower) in the wing-body coordinate system of the bird. Ground and wind velocity were estimated using the measured position and orientation of the video camera, bird and sonic anemometer relative to the tower. The figure shows the geometric model of flight O1 and the coordinate systems of the anemometer, tower, global calibration and bird. For the bird, the wing-body coordinate system is shown in addition to the wing-body coordinate system rotated about the spanwise axis to align with gravity.

3.5 Results

3.5.1 Flight conditions

In this section, the flight conditions are described using the flow conditions relative to the bird in wing-body coordinates combined with observations from the video footage. Estimations of the true air speed, angle of attack and angle of sideslip showed significant temporal variation caused by the wind (table 3.1 and figure 3.9).

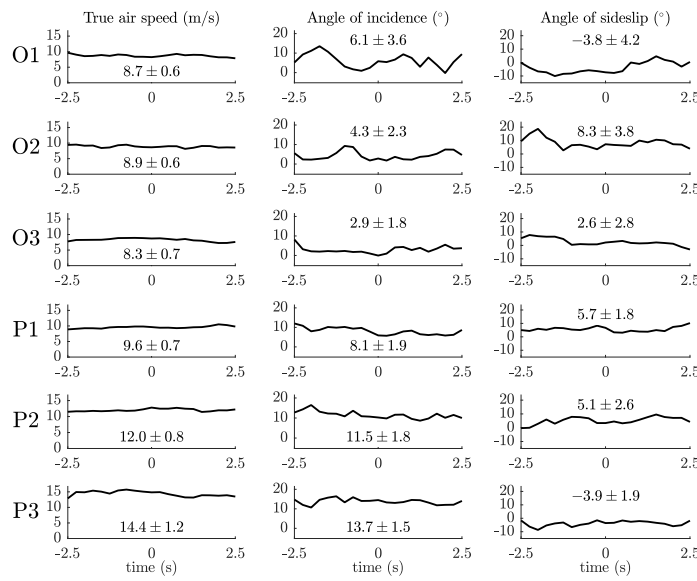


Fig. 3.9 The effect of wind velocity variation on true air speed, mean wing angle of attack and angle of sideslip, assuming constant ground velocity and orientation of the bird, labelled with mean \pm standard deviation. This data provides an *indication* of the temporal variation in flow conditions experienced by the bird due to the wind, not their precisely measured values during the flight. The standard deviations are based on the 20 plotted anemometer samples at 4 Hz covering ± 2.5 s from the point at which the images were obtained for each flight. Ground velocity is based on the mean velocity across the measurement volume based on video footage.

Spatial variation in flow conditions has also been shown to be significant at the height at which the birds typically flew [29–31, 149]. This spatial and temporal variation in wind velocity was likely to have required the birds to make corrections to maintain a constant heading [150].

The video footage (see Appendix A) shows that despite variation in wind velocity, the trajectories of both birds were relatively smooth and direct. The barn owl flew with a consistent flap-glide-perch sequence and the three flights (O1-O3) were representative

of all 10 flights conducted during fieldwork. Above the fence, the owl was banked slightly to the right in O1 and O2 and slightly to the left in O3. Flight O1 shows a roll to the left, flight O2 shows a fairly constant bank angle and flight O3 shows a roll to the right, across the measurement volume. All the barn owl flights were completed with a perch manoeuvre onto the trainer’s glove, initiated just beyond the measurement volume. An interesting feature of these flights was the continuous, low frequency, low amplitude, changes in dihedral angle. In flights O1 and O3, upward deflections of the secondary flight feathers occurred proximally on the right wing as the bird flew through the centre of the measurement volume (left wing not visible in tower video for O1).

The glide phase of the peregrine flights (P1-P3) began earlier than the barn owl, well before the fence, with a clear loss of altitude across the measurement volume. The peregrine was banked slightly to the left prior to the fence during P1, after which the wings appear to level out through the measurement volume. The wings appeared relatively level through the measurement volume during P2 and P3, with the velocity and aft sweep clearly higher than during P1. During P3, the video shows a slight roll to the left immediately after the centre of the measurement volume, coinciding with the lowering of the left wing tip.

Flight data derived from the reconstructed points, video footage and anemometer are provided in table 3.1. The barn owl flights (O1-O3) showed generally similar span, chord and area with negligible altitude change, suggesting that the bird was slowing down. The peregrine reduced its wing span, area and aspect ratio with increasing air speed and angle of attack, consistent with the findings of similar sized birds gliding in wind tunnels [11, 81, 151, 152]. The glide angles and altitudes were very similar for all three configurations showing that the bird was able to achieve consistent approach trajectories (lift-to-drag ratio ~ 10) despite significant changes in flight conditions and configuration. The peregrine had a significantly higher wing loading than the barn owl due to its higher mass and lower wing area. This required it to fly at a greater velocity and/or angle of attack than the barn owl in order to generate sufficient lift.

For both birds, the tail operated at angles of attack between 18° and 29° though this may have been slightly reduced due to the wing’s downwash (see section 3.6.3). Tail twisting was also evident based on the measured geometry and the video footage, indicating its use for correctional control.

	Barn owl			Peregrine		
Flight	O1	O2	O3	P1	P2	P3
Mass (g)	312	312	312	645	645	645
Wing span (mm)	818	864	820	908	666	562
Mean aerodynamic chord (mm)	126	129	128	102	102	109
Wing area (m ²)	0.117	0.126	0.118	0.103	0.081	0.076
Aspect ratio	5.7	5.9	5.7	8.0	5.5	4.2
Wing loading (N/m ²)	26.2	24.3	25.9	61.4	78.1	83.3
Ground velocity (m/s)	6.3 ± 0.2	6.0 ± 0.2	6.7 ± 0.2	8.6 ± 0.3	9.7 ± 0.4	10.6 ± 0.4
True air speed (m/s)	8.7 ± 0.6	8.9 ± 0.6	8.3 ± 0.7	9.6 ± 0.7	12.0 ± 0.8	14.4 ± 1.2
Reynolds number	71 × 10 ³	75 × 10 ³	69 × 10 ³	64 × 10 ³	80 × 10 ³	102 × 10 ³
Mean wing angle of attack (α_{wing}) ± s.d. (°)	6.1 ± 3.6	4.3 ± 2.3	2.9 ± 1.8	8.1 ± 1.9	11.5 ± 1.8	13.7 ± 1.5
Tail angle of attack ± s.d. (°)	20.7 ± 3.6	28.5 ± 2.3	17.8 ± 1.8	24.2 ± 1.9	18.6 ± 1.8	19.1 ± 1.5
Tail twist (°)	-4.7	12.6	-5.2	11.0	-0.3	5.1
Body angle of attack (α_{wb}) ± s.d. (°)	5.1 ± 3.6	8.9 ± 2.3	9.0 ± 1.8	5.6 ± 1.9	12.0 ± 1.8	12.8 ± 1.5
Angle of sideslip ± s.d. (°)	-3.8 ± 4.2	8.3 ± 3.8	2.6 ± 2.8	5.7 ± 1.8	5.1 ± 2.6	-3.9 ± 1.9
Lift coefficient	0.60 ^{+0.09} _{-0.07}	0.53 ^{+0.08} _{-0.07}	0.65 ^{+0.13} _{-0.10}	1.15 ^{+0.19} _{-0.15}	0.94 ^{+0.14} _{-0.11}	0.69 ^{+0.13} _{-0.10}
Roll attitude (°)	1.9	6.5	8.7	2.3	1.8	-2.4
Altitude (m)	1.34	1.35	1.31	1.27	1.30	1.10
Altitude loss (mm)	9	62	-40	214	227	229
Glide angle (°)	0.25	1.7	-1.0	5.3	5.9	5.4

Table 3.1 Flight data derived from the geometry, video and anemometer data. The error in ground velocity was estimated assuming ± 1 frame error at 100 fps. The error in true air speed was the sum of the ground velocity error and the standard deviation of the wind velocity error. The error in angle of attack and sideslip was due only to changes in wind velocity since the additional error due to ground velocity error was $< 0.1^\circ$. Tail twist and roll attitude are positive when the right side of the bird moves down.

3.5.2 Spline fitting

Figure 3.10 shows direct comparison between the raw points and the mean camber, dorsal and ventral splines for ten sections per wing from flight O1. Each section (viewed laterally) is aligned to the corresponding leading edge position on the planform view of the edge spline¹⁰. The planform is included to provide a sense of the position of each section on the wing. Figure 3.11 shows the equivalent plot of peregrine flight P1. The views of the raw data points clearly reveal the benefits and limitations of the surface reconstruction process described in chapter 2. Despite the challenges described previously (section 3.4.1), it is clear that the data provides a reasonable representation of the gross morphology of the wing. The mean camber, dorsal and ventral splines (figure 3.10) appear to represent the raw points reasonably accurately. Although the section spline fitting process was complex due to the challenges associated with photogrammetric surface reconstructions and the management of multiple datasets, the end result was a spanwise set of mean camber, dorsal and ventral splines representative of the raw points. For all flights, nearest-neighbour comparison between the raw points and the dorsal and ventral splines showed standard deviations less than 1 mm (table 3.2). The spline means were close to zero, implying that the fitting algorithms had worked correctly. The linear and quadratic polynomial fits had standard deviations less than 2 mm, with the increased error likely due to increased noise in the sections where these were required.

	Spline mean (mm)	Spline s.d. (mm)	Polynomial s.d. (mm)
O1	-0.005	0.75	1.10
O2	-0.010	0.74	1.14
O3	-0.002	0.82	1.14
P1	0.020	0.77	1.60
P2	0.015	0.85	1.77
P3	-0.0014	0.60	1.22

Table 3.2 Nearest neighbour comparison between the fitted splines and polynomials and the original raw points for the barn owl (O1-O3) and peregrine (P1-P3) flights.

¹⁰This is why the trailing edges don't quite match

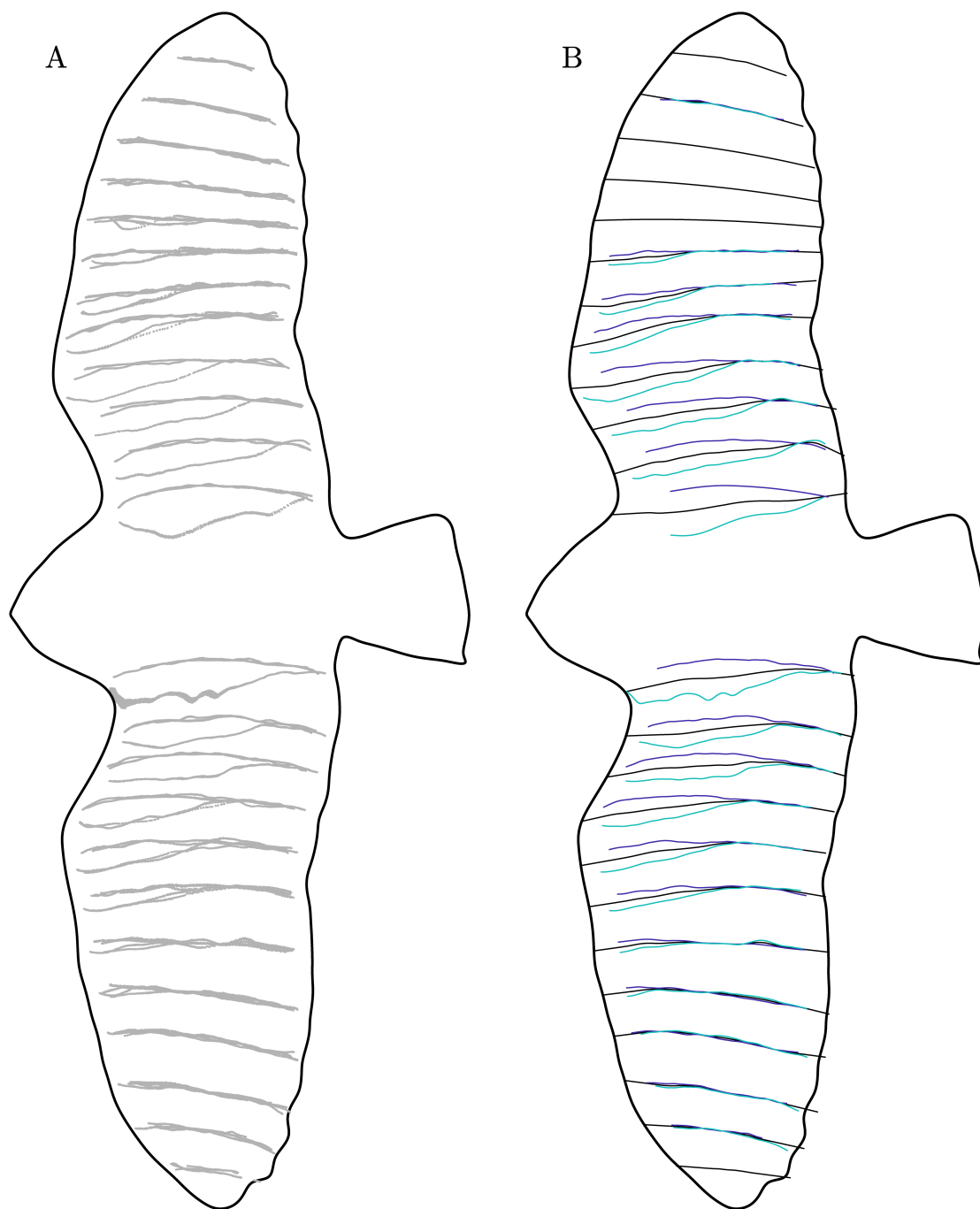


Fig. 3.10 Comparison between A) raw data points and B) estimations of the mean camber, dorsal and ventral splines (or polynomials) for flight O1. In B, the dorsal surface is given a lower intensity than the ventral surface to aid visualisation. For sections where ‘fit to all’ linear or quadratic fitting was used, only the resulting mean camber line is shown. Note that the edge spline is shown based on a dorsoventral view, while the sections are shown based on a lateral view.

To provide further evidence that the splined geometry was representative to the free-gliding bird, comparison was made between the splined mean camber lines of the laser scanned and photogrammetrically measured model gull introduced in chapter 2 section 2.7. Figure 3.12 shows this comparison, in which the same spline algorithms were applied to both the laser scan and stereo reconstructed point clouds. A key difference was that the leading and trailing edges of the laser scan were very well defined, such that this comparison provided a good indication of any potential accuracy losses around the leading and trailing edges, where photogrammetric data were removed due to low accuracy. Figure 3.12C-F clearly shows that the photogrammetry and spline fitting process provided very accurate representations of the overall shape of the bird, in terms of the camber, twist, sweep and dihedral. The thickness was also reasonably accurately represented, as shown by Figure 3.12B. This analysis provided strong support for the high accuracy of the equivalent data shown in section 3.5.3 for the free-gliding birds.

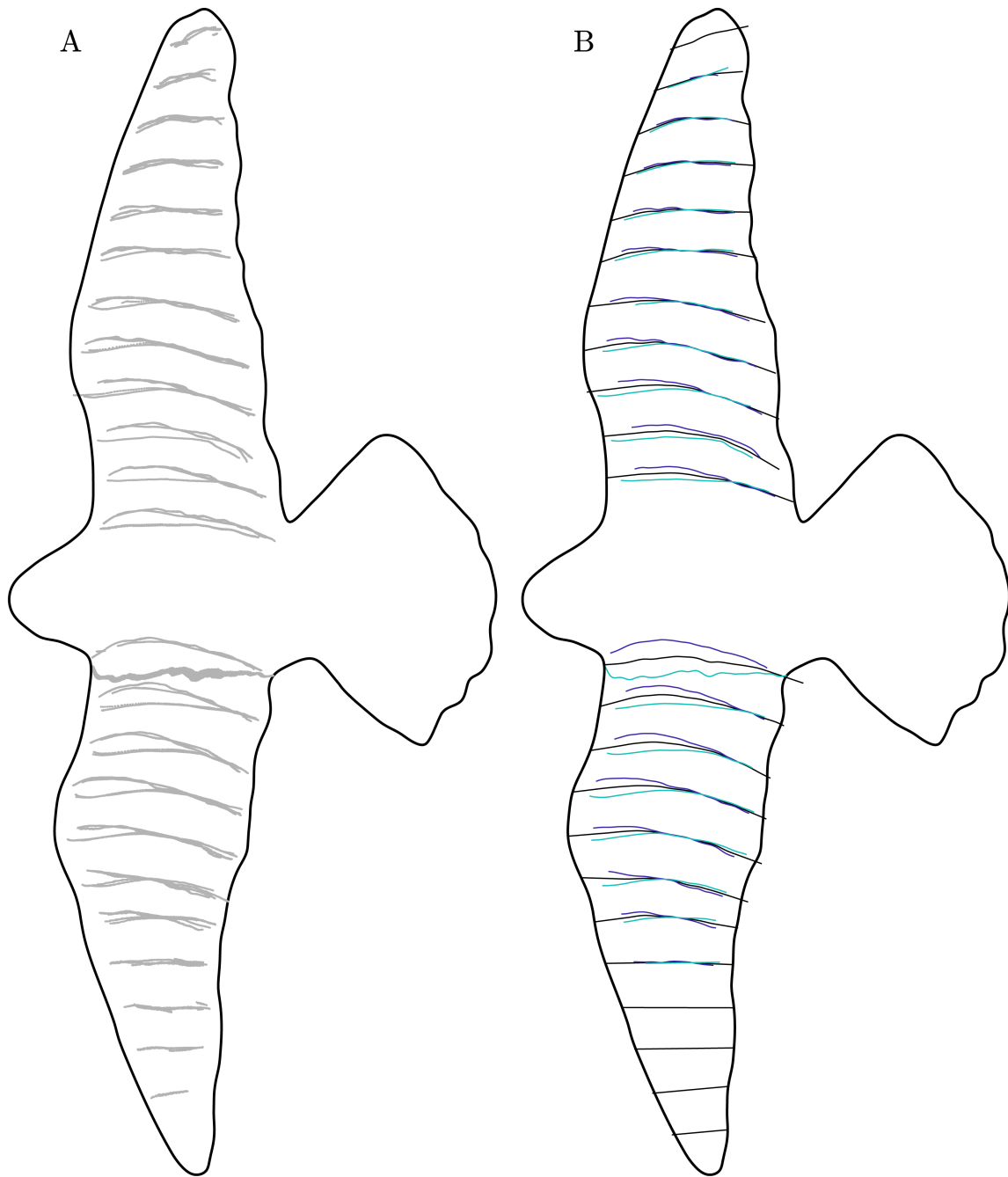


Fig. 3.11 Comparison between A) raw data points and B) estimations of the mean camber, dorsal and ventral splines (or polynomials) for flight P1. In B, the dorsal surface is given a lower intensity than the ventral surface to aid visualisation. For sections where linear or quadratic fitting was used, only the resulting mean camber line is shown. Note that the edge spline is shown based on a dorsoventral view, while the sections are shown based on a lateral view.

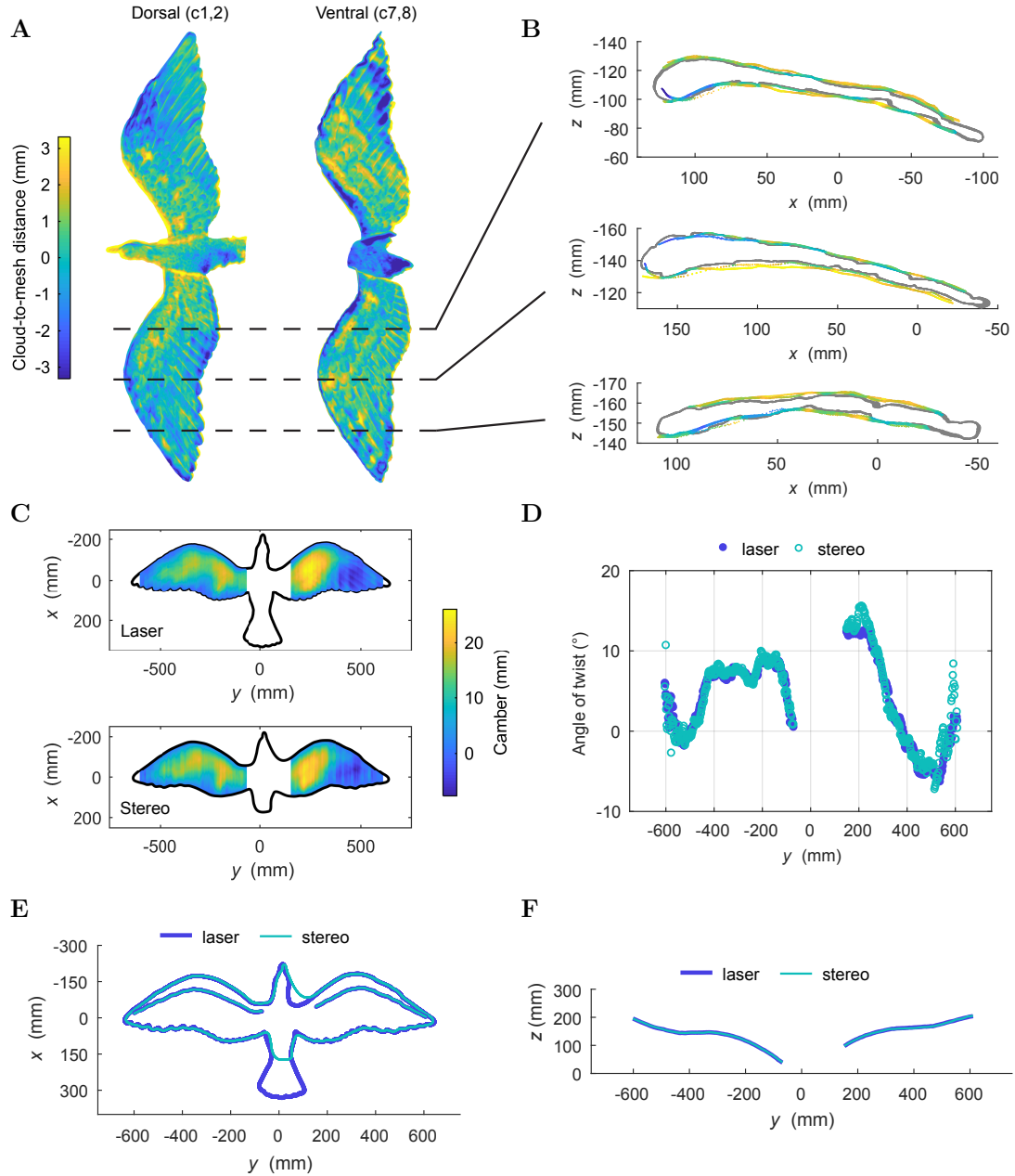


Fig. 3.12 Assessment of the accuracy of the stereo reconstructions by comparing with a high accuracy laser scan of a fibreglass gull model. A) Planform views of the errors for stereo reconstructions (edges retained) individually aligned to the laser scan. B) Cross-sections through the wing showing the difference between the laser scan (grey points) and the reconstructed points based on collective alignment to the laser scan. The points are coloured by their error value using the same colour scale as in A. C) Scalar fields quantifying distance between the mean camber line and chord line, as measured perpendicular to the chord line, for sections every 2 mm along the span for the laser scan and the stereo-photogrammetry reconstruction. D) Spanwise twist distributions for both datasets. E) Dorsoventral view of both datasets showing the quarter-chord wing sweep and the planform outline. F) Posteroanterior view of the quarter-chord of both datasets to show wing dihedral.

3.5.3 Wing shapes

In this section, plots of spanwise camber, angle of attack, sweep, dihedral and thickness are presented (figures 3.13 to 3.15). Figure 3.13 shows the span and chordwise variation in camber for each flight. Both the peregrine and the barn owl had positively cambered wings, with higher camber in the arm region than in the hand. Proximally, the magnitude and extent of the camber was greater in the peregrine than the barn owl. Subtle variations in camber asymmetry occurred between flights. For example, the left wing of O1 showed slightly more camber distally than the right wing, while a similar but reversed asymmetry was visible in O3. The camber in O2 was also slightly larger distally than O3 and the right wing of O1. In the spanwise direction, the position of maximum camber moved from approximately 75% chord proximally to 50% chord distally in O1, O3 and the left wing of O2. The peregrine showed rapid reduction in camber at ± 200 mm along the span, such that distally, the camber was of similar magnitude to the barn owl. The camber reduced between P1 and P3, corresponding with the reduced lift coefficient requirement between these flights (table 3.1). Careful examination of the raw points suggests that the several small localised regions of negative camber represent genuine features of the reconstructed points.

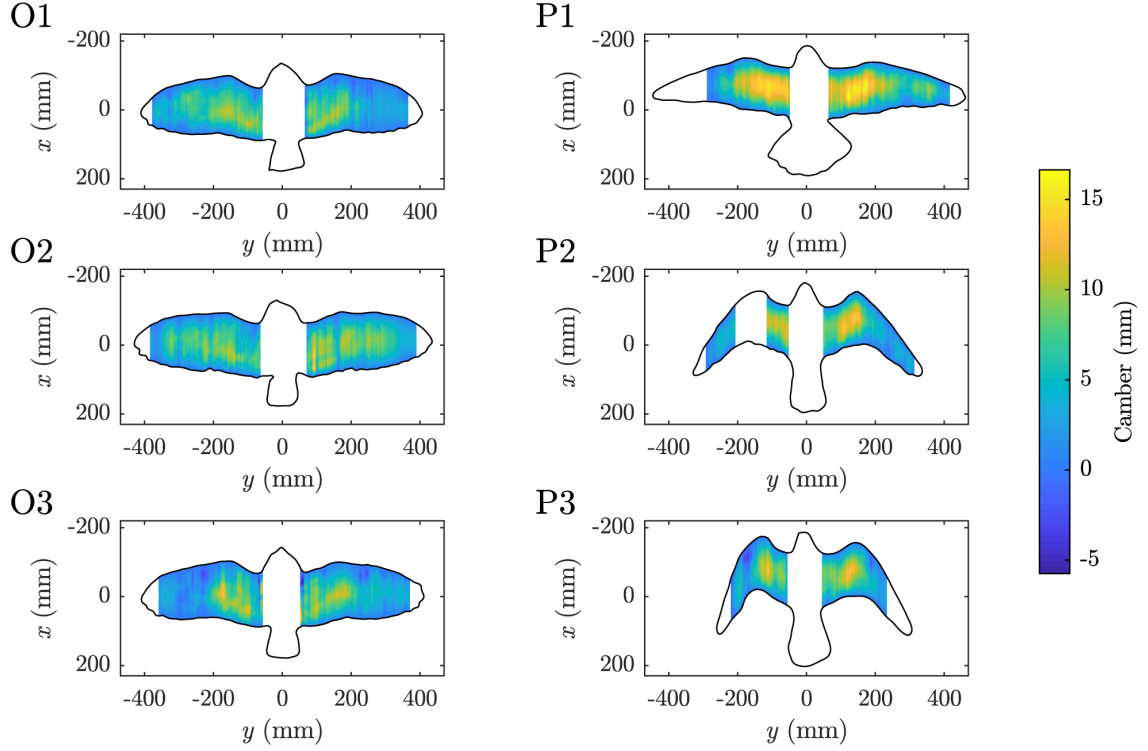


Fig. 3.13 Scalar fields quantifying the distance between the mean camber line and chord line, perpendicular to the chord line, for sections every 2 mm along the span for the barn owl (O1-O3) and peregrine (P1-P3) flights. Uncoloured regions represent the body, tail and regions with reduced data quality (i.e. near the wing tips) or where linear fitting was used to generate the mean camber line. Camber distribution normalised by the local chord length showed the same distribution as the absolute values, both between flights and birds.

Figure 3.14 compares spanwise angle of attack, sweep and dihedral between flights. The angle of attack measurements in figure 3.14A were referenced against the mean flow velocity vector for the flight. The data should therefore be interpreted as the geometric twist of the wing relative to the mean flow velocity for each flight (see table 3.1 and figure 3.9). Wind velocity close to the ground is known to vary both temporally and spatially [29–32, 34, 35]. The temporal variation was captured by the anemometer (6 m from the bird), however it was not possible to capture the spatial variation. The actual spanwise angle of attack may therefore have been different to that plotted. Figure 3.14A can also be interpreted as a geometric twist distribution, since it is based on the measured geometry of the wing. Both birds showed significant variation in angle of twist along the span, with a distinctive change in gradient occurring in the vicinity of the wrist and manus. The barn owl adopted a relatively

consistent wing morphology between flights combining forward sweep with washout (pronation) proximally, and aft sweep with wash-in (supination) distally. The sweep angles were subtle however, with flight O2 in particular showing minimal aft-sweep distally. In contrast to the consistent wing configuration, the tail angle of attack and twist varied between 18° to 29° and -5° to 13° respectively (table 3.1). The peregrine combined forward sweep with wash-in proximally and aft sweep with washout distally. Between P1 and P3, the magnitude of the proximal wash-in increased on the left wing while the distal washout decreased in both wings. For all flights, the wings showed overall anhedral, though the barn owl featured some dihedral proximally. The shapes observed are the result of both ‘active’ (bird acting on flow) and ‘passive’ (flow acting on bird) mechanisms that cannot be easily distinguished from this data.

Changes in configuration and asymmetries between the wings are also revealed through figure 3.14. The barn owl featured twist asymmetry proximally in O1 and O3 and distally in O2. Between P1 and P3, the peregrine swept its wings back, increased anhedral and reduced washout distally. The tail was also widely spread (abducted) in P1, whereas in P2 and P3 it was furled (adducted). In P3, the right wing was 40 mm more extended than the left, equivalent to approximately 16% difference in area, and corresponded to a subtle asymmetry in sweep, where the left wrist was more cranial than the right. The video footage showed the peregrine rolling to the left immediately after the centre of the measurement volume, suggesting that this asymmetry was used for correctional control.

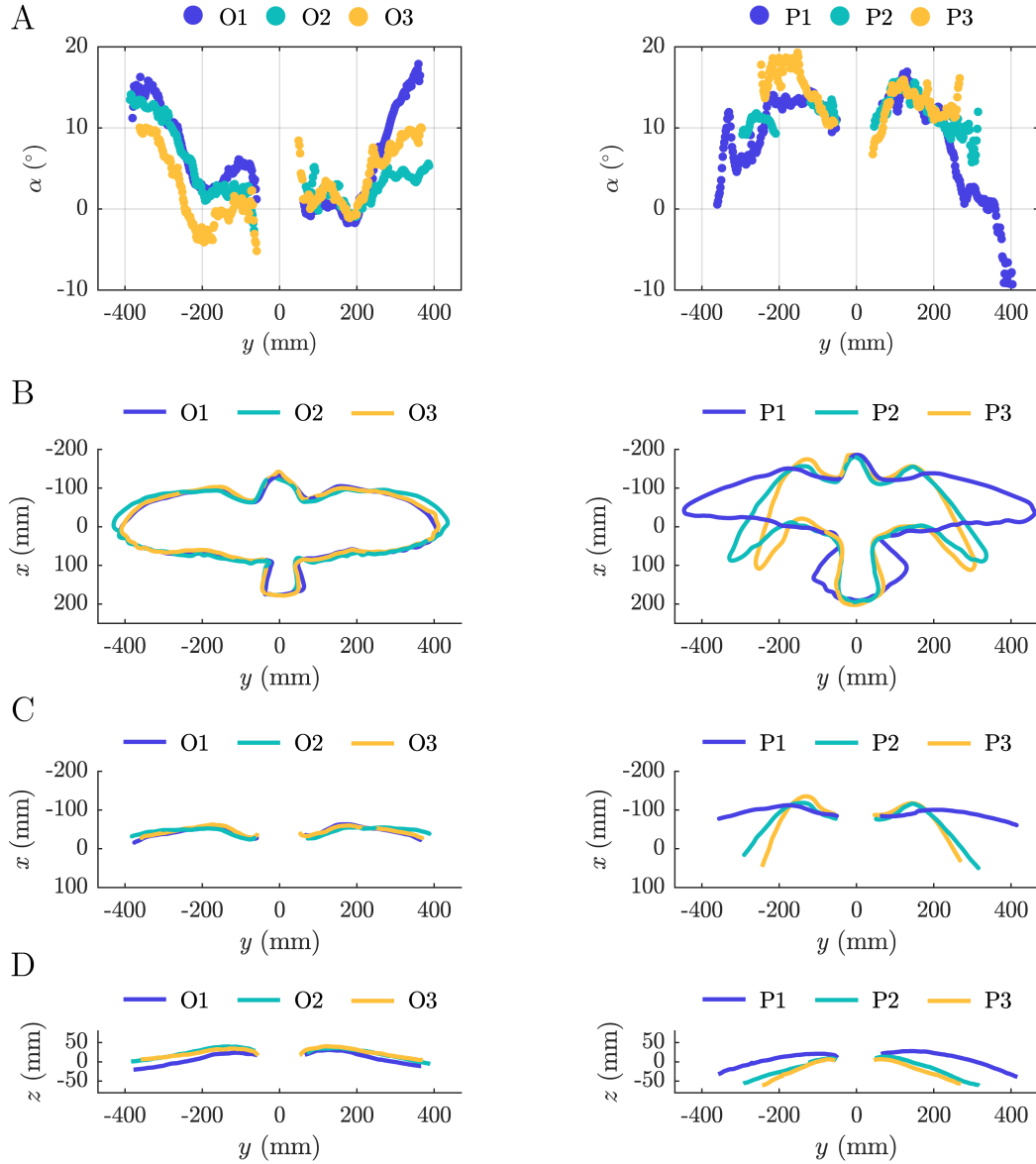


Fig. 3.14 Comparison between spanwise A) angle of attack (local chord vs. freestream) B) planform outline showing overall wing and tail configuration C) dorsoventral view of the quarter-chord to show wing sweep and D) posteroanterior view of the quarter-chord to show wing dihedral for the barn owl (O1-O3) and peregrine (P1-P3) flights.

Figure 3.15 shows the spanwise variation in wing thickness, and reveals features consistent with the known positions of the bones, muscles and feathers [153]. The maximum thickness of the barn owl (~ 20 mm) was higher than the peregrine (~ 16 mm), though the maximum thickness to chord ratios ($\sim 12\%$) were similar. The increased thickness distally on the right wing of P2 may be due to the aft sweep and

increased overlap of the feathers. Unfortunately this could not be confirmed from P3, due to the reduced quality reconstruction near the wing tips for the dorsal surface. The thickness distribution of P1 was slightly asymmetric, with the maximum thickness of the left wing approximately 4 mm larger than the right wing. There was no obvious anatomical explanation for this, given the symmetry of P2 and P3 in the arm wing, and the span symmetry of P1. Closer examination of the stereo reconstructions of the dorsal surface of P1 revealed a local disagreement between the two datasets in the region of the arm wing that likely accounts for this asymmetry; this level of disagreement was not present in any of the other flights.

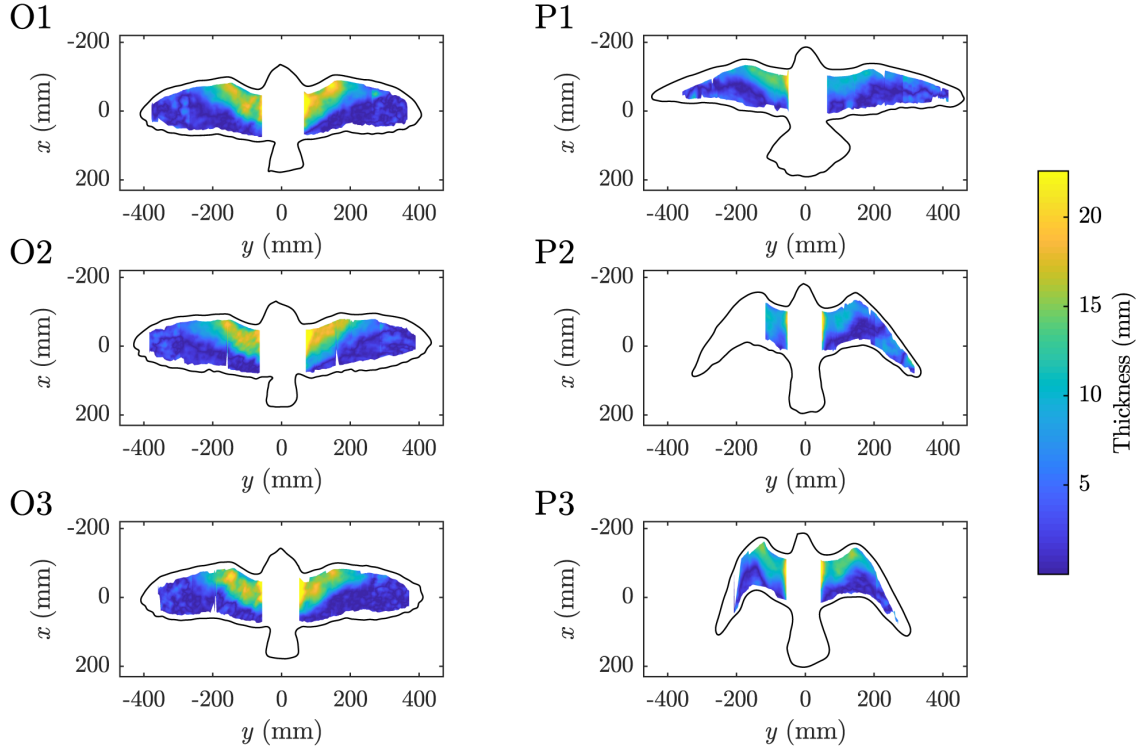


Fig. 3.15 Planform views showing thickness distributions for the barn owl (O1 - O3) and peregrine (P1 - P3). The chordwise data range varies with spanwise position because thickness can only be calculated for the shared range of the dorsal and ventral splines, which changes from one section to the next. Towards the wing tips, the lack of thickness data is due to decreasing data quality in these regions. The colourmap range has been adjusted to saturate at just over 22 mm in order to show the variation in thickness more clearly. The saturated regions are located immediately adjacent to the bird's body.

3.6 Discussion

3.6.1 Summary of results

The results showed that the barn owl flew relatively consistently in terms of speed, angle of attack and configuration for the three flights presented, and these were generally representative of all ten flights carried out during data collection. Measurements of the wing showed positive camber that reduced in magnitude distally, combined with significant spanwise wash-in, a small amount of aft sweep (O1 and O3) and moderate anhedral distally that was slightly increased during O1. Conversely, the peregrine flights showed significant differences in flight speed, angle of attack, wing twist, sweep, dihedral and tail configuration.

3.6.2 Longitudinal static stability

We now address the question: can longitudinal static stability be determined for these birds, based purely on their geometry, as discussed in section 3.3? Making this assessment without quantifying the position of the centre of mass and neutral point is based on the assumption of a linear moment slope, and the fact that a positive zero-lift pitching moment is required to balance a stable configuration, while the opposite is true for an unstable configuration. The question may therefore be re-stated: does the measured combination of camber, twist, sweep and tail angle of attack indicate a nose-down or a nose-up zero-lift pitching moment (figure 3.4)?

Variation in the spanwise geometry of both birds was complex in comparison with most conventional aircraft. The strong positive camber in the arm wing, and continued positive camber distally, would contribute towards a nose-down (i.e. negative) zero-lift pitching moment (figure 3.4B). Reflex camber is sometimes used in tailless aircraft to negate or minimise this moment [145], but was only present in a few very localised instances. Nearly all conventional aircraft have positively cambered wings, and require some combination of a low centre of mass, aft-sweep and wash-out or an aft-tail with longitudinal dihedral to provide a net nose-up zero-lift pitching moment [96]. Although the barn owl showed combinations of forward sweep with wash-out proximally, and aft-sweep with wash-in distally, the additional variation in camber makes it difficult to assess whether the zero-lift pitching moment contribution of these features was positive or negative. The combination of sweep and twist would then have a negligible impact on the zero-lift pitching moment. Furthermore, the small magnitude of the

sweep, particularly for O2, suggested that any contribution from the wings towards zero-lift pitching moment may have been quite small. Based on these observations, it seems plausible that the overall zero-lift moment of the wings was negative. The combinations of forward sweep with wash-in and aft sweep with wash-out for the peregrine, particularly P2 and P3, suggest that these features would have generated a nose-up zero-lift pitching moment. For these flights, the spanwise reduction in camber complements the sweep and twist as a way of contributing towards a positive zero lift pitching moment.

Longitudinal dihedral is the angle between the zero-lift lines of the wing and tail, and should be positive (i.e. tail at lower angle than wings) to generate a nose-up zero-lift pitching moment [71, 96, 145]. Table 3.3 shows the approximate range in wing angle of attack from figure 3.14A compared with the nominal tail attack angles from table 3.1. The variation in wing and tail angle of attack from table 3.1 are left out, since they were based on the time-dependent variation in angle of attack due to variation in the wind velocity and apply similarly to both the wing and tail at any given moment in time.

	Wing angle of attack range (°)	Tail angle of attack (°)
O1	-2 to 18 (3 to 23)	20.7
O2	-2 to 13 (3 to 18)	28.5
O3	-5 to 10 (0 to 15)	17.8
P1	-10 to 16 (-5 to 21)	24.2
P2	6 to 14 (11 to 19)	18.6
P3	7 to 19 (12 to 24)	19.1

Table 3.3 Comparing the relative angles of the wing and tail to assess longitudinal dihedral for the barn owl (O1-O3) and peregrine (P1-P3) flights. Values in parentheses are referred a local section zero-lift line assumed to be 5° above the chord line.

Longitudinal dihedral may be estimated by assuming that the zero-lift line of the tail was coincident with its elevation angle (due to the negligible camber observed) and that the zero lift line each wing section was approximately 5° above the chord line (values in parentheses in table 3.3). The latter was based on the approximate zero-lift angle of a Steppe eagle (*Aquila nipalensis*) arm wing section at a Reynolds number of 1×10^5 [119]. Since the zero-lift angle of the hand-wing (lower camber) was likely to be of lower magnitude, this assumption represents a likely upper limit. Assessment

of table 3.3 and figure 3.14A suggests that the majority of the wing had a zero-lift angle that was lower than the tail for all flights (i.e. longitudinal anhedral) except P3 where the left wing distally had higher angles. This does not mean that P3 had an overall longitudinal dihedral however, since the low camber distally on the left wing (where the angle of attack of the wing was higher than the tail) probably featured a zero-lift angle much smaller than 5° relative to the chord line. These results suggest therefore, that for all flights, the zero-lift pitching moment of the longitudinal dihedral was negative (nose-down). The magnitude of this nose-down moment was likely to be small for the barn owl due to its relatively small tail, and similarly smaller for P2 and P2 compared with P1 due to the extent of tail spreading.

In summary, the geometry of the barn owl does not appear to exhibit any geometric features that would help to generate a nose-up zero-lift pitching moment to counter strong positive camber in the wings, and negative longitudinal dihedral. It would be reasonable to expect more in-depth analysis (i.e. estimation of the centre of mass and neutral point) to show that it was longitudinally statically unstable. The geometry of the peregrine flights was more difficult to assess because the combination of sweep and twist might have generated a larger nose-up pitching moment than the positive camber and longitudinal anhedral.

3.6.3 Flight control

In this section the glide shapes and video footage are discussed in terms of correctional control, which is required to maintain a desired flight path whether a configuration is stable or unstable [39]. Wing asymmetry was observed that could have been due to correctional control or passive deflections from gusts of wind. Such asymmetries were not unexpected as the video footage and wind velocity data showed temporal variation in angle of attack, sideslip and the bird's overall shape. Spatial variation in wind velocity could also have resulted in these asymmetries due to the structural flexibility of the feathers.

The barn owl reconstructions revealed asymmetry in camber (figure 3.13) and spanwise angle of attack (figure 3.14A) and tail twisting (table 3.1). Between the fence and the centre of the measurement volume, O1 and O3 showed rolls to the left and right respectively, corresponding to asymmetry in camber distally and angle of attack proximally, that may have been used to annul the roll rate [99]. During O1, upward deflections of the secondary flight feathers on the right wing were observed in the video footage that may correspond to the proximal twist asymmetry in figure 3.14A.

The peregrine flights P1 and P2 were generally symmetric, while P3 showed asymmetry in span and sweep due to the partial retraction of the left wing (figure 3.14B). This corresponds to the video footage which shows the bird rolling to the left immediately after the centre of the measurement volume. This was consistent with observations of birds using span asymmetry as a means of roll control [88, 100, 154]. The peregrine showed significant variation in sweep, span, angle of attack, flight velocity and tail spread across the reconstructed flights (table 3.1 and figure 3.14B), consistent with observations of birds trained to glide steadily in tilting wind tunnels [11, 81, 106, 151, 152, 155]. Birds actively modulate their wing area with angle of attack and flow velocity to control their lift to drag ratio. Aerodynamic force measurements on the wings of dead peregrines showed that the lift to drag ratio was insensitive to changes in sweep angle at a given angle of attack, and may allow them to modulate velocity and wing area without affecting glide angle [19]. The present results reveal that the glide angle of the peregrine varied by less than 0.5° between flights, despite significant changes in air speed, angle of attack, camber, wing sweep, anhedral, tail spread and tail angle of attack. This suggests that a range of geometric configurations can generate highly consistent glide performance.

Bird's tails may contribute towards longitudinal stability and control [63, 79, 150], increased lift during slow and/or manoeuvring flight [63, 81, 103, 106, 152] and drag reduction [105]. The widely spread tail in P1 may have been required for weight support at the slower speed relative to P2 and P3 [63, 106]. Wind tunnel experiments suggest that although increasing tail spread has a negligible (and sometimes detrimental) effect on lift coefficient, the increased area still increases overall lift production at a given velocity and angle of attack [79, 107]. This may also have enhanced the control effectiveness of the tail in P1 at low-speed, where vulnerability to gust disturbances was slightly increased. The tail operated at high attack angles of 18° to 29° , though these would be reduced by up to 3° due to the downwash angle, ϵ , of the wing

$$\epsilon = \frac{C_L}{\pi A}, \quad (3.8)$$

assuming an elliptical lift distribution where C_L is lift coefficient and A is aspect ratio [3]. Even accounting for downwash, the measured tail attack angles were beyond the stall angle of most aerofoils suggesting that the tail may also be used to increase drag during final approach to landing. It is unlikely the tail acted like a delta wing during O1-O3 and P2-P3 because it was fully furled. This may also be the case for P1, based

on wind tunnel studies with frozen cadavers that showed delta wing theory becomes unreliable at spread angles greater than 60° . Tail twist angles between -5° and 13° (table 3.1) suggest it was used for correctional control similar to observations of soaring birds and experience with bird-like model gliders [95]. Correctional control with tail twisting has also been observed using on-board camera footage of a soaring steppe eagle *Aquila nipalensis* which revealed how the tail might be used to counteract the spiral mode and adverse yaw during banked turns [64, 65].

3.7 Conclusions and recommendations

In this chapter, simple flight dynamics theory was used to predict geometric features that would be required to balance longitudinally statically stable or unstable configurations. This was based on the assumption of a linear moment slope and the need for a positive zero-lift pitching moment to balance a stable configuration (and vice-versa for unstable configurations). To describe the geometry, the raw point clouds were sectioned along the span every 2 mm and spline fitting was used to represent the mean camber, dorsal and ventral splines in each section. Tail elevation and twist were estimated, along with spanwise camber, twist, sweep, dihedral and thickness to facilitate descriptions of the bird’s geometry. The geometric features of the barn owl suggested a negative zero-lift pitching moment, indicating it was longitudinal statically unstable. It was not possible to suggest the net contribution of the peregrine geometry to zero-lift pitching moment from geometry alone. Video footage of each flight and wind velocity data from a sonic anemometer were used to estimate the air velocity and attack angle of each flight. Possible mechanisms for flight control were also discussed based on the video footage and the measured asymmetries in span, camber and twist.

These estimates of wing and tail geometry allowed detailed insights into the complexity of avian surface geometry during gliding flight, including subtle asymmetries between the wings. The conclusions drawn about flight stability based only on geometric form are limited to longitudinal static stability only; nothing can be deduced about longitudinal dynamics or lateral-directional stability. Lateral-directional stability in birds has previously been discussed based on general observations from overall shape [27, 68, 76, 77, 94] and the estimation of derivatives based on highly simplified ‘bird-like’ shapes [85–88, 92]. However, due to the complex coupling inherent to lateral-directional dynamics, only a full dynamic model based on the correct overall shape and inertial properties can provide the necessary detail needed to further under-

standing. This is done in chapters 4 and 5, which describe methods used to develop the coupled equations of motion for the measured glide shapes. These chapters overcome the limitations of the present qualitative analysis, (1) by quantifying the relative positions of the centre of mass and neutral point to quantify longitudinal static stability and (2) through quantification of the linearised equations of motion for each glide shape and subsequent small perturbation stability analysis.

CHAPTER 4

HOW WING AND TAIL CONFIGURATION INFLUENCE THE CENTRE OF MASS AND MOMENTS OF INERTIA OF FREE-GLIDING BIRDS OF PREY

4.1 Chapter summary

Birds control their flight by morphing their wings and tail, influencing not just aerodynamic forces and moments, but also their mass distribution. In this chapter, the effect of glide configuration on the inertia tensor and centre of mass position is investigated in three species of birds using X-ray computed tomography (CT). Cadavers of two naturally deceased barn owls (*Tyto alba*), four peregrine falcons (*Falco peregrinus*) and a sparrow hawk (*Accipiter nisus*) were CT-scanned in approximate glide configurations. A phantom set was used to generate calibration curves correlating Hounsfield Units (via the grey values) with physical density, enabling the centre of mass and inertia tensor of the birds to be calculated. The method was validated using a trifilar pendulum, which demonstrated that the results for the inertia tensor using the CT approach were accurate to within 10%. The ‘virtual’ and physical masses of the bird’s appendages were also in close agreement, further confirming the accuracy of this approach. To estimate the centre of mass and inertia tensor of the free-gliding configurations presented in chapters 2 and 3, the cadavers that most closely matched the live birds were segmented and aligned to the photogrammetric surface reconstructions. This showed that variation in wing sweep between the peregrine flights had negligible influence of the centre of mass position, but did have a small impact on the principal components of inertia. Fully retracting the wings resulted in a significant reduction in roll inertia, halved yaw inertia and made almost no difference to pitch inertia. Birds have a significantly lower roll moment of inertia compared to model aircraft of similar mass and span, suggesting that reduced inertial damping in roll is no hindrance to effective flight control in these animals, despite the turbulent conditions in which they fly.

4.2 Chapter structure

This chapter begins by introducing the concept of mass moment of inertia and its relevance, along with the centre of mass, to flight dynamics. A brief literature review is provided describing methods used in the field of animal flight for estimating the centre of mass and inertia tensor of birds and bats. The principles of X-ray computed tomography (CT) are then described, and it is argued that this might represent an improved method for estimating the inertial properties of birds than those used previously. Methods are described in which naturally deceased barn owl, peregrine and sparrow hawk cadavers were CT scanned, and how the data were used to estimate the centre of mass and inertia tensor based on the photogrammetrically measured glide configurations discussed in chapters 2 and 3. Techniques to validate these results are also described. Estimates of the centre of mass and inertia tensor for the barn owl and peregrine flights from previous chapters are then presented and discussed in terms of their implications for flight stability and control.

4.3 Introduction

The flight dynamics of birds and aircraft are determined to a large extent by their centre of mass position (CoM) and mass moment of inertia (MoI) tensor [38, 96]. In addition to being the point about which a body rotates, the CoM is crucially important for quantifying longitudinal static stability [38, 96]. The inertia tensor is the 3×3 array describing the distribution of mass in an object, in three-dimensional Cartesian coordinates [156]. The diagonal elements, I_{xx} , I_{yy} and I_{zz} , are called the principle components of inertia (PCI) and define the MoI about the x , y and z axes respectively. The off-diagonal elements, I_{xy} , I_{xz} and I_{yz} , are called the products of inertia, and define cross-coupling that may occur in angular motion due to asymmetries of the body about its CoM and coordinate axes. In matrix form, Newton's second law for rotation may be written,

$$\begin{bmatrix} M_x \\ M_y \\ M_z \end{bmatrix} = \begin{bmatrix} I_{xx} & -I_{xy} & -I_{xz} \\ -I_{xy} & I_{yy} & -I_{yz} \\ -I_{xz} & -I_{yz} & I_{zz} \end{bmatrix} \begin{bmatrix} \dot{\omega}_x \\ \dot{\omega}_y \\ \dot{\omega}_z \end{bmatrix} \quad (4.1)$$

where ω is angular velocity (with the dot denoting its derivative, angular acceleration), M is applied moment and the subscripts, x , y and z refer to the coordinate axes about which these rotations are described. Equation (4.1) represents the foundation of flight dynamics analysis, and is discussed in more detail in chapter 5. Further information on the inertia tensor and the relevant equations may be found in introductory dynamics texts [156].

Estimates of the CoM and MoI of complete birds are scarce [157]. Within animal flight research, estimates CoM have been carried out by hanging frozen specimens from different positions and recording the position of a plumb line against the body. Marking the plumb line position from three positions leaves a central triangle, whose centroid provides an estimate for the centre of mass and whose size is indicative of the error [76, 158]. The commonly used approach for estimating MoI is ‘strip analysis’, which has been used to estimate the moments of inertia of single wings about the humeral head for analysis of flapping flight [159–163]. In this approach, the wing is physically divided into spanwise sections (cuts are parallel to wing chord) which are then individually weighed and their centroids recorded (planform view). The wing MoI, I_w , is then calculated using

$$I_w = \sum_{i=1}^n m_i r_i^2, \quad (4.2)$$

where m_i is the mass of each wing strip and r_i is the distance between the humeral head and the strip centroid. This approach was found to be accurate to within 5% if at least 15 strips were used per wing [162]. Pendulum approaches have also been used, in which the time period of oscillation and the dimensions of the pendulum are used to estimate the MoI [158, 164]. In rare instances, all three principle components of inertia have been estimated although the methods and their validation were not described in detail [158, 165]. Three-dimensional transformation of wing MoI estimates onto wingbeat kinematics has allowed MoI to be estimated throughout the wingbeat cycle in a few studies with birds [158, 165] and bats [166, 167].

More recently, X-ray computed tomography (CT) has been used to estimate the inertial properties of extant animals including birds (*Gallus gallus*, including junglefowl and broiler chickens) and a crocodile (*Crocodylus johnstoni*) to inform similar models of the extinct dinosaur, *Tyrannosaurus rex* [168, 169]. In this approach, the inertial model is divided into volumetric regions of distinct tissue types, or hollow regions containing only air. The grey values of the scanned regions are linearly proportional

to the relative density of the tissue, such that threshold based segmentation could be used to separate bones, muscles and air. The advantage this approach is the ability to generate deformable, articulated biomechanical models with the correct regional densities, allowing more accurate CoM and MoI estimation (fully three-dimensional), and assessment of error through sensitivity studies. This approach informed the method described in this chapter to estimate the inertial properties of free-gliding birds, due to its obvious advantages over previously used methods. Imaging techniques including CT, magnetic resonance imaging (MRI) and photogrammetry have all been used for estimating the inertial properties of humans [170, 171].

A helpful overview of CT technology may be found in Goldman [172], with some of the key principles described below. In simple terms, CT scanners consist of an X-ray emitter and detector that lie either side of the object being scanned (usually referred to as the patient, due to the medical context in which CT was developed). The space through which the X-rays pass is divided into an imaginary three-dimensional array of cubes called voxels (3D pixels), which may be thought of as a stack of two-dimensional images arranged along the axis of the scanner. For each scanned two-dimensional image (or slice), the detector and emitter rotate around the patient. The difference between the emitted and detected X-ray intensity at each position is a function of the attenuation of the patient

$$\begin{aligned} X &= \sum_{j=1}^n \mu_j \Delta_j, \\ X &= -\ln \left(\frac{N_e}{N_d} \right), \end{aligned} \tag{4.3}$$

where X is the attenuation of the ray, μ_j and Δ_j are the attenuation coefficient and width of the j th voxel and N_e and N_d are the intensities of the emitted and detected rays respectively. The attenuation coefficients depend on the atomic composition of the material present in the location of each voxel, and in the earliest CT scanners, were calculated simply by solving simultaneous equations based on the known emitted and detected ray intensities obtained from rotation around the patient. However, modern scanners use ‘filtered backprojection’ and image filtering algorithms to estimate the attenuation coefficients in the voxel array. Each CT image is therefore a representation of the attenuation of the various regions of the patient contained within the scanned slice. The attenuation is described in terms of ‘CT numbers’ in ‘Hounsfield units, HU,

$$HU = \frac{1000 (\mu_{voxel} - \mu_{water})}{\mu_{water}}, \quad (4.4)$$

where μ_{voxel} and μ_{water} are the attenuation coefficients of the patient and of distilled water respectively. CT numbers therefore represent the relative density between voxels in the scan, with $HU = 0$ for water when the scanner has been properly calibrated.

A reasonable approximation for absolute density is obtained [173] using

$$\rho = 1000 + HU, \quad (4.5)$$

and has been used to estimate the mass of body organs such as the lungs and brain [174, 175]. However, this approach is best used for objects whose density is close to water, since HU estimates for air using equation (4.5), even on recently calibrated scanners, have been shown to vary depending on scanner, scanner settings and date [176]. To accurately estimate the densities of materials very different to water (i.e. air and bone), it is necessary to use calibration phantoms (objects of known, uniform physical density) across the range of densities of interest, to estimate an improved calibration. This approach works very effectively for estimating the physical density of wood, as long as sufficient X-ray voltage is provided (120kVp) [177–179]. In these studies, the linear correlation between CT number and absolute density based on these calibration techniques was high (typically $R^2 > 0.9$). One potential issue in CT scanning is beam hardening, a process in which the attenuation of material further away from the emitter appears less dense than material of the same density closer to the emitter [172]. This is due to preferential attenuation of the lower-energy photons in the beam, such that deeper materials experience a higher proportion of high-energy in the X-rays, lowering their attenuation. This is corrected for in modern CT scanners, but can still lead to potential errors in the attenuation coefficients. However, in tests with blocks of wood, the beam hardening effects were found to be negligible. In summary, properly calibrated CT scans of appropriate voltage can be used to accurately estimate the density of plant and human tissue. This approach was therefore used to estimate the inertial properties of birds due to its reported high accuracy and potential benefits compared with previously used methods in the animal flight literature.

	Barn owls <i>Tyto alba</i>		Peregrines <i>Falco peregrinus</i>				Sparrow hawk <i>Accipiter nisus</i>
Cadaver ID	bo1	bo2	pf1	pf2	pf3	pf4	sh1
Maturity	A	A	J	J	A	A	J
Sex	M	M	M	M	F	M	F
Mass (g)	296	231	593	588	525	659	164
Span (mm)	956	917	942	991	1101	962	690
Emaciation (g)	N	69	77	82	575	N	96
Emaciation (%)	None	23	11	12	52	None	37
Mass loss (%)	1.69	1.30	1.69	-0.51	0.57	0.46	4.27

Table 4.1 Bird cadavers used for data analysis, with ‘A’ and ‘J’ referring to adult and juvenile respectively and ‘M’ and ‘F’ referring to male and female. The stated mass was estimated as close to death as possible. Span was estimated using photographs containing a reference scale. Emaciation was based on comparison of the measured mass with the average healthy mass for the species and sex [180], with ‘N’ referring to negligible mass loss. Mass loss was based on recordings before and after the collection of experimental data, which took place over 3 days. Overnight, the birds were refrigerated in sealed plastic bags to minimise mass loss.

4.4 Material and methods

4.4.1 Bird cadavers and preparation

To obtain reasonable estimates of the centre of mass (CoM) and mass moment of inertia (MoI) tensor of the freely gliding barn owl and peregrine introduced in chapter 2, it was important to obtain cadavers of similar mass and span. Furthermore, sexual dimorphism in peregrines made it important to obtain male cadavers of this species (females are significantly heavier than males). Since both barn owls and peregrines are protected by UK law, it was necessary to obtain naturally deceased specimens, which was not straightforward. Of the 47 animal rescue centres, falconry centres, zoos and veterinary centres contacted, only three were able to provide cadavers over the course of one year. In several instances, the birds were injured and/or emaciated, a familiar problem when using naturally deceased birds [161, 162]. Table 4.1 lists the cadavers used to obtain the results presented in this chapter. Birds that were severely emaciated included the barn owl, bo2, the peregrine, pf3. A sparrow hawk, sh1, was included in the dataset, although it was emaciated.



Fig. 4.1 Barn owl cadaver, bo2, secured to pre-cut sundeal board with timber pins (golf tees) and separated from the board by polystyrene sheet. A 30 cm steel rule is located at the bottom of the image for scale.

The cadavers were defrosted, and their wings stretched out for both CT scanning (see section 4.4.2) and trifilar pendulum testing (see section 4.4.5). It was important to provide a lightweight, stiff, flat surface to support the bird in the same posture throughout data collection, transportation and overnight refrigeration. As shown in figure 4.1, the dorsal surface of each cadaver was placed on pieces of pre-cut sundeal board. A radiolucent cushion of polystyrene foam was placed underneath the bird's dorsal surface to facilitate segmentation of the CT scan data from the sundeal board. Timber pins (golf tees) were carefully inserted through the bird's wrists into pre-drilled pilot holes in the sundeal board to keep the wings outstretched, while lightweight (6lb) fishing line was used to secure the head, legs and outer primaries. These measures ensured the birds remained in a relatively fixed position during data collection. The cadavers bo1 and pf4 were chosen for much of the analysis, since these were the healthiest and closest in mass to the live barn owl and peregrine introduced in chapters 2 and 3.

4.4.2 CT scanner and calibration

Each cadaver was CT scanned (LightSpeed RT16, General Electric, Boston, Massachusetts, USA) with a voltage and current of 120 kVp and 200 mA respectively and a spiral pitch factor of 0.9375. Each image in the stack had a resolution of 512×512 pixels and was separated by 1.25 mm with pixel widths ranging from 0.68 mm to 0.98 mm

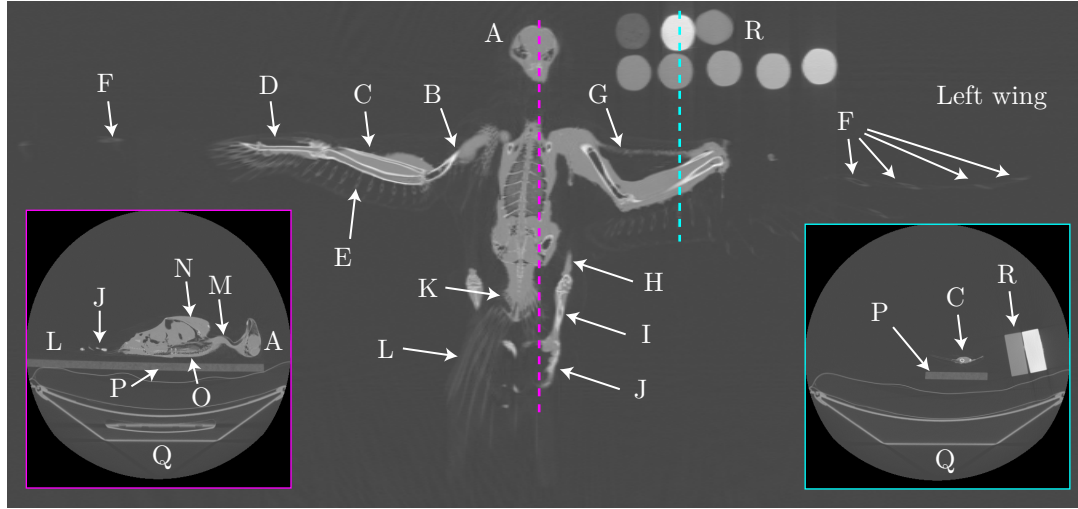


Fig. 4.2 Example 16-bit images from two different image stack directions for the peregrine falcon, pf1 showing: A - head, B - humerus, C - radius and ulna, D - manus, E - rachis inserts, F - primary remiges shafts, G - patagium, H - tibiotarsus, I - tarsometatarsus, J - digits (from feet), K - pygostyle, L - rectrices, M - cervical spine, N - pectoralis, O - dorsal vertebrae, P - sundeal board, Q - patient support, R - calibration phantoms.

depending on the field of view used for each cadaver. Image stacks were extracted in 16-bit format along axes roughly equivalent to the bird's dorsoventral and mediolateral axes, with examples shown in figure 4.2.

For each scan, a linear calibration curve was generated correlating the grey-values from the CT scan with the absolute density of eight tissue characterisation phantoms (Gamex 467, Sun Nuclear, Melbourne, Australia) with densities ranging from 450 kg/m^3 to 1820 kg/m^3 . Images from 25%, 50% and 75% planes approximately orthogonal to each phantom's longitudinal axis were used to obtain grey value samples by manually drawing an ellipse around each phantom. Regions of air were also sampled in a similar manner. The phantoms were scanned alongside each bird cadaver, and separate calibration curves were generated for each scan (figure 4.3). Cadavers bo1 and pf4 were also scanned with fully retracted wings.

4.4.3 Estimation of inertial properties

The known pixel size and slice thickness of the CT image stack was used, along with the 16-bit voxel grey values and scan calibration curve, to generate a data array containing

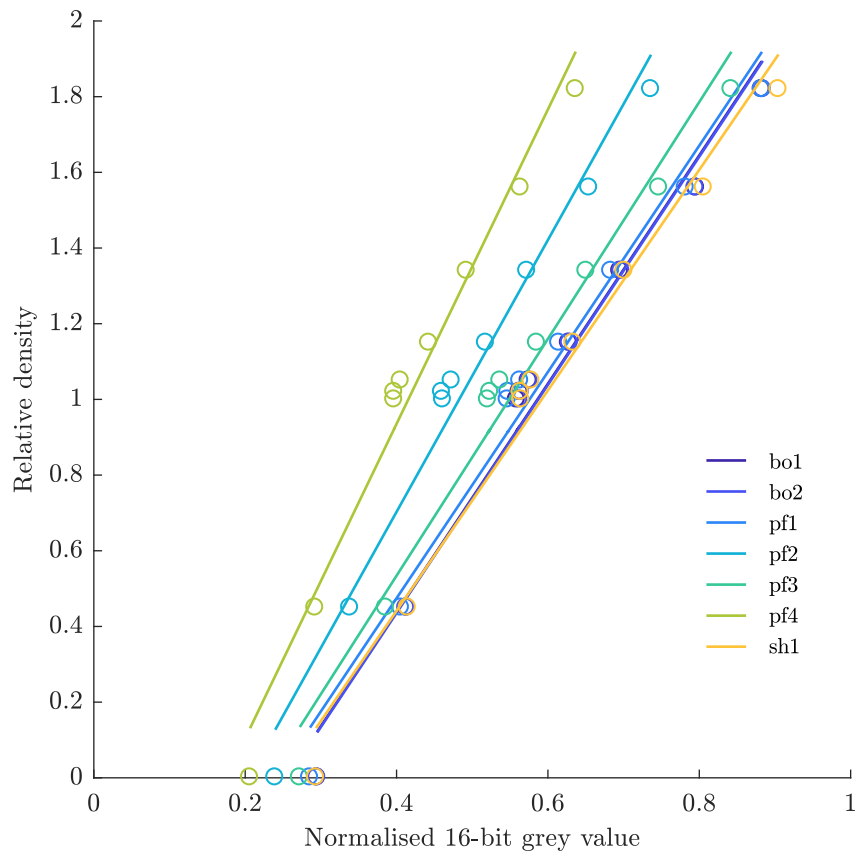


Fig. 4.3 Linear calibrations for each CT-scanned bird cadaver based on tissue characterisation phantoms (points). The variation in these calibration curves, possibly due to changes in the field of view or the mapping of CT numbers to grey-values, illustrates the importance of obtaining a calibration curve for each individual scan.

the 3D coordinates of the voxels, their density and mass using

$$\begin{aligned}
x &= u\Delta_x, \\
y &= t\Delta_y, \\
z &= v\Delta_z, \\
\rho &= \frac{\partial \rho}{\partial g}g + \rho_0, \\
V &= \Delta_x\Delta_y\Delta_z, \\
m &= \rho V,
\end{aligned} \tag{4.6}$$

where Δ_x , Δ_y and Δ_z are voxel dimensions, u , t and v are pixel coordinates in the x , y and z directions respectively, ρ is the mean material density of each voxel, g is grey-value, ρ_0 is the density assigned by the calibration curve when grey value is zero, m is voxel mass and V is voxel volume. Figure 4.4 shows example visualisations of the data in this format for the barn owl, bo1, where the colour map corresponds to the mean density within each voxel. Figure 4.5 shows the corresponding histogram, with peaks at very low density corresponding to the feathers and soft tissues near 1000 kg/m³. It should be noted that the densities are based on the volumetrically weighted mean of all the materials inside each voxel, and therefore do not necessarily represent the absolute density of the represented tissue. For example, although feather shafts are made from β -keratin (density approximately 940 kg/m³), the fact that they are hollow means that the mean density of their voxels is significantly lower than their actual density due to the presence of air. As demonstrated in section 4.5.1, this does not affect the accuracy of the method since the mass of the voxel is based on a correspondingly larger volume than the actual volume of the feather shaft contained within the voxel. This was confirmed by comparing the CT estimated mass of a single outer primary with that measured using a mass balance; both gave a result of approximately 1 g (see section 4.5.1).

The three-dimensional voxel coordinates and their assigned mean density and mass were exported into CloudCompare [143] for straightforward viewing and manipulation as a point cloud (i.e. voxels represented as point masses). It was then necessary to determine a density threshold in order to separate the bird and board from the surrounding air. Initially, a conservative threshold was applied to remove most of the voxels representing air, while still retaining the bird's feathers and a reasonable amount of noise. The bird and the board were then manually segmented, which was

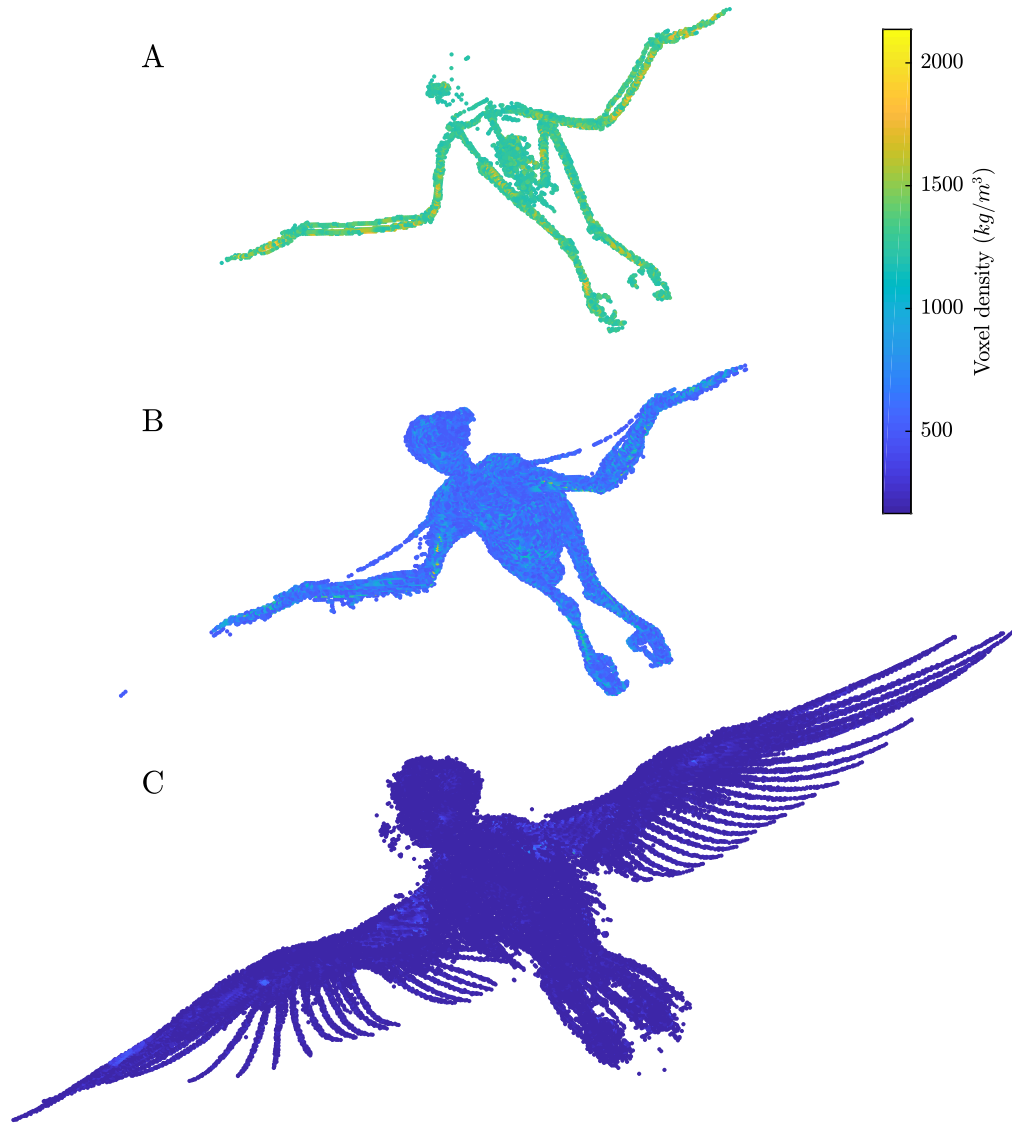


Fig. 4.4 Representation of CT image stack as a 3D point cloud, $x|y|z|\rho$, for the barn owl, bo1, with the scalar field corresponding to the voxel mean density obtained from the scanner calibration. Segmentation thresholds of 1200 kg/m^3 , 500 kg/m^3 , 166 kg/m^3 were used in A, B and C respectively to reveal the bones, skin and muscles and feathers.

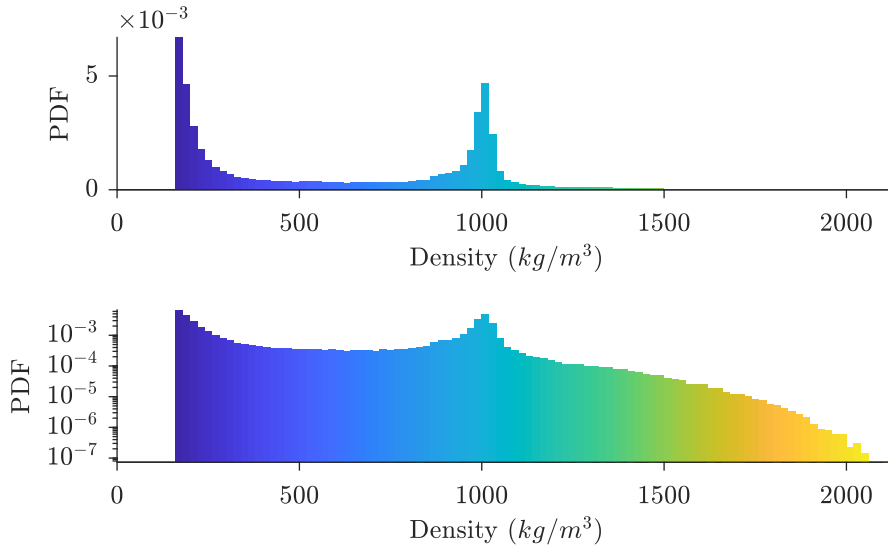


Fig. 4.5 Voxel density probability density function (PDF) for the barn owl, bo1, plotted with both linear and logarithmic axis scaling showing peaks corresponding to feathers and soft tissues. These plots are representative of the other bird cadavers.

straightforward due to the polystyrene layer between them (see section 4.4.1). A simple program was written in Matlab to gradually increase the segmentation threshold of the bird and board (separately) until the the CT-measured total mass (the sum of the voxel masses) was within 1 g the known total mass from the weighed cadaver and board. The scanned cadaver was then segmented (referred to here as ‘virtual dissection’), as shown in figure 4.6.

The virtually dissected appendages were then manually aligned to the photogrammetric surface reconstructions of the free-gliding birds described in chapter 2. The aim of this process was to obtain estimates of the CoM and MoI of the free-gliding birds for two distinct purposes. Firstly, it was necessary to quantify how the CoM and MoI changed due to changes in wing configuration between flights, based on the reasonable assumption that the remainder of the bird was fixed (i.e. head, torso, legs). This meant that all the cadavers for each species needed to have their non-moving parts consistently aligned both within a flight (intra-flight) and between flights (inter-flight). Secondly, it was necessary to quantify the CoM and MoI in the wing-body coordinate system (see chapter 2 figure 2.6) used for flight dynamics analysis (see chapter 5). This second requirement also included the first requirement - consistency of both intra- and inter-flight alignment of the cadavers to the photogrammetric surface reconstructions.



Fig. 4.6 The ‘virtual dissection’ of the barn owl, bo1, into: A - torso, B - humeri, C- radii/ulnae, D - manus, E - head and cervical spine, F - tibiotarsae, G - tarsometatarsae and digits, H - pygostyle and rectrices. The lower view shows the complete bird while the upper view shows the same view with a threshold of 1200 kg/m^3 to reveal bone.

This process was relatively complex, and is described in detail in Appendix C. Accuracy in the alignment process was achieved by matching key visual features in both the CT data and textured surface reconstructions, such as the beak, eyes, wing leading edge and talons. Example alignments are shown in figure 4.7 for cadavers bo1 and pf4.

For each CT dataset, the CoM position was calculated using

$$\bar{p} = \frac{\sum_{i=1}^n \rho_i V_i p_i}{\sum_{i=1}^n \rho_i V_i}, \quad (4.7)$$

where p represents either the x , y or z ordinates of each voxel in the scan, ρ_i represents the interpolated mean density of the voxel based on the scan calibration and V_i is the volume of each voxel. The datasets were then translated so that the CoM was at the origin (referred to here as ‘bird coordinates’), and the inertia tensor calculated using

$$\begin{aligned} I_{xx} &= \sum_{i=1}^n \rho_i V_i (y_i^2 + z_i^2), \\ I_{yy} &= \sum_{i=1}^n \rho_i V_i (x_i^2 + z_i^2), \\ I_{zz} &= \sum_{i=1}^n \rho_i V_i (x_i^2 + y_i^2), \\ I_{xy} &= \sum_{i=1}^n \rho_i V_i x_i y_i, \\ I_{xz} &= \sum_{i=1}^n \rho_i V_i x_i z_i, \\ I_{yz} &= \sum_{i=1}^n \rho_i V_i y_i z_i. \end{aligned} \quad (4.8)$$

The principal components and axes of inertia were also calculated for each CT dataset by calculating the eigenvalues and eigenvectors of the inertia tensor in bird coordinates. This is a standard technique that may be found in dynamics texts [156]. When an object is located relative to its principal axes, the diagonal elements of the inertia tensor are zero. Visualisations of the PAI and corresponding PCI are compared with the inertia tensors obtained from bird coordinates (see section 4.4.2) in Appendix B. These showed that ‘bird coordinates’ were within approximately 10° of the principal axes of inertia.

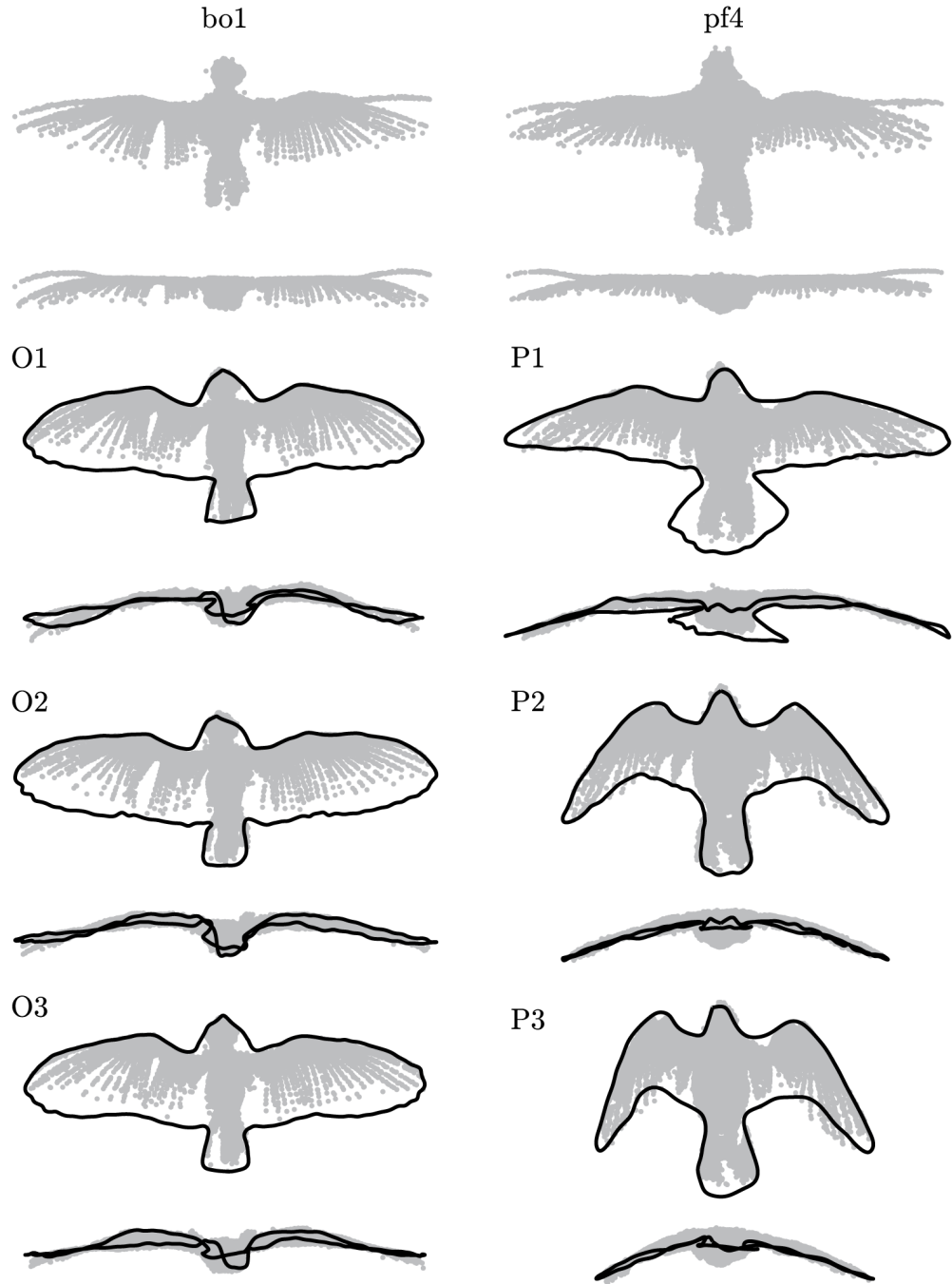


Fig. 4.7 To estimate the centre of mass and inertia tensor of the free-gliding barn owl (O1-O3) and peregrine (P1-P3) flights described in chapters 2 and 3, the CT-data were manually segmented and aligned to the photogrammetric surface reconstructions of the bird's surface. This figure shows only the edge spline and the CT-data for barn owl, bo1, and peregrine, pf4, for clarity. The CT tail data were not spread with the tail in P1, which probably had a negligible effect on I_{xx} and I_{zz} due to the proximity to the axes system and low mass of the tail.

4.4.4 Method validation summary

The CT-based CoM and MoI approach was validated with two different approaches. In the first approach, the cadavers were dissected to separate the head and cervical spine, torso, tibiotarsae, tarsometatarsae (and digits) and wings. Each wing was cut into three pieces at the elbow and wrist joints. The pieces were then weighed using a mass balance to a resolution of 0.1 g (LE341001P, Sartorius, Göttingen, Germany). The weighed masses were then compared with the virtually dissected appendage masses from the CT scans (see figure 4.6). In the second approach, a trifilar pendulum (TP) was used to estimate the MoI about the dorsoventral axis for comparison with the CT-based estimate. The TP was itself validated using accurately machined nylon blocks, whose MoI was calculated analytically. This second approach is now described in more detail.

4.4.5 Trifilar pendulum overview

Figure 4.8 shows the plan view of the TP setup, consisting of triangular base, sundeala board, bird and gyro suspended using 60lb nylon fishing line (referred to here as ‘cables’) and allowed to oscillate about its centre of rotation. The MoI of the TP, I_{TP} , was estimated assuming it behaved as a single degree of freedom dynamic system rotating about its centre of mass, with small rotation angles such that

$$I_{TP} = \frac{mgR^2\tau^2}{4\pi^2L}, \quad (4.9)$$

where m is the mass of the TP, g is gravitational acceleration, R is the distance between the cables and the centre of rotation, τ is the period of oscillation and L is the mean length of the cables [73]. The difference between the TP MoI with and without the object of interest, provided an estimate of its MoI about the axis of rotation. To ensure consistency with the model assumptions, a spirit level was used to ensure the TP base was horizontal, and only small oscillation amplitudes were applied. The pendulum base was constructed from a foam-ply sandwich structure to minimise its mass relative to the bird, a necessary measure for high accuracy.

The masses of the bird, board, base and gyro were obtained using an electronic balance with a resolution of 0.1 g (LE341001P, Sartorius, Göttingen, Germany) and the length of the supporting fishing line was calculated using a tape measure. The lengths of the cables were measured with a tape measure and averaged, and the distances

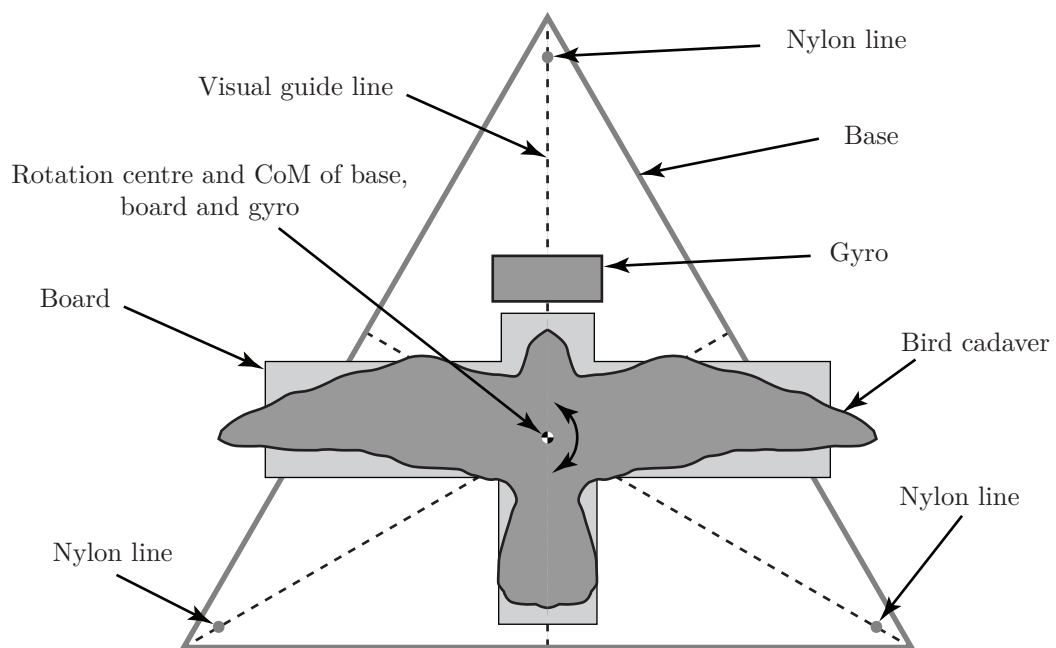


Fig. 4.8 Plan view schematic of TP arrangement. The centre of mass of the board and gyro was carefully located at the centre of rotation of the TP. The guessed centre of mass position of the bird was also aligned with the centre of rotation of the TP, with the error in the offset corrected for later using computed tomography data (see figure 4.9 and discussion).

between the cables and the centre of rotation were measured with a steel rule and also averaged. The time period was measured by sampling angular velocity at 70 Hz using the inbuilt gyroscope from a smartphone (Xperia Z1 Compact, Sony, Tokyo, Japan) and an application designed to retrieve the relevant data from the device (Sensor Kinetics Pro, Innoventions Inc., Houston, USA).

To minimise errors introduced by pendulum sway, only the final 60 s data from 180 s oscillation was used to estimate the time-period. A curve fit based on a damped harmonic oscillator was then applied to the angular velocity data using Matlab [139], based on equations (4.10) to (4.12) [181],

$$x(t) = X e^{-\zeta \omega_n t} (\cos(\omega_d t - \phi), \quad (4.10)$$

$$\dot{x}(t) = X \omega_n e^{-\zeta \omega_n t} \left[\sin(\phi - \omega_d t) \sqrt{1 - \zeta^2} - \zeta \cos(\phi - \omega_d t) \right], \quad (4.11)$$

$$\omega_d = \omega_n \sqrt{1 - \zeta^2}, \quad (4.12)$$

$$T = \frac{2\pi}{\omega_d}, \quad (4.13)$$

where x is displacement, t is time, ζ is damping coefficient, ω_d and ω_n are damped and undamped natural frequencies and X and ϕ are the amplitude and phase respectively. The curve fit coefficient corresponding to the damped natural frequency was used to obtain the period of oscillation, T , and was based on the mean of three independent measurements.

4.4.6 Trifilar pendulum accuracy assessment

To ascertain the accuracy of the TP, two nylon blocks were machined to sizes and masses approximately equivalent to the body sizes of the freely flying peregrine and barn owl (see chapter 3 table 3.1). Each block was weighed using a high accuracy mass balance (EW 620-3NM, Kern, Balingen, Germany) and measured using a vernier caliper. The MoI of each cuboid, I_z , was calculated analytically using

$$I_z = \frac{m}{12}(x^2 + y^2), \quad (4.14)$$

where m , x and y are the mass and dimensions of the block along its length and width respectively.

Table 4.2 shows comparison between the analytically and experimentally calculated values of the block MoI, I_z . The error in the analytical MoI estimates was calculated using

$$\frac{\delta I_z}{I_z} = \frac{\partial I_z}{\partial m} \frac{\delta m}{I_z} + \frac{\partial I_z}{\partial x} \frac{\delta x}{I_z} + \frac{\partial I_z}{\partial y} \frac{\delta y}{I_z}, \quad (4.15)$$

where the δ terms indicate the estimated fractional error of each individually measured value. Assuming the block material was homogeneous, this gave analytical errors of less than 0.003% (table 4.2).

The higher TP accuracy of the large block was due to the higher ratio of inertia between the TP with and without the block. The increased inertia reduces the time period, which in turn, reduces the fractional error in the time period estimation.

	Small block	Large block
Dimensions (mm) ± 0.01 mm	$200 \times 40 \times 34$	$200 \times 70 \times 40$
Mass (g) ± 0.001 g	312.25	641.03
Analytical I_z	$1.083 \times 10^{-3} \pm 0.003\%$	$2.399 \times 10^{-3} \pm 0.001\%$
TP I_z	1.119×10^{-3}	2.402×10^{-3}
TP error	3.3%	0.1%

Table 4.2 Comparison between the analytically and experimentally calculated inertia, I_z , of two machined nylon blocks of the same mass as the freely flying barn owl and peregrine in chapter 3. These results represent the worst case error, since their MoI would have been lower than for real birds due to their shape - i.e. the blocks lack features representing wings (see table 4.3)

4.4.7 Trifilar pendulum bird MoI estimation

To estimate the MoI of the bird cadavers, a modified form of equation (4.9) was used that took into account misalignment between the CoM's of the pendulum and the bird [182]

$$I_{dv} = \frac{R^2 g \tau^2}{4\pi^2 L} (m_P + m_B) - I_P - \frac{m_B D_{CoM}^2}{m_P + m_B} (m_P + \frac{m_B g \tau^2}{4\pi^2 L}), \quad (4.16)$$

where I_{dv} is the MoI of the bird about its dorsoventral axis, m_B and m_P are the masses of the bird and the pendulum without the bird respectively, I_P is the MoI measured by the TP without the bird, τ is the time period with the bird, and D_{CoM}

is the CoM offset between the bird and the TP centre of rotation. This equation was required, because unlike the pendulum base, board and gyro, the CoM of the bird was not known. The CoM of the pendulum without the bird was carefully aligned to the centre of rotation by calculating the combined CoM of the gyro and the board, using their dimensions (i.e. assuming uniform density). However, the best-guess placement of the bird resulted in some small mis-alignment between the CoM of the pendulum and its centre of rotation. To estimate the alignment error, the CT data were used to estimate the CoM positions of the bird and board with respect to one another. The scan data were first transformed so that its orientation was matched to the orientation of the bird and board on the TP. This was done by translating the CoM of the board to the origin and then fitting a plane to the board to obtain a rotation matrix such that the vector normal to the plane was aligned with the z axis (equivalent to the TP axis of rotation). This transformation was applied to both the board and the bird, and the procedure described by figure 4.9 was then carried out. The equivalent CT estimate of I_{dv} was obtained using equation (4.8) after translating the bird scan data so the origin was at the CoM (using equation (4.7)).

4.5 Results

4.5.1 Method validation

Comparison between relative mass contributions of the physically and virtually dissected appendages is shown in figure 4.10, based on the means of each species (not including pf3 as it did not undergo physical dissection). The similarity of the mass breakdown between physical and virtual dissection demonstrates the accuracy of the CT calibrations, and shows that the product of the mean voxel density with its volume provided a reasonable estimate of the voxel mass (see section 4.4.3).

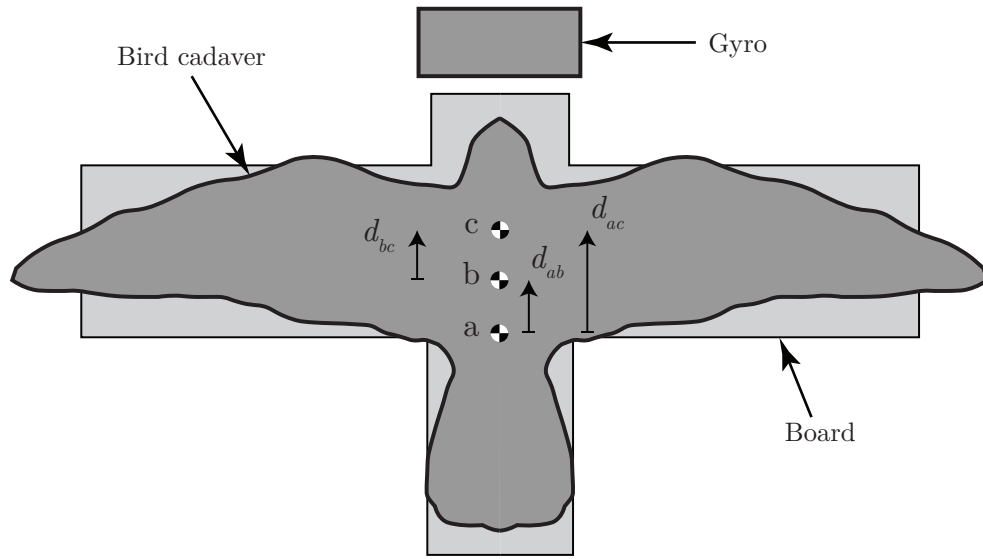


Fig. 4.9 Calculation of the CoM mis-alignment of the bird cadaver on the TP using CT data for the bird and board. The CoM of the board is labelled ‘a’, the CoM of the pendulum base, board and gyro is labelled ‘b’ (this was aligned to the centre of rotation) and the CoM of the bird is labelled ‘c’. The misalignment of the bird’s CoM on the pendulum is d_{bc} (equivalent to D in equation (4.16)) and was calculated by subtracting d_{ab} from d_{ac} . The distance, d_{ab} was estimated based on the dimensions and masses of the pendulum base, gyro and board. To obtain d_{ac} , the centre of mass of the board and bird were calculated and compared using the CT data.

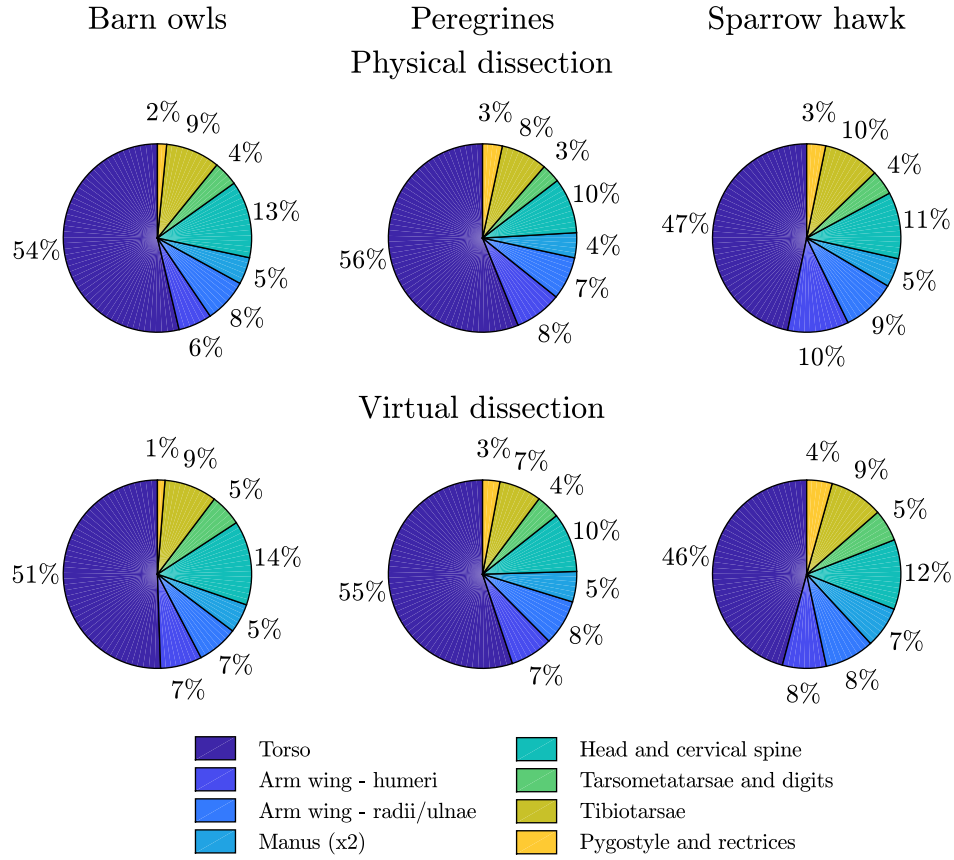


Fig. 4.10 Validation of the CT-based CoM and MoI measurement approach by comparing the masses of the virtually and physically dissected cadavers. Each chart is based on the mean contribution of each appendage from all the available cadavers. Given the small sample size, this was not intended as a species comparison, but mainly to demonstrate the mass estimation accuracy of the calibrated CT data.

Table 4.3 shows a comparison between the CT and TP MoI estimates for all the cadavers. As a general rule, the CT-based MoI estimation was accurate to within 10% of that measured using the TP, which itself was accurate to within at least 3.3% (table 4.2). Correcting for TP CoM misalignment (section 4.4.7) was important when it was more than 20 mm, and resulted in accuracy increases of up to 10%. MoI was also calculated assuming uniform density to assess the impact of the CT calibration on the accuracy of the results. Applying the mean density of the entire bird to every voxel resulted in overestimation of I_{dv} up to 58% which was probably due to the increased voxel masses in the hand wing. The displacement of the estimated CoM position based on a uniform density assumption was also estimated and showed no more than 5 mm difference (or up to 4% mean aerodynamic chord).

	bo1	bo2	pf1	pf2	pf3	pf4	sh1
CoM misalignment (mm)	-31	-29	-12	-11	-19	-8	-28
TP I_{dv} ($\times 10^{-3}$ kgm ²)	1.98	1.86	4.58	4.23	6.83	4.59	1.09
CT I_{dv} ($\times 10^{-3}$ kgm ²)	1.82	1.67	4.61	4.37	6.70	4.90	1.09
CT vs. TP (% error)	-8.1	-10.3	0.7	3.2	-1.8	6.8	0.2

Table 4.3 Comparison between trifilar pendulum and CT measured dorsoventral MoI.

Further confirmation of the accuracy of the CT-based MoI estimations was provided by comparison with wing MoI obtained using ‘strip’ analysis (figure 4.11) [162]. The present results were in close agreement with this data, providing further support for this allometric relationship.

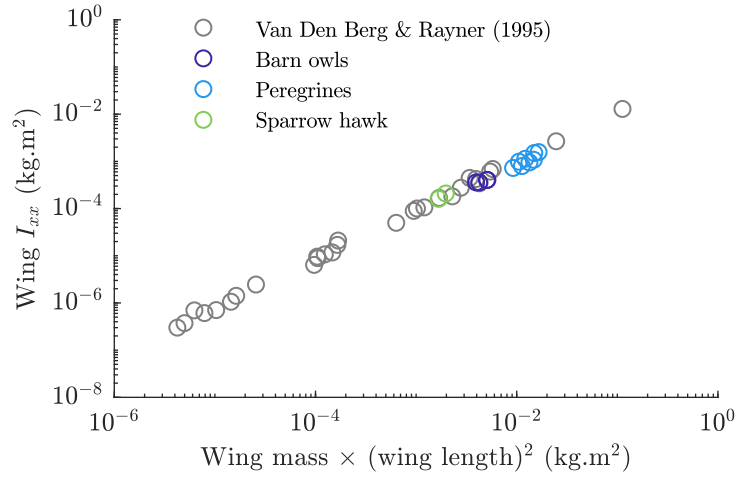


Fig. 4.11 Comparison between wing MoI measurements using ‘strip analysis’ [162] and the present results obtained using CT scanning. The wing MoI was measured about an axis passing through the humeral head and parallel to the x -axis of the principal axes of inertia.

4.5.2 Cadaver CoM and MoI

Figure 4.12 shows the contribution of the body, wings, head & cervical spine (neck) and legs & tail towards the total mass of the bird using the virtually dissected CT data (see figure 4.6). The total masses of cadavers bo1 and pf4 were within 3% of typical healthy weight [180], while the remaining cadavers experienced some degree of emaciation. Cadavers pf3 and sh1 were severely emaciated (52% and 37% below a typical healthy mass for the species - see table 4.1), while corresponding values

for bo2, pf1 and pf2 were 23%, 11% and 12%, suggesting that the emaciation was less severe. Figure 4.12 shows that most of the difference in total mass between the healthy and emaciated birds was accounted for by the difference in body mass. The wings, head/neck and legs/tail were relatively similar between healthy and emaciated cadavers suggesting that, similar to migrating birds, energy reserves were distributed around the torso [153].

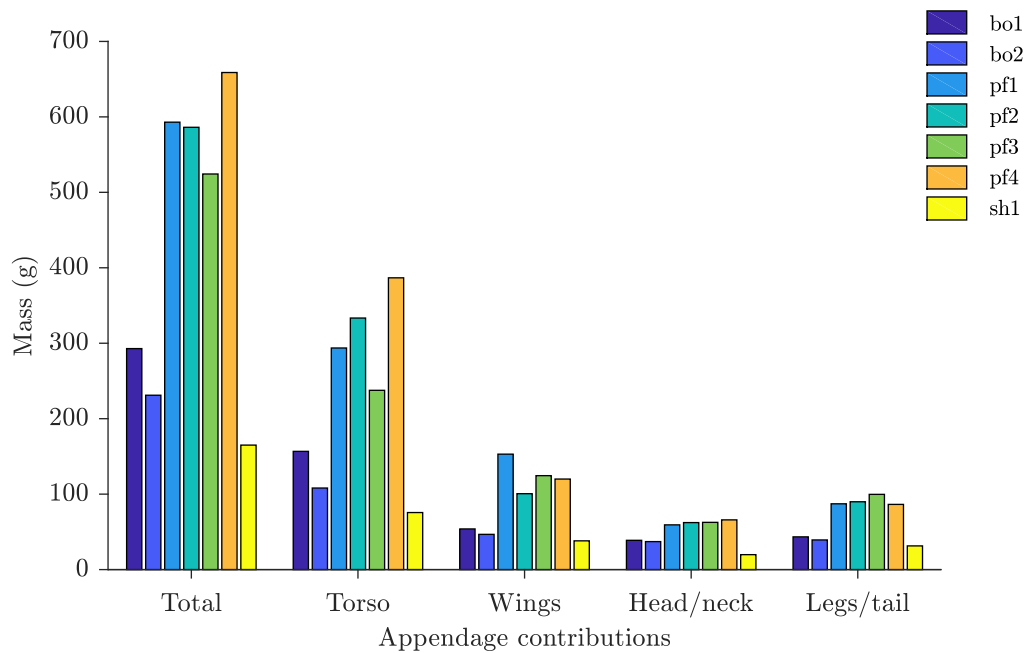


Fig. 4.12 Comparison between cadavers to assess both the relative contributions of the appendages to total mass between the cadavers and the impact of emaciation.

The PCI were lower for emaciated cadavers bo2, pf1 and pf2 compared with their healthy counterparts bo1 and pf4, but by less than the mass difference. This was because most of the mass loss occurred in the body, close to the rotational axes about which the PCI were estimated. Since MoI was less sensitive to emaciation than total mass, it was considered reasonable to include bo2, pf1 and pf2 in further analysis. Despite its comparatively severe emaciation, pf3 had the highest MoI due to its larger span (table 4.1). This was expected since pf3 was female, while the remaining peregrine cadavers were male (female peregrines are larger than males). Since the emaciation of pf3 was so severe, it was excluded from further analysis. The emaciation of sh1 was also severe, but since it was the only sparrow hawk cadaver available, it was retained

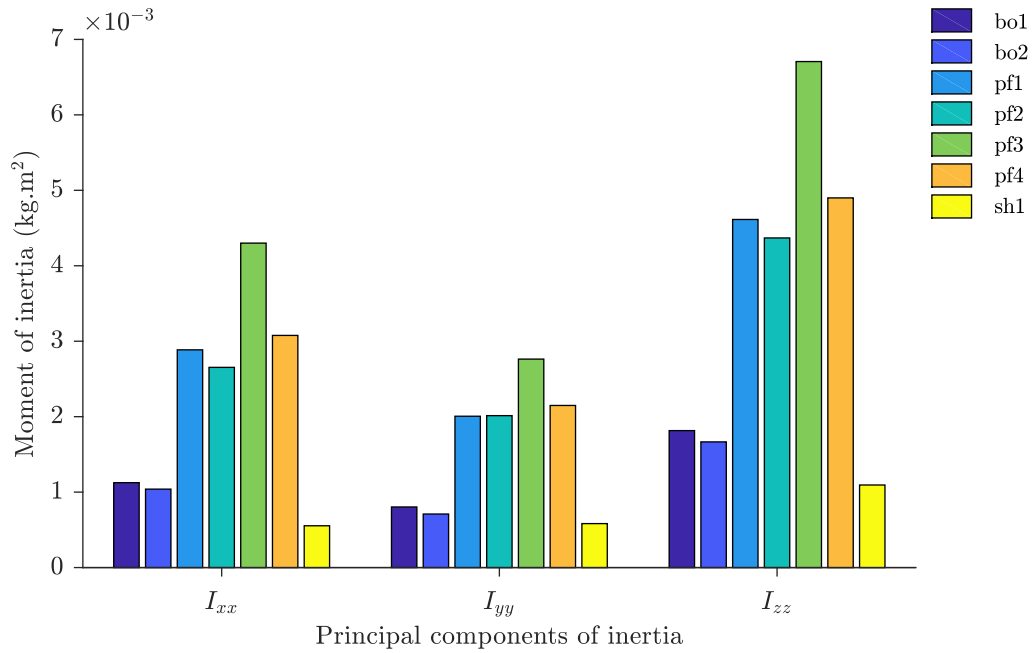


Fig. 4.13 Comparison of the principal components of inertia between cadavers.

in the dataset. The following results for sh1 should therefore be interpreted in light of its severely emaciated condition.

Figures 4.14 to 4.16 show the differences between mass and moment of inertia distribution in the cadavers bo1, pf4 and sh1. In figure 4.14, the CT data were projected onto the x - y , y - z and x - z planes and resampled using a grid to visualise the distribution in mass and inertia. For each individual projection, the data were normalised to clearly show where mass and inertia were highly concentrated. The projected mass distributions (left-column) showed mass concentration in the body due to the increased volume and density of tissue. Mass was also more concentrated around the wing bones and muscles, compared with the feathered regions of the wing and the patagium. Interestingly, the anteroposterior view (B) shows the peak mass concentration dorsally, due to the dorsal positions of the head and legs of the bird. This is somewhat contrary to the generally accepted assumption that the low body, and weight of the internal organs must imply that birds have a ventrally skewed centre of mass position [76]. However, this could also be because the bird was placed dorsal surface down in the scanner. The general pattern of mass distribution between species and between cadavers was similar. The projected moment of inertia distribu-

tions (right-column) showed a significant shift in concentration, compared with mass distribution, from the body to the wing bones, head, tarsometatarsae and digits. In particular, the moment of inertia was concentrated in the bones and muscles of the manus, consistent with previous findings [162]. This is because moment of inertia is proportional to radius squared, such that the inertia distally remains relatively high despite the low mass of the flight feathers. Again the inertia distribution was similar between species and cadavers.

The relative contributions of the dissected appendages to mass and moments of inertia are provided in figure 4.15 for cadavers, bo1, pf4 and sh1 (see figure 4.6 for legend definitions). The bird's body contributed to between 50% - 60% of the total mass, of which approximately 17% was likely due to the pectoral muscles [183]. The wings contributed between 18% - 23% of the total mass, consistent with previous findings [161], although this may be overestimated for the sparrowhawk assuming of the mass loss due to emaciation was from the body (see figure 4.12). The pygostyle and rectrices, contributed no more than 4% of the total mass. Interestingly, the bird's head was more than half the total mass of the wings while the combined mass of the tibiotarsae, tarsometatarsae and digits was approximately three-quarters the total mass of the wings.

There were significant differences between the mass and MoI contributions of the appendages. Despite contributing only 20% of the total mass, the wing contributed approximately 85% to I_{xx} and almost 50% I_{zz} . Conversely, the wing contributed only 10% to I_{yy} due to its low mass and distribution radially from the y -axis. Although the manus constituted only 5-7% of the total mass, it contributed 57-63% towards I_{xx} and 32-40% towards I_{zz} due to its distal location. Similarly, the head, legs and tail contributed up to 80% towards I_{yy} despite comprising no more the 30% of total mass. About all axes, the contribution of the body towards PCI was relatively small ($< 17\%$), with the exception of the peregrine's I_{yy} (29%). The peregrine's body contributed slightly more to total mass (59%) than the barn owl (54%) or sparrowhawk (46%). It also had a higher body length to wing span ratio (0.41) compared to the barn owl (0.34). The sparrowhawk had a body length to wing span ratio higher than the peregrine (0.57) due to its relatively long tail feathers, which may explain the slightly higher contribution of the pygostyle and rectrices to I_{yy} . Conversely, the short tail of the barn owl contributed less than 3% to the PCI.

Figure 4.16 shows the spanwise contribution of the wings and body towards I_{xx} and reveals features consistent with strip analysis of a house sparrow (*Passer domes-*

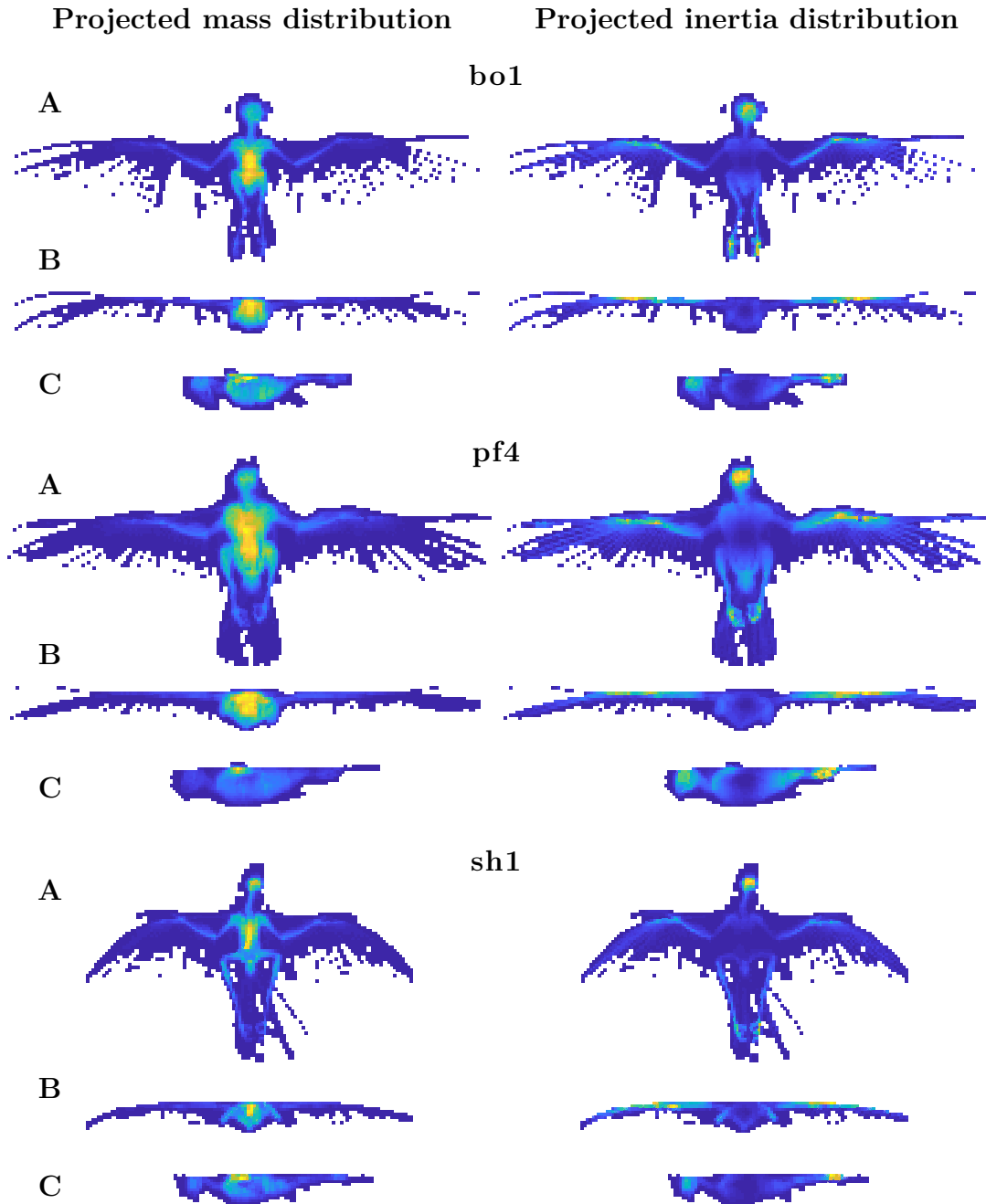


Fig. 4.14 Grid-sampled projections of mass (left-column) and moment of inertia (right-column) for the barn owl, bo1, peregrine, pf4, and sparrow hawk, sh1, cadavers, using their calibrated CT-scan data. Each cadaver shows A) dorsoventral (I_{zz}), B) anteroposterior (I_{xx}) and C) lateral (I_{yy}) views. In each instance, the data were normalized by the maximum value, with the bright and dark colours corresponding to high and low values respectively.

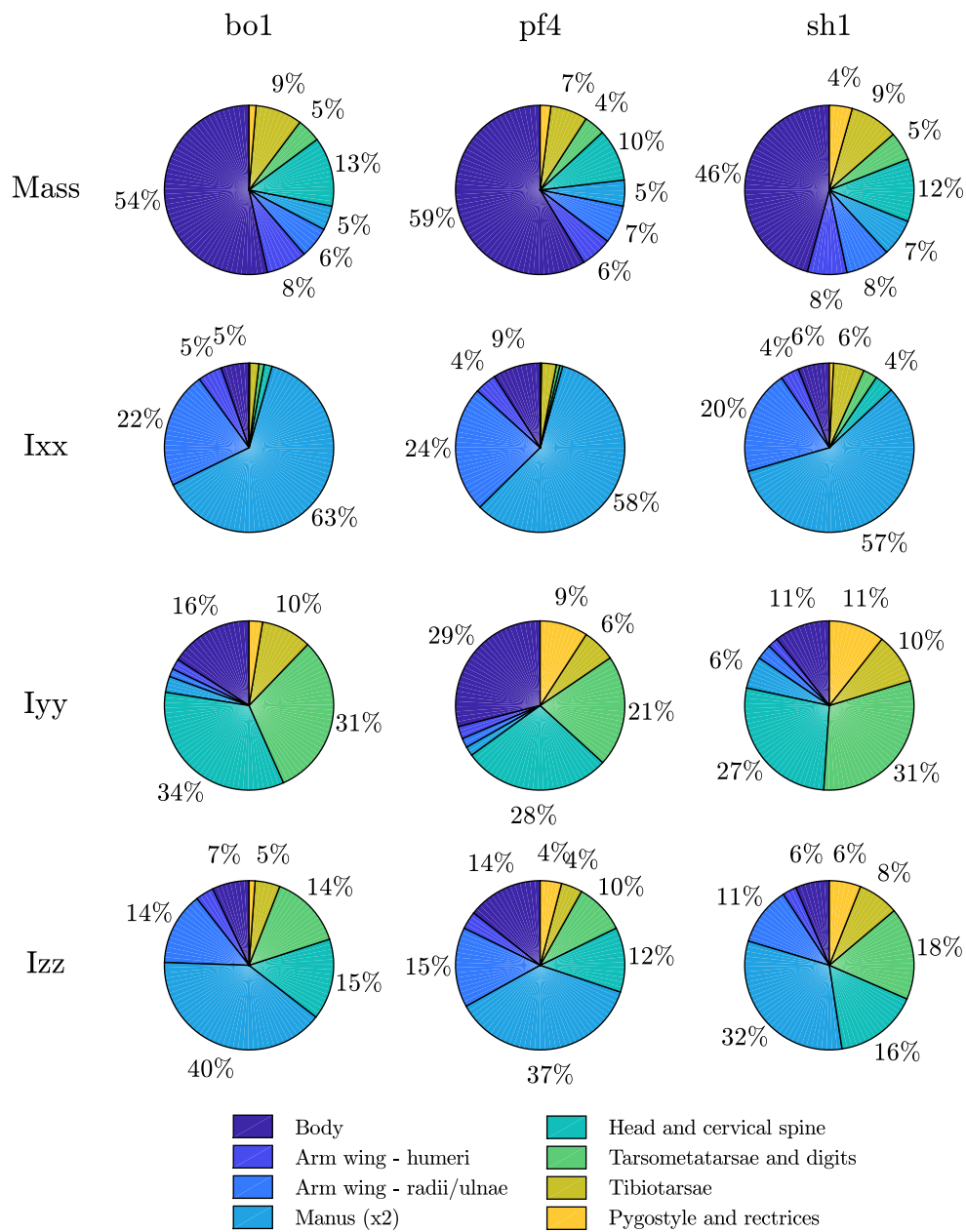


Fig. 4.15 The relative contributions of various appendages to the total mass and the principal components of inertia for the healthy barn owl and peregrine cadavers, and the emaciated sparrowhawk cadaver. Segments below 3% not labelled.

ticus), blackbird (*Turdus merula*) and house swift (*Apus afinis*) [162, 184, 185], but at significantly higher spatial resolution. These features include gradually reducing mass distally (figure 4.16A) and a ‘double-bell’ in inertia in the vicinity of the wrist joint and manus (figure 4.16B). Close inspection of the scan data revealed that the trough of the double-bell proximally of ± 0.5 normalised span corresponded with the spatium intermetacarpale in the manus, while the peaks corresponded with the wrist joint and the pila cranialis [186]. The significant asymmetry in I_{xx} for pf1 and pf4 corresponds to trauma in the left and right wings respectively (i.e. the wings with higher peaks), where the increased inertia may be due to excess fluid from inflammatory response [187]. This may account for the slightly higher I_{xx} and I_{zz} values of pf1 and pf4 compared with pf2 in figure 4.13, which would otherwise be unexpected given the higher wing span of pf2 (see table 4.1).

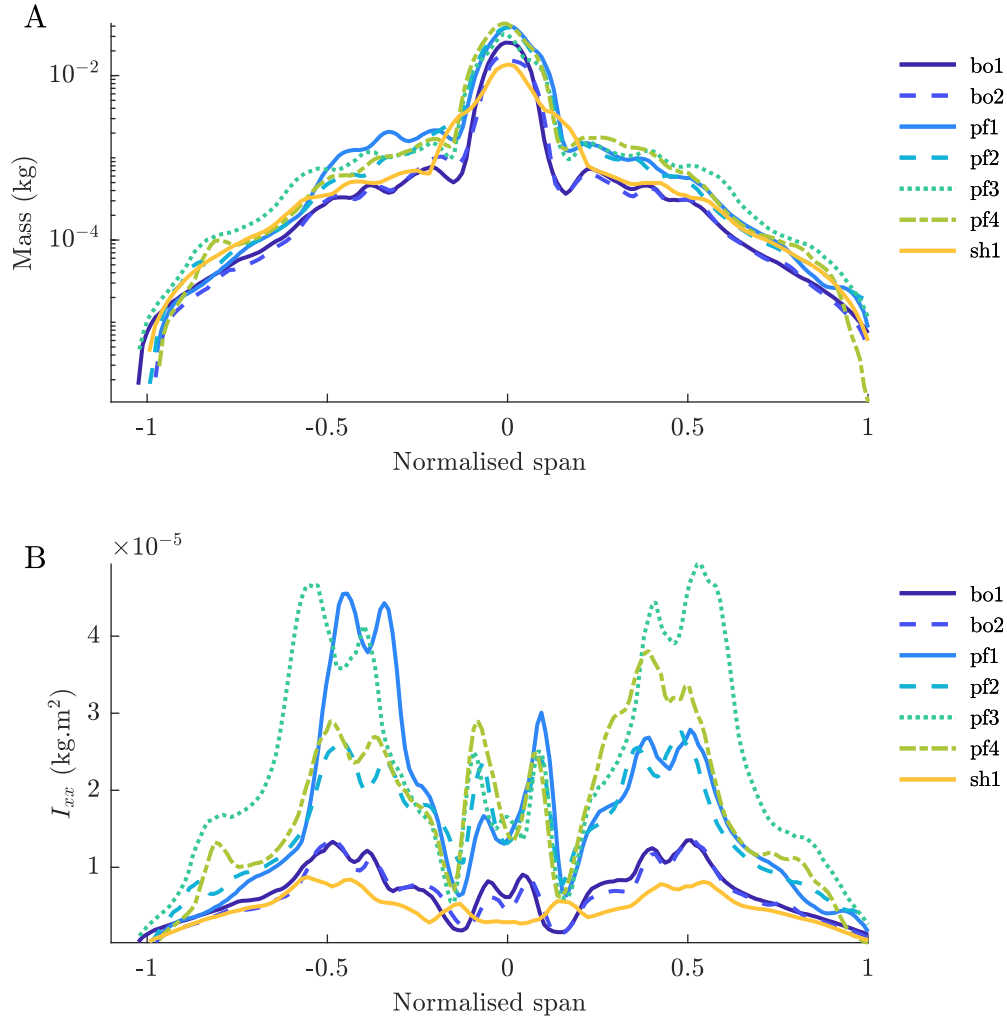


Fig. 4.16 The spanwise contribution towards total mass and I_{xx} for all cadavers, showing the previously observed ‘double-bell’ shape moment of inertia distribution. The asymmetries in pf1 and pf4 correspond to wing trauma in the left and right wings respectively.

4.5.3 Free-flight centre of mass and moment of inertia

Figure 4.17 shows dorsoventral and posteroanterior views of the edge splines (see chapters 2 and 3) and CT data (with threshold = 1100 kg/m^3) for the barn owl and peregrine flights after intra- and inter- flight alignment (see Appendix C). The plotted CoM positions are based on the mean positions for bo1, bo2, pf1, pf2 and pf4. The CT data is from bo1 and pf4 for clarity; due to intra-flight alignment, the remaining cadavers were almost directly aligned with these. The raw data is provided in tables 4.4 and 4.5 for the individual cadavers, and shows a maximum inter-flight variation in the

	bo1	bo2	Mean	Range ('intra-flight')
O1	-20.48	-22.98	-21.73	2.50
O2	-20.19	-22.58	-21.38	2.39
O3	-21.91	-24.84	-23.37	2.93
Range ('inter-flight')	0.72	2.26	1.99	

Table 4.4 Variation in the anteroposterior (x -axis) position of the centre of mass in wing-body coordinates (in mm) for the barn owl flights (O1-O3).

	pf1	pf2	pf4	Mean	Range ('intra-flight')
P1	-57.53	-57.95	-56.06	-57.18	1.89
P2	-55.63	-56.23	-54.58	-55.48	1.65
P3	-55.35	-55.71	-54.14	-55.07	1.57
Range ('inter-flight')	2.18	2.24	1.92	2.11	

Table 4.5 Variation in the anteroposterior position of the centre of mass in wing-body coordinates (in mm) for the peregrine flights P1 to P3.

anteroposterior direction of the CoM of 2.26 mm.

Figure 4.18 shows PCI for the barn owl and peregrine flights, in addition to configurations in which the wings were fully protracted and retracted. The fully retracted dataset was based on additional CT scan data in which the birds' wings were fully folded against the torso. The barn owl PCI were similar, based on its consistent configuration between flights. PCI were also consistent between P1 and the fully protracted peregrine configuration, as expected. By partially retracting its wings, the peregrine's I_{xx} reduced by 19% (P2) and 27% (P3) relative to P1, I_{yy} increased by 7% (P2) and 16% (P3) and I_{zz} reduced by 8% (P2) and 9% (P3). The relative quantities of the PCI were similar between the two species for wings protracted, O1-O3 and P1, with the values of I_{yy} and I_{zz} being approximately $0.66I_{xx}$ and $1.66I_{xx}$ respectively. In P2, the magnitudes of I_{xx} and I_{yy} were almost equivalent, while for P3 I_{yy} was $1.15I_{xx}$ and I_{zz} was $2.03I_{xx}$. As expected, fully retracting the wings had the most significant influence on the I_{xx} and I_{zz} , which reduced by 83% and 49% respectively for the barn owl, with similar reductions for the peregrine. For both species, I_{yy} was relatively insensitive to wing retraction/protraction, which increased by 5% for the barn owl and 2% for the peregrine. This suggests that as the wings are retracted, I_{yy} undergoes a small initial increase, followed by a similarly small decrease (compare I_{yy} for P1, P3 and 'wings retracted' in figure 4.18B).

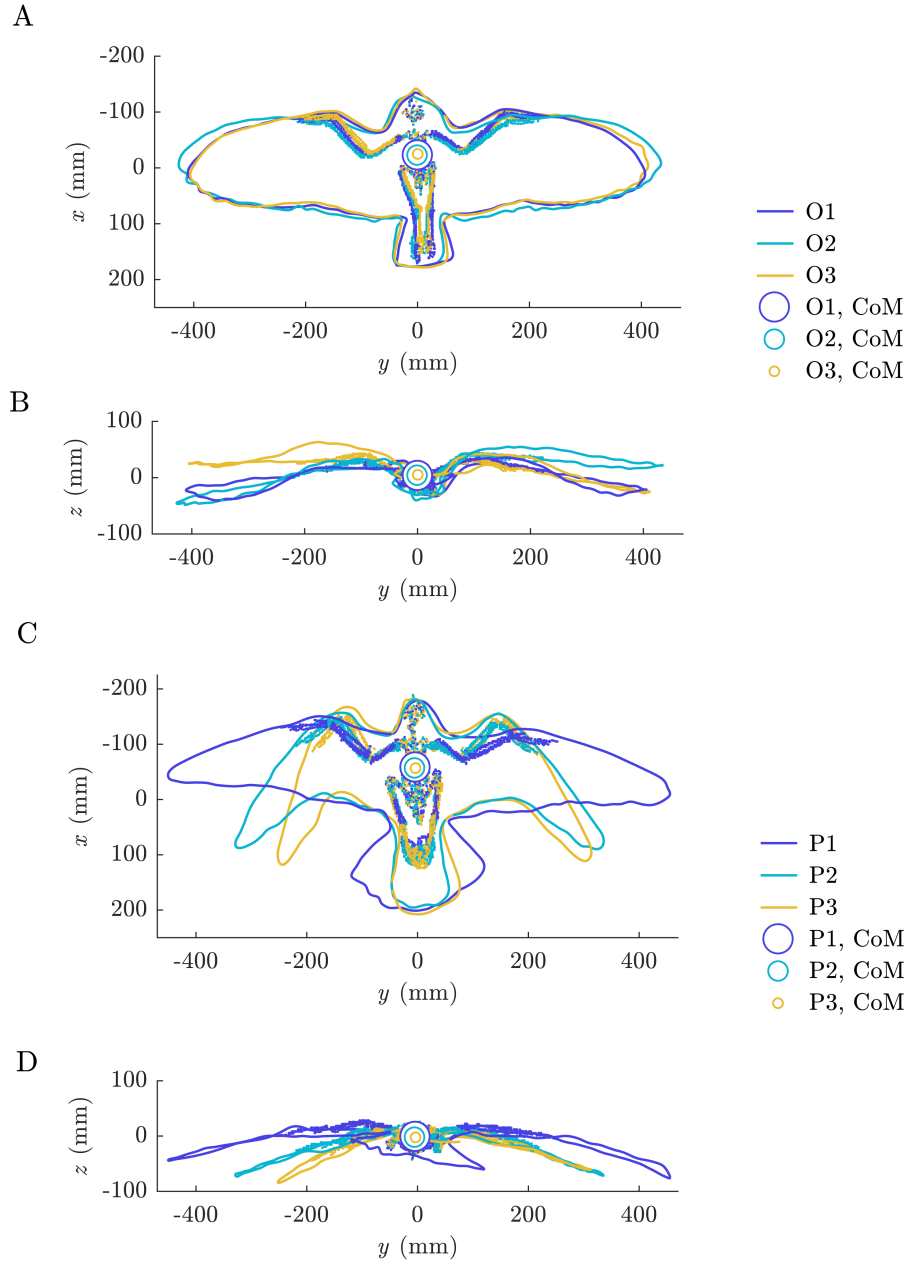


Fig. 4.17 Visualisation of the flight-aligned CT data with a threshold of 1100 kg/m^3 applied to show the skeletal movement. Scan data for bo1 and pf4 is shown for clarity; the remaining cadavers were almost directly aligned with these. A) Dorsoventral view of the barn owl. B) Anteroposterior view of the barn owl. C) Dorsoventral view of the peregrine. D) Anteroposterior view of the peregrine. The CoM position between flights is plotted based on the means from bo1 and bo2 for the barn owl flights, and pf1, pf2 and pf4 for the peregrine flights. The position of the head, neck and body is consistent between cadavers and flights, such that only the effect of wing and leg movement on the CoM position is captured.

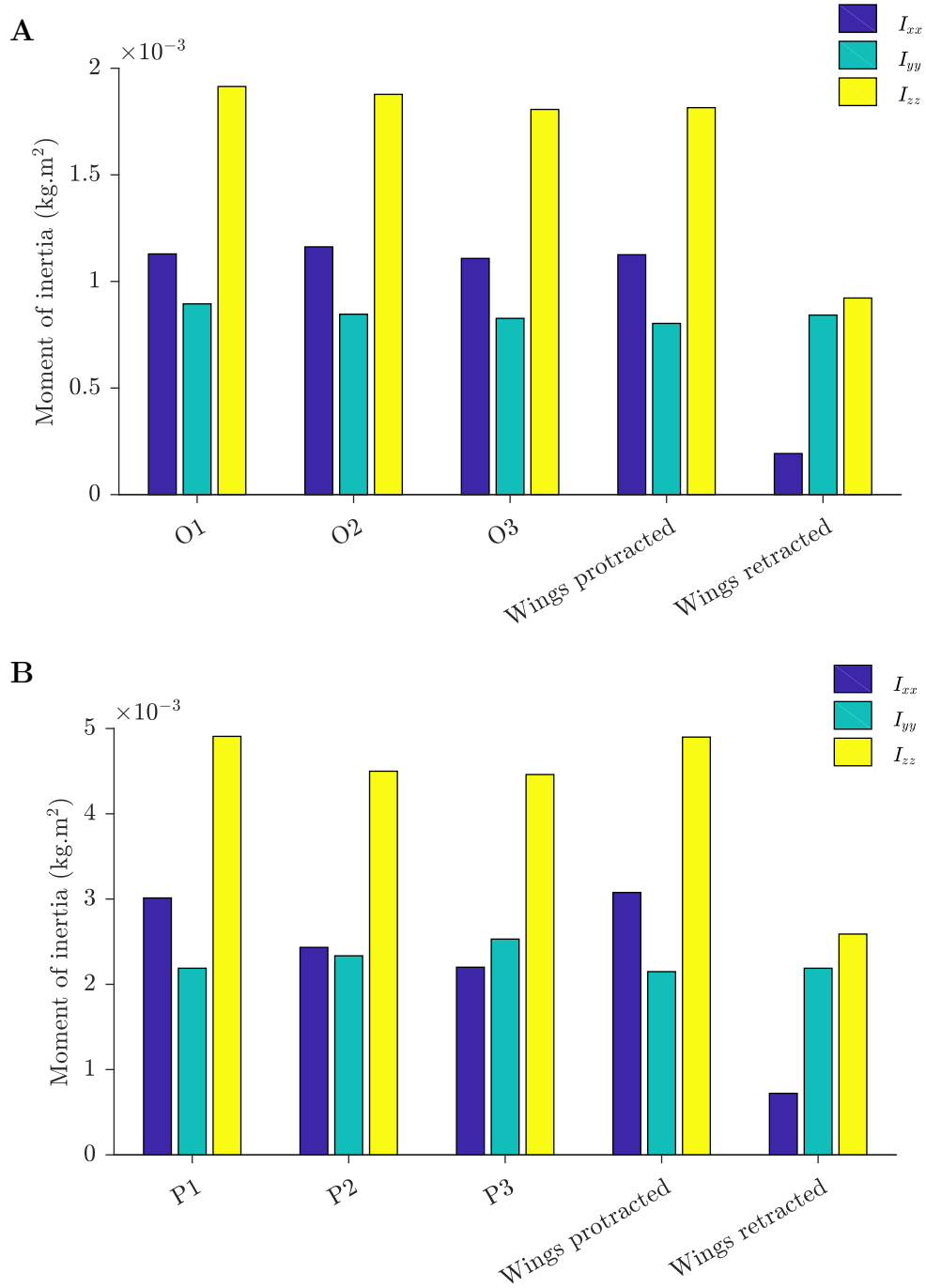


Fig. 4.18 The influence of geometric configuration on the principal components of inertia for the A) barn owl, bo1, and B) peregrine, pf4. In addition to the barn owl (O1-O3) and peregrine (P1-P3) flights, data for wings fully protracted and fully retracted are presented. The fully retracted case is based on additional scan data for which the bird's wings were manually folded against the body.

For the flight dynamics analysis in chapter 5, the MoI of bo1 and pf4 were used to represent the MoI of the free-gliding barn owl and peregrine since these represented fully healthy, adult cadavers. It was therefore necessary to understand how much MoI error might be introduced due to small differences in mass and span between the cadavers and live birds. Figure 4.19 shows the PCI of cadavers bo1, bo2, pf1, pf2 and pf4 in their ‘wings protracted’ configuration plotted against the product of mass and span squared. A linear fit was applied to the data to enable interpolation of the PCI of the live birds for flights O2 and P1, in which the wings were closest to being fully protracted (see table 3.1).

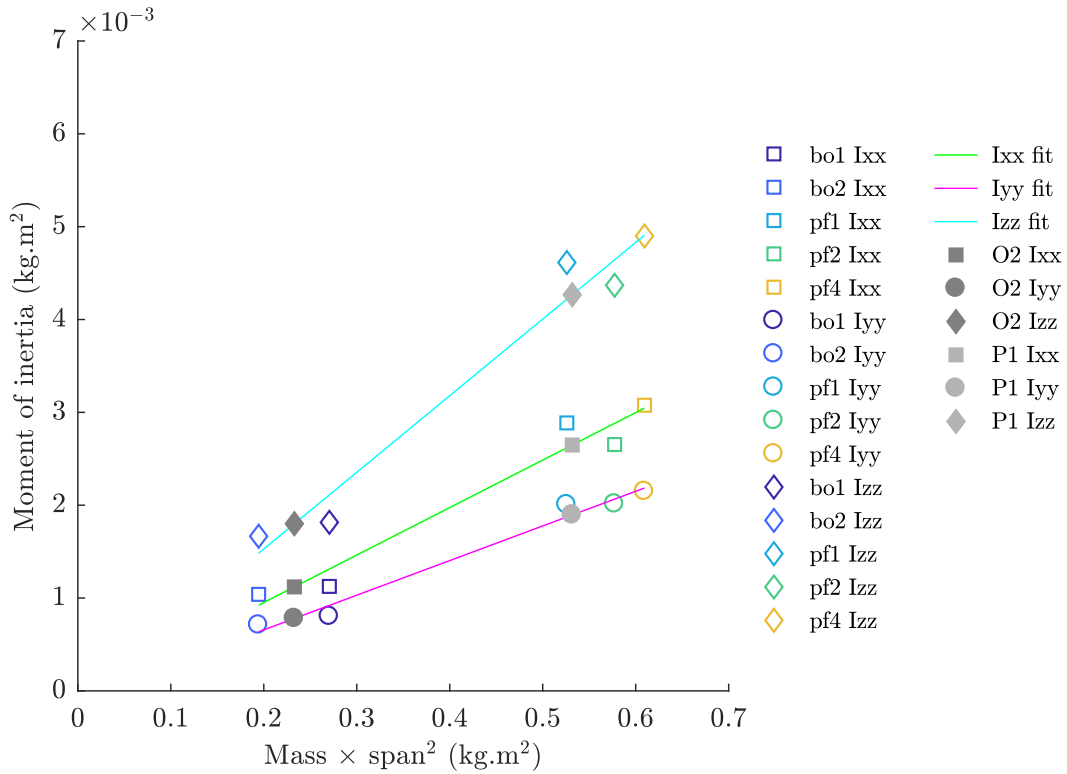


Fig. 4.19 Estimation of the principal components of inertia for the free-gliding barn owl and peregrine, with wings protracted, may be made using their wing span and mass, based on linear fitting to the principal components of inertia of the cadavers. Flights O2 and P1 were chosen for interpolation because they had the highest wing span. The linear fit is intended to provide an approximation of the sensitivity of MoI vs. mass and span within each species.

These results show that PCI could be overestimated by up to 15% for pf4 and 1% for bo1 respectively. This result, in conjunction with the method validation using

the trifilar pendulum, was used to inform the MoI based sensitivity study described in chapter 5 based on the worst case of 15% applied to both birds.

4.6 Discussion

4.6.1 Method

In this study, calibrated X-ray computed tomography (CT) was used to estimate the inertia tensors of free-gliding birds, an approach that represents an improvement compared with the generally adopted method of wing strip analysis. The main advantages of the CT-based approach are the high accuracy, quantification of the complete inertia tensor and the subsequent ease of data manipulation¹. Thresholding, segmentation and coordinate system transformation can all be applied to the scan data, offering significant benefits compared with strip analysis. This approach would ideally be used on anaesthetized animals in conjunction with free-flight measurements from the same individuals, which is often not possible (i.e. this study and Riskin et al. [166]). The voxel sizes used to integrate the inertia tensor with this approach were significantly smaller than the wing pieces used in strip analysis, which need to be as small as possible to avoid significant increases in error. For example, Van den Berg & Rayner [162] note that at least 15 strips were required to reduce the wing moment of inertia error below 5%. The difficulty of manually dissecting very small animals into small strips could be overcome using this method with micro-CT.

Validation of the method through mass comparison of physically and virtually dissected appendages and with a trifilar pendulum, confirmed previous studies in which CT was shown to be an effective method for estimating absolute density in biological materials [174, 175, 177–179]. Moreover, MoI estimates of individual wings about their humeral head compared favourably with previously determined values [162]. This suggests that previous studies advising caution over the use of CT for absolute density estimation [176] may only apply to older generations of scanner technology [178]. However, this approach should not be used with cone-beam computed tomography, due to specific issues with this type of CT-scanner for estimating absolute density [188]. Furthermore, although the method worked effectively in this instance, it is good practice to validate CT-based inertia estimates to build confidence the results.

¹Because the data is available digitally, the animal's pose can be easily altered to quantify, for example, how mass distribution changes through the flap cycle.

This method could be used without scanner calibration to provide reasonable estimates of the centre of mass position (in this instance, typically within 5 mm accuracy). This was not the case of moment of inertia estimates however, as this resulted in 58% error. The density of the voxels representing feathers distally on the wings significantly increases with the mean density assumption, which explains the overestimate. This emphasises fact that this approach does not provide accurate density estimates for material present within individual voxels. For example, if a voxel contains feather and air, it's 'density' will be lower than that of β -keratin, the material from which feathers are made. However, the mass of the voxel still provides an accurate estimate for the enclosed solid material, based on comparison between physically and 'virtually' weighed outer primary feathers and the appendage mass comparison presented in figure 4.10.

Although the method was validated and shown to be relatively accurate, manual positioning of the segmented appendages, particularly the torso, could have resulted in an incorrect estimate of the centre of mass position of the bird relative to the photogrammetric surface reconstructions. The sensitivity of the centre of mass position to variation in the position of the head, cervical spine, torso, legs and tail was therefore assessed for flights O1, P1 and P3. Moving these appendages forward by 10 mm resulted in the centre of mass moving forward by 8 mm for all flights. The wings were excluded because their proportion of the total mass was relatively small and because of the reduced ambiguity in their alignment to the leading edge of the photogrammetrically measured wing. This resulted in the CT measured head, clearly protruding from the surface reconstruction to which had originally been aligned. A second transformation of 10 mm was then applied to the torso, legs and tail, resulting in a further 7 mm forward movement of the centre of mass position across all three flights. The CT data for the neck and torso were then clearly overlapping, with the neck squashed between the head and torso. This configuration clearly represented a worst case estimate for the forward limit of the centre of mass based on manual alignment uncertainty between the CT and photogrammetrically measured bird. Assuming similar alignment errors caudally (i.e. applied in the opposite direction), the error in centre of mass position could have been ± 15 mm. This error estimation was used for subsequent sensitivity analysis of longitudinal stability (see chapter 5). The variation in the inertia tensor was zero for I_{xx} (as expected), approximately 15% for I_{yy} and up to 10% for I_{zz} . Subsequent inertia sensitivity studies were based on the worst case combined error based on 10% accuracy of the CT-based approach (table 4.3), 15%

error due to differences between the cadavers (figure 4.19) and the live birds and the various potential changes in PCI due to CoM position described above. By summing these contributions, the subsequent inertia sensitivity studies were based on the worst case errors of $\pm 25\%$ in I_{xx} , $\pm 40\%$ in I_{yy} and $\pm 35\%$ in I_{zz} .

4.6.2 Flight dynamics and inertia

From Newton's second law, mass moment of inertia (MoI) quantifies resistance to rotational acceleration by applied torques or moments in the same way that mass quantifies resistance to rectilinear acceleration by applied forces [156]. Higher MoI should therefore reduce the agility of a bird or aircraft such that larger control deflections or stronger gusts of wind are required to generate a given rotational acceleration from equilibrium flight. Comparison between the roll and pitch moments of inertia between birds and aircraft of similar size and mass shows that the MoI of birds is significantly lower (table 4.6).

	Mass (g)	Span (mm)	$I_{xx} \times 10^{-3}$ (kg.m ²)	$I_{yy} \times 10^{-3}$ (kg.m ²)
Barn owl (O2)	312	864	1.13	0.90
Peregrine (P1)	645	908	3.03	2.20
Rose-breasted cockatoo [165]	289	772	1.29	0.45
Foam UAV [35]	470	770	53*	133*
Morphing UAV [189]	330	840	10	-
Prototype raven model [95]	510	1270	20.5	5.4
Raven II [95]	476	1270	14.7	3.9

Table 4.6 Comparison of roll (I_{xx}) and pitch (I_{yy}) moments of inertia between birds and aircraft of similar mass and span. *The data for the foam UAV was particularly high, and could represent a measurement error or typo in the decimal place.

This highlights the extent to which avian wings are configured to minimise inertia, with much of their mass concentrated proximally in the humerus, with the major flight muscles contained within the body, close to the centre of mass (figures 4.14 and 4.16) [190]. The wing bones reduce in diameter distally [153], and even the feathers with their hollow shafts and relatively low density material taper distally. Despite its relatively large inertia (compared to its avian counterparts), attempts to fly the foam UAV in a large (12 m \times 4 m) wind tunnel at 8 m/s, with turbulence intensity of 6%, often resulted in crashes [35]. At turbulence intensities of 14%, more typical of flow near to the ground at similar velocity, the aircraft was impossible to fly [32].

During these wind tunnel experiments, the roll moment of inertia of the foam UAV was increased by a factor of 1.6 by placing masses at the wing tips. This had the effect of reducing the sensitivity to disturbances, although the magnitude of the aileron inputs needed for successful handling were also higher. As expected, increasing roll inertia made the aircraft less sensitive to both gust perturbations and control deflections, demonstrating the trade-off between stability and manoeuvrability. This observation, along with the significant difference in MoI between birds and aircraft, suggests that although birds accelerate more from a given atmospheric disturbance, they may also be more responsive in terms of the corrections needed to counteract the acceleration. Unlike the foam UAV and human pilot, birds do not crash regularly when flying in similar conditions, despite their significantly lower inertia. This might imply that the increase in agility conferred by low inertia is beneficial for maintaining control in turbulent conditions, due to the increased responsiveness of correctional control inputs, as long as a suitably fast control system is utilised. Feather elasticity could also help with gust rejection.

Another potential advantage of low wing inertia is reduction in the power required for flapping flight [162]. During every wing beat cycle, both wings must be accelerated and decelerated twice, which requires energy. Some uncertainty exists about precisely how much of the cost of flapping consists of ‘wasted’ inertial power, since the work done to accelerate the wing may be used to do useful aerodynamic work (i.e. provide lift and/or thrust) during the deceleration phase of the down-stroke, or even during the upstroke via elastic energy stored in the supracoracoideus tendon [27, 162, 165, 191]. Irrespective of the debate surrounding how much inertial work is transferred into the aerodynamic work, the energy required to accelerate the wing is still proportional to the its MoI. This may be one reason why birds and bats retract their wings during the upstroke. For example, inertial modelling of pteropodid bat wings suggests they could reduce inertial power by 35% by retracting their wings during the upstroke compared with rigid, fully protracted wings [166]. Since it is obviously advantageous for animals to save energy, power reduction may be one of the critical factors that explains the low wing inertia of birds. Low wing inertia also enhances manoeuvrability, which is advantageous in the ‘arms race’ between predator and prey [192]. The presence of flexible, lightweight structures distally may also help with damage tolerance, which is import during flight through cluttered, arboreal environments.

There are however circumstances in which higher wing inertia can be beneficial. At low speeds, aerodynamic forces and moments are reduced, which limits the effec-

tiveness of control deflections. This could be problematic during low-speed phases of a flight such as take-off, hover and landing. In these circumstances, flying animals could use their appendages to generate ‘zero net angular momentum’ manoeuvres, similar to those of falling cats [193] or geckos [194]. These animals can rotate while falling, despite zero initial angular momentum, without violating conservation of momentum. During these manoeuvres, the angular momentum of individual appendages and torso is non-zero, but net angular momentum is zero. Studies on theoretically and experimentally derived dynamic models of bats suggest that they can use their wing inertia to perform ‘heels-over-head’ landing manoeuvres at very low flight speeds [167]. The control effectiveness of appendage inertia increases with both size and the ratio between wing and body inertia [167]. The ratio between wing and body inertia of the barn owl, peregrine and sparrow hawk was approximately 9 for I_{xx} , 0.1 for I_{yy} and just over 1 for I_{zz} (figure 4.15), while for smaller *C. perspicillata*, I_{xx} was 5 [167]. This suggests that wing retraction could be used by birds for manoeuvre control, especially at low speeds where aerodynamic forces are significantly reduced. This is supported by comparison of the protracted and retracted moments of inertia (figure 4.18), which showed negligible change in I_{yy} , 83% change in I_{xx} and a 50% change to I_{zz} . However, dynamic modelling of low-speed manoeuvres performed by birds would need to be carried out to provide supporting evidence of this suggestion.

It has also been suggested that birds may control manoeuvres using postural adjustments to vary their centre of mass (CoM), similar to hang-glider pilots [39]. Figure 4.17 and table 4.5 shows that significant changes in sweep and dihedral by the peregrine between P1 and P3 did not alter the centre of mass position by more than approximately 2 mm (approximately 2% mean aerodynamic chord of P1). This analysis was based on precise alignment of the head, neck, torso and legs between cadavers and flights, such that the changes in centre of mass were only due to wing movement between flights. The lack of CoM movement may be due to cancelling out between the anterior movement of the radius, ulna and proximal manus with the posterior movement of the distal manus and primary flight feathers, such that the net effect on the centre of mass was negligible (figure 4.17). Furthermore, the majority of the postural change occurs in the low mass hand wing region, while only small changes in position occur in the arm wing, where the heavier bones and muscles are located (figure 4.15). Changes in wing sweep between P1 and P3 also had the least effect on I_{yy} compared with I_{xx} and I_{zz} , with a change of approximately 14% (figure 4.18). Dynamic analysis is required to quantify the effect of this small change in I_{yy} on stability (see

chapter 5). However, the small changes to centre of mass position and I_{yy} imply that inertial changes due to wing morphing have a negligible effect on longitudinal stability. This might simplify the problem of longitudinal (and yaw) control, because only the aerodynamically generated variables change significantly with wing pose [81]. This also shows that active pitch control is achieved solely through movement of the centre of pressure. Many birds lower their legs during certain flight phases to increase their rate of descent via a reduced lift-to-drag ratio [69, 70]. Applying a similar posture to the CT data from flight O1 (tibiotarsae and tarsometatarsae extended down) resulted in the cranial and ventral movement of the centre of mass of approximately 5 mm. Lowering the legs, would therefore have the effect of increasing longitudinal static stability (or reducing longitudinal static instability). This however, would also affect longitudinal balance, since the drag acting on the legs below the centre of mass would generate an increased nose-down moment.

Changes in wing sweep and dihedral probably do affect lateral-directional dynamics. Roll and yaw MoI, I_{xx} and I_{zz} , were sensitive to wing span, reducing by approximately 80% and 50% respectively between fully protracted and fully retracted wings for both the barn owl and peregrine (figure 4.18). Using conservation of angular momentum, birds could make use of these inertial changes to rapidly increase their roll rate during manoeuvres, similar to pirouetting ice-skaters [39]. Experiments with rose-breasted cockatoos showed that wing inertia influenced the instantaneous roll angle within wingbeats, although aerodynamic effects were primary in roll control during flapping flight [158, 165]. This suggests that inertial changes to wing posture may be more significant during gliding rather than flapping, and may have contributed towards the left-roll manoeuvre observed in the video footage and span-asymmetry of P3.

4.7 Conclusions and recommendations

The overall aim of this chapter was to provide accurate estimates of the centre of mass position and inertia tensor of the free-gliding barn owl and peregrine introduced in chapters 2 and 3, thus facilitating the flight dynamics analysis described in chapter 5. Comparison with model aircraft of similar mass and span suggests that by comparison, birds are more manoeuvrable and sensitive to gust perturbations due to their low MoI².

²This assumes that birds and model aircraft have similar aerodynamic control effectiveness, which has not been assessed here.

This is due to their wing anatomy, which concentrates mass proximally and may be primarily due to an evolutionary drive towards power reduction during flapping flight, among other factors. Despite having very low MoI, the ratio of wing to body MoI in the barn owl and peregrine was still sufficient to facilitate low-speed ‘zero angular momentum’ turns observed in some bats. However, experimental evidence similar to that provided for bats would need to be obtained to prove whether or not birds use their appendage inertia for manoeuvring. Centre of mass and pitch MoI were insensitive to significant changes in wing sweep and dihedral suggesting that, for these species and the flight styles assessed, longitudinal stability was largely unaffected by inertial factors due to wing morphing. The relative proportions of the principle components of inertia suggest that birds are least sensitive to gust and control inputs about their yaw axis, compared with pitch and roll. Despite flying in high turbulence conditions (up to 40% near the ground [31]) birds do not easily lose control, unlike human-piloted model aircraft of similar size [35]. This could be due in part to their very low moments of inertia, which although increasing susceptibility to gust perturbations, also confer increased control effectiveness.

The approach used in this chapter represents an improvement compared with the strips method commonly used in the study of animal flight. The use of calibrated CT for estimating the mass of each scanned voxel provided accurate estimates (error < 10%) of MoI, based on comparison with results from a trifilar pendulum. The centre of mass estimate using this method was also very accurate, based on mass comparison between physically and ‘virtually’ dissected cadavers, and the fact that the CoM position did not vary significantly when the voxels were given uniform mass. This method could be applied to anaesthetized animals, allowing the inertial data to be used in conjunction with kinematic data from the same free-flying animal. Even with cadavers, this approach is non-destructive, allowing re-use of carcasses that are often difficult to obtain. CT data is easy to manipulate, and enables calculation of the inertia tensor of any appendage, in any coordinate system.

Future work could utilise CT scans of birds to generate inertial models based on multi-degree of freedom articulated joints. This would allow questions raised about zero angular momentum turns to be explored in relation to perch manoeuvres, or how birds deal with perturbations at very low speed. In general, the datasets obtainable with this approach should be combined with kinematic data obtained in free-flight experiments to allow accurate dynamic modelling of a wide range of manoeuvres carried out by flying animals. These might include the stooping flight dynamics of peregrines,

the gust alleviation mechanisms in steady gliding flight or inertial mechanisms involved in the control of flapping flight. In particular, it would be interesting to use the method at very small scales for insect flight mechanics where the strips and pendulum methods are unsuitable.

FLIGHT STABILITY ANALYSIS OF FREE-GLIDING BIRDS OF PREY

5.1 Chapter summary

Birds adopt a variety of wing and tail configurations during gliding flight, yet it is currently unclear whether these configurations are inherently stable or unstable. Stability influences manoeuvrability and may therefore have a significant impact on behaviours such as foraging, obstacle avoidance and predator evasion. By combining photogrammetric 3D surface reconstructions of a free-gliding barn owl (*Tyto alba*) and peregrine falcon (*Falco peregrinus*) with X-ray computed tomography (CT) scans of similar sized cadavers of the same species, it was possible to accurately estimate the in-flight aerodynamic shape of the birds and their inertial properties. Linear flight dynamics models were then generated using Athena Vortex Lattice (AVL), a computational aerodynamics tool used for aircraft design. The results showed that both the barn owl and peregrine were highly longitudinally statically unstable in glide for all three flights recorded for each species. The peregrine altered its wing and tail configuration with speed, and featured varying degrees of camber, twist, sweep and dihedral that resulted in distinct changes to its degree of longitudinal and lateral-directional stability. Similar to unstable combat aircraft, both birds had a pitch divergence mode and a so-called ‘third oscillatory mode’, very similar to the phugoid. They also had an unstable spiral mode, and two of the peregrine flights had a dutch roll mode. The barn owl flights and the fully protracted peregrine configuration did not have a dutch roll mode. Instead, the barn owl had a spiral-like mode that was highly unstable, while the peregrine had additional stable roll and spiral modes. Structural compliance and neural feedback are probably used to stabilise the flight of these two birds. This is based on the fact that neural feedback alone may not be sufficiently fast, given the very small time constants of the pitch divergence mode. The instability and manoeuvrability observed, may reflect the need for these predatory birds to catch highly manoeuvrable prey either in the air or on the ground.

5.2 Chapter structure

In this chapter, the original aim of quantifying the flight stability of free-gliding birds of prey is realised. Previous chapters focussed on the task of obtaining the required inputs - surface geometry (chapters 2 and 3), centre of mass and the inertia tensor (chapter 4). Here, the final refinement of the surface geometry into 3D-printable shapes and aerodynamically useful spanwise sections is described. The refined models are used for wind tunnel testing and computational aerodynamics analysis using a vortex lattice method. The aerodynamic and inertial results are then combined into a linearised flight dynamics model, treating the bird as a rigid, six-degree-of-freedom system. The stability of each flight is then described based on these models, and discussed in terms of the implications for real birds, which are highly flexible and utilise neural feedback during flight. The chapter concludes with the key findings, limitations of the methods used and suggestions for future work.

5.3 Introduction

Soaring birds of prey appear to glide effortlessly through the atmosphere, yet it is likely that they require continuous correctional control to maintain steady flight. The amplitude and frequency of such correctional control depends on the degree of inherent stability that the bird possesses by virtue of its shape and mass distribution. If birds are unstable, they would require rapid, continuous corrective control inputs to avoid divergence from equilibrium. This is the case for modern high-performance combat aircraft, designed to be longitudinally unstable for enhanced manoeuvrability, but requiring rapid ‘inner loop’ feedback control to maintain control [72, 195]. The greater the instability, the faster and smaller the control inputs are likely to be, making them difficult to observe visually. A stable bird could fix its wings in place by bracing its musculature and allowing its inherent stability to maintain equilibrium, rather like relatively rigid, conventional subsonic aircraft. If its dynamic modes were poorly damped, correctional control might still need to be utilised (even with a stable configuration) for smooth flight. This scenario would be similar to a conventional aircraft with stable but undesirable open-loop handling qualities. In this situation, feedback control is usually used in a ‘stability augmentation system’ to provide additional damping from the control surfaces, improving handling [38]. By definition, a stable system is more resistant to disturbances from gusts of wind compared with an unstable system, which

also means greater control forces are required during manoeuvring. Almost nothing is known about how birds trade-off stability and manoeuvrability, yet knowledge of this would facilitate improved understanding of both their ecology and flight control system. It may also provide insight for improved stability and control of unmanned air vehicles of similar size to birds, since the latter exhibit a superior performance in atmospheric turbulence.

Thomas & Taylor [76] estimated the longitudinal static stability of 15 species of birds using cadavers. The results of this analysis showed that in 11 of the 15 species, the wing aerodynamic centre was behind the bird's centre of mass, implying longitudinal static stability. This study was reliant on manually configuring the wings, and assumed that a fully protracted, forward-swept wing would have resulted in the most unstable configuration. This assumption was consistent with observations of a Harris Hawk (*Parabuteo unicinctus*) gliding in a tilting wind tunnel, which showed that the centre of area with a protracted wing was further forward than with a retracted wing [81]. The bird also spread and lowered its tail at lower speeds when the wings were fully spread to provide pitch equilibrium by counteracting the forward movement of the centre of pressure due to the wings. Lateral-directional stability derivatives have been quantified for bird-like shapes using inviscid computational fluid dynamics [28, 69, 85–89, 91, 92, 97, 97]. These studies highlighted the effect of subtle geometric changes and trim condition on lateral-directional stability. For example, small changes in distal wing sweep and lift coefficient can have profound implications for weathercock stability, to the extent that a bird can change from a stable to an unstable configuration. This high degree of sensitivity between directional stability and wing shape is due to the lack of vertical fin in birds, compared with conventional aircraft.

A widely held view is that birds have evolved increasing levels of instability from their initially stable ancestors [8, 9, 68, 100, 196, 197]. The enhanced manoeuvrability and increased lift to drag ratio of unstable configurations (improving energy efficiency [76] and reducing stall speed [9]) are assumed to have driven this development through natural selection. This perspective assumes the absence of neural feedback mechanisms required for unstable flight in early birds. The gradual shortening of the avian tail observed from fossils is used to support this hypothesis, based on its original importance for pitch and yaw stabilisation [27, 67]. However, the shortening of a long bony tail may also have led to cranial movement of the centre of mass, leaving the static margin unchanged [76]. Wind tunnel tests with models of extinct animals supports gradual development from stable to unstable configurations [80], but this of course depends on

the fidelity of the models used. The idea that natural selection would favour increasingly unstable configurations makes sense given the importance of manoeuvrability in the ‘arms race’ between predator and prey [192, 198]. However, the stability of extant birds has not yet been quantified based on the configurations adopted in free-flight, and measurements of extinct animals will always carry significant uncertainty both in terms of the overall shape and inertial properties (i.e. centre of mass and inertia tensor).

Current understanding of avian flight dynamics is therefore based on a small number of quantitative studies, the fossils of extinct ancestors of birds and a sensible evolutionary hypothesis. Quantitative studies with bird cadavers, or highly simplified bird-like geometries, are likely to be unrepresentative of free-gliding birds [21–23, 119, 199]. In the only known study of longitudinal stability with a free-gliding bird, planform measurements and estimates of tail elevation and spread suggested that the centre of pressure was forward of the centre of mass, which might imply longitudinal statical instability [81]. In chapter 3, surface reconstructions of a free-gliding barn owl and peregrine falcon were used to qualitatively assess longitudinal stability by inferring the zero-lift pitching moment from camber, twist, sweep and longitudinal dihedral. This analysis implied that the barn owl was longitudinally statically unstable based on its positively cambered wing, longitudinal anhedral, aft sweep with wash in and wing anhedral (chapter 3). A similar inference was not possible for the peregrine, because some geometric features (i.e. positive camber and longitudinal anhedral) would have generated a nose-down zero lift pitching moment, while others (aft-sweep and wash out) would have generated a nose-up zero lift pitching moment. Inferring longitudinal stability or instability from geometry alone is only possible if all the pertinent geometric features point towards a positive or negative zero-lift pitching moment respectively. Moreover, geometry alone only provides a binary (i.e. stable or unstable) indication of longitudinal stability, and cannot be used to safely infer anything about lateral-directional stability.

In this chapter, we quantify the static and dynamic stability of the barn owl (*Tyto alba*) and peregrine falcon (*Falco peregrinus*) flights introduced in chapters 2 to 4, based on their glide geometry and inertial properties. Aerodynamic models were used to obtain the aerodynamic derivatives (i.e. changes in forces and moments with respect to angles and rotational velocities) of each flight, about its trim condition. Linearised, rigid body flight dynamics models with six-degrees-of-freedom were then created by combining the aerodynamic derivatives with the inertial properties (ob-

tained in chapter 4) into a linear time invariant state-space model of the system [38]. The stability of each flight was then estimated using eigenvalue analysis to obtain the dynamic modes. Sensitivity analyses were also conducted based on the estimated range of uncertainty for trim angle of attack, centre of mass position and the inertia tensor. Wind tunnel testing with a 3D-printed model of the barn owl surface geometry from flight O1 was used to validate the longitudinal derivatives of the aerodynamic model. To the best of our knowledge, these models represent the first ever quantification of the flight stability of free-gliding birds.

5.4 Material and Methods

5.4.1 Geometry refinement

5.4.1.1 Overview

This section describes the process of generating a watertight surface mesh based on the photogrammetric reconstructions of the free-gliding birds described in chapter 2. The first stages of this process were described in chapter 3 section 3.4.1, where mean camber, dorsal and ventral splines were generated from sections every 2 mm along the span. This allowed detailed description of spanwise camber, twist, dihedral, sweep and thickness, however the splines still did not represent closed-form aerofoils amenable to aerodynamic analysis (see figures 3.5, 3.10 and 3.11). The motivation behind generating a watertight surface mesh was the ability to 3D print the glide geometries for use in wind tunnel testing, so that computational aerodynamic analyses could be experimentally validated. However, meshing the surface geometry of a gliding bird from the photogrammetric measurements was complex for various reasons, including the large, thin regions of the wing composed entirely of feathers and gaps in the reconstructed surfaces around the edge of the bird (see chapter 2). In this section, methods are described in which watertight surface meshes were obtained based on closed-loop aerofoil fits to sections every 2 mm along the span, including the torso. This approach resulted in a refined point cloud representative of the entire bird, making it possible to generate a watertight surface mesh. This process was complex, due to the need for a good quality closed-loop aerofoil fit for approximately 400 sections along the span, with varying data quality, coverage and geometry. The algorithms needed to be robust; any gaps, or poorly fitted sections rapidly increased both meshing difficulty and geometric accuracy.

5.4.1.2 Section categorisation

In order to ensure robust section fitting, it was necessary to categorise geometrically distinct regions in the spanwise direction that would need to be treated differently. Categorising the sections allowed tailoring of the downstream fitting algorithms to the general geometric form found in each distinct region. This categorisation is shown in figure 5.1 and was only loosely related to the anatomy of birds. The boundary between the arm wing and body was based on the definition used by Pennycuik [147], but

where necessary was adjusted to achieve the best fitting results with the fitting algorithms. The distinction between wing/tail tip and hand wing should not be taken to mean that the wing tip doesn't belong to the hand wing in the anatomical sense. These distinctions were made to facilitate robust geometric fitting, not for precisely describing avian anatomy. The boundaries between each region in figure 5.1 were chosen as follows:

- **Wing/tail tip:** Wing or tail sections where the quality and chord-wise coverage of the raw point clouds reduced such that fitting was not viable and assumptions were made about the geometry (see 'no fit' regions in figure 3.6).
- **Hand wing:** Wing sections consisting entirely of feathers with very low thickness across the entire chord.
- **Arm wing:** Wing sections with thickening near the leading edge caused by the wing bones and muscles, including the manus.
- **Body:** Sections where the thickness became too large to be considered as part of the wing. This did not neatly coincide with the point joining the wing trailing edge with the tail leading edge, as indicated by the dashed line in figure 5.1.
- **Partly tail:** These were sections in which the tail data were spatially isolated from wing or body geometry, and such that two distinct section fits were required.

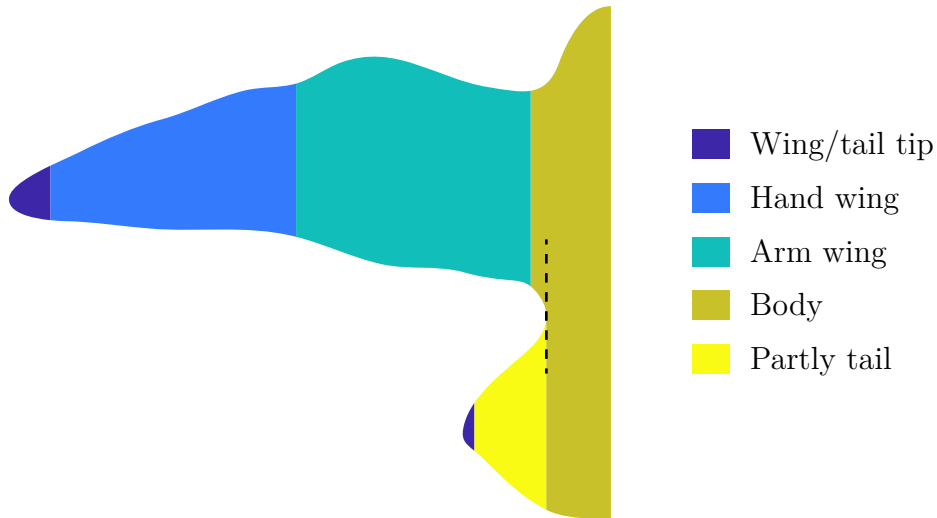


Fig. 5.1 In order to enhance the robustness of the section fitting process, it was necessary to first categorise the sections into distinct regions. The names given are only loosely anatomical.

5.4.1.3 Arm wing

Previous research in which bird cadavers were laser-scanned and 3D-printed showed that ‘Birnbaum-Glauert’ polynomials could be used to effectively model the cross-sectional geometry of avian wings [4, 51, 200]. These polynomials were also successfully fitted to photogrammetric reconstructions of a barn owl throughout its flap cycle [61]. The Birnbaum-Glauert mean camber line is defined by

$$\frac{z_c}{c} = \frac{z_{c_{max}}}{c} \cdot \eta (1 - \eta) \sum_{n=1}^{\infty} S_n \cdot (2\eta - 1)^{n-1}, \quad (5.1)$$

where z_c are the z-ordinates of the mean camber line, c is chord, $z_{c_{max}}$ is the maximum camber, η is the normalised chordwise coordinate and S_n are the coefficients of the polynomial of order $n - 1$. These were fitted to the mean camber splines described in chapter 3 section 3.4.1, with $n = 4$, allowing two inflection points to describe the minority of reflex cambered sections. This process required the prior normalisation of the spline-based mean camber lines which was carried out by translating the leading edge to the origin, followed by rotating the section to nullify the twist angle, followed by scaling the chord to unity. The inverse of this transformation was then applied to the Birnbaum-Glauert mean camber line to obtain the dimensional equivalent for the section. The Birnbaum-Glauert thickness distribution is defined by

$$\frac{z_t}{c} = \frac{z_{t_{max}}}{c} \cdot \sum_{n=1}^{\infty} A_n \cdot (\eta^{n+1} - \sqrt{\eta}), \quad (5.2)$$

where the notation is the same as for equation (5.1) except for the subscript t representing thickness distribution and A_n being equivalent to S_n . The thickness distribution was obtained by fitting equation (5.2) with $n = 4$ to thickness distribution data obtained from the dorsal and ventral splines discussed in chapter 3 section 3.4.1. These splines commonly self-intersected in the very thin feather-only regions of the wing, so the absolute thickness was used to avoid negative values (chapter 3 section 3.4.1). This resulted in generally representative curve fits around the thick portion of the section, however the initial curve-fit along the very thin secondary flight feather portion of the section required adjustment as shown by ‘B-G init’ in figure 5.2. To ensure that the thickness distribution was both robust and representative of secondary flight feather taper, a modification was made to the posterior portion of the distributions. First, a linear ‘feather taper’ (see figure 5.2) was defined from the chordwise position posterior

to the point of maximum thickness at which the total thickness dropped below 2 mm. This value was based on the approximate outer primary shaft thickness from a barn owl and peregrine, a quarter of the way between the root and tip, using the cadavers described in chapter 4 section 4.4.1. A second Birnbaum-Glauert thickness distribution was then fitted as before, but with the data aft of the feather root being replaced by the feather taper data. This is referred to as ‘B-G taper’ in figure 5.2, and resulted in a more representative gradual taper than ‘B-G init’. Finally, a spline was used to generate a smooth distribution based on both ‘B-G taper’ and the ‘Feather taper’ to produce the ‘final’ thickness distribution in figure 5.2.

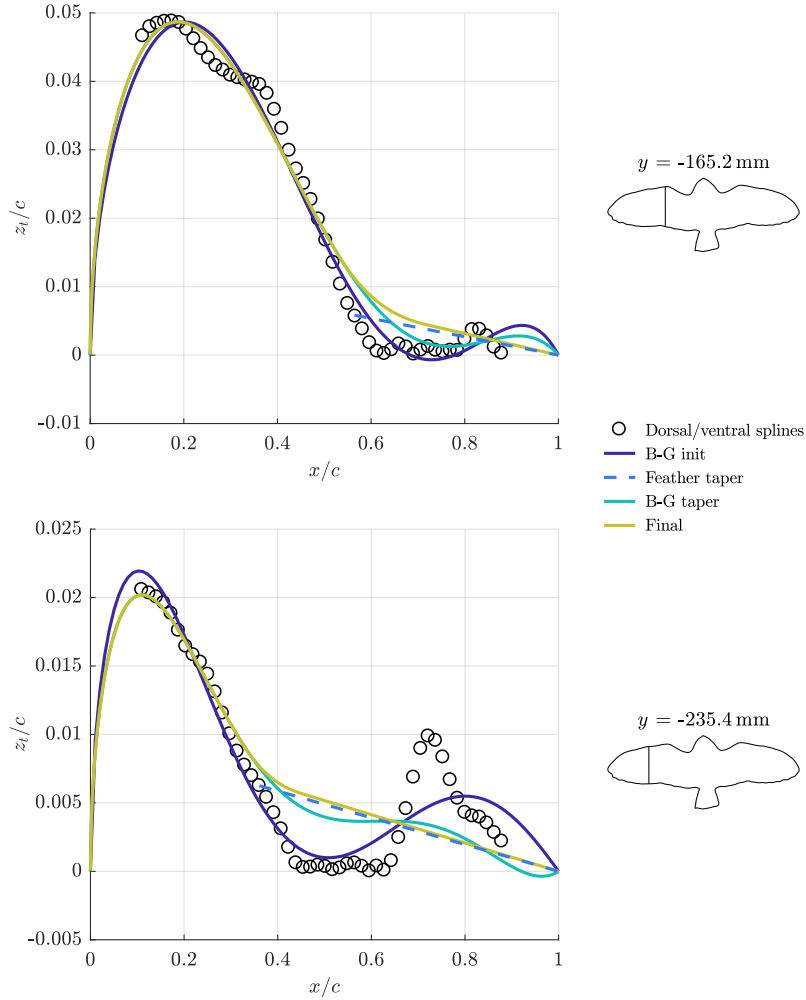


Fig. 5.2 Example modifications to the Birnbaum-Glauert thickness distribution used for the arm wing aerofoils. Two sections from flight O1 are shown to illustrate how the process works. The upper plot is a representative example, while the lower plot shows a section with noise in the raw data close to the trailing edge.

After generating the normalised mean camber line and thickness distribution, the aerofoil was generated simply by adding and subtracting the thickness distribution to the mean camber line to obtain the dorsal and ventral lines. The normalised aerofoil was then transformed back to dimensional coordinates, as shown in figure 5.3. The main advantages of using polynomials designed for aerofoil generation included the robustness of overall process, the guaranteed smooth leading edge and the amenability of each section to computational aerodynamic analysis.

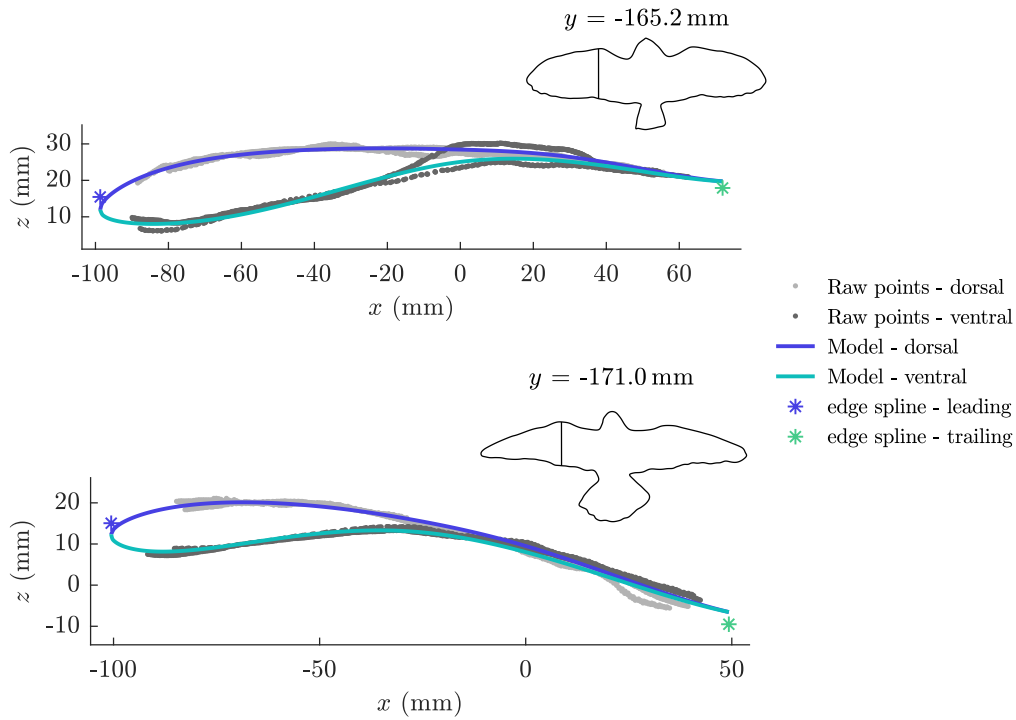


Fig. 5.3 Comparison between the raw data the final model used on representative arm wing sections from flights O1 (top) and P1 (bottom).

5.4.1.4 Hand wing

Similar to the arm wing, the hand wing sections were generated by the addition of a thickness distribution with a mean camber line. The differences between the hand wing and arm wing fitting approach were the use of a lower order mean camber line fit ($n = 3$ in equation (5.1)) and the assumption that a modified NACA 4-series thickness distribution, with a maximum thickness equal to 2 mm, provided a reasonable model for the region of the wing comprising entirely of feathers. Distally, the maximum thickness may have fallen below 2 mm, while proximally it may have

exceeded 2 mm, however this choice ensured the hand wing was both very thin, viable for 3D printing and not liable to deflect or deform significantly during planned wind tunnel testing. The modified NACA 4-digit series thickness distribution [201] was used because it allowed selection of the position of maximum thickness, unlike the standard NACA 4-series. The coefficient defining the leading edge radius, a_0 , was given its ‘nominal’ value of 0.2969¹, resulting in a relatively sharp leading edge. For high-fidelity, fine-scale flow modelling of avian wings, the sharpness could be increased and the barn owl’s serrated structures could also be modelled [56, 202]. However, given the resolution of the planned manufacturing technique (~ 1 mm) and the planned vortex lattice flight dynamics modelling, it was not considered that variations in the leading edge radius would significantly influence the results. The chosen position of maximum thickness was based on the measured thickness distributions of the most distal arm wing sections, and was approximately 10% chord from the leading edge for both the barn owl and peregrine. As with the arm wing, the aerofoils were generated in normalised coordinates and then transformed back into dimensional coordinates, as shown in figure 5.4.

¹Precision to four decimal places would not have been necessary for the current study, but is provided anyway based on the literature.

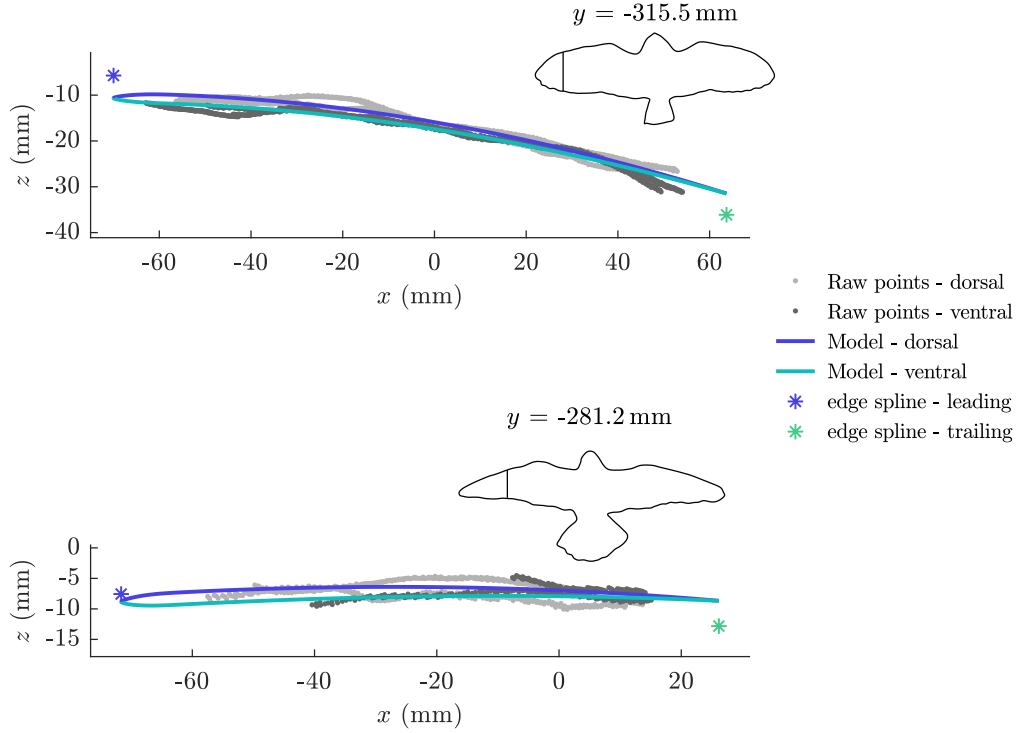


Fig. 5.4 Comparison between the raw data the final model used on representative hand wing sections from flights O1 (top) and P1 (bottom).

5.4.1.5 Body

The body was the most complex section type to fit robustly, due to the differences in head shape between the two birds, and the fact that section geometry varied more than the arm or hand wing in the spanwise direction. For example, some body sections narrowed to a relatively long, thin trailing edge comprising only rectrices, while other sections remained relatively thick very close to the trailing edge, due to the reconstructed legs and feet. A robust method was developed in which the anterior and posterior regions of each section were individually splined and then joined together. The main reason for treating the anterior and posterior sections separately was to ensure robust fitting of the long vertical portion of the barn owl's face. The algorithm used the following steps:

1. The points from each section were split into anterior and posterior datasets using a threshold in x approximately 20% chord from the leading edge.
2. The spline-based approach described in chapter 3 figure 3.5 was used to fit

mean camber, dorsal and ventral lines to the posterior dataset. The thickness distribution of the posterior dataset was adapted similarly to the arm wing, so that below 2 mm it tapered linearly to the trailing edge point. However, some sections contained legs and talons such that the thickness did not drop below 2 mm. In these instances, a taper was applied from the most-aft point of the measured thickness distribution to the trailing edge point.

3. The anterior dataset was converted to polar coordinates and resampled at discrete angles. An interpolating spline was then fitted to the resampled points to form a relatively accurate representation of the face profile.
4. The anterior dataset was stretched so that the forward most point was level with the edge spline data point representing the leading edge position². This ensured that there was no discontinuity in leading edge position at the interface between the arm wing and body due to the differences in fitting approach. This stretch had a small impact ($< 3\%$ chord) on these sections.
5. The posterior and anterior splines were joined together to form a closed-loop. This was done by fitting a cubic interpolating spline through both anterior and posterior data.

This algorithm robustly generated closed-loop representations of the body sections, with examples shown in figure 5.5.

²This anterior stretch is why the splines are not perfectly aligned with the raw points around the bird's face in figure 5.5

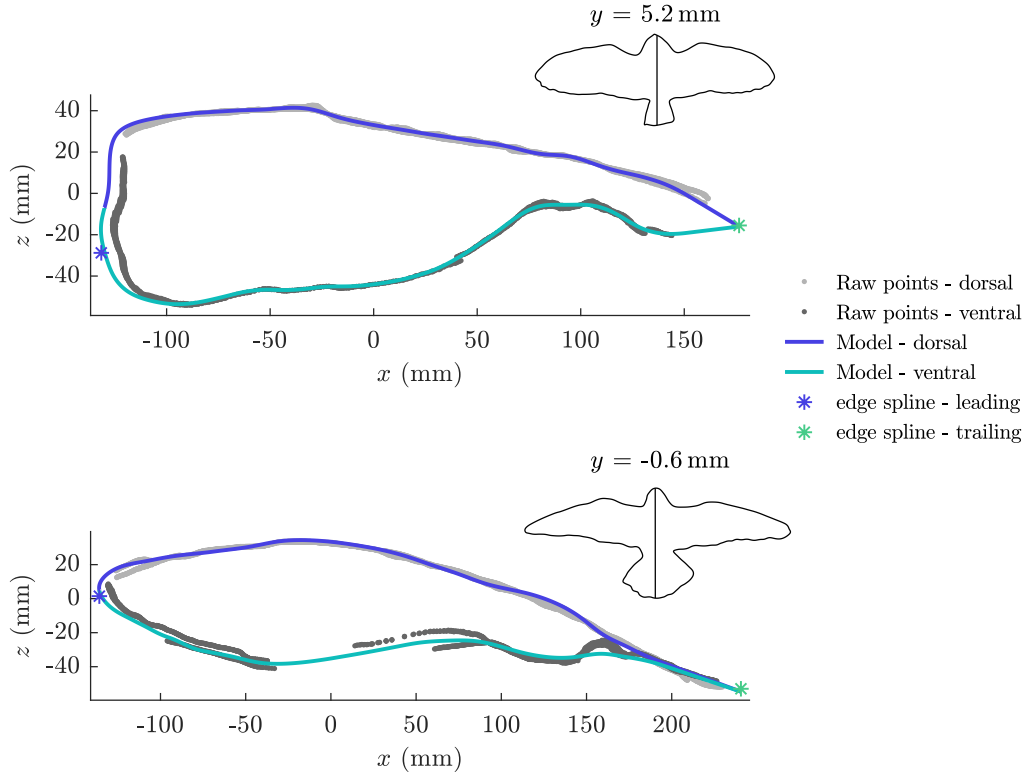


Fig. 5.5 Comparison between the raw data the final model used on representative body sections from flights O1 (top) and P1 (bottom). These examples illustrate some of the challenges faced by the algorithm: differences in face shape, gaps in the data and differences in tail profile.

5.4.1.6 Partly tail

Linear fits were applied to the tail data for sections where it was isolated from the wing or body and therefore consisted entirely of feathers. For these sections, the domain of each tail chord line was determined using the edge spline, similarly to the wing and body. The thickness distributions were defined in the same way as the hand wing (see section 5.4.1.4). The wing or body data in a section containing partly tail was treated as described in sections 5.4.1.3 and 5.4.1.5.

5.4.1.7 Wing and tail tips

The wing and tail tip sections were given the same normalised section profile as the most distal hand wing or partly tail section. Each copied section was translated and scaled such that its position, chord length and thickness varied according to the

centroid and chord of the edge spline leading and trailing edge points. The process was considered the best possible approach given the lack of stereo reconstruction data in these regions.

5.4.1.8 Section visualisations

The end result of the section fitting process is illustrated in figures 5.6 and 5.7. In figure 5.6, the raw points and corresponding section fits of 20 sections along the span are shown for flights O1 and P1, along with the edge spline. To illustrate the robustness of the method, which was necessary to enable the geometry to be 3D printed, figure 5.7 shows 100 of the approximately 400 sections fitted along the span. The accuracy of this fitting approach is quantified in section 5.4.1.9.

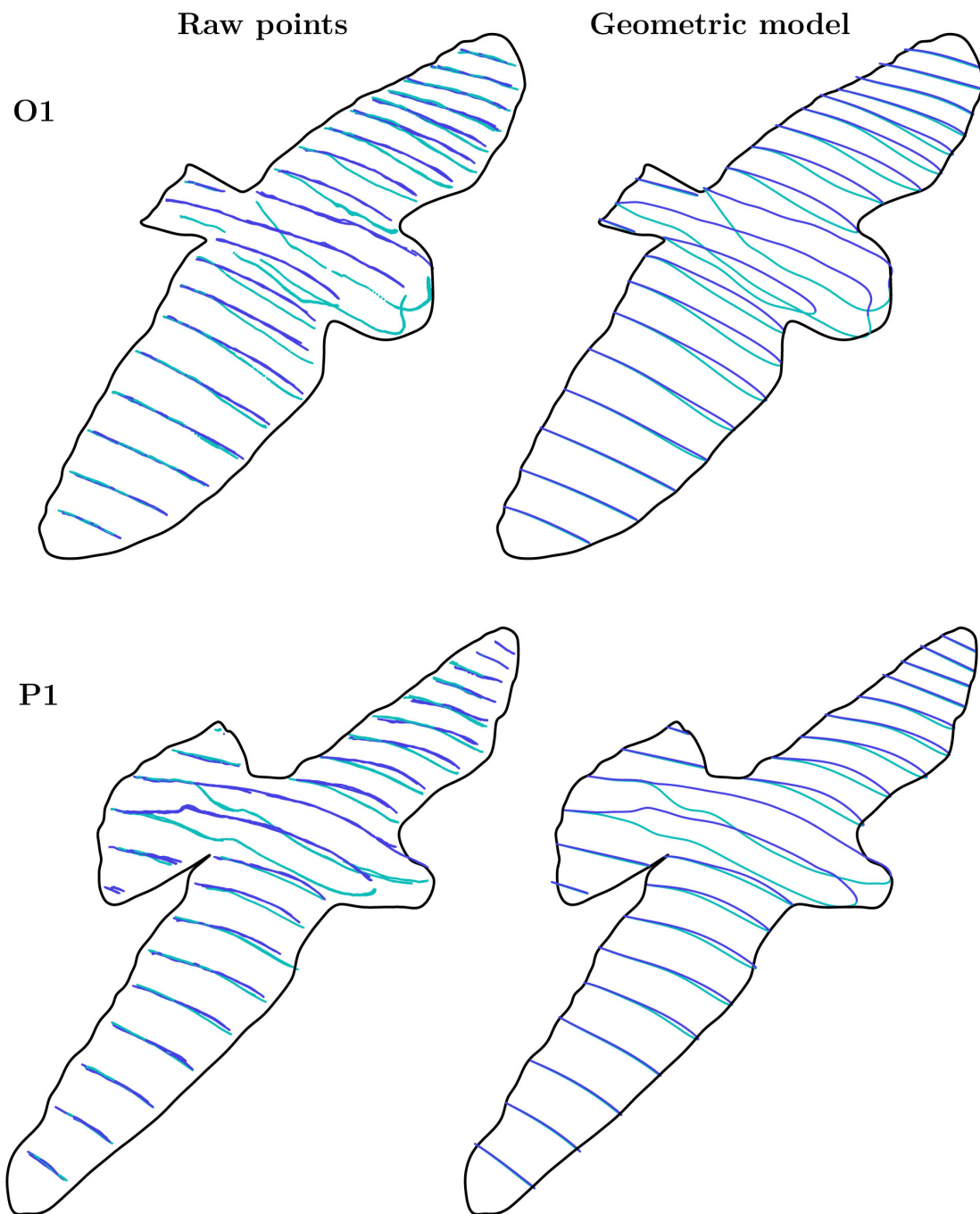


Fig. 5.6 Comparison between the raw points and the final geometric model for 20 sections from flights O1 and P1. The dorsal and ventral surfaces are distinguished by colour.

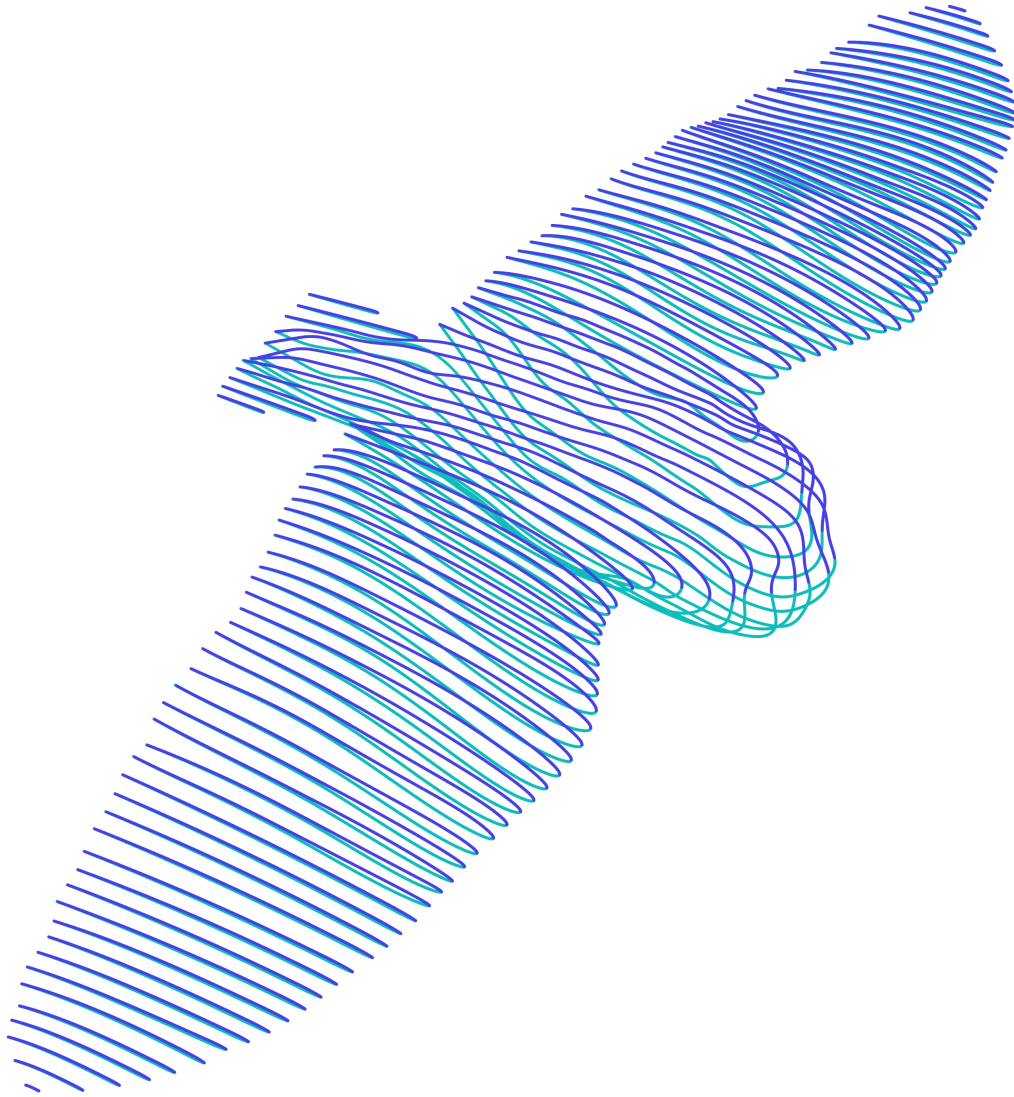


Fig. 5.7 View of flight O1 showing 100 of the approximately 400 sections generated. The dorsal and ventral surfaces are distinguished by colour.

5.4.1.9 Meshing

A watertight mesh was generated for flights O1 and P1 based on the closed-loop points in figure 5.7 for all sections. To generate a manifold, 3D-printable surface mesh, it was necessary to modify the thickness distributions so that the trailing edge was 1 mm thick rather than ending in a sharp point. This kept the dorsal and ventral surfaces of the feathered regions sufficiently far apart to avoid meshing errors in these regions. The point cloud ‘normals’ (vectors orthogonal to the local surface gradient) were

calculated for the dorsal and ventral datasets separately using CloudCompare [143]. Here, it was important to orient *all* the normals facing outwards (or inwards) from the bird’s point-based surface, which was why the dorsal and ventral point clouds were kept separate during this step. The two datasets were then merged, and exported into commercially available software (Geomagic Wrap, 3D Systems, Rock Hill, South Carolina, USA) for meshing. This software featured manual hole filling and very effective mesh repair tools that were required to obtain the fully manifold mesh shown in figure 5.8. Comparison of the generated mesh with the raw point cloud (with the edges removed) gave mean \pm standard deviation cloud-to-mesh distances of $-0.13\text{ mm} \pm 1.04\text{ mm}$ and $-0.01 \pm 1.35\text{ mm}$ for flights O1 and P1 respectively. Due to time and budget constraints, additional flights were not meshed. The stretching of the anterior portion of the body sections to preserve spanwise continuity in chord (see step 4 in section 5.4.1.5) was the primary reason for the non-zero mean in flight O1. Removal of the bird’s face from O1 and P1 reduced the standard deviations to $\pm 0.86\text{ mm}$ and $\pm 1.05\text{ mm}$ respectively. These results show that the process of converting the raw points into the final mesh was faithful to the raw stereo reconstruction data.

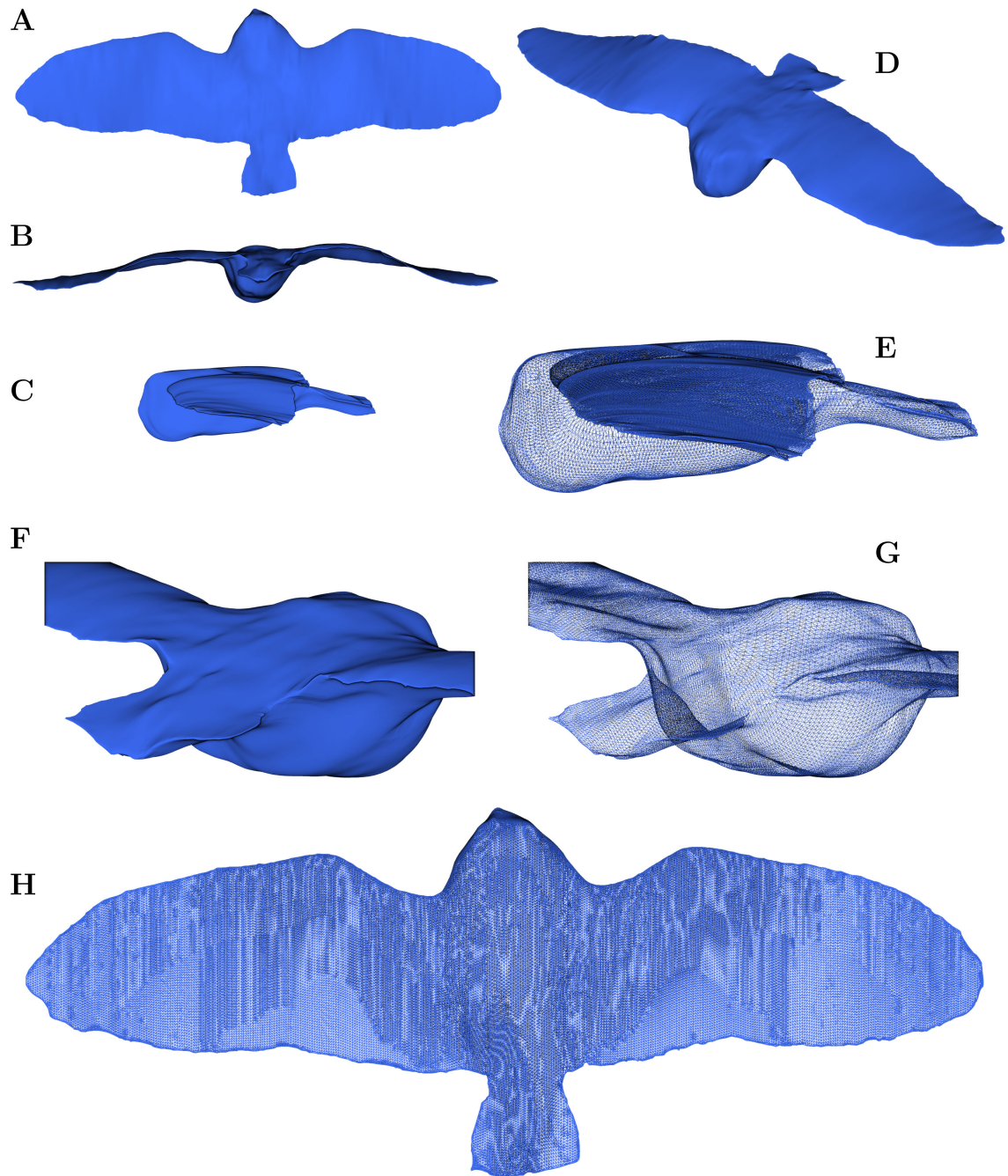


Fig. 5.8 Watertight surface mesh for flight O1 used for wind tunnel testing. Views A), B), C) and F) show dorsoventral, posteroanterior, lateral views and the wing/tail/body interface respectively, rendered as a continuous surface. Views E), G) and H) show similar views rendered to show the mesh elements.

5.4.2 Wind tunnel testing

5.4.2.1 Experimental setup

Wind tunnel testing was carried out for flight O1, with the aim of validating the computational aerodynamic analysis (described later in section 5.4.3) with respect to longitudinal aerodynamic forces, moments and derivatives. The low-turbulence wind tunnel at the University of Bristol was used for testing and features a corner filleted rectangular test section measuring 0.8 m wide, 0.6 m high and 1.6 m long with a turbulence intensity $<0.1\%$ and stable flow velocity between 10 m/s and 90 m/s [203]. In order to minimise interference effects with the tunnel walls, it was necessary to ensure the maximum span did not exceed 80% of the tunnel width [148]. It was also necessary to make the bird as large as possible to maximise the likelihood of successful 3D printing, since the wings were thin distally. A scale factor of 0.78 was therefore applied to reduce the span of flight O1 to 0.64 m. Commercially available software (Geomagic Design X, 3D Systems, Rock Hill, South Carolina, USA) was used to convert the surface mesh of flight O1 (figure 5.11) into a computer-aided-design (CAD) model so it could be adapted for integration with a sting and a T-piece for measuring the angle of attack of the wing-body x -axis with respect to the flow (figure 5.10)³. A single sting affixed to the dorsal surface was chosen to facilitate additional testing of variable pitch incidence tails for a research project not discussed here. The model was 3D-printed (Fortus 400mc, Statasys, Minneapolis, USA) in Acrylonitrile butadiene styrene (ABS) from separate pieces that included the left wing/torso, right wing/torso, central body plate and tail. The wing/torso halves were bolted to the central plate through lateral holes in the torso that were filled in with putty during testing, while the tail was bolted to the torso via a rectangular slot. The central plate provided the sting interface and a slot where a 3D-printed T-piece was inserted to provide an accessible datum face for angle of attack measurement with a digital inclinometer (Universal supplies, Ltd, Chichester, UK) (figure 5.10D). During testing, the empty slot was filled with a matching insert (figure 5.10E) that housed a small magnet for ease of removal in-between measurements.

³Due to time constraints, streamlined fairing was not added to the sting.

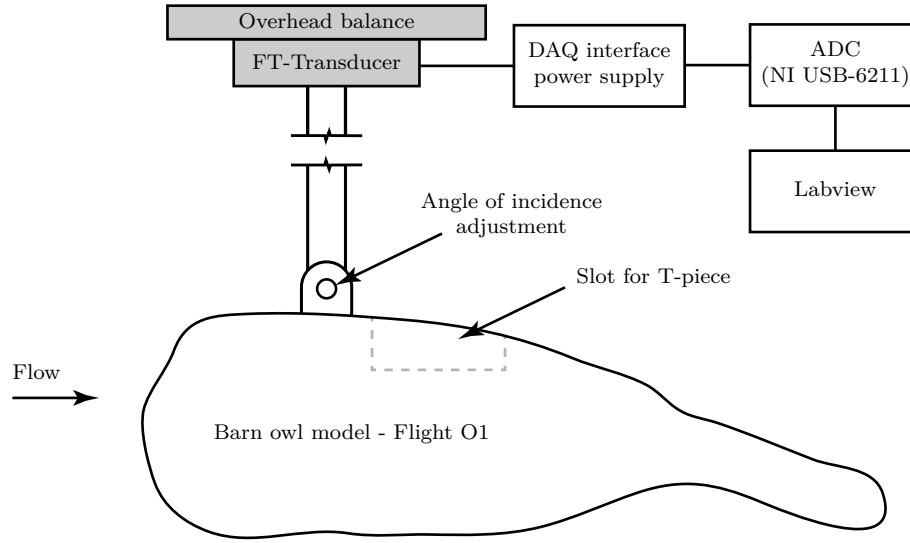


Fig. 5.9 Side-view of the wind tunnel experimental setup.

Lift, drag and pitching moment were measured using a pre-calibrated force-torque transducer (FTT) (Mini45, ATI Industrial Automation, Apex, North Carolina, USA). The FTT was selected in preference to the pre-installed overhead balance to avoid the need for a second sting for the measurement of pitching moment. The stated accuracy in drag of the FTT (0.0625 N) was also marginally superior to that of the overhead balance (0.1 N). The sting consisted of a 0.68 m long, 16 mm diameter round steel bar that was welded to a flange specifically designed to interface with the force-torque transducer. A drag (and moment) pre-load of 2.2 kg was applied to the sting to ensure the these measurements were outside the non-linear range of the sensor (drag was < 3 N). Angle of attack was manually adjusted by loosening and tightening the bolted interface between the sting and the central plate. The FTT was bolted to a 10 mm thick steel plate (figure 5.10C) that was mounted to the pre-installed 3-component balance (Aerotech ATE Ltd, Heathfield, UK). The lift and drag from the pre-calibrated overhead balance were also recorded.

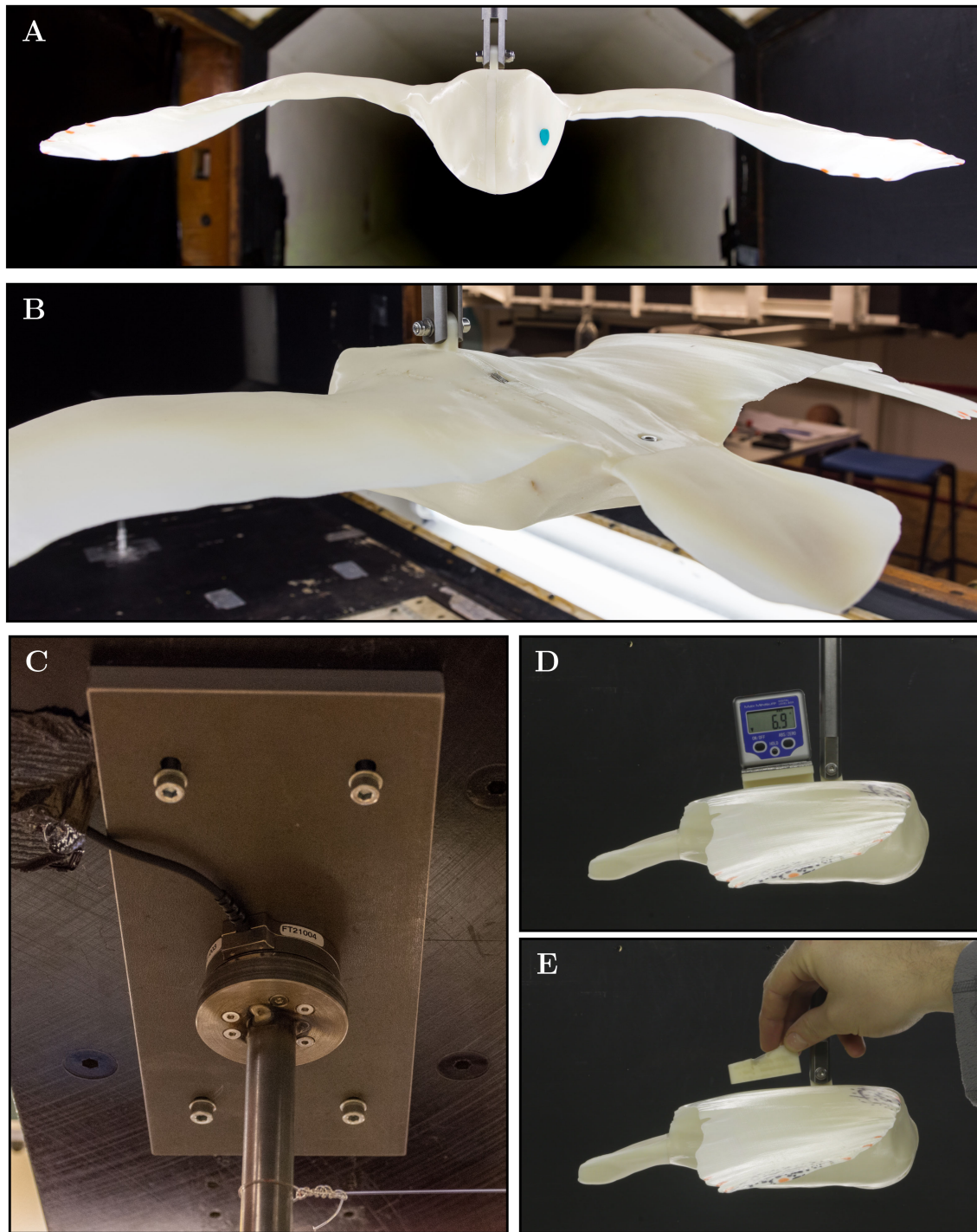


Fig. 5.10 Images of the wind tunnel experimental setup showing A) anteroposterior view of the 3D printed ABS model and sting attachment. The holes for the bolts connecting each half-bird were filled with plasticine. B) Wing/tail/body interface close-up view showing the tail bolt C) ATI Mini45 force-torque transducer attached to the Aerotech 3-component overhead balance D) technique for measuring the angle of attack using an inclinometer E) the T-piece slot was filled during testing.

Flow velocities of 10, 15, 20 and 25 m/s were tested, corresponding to Reynolds numbers between approximately 70×10^3 to 170×10^3 , in order to assess the sensitivity of the measurements to viscous effects. The Reynolds number of flight O1 was approximately 70×10^3 , corresponding to a flow velocity of 10 m/s for the wind tunnel test. Testing at lower Reynolds numbers would have required a change in fluid medium or a reduction in model size or flow velocity. The first of these options was rejected based on the available facilities, a reduction in model size would have compromised the robustness of the manufacturing process due to the very thin wing thickness distally and a reduction in flow velocity would have risked instability of the wind tunnel's control system. Gathering data at higher flow velocities also provided additional datasets that could be used if the drag error was unacceptably high at the lower velocities (assuming the measurements were relatively insensitive to Reynolds number). The model was tested at angles between -5° and 7° in order to provide a comprehensive range against which to validate computational models⁴. Angle of attack was referenced against the x -axis of the wing-body coordinate system of the bird (chapter 2 section 2.6.5), which was estimated to be $5.1^\circ \pm 3.6^\circ$ (table 3.1). After 60 s at each test point (to allow the transducer to settle), data were sampled for 10 s at sample rates of 1 kHz for the FTT and 300 Hz for the overhead balance⁵. At every test point, data were collected with the flow off to enable it to be zeroed in post-processing. By turning the flow off for each test point, any potential low Reynolds number hysteresis effects were avoided [204, 205]. Measurements were also obtained for the sting without the model to allow the sting drag and pitching moment to be removed. At each test point, the mean from all the sampled data were used to represent the steady state value. Each test point was repeated at least three times.

5.4.2.2 Model deformation

Two possible sources of model deformation were identified that could influence the quality of the results. The first was the possibility of the model plastically warping following manufacture, the second was the likely elastic deformation due to aerodynamic loads, especially towards the wing tips at higher angles of attack and flow velocity. To check for warping, the left and right model halves were laser scanned (Faro Edge, Faro, Orlando, Florida, USA), to a stated accuracy of ± 0.034 mm, following manu-

⁴This range included the 5.1° estimated previously (table 3.1), with limits to mitigate risk of structural failure but with sufficient range to confirm the linearity of important aerodynamic derivatives such as the lift and moment slopes.

⁵The maximum available rate for the overhead balance

facture and on completion of wind tunnel testing. The scan data were aligned to the original mesh using iterative closest point alignment, followed by computation of the cloud-to-mesh distances in CloudCompare [143]. The scan results shown in figure 5.11 suggest that although the 3D-printed model did not significantly change shape during the wind tunnel testing, it may have warped slightly following manufacture. This could be due to immersion in a warm acetone bath immediately after printing for the removal of the support material.

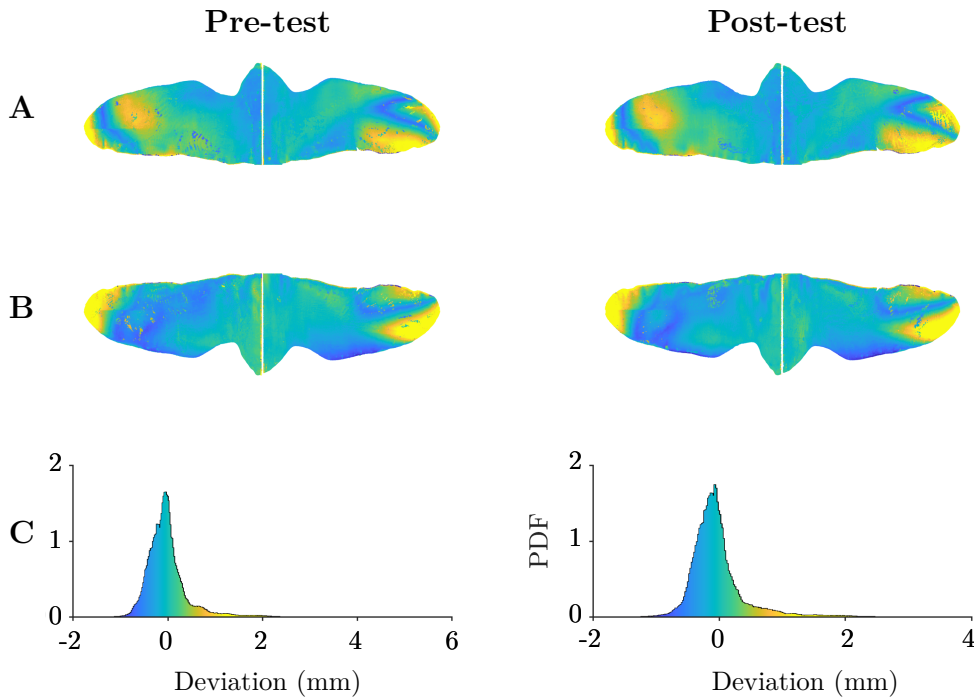


Fig. 5.11 Cloud to mesh comparison between the laser-scanned 3D-printed barn owl model and the original mesh before and after 2-weeks of wind tunnel testing. A) dorsal surface, B) ventral surface, C) histograms for dorsal and ventral surfaces pre- and post-test, with corresponding colour maps.

To check for elastic deformation during aerodynamic loading, the approximate vertical displacement of the loaded wing was measured using a digital camera (70D, Canon, Tokyo, Japan), calibrated with a ruler placed vertically against the wing tip. At a flow velocity of 20 m/s and angle of attack of 7° (worst case), the right wing tip deflected by 6 mm while at 10 m/s the tip deflection was negligible. These unwanted deformations could have been eliminated by 3D printing in steel, but the small magnitude of these effects did not justify the additional high cost.

5.4.2.3 Transducer calibration checks

To check the quality of the force and moment data, calibration checks were carried out prior to each day of testing. This was achieved by inserting a ‘dummy’ tail into the slot where the real tail was located. A 60 lb nylon fishing line was attached to the dummy tail, and weights were hung to simulate the aerodynamic loads (20 g to 100 g in increments of 20 g and 100 g to 1 kg in increments of 100 g). For drag, a low-friction pulley was used. The results of these checks are shown in figure 5.12 for the FTT and figure 5.13 for the overhead balance. As expected, lift and pitching moment were significantly more accurate than drag due to the larger magnitude changes in their values. The FTT was more accurate in lift while the overhead balance was more accurate in drag. For this reason, the overhead balance drag values were used in preference to the FTT. The drag from the overhead balance was corrected based on the calibration checks using a linear fit to all the error data obtained during testing, within the 3 N range of drag values (figure 5.14). The gradient of this fit was used to correct the measured drag values using,

$$D_c = \frac{D_u}{\frac{\partial D_e}{\partial D_a} + 1} \quad (5.3)$$

where D_c is the corrected drag, D_e and D_a are the absolute drag error and absolute drag from the calibration plotted in figures 5.13 and 5.14 and D_u is the uncorrected drag measured during each test condition.

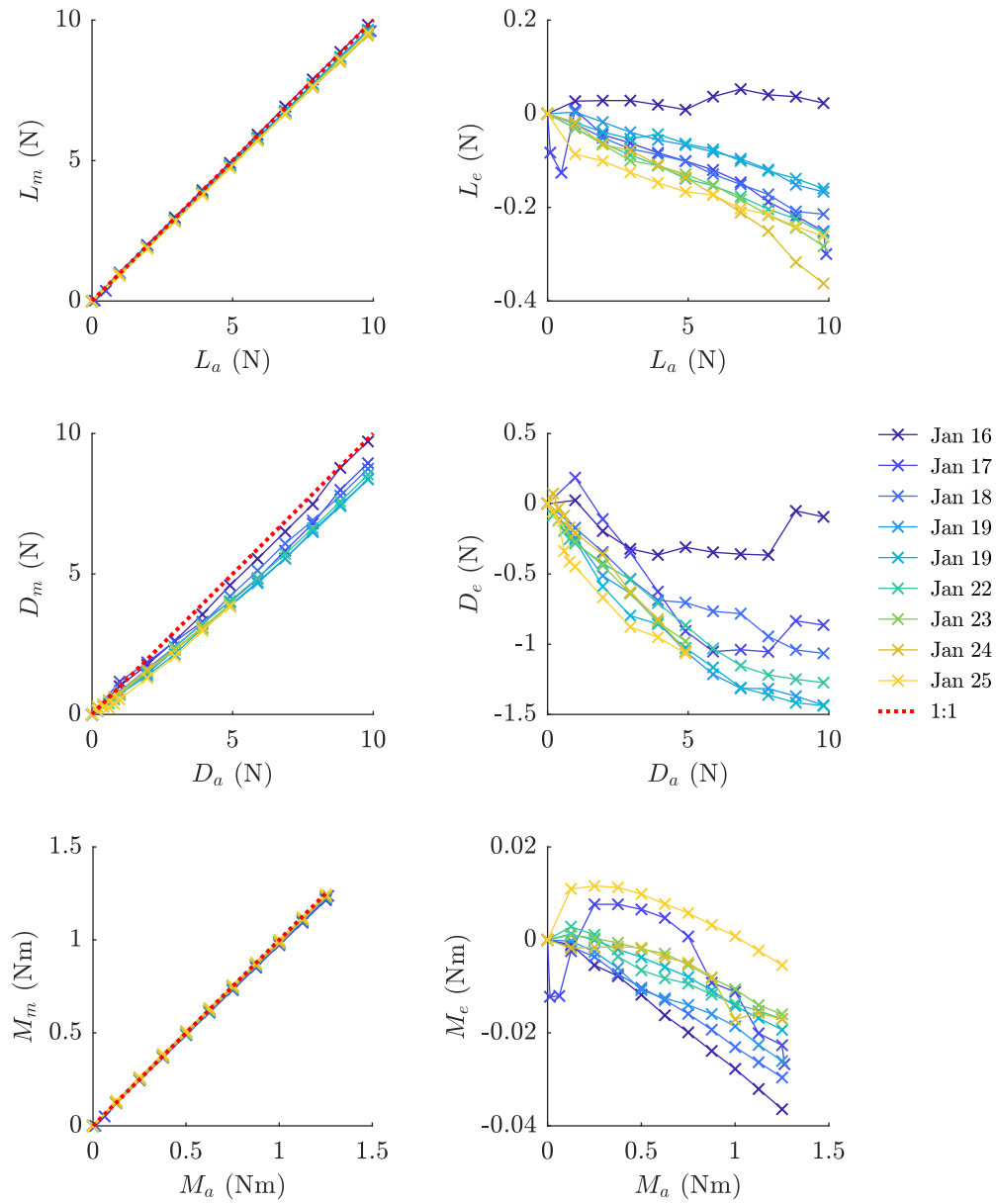


Fig. 5.12 Calibration checks carried out for lift, drag and pitching moment measurements from the force-torque transducer (ATI Mini45). The subscripts a , m and e refer to applied loads, measured loads and absolute error respectively.

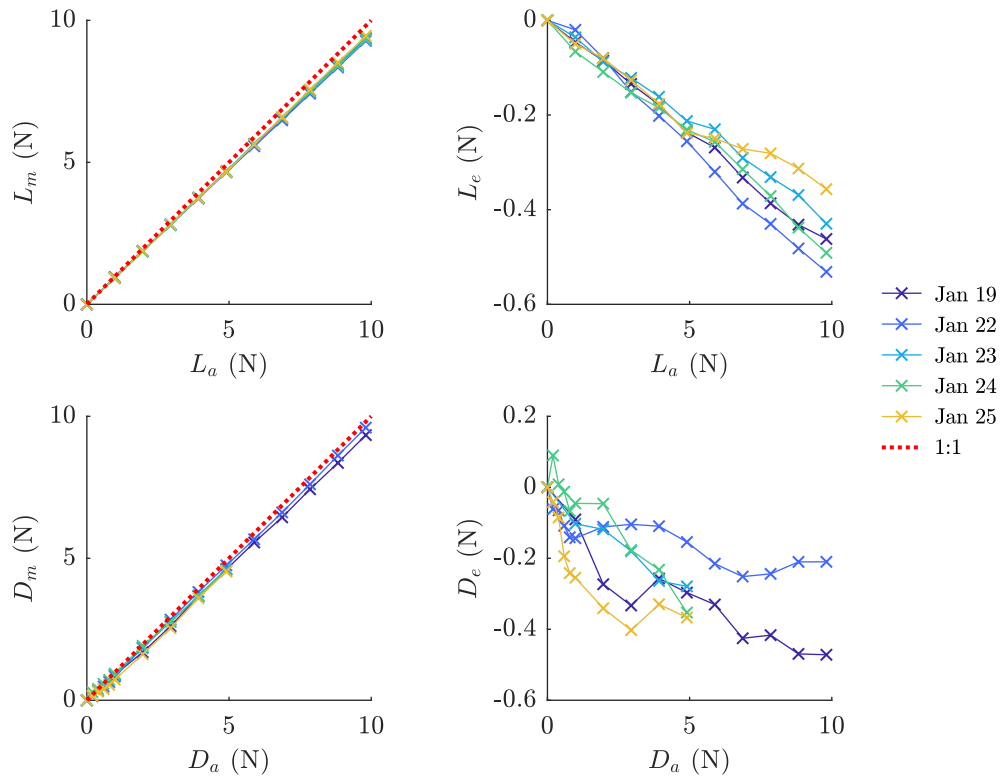


Fig. 5.13 Calibration checks carried out for lift and drag measurements from the Aerotech 3-component overhead balance installed in the low-turbulence wind tunnel. The subscripts a , m and e refer to applied loads, measured loads and absolute error respectively.

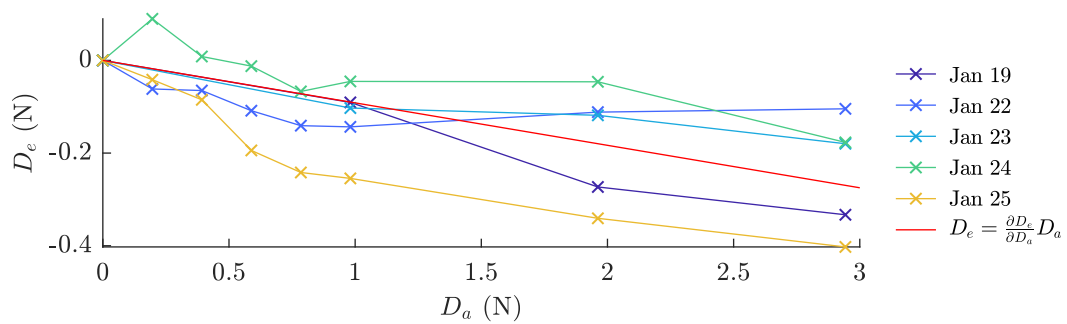


Fig. 5.14 Drag measurements from the overhead balance were corrected based on a linear fit through the drag error data up to 3 N estimated throughout the testing period using a weight and pulley system. The correction results in a 10% increase to the drag measurements. The subscripts a and e refer to applied loads and absolute error respectively.

5.4.2.4 Post-processing

The data were post-processed as follows:

1. Zero the data by subtracting the mean from the unloaded case, from the mean of the loaded case.
2. Subtract the forces and moments due to the sting based on the mean values from three repeats at each velocity.
3. Calculate the pitching moment about the centre of mass of the bird. This was calculated according to figure 5.15 and equations (5.4) to (5.6):

$$M_{CoM} + M_T - Ll_x - Dl_z = 0 \quad (5.4)$$

$$L = -F_z \quad (5.5)$$

$$D = -F_x. \quad (5.6)$$

At this point the drag was corrected as discussed in section 5.4.2.3.

4. Remove outliers. These were defined as data points more than three standard deviations from linear and quadratic curve fits to the data.

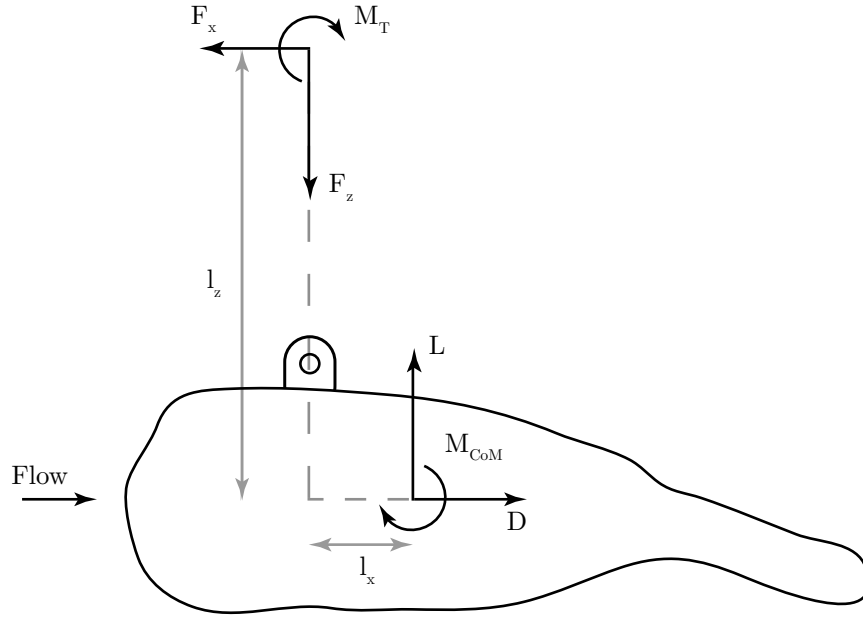


Fig. 5.15 Free-body diagram showing how the pitching moment about the bird's centre of mass was calculated.

The influence of corrections for solid blockage, wake blockage, streamline curvature, downwash, up- and cross-flow and horizontal buoyancy was explored [148]. The test section of the wind tunnel was designed to expand in cross-sectional area, thus mitigating the effects of horizontal buoyancy. The remaining corrections were small ($< 1\%$), were mainly concerned with absolute values rather than the derivatives, and were therefore not applied.

5.4.3 Flight dynamics modelling

5.4.3.1 Overview

The dynamic stability of each flight was modelled based on six-degree-of-freedom (6-DoF) rigid body assumptions and small perturbations from trim. This approach is commonly used for stability analysis of conventional aircraft about a specific flight condition, and first involves the derivation of the equations of motion. These equations represent Newton's second law for rectilinear and rotational motion, which for a 6-DoF system is described by six equations. Derivation of these may be found in flight dynamics texts [38, 96]. In their pure form, these equations are non-linear and require complex numerical solutions. However, they can be linearised and solved analytically

by assuming small perturbations from trim, significantly simplifying their solution. This process involved the following assumptions:

1. The bird was initially in equilibrium, or trim (forces and moments sum to zero).
2. Zero sideslip velocity and atmospheric disturbances.
3. All forces and moments are calculated about the centre of mass.
4. Aerodynamic forces and moments are linear with respect to changes in state such as velocity and angle.
5. The aerodynamic forces and moments due to control surface deflections, when included in the model, are assumed to be linear with control surface angle.
6. The products of linear or angular velocity perturbations in the non-linear equations of motion are zero based on the assumption of small perturbations.

The advantage of these modelling assumptions is the simplification afforded to the solution of the dynamic equations. They also represent a simplification of the real system because the barn owl and peregrine were flying outdoors with some sideslip and were probably not perfectly trimmed. The assumption of a rigid body was also not true of real birds, with their highly compliant wing structures. However, these modelling assumptions were considered reasonable for the first explorations into avian flight stability because they provided fundamental models of the system that could later be refined if desired. To solve the linearised equations of motion, both inertial and aerodynamic inputs were required, including the centre of mass position and total mass, the mass moment of inertia tensor, trim velocity and trim angles (relative to flow and earth). The inertial inputs were obtained based on the analysis described in chapter 4, while the aerodynamic inputs were obtained using a vortex lattice method described in section 5.4.3.3.

5.4.3.2 Dynamic model

Each flight was modelled based on the coupled, linearised, six-degree-of-freedom rigid-body equations of motion for which asymmetry was assumed important (i.e. I_{xy} and I_{yz} were non-zero). In matrix form these are written:

$$\mathbf{M}\dot{\mathbf{x}}(t) = \mathbf{A}'\mathbf{x}(t) \quad (5.7)$$

$$\mathbf{M} = \begin{bmatrix} m & -\dot{X}_{\dot{w}} & 0 & 0 & 0 & 0 & 0 & 0 & 0 \\ 0 & m - \dot{Z}_{\dot{w}} & 0 & 0 & 0 & 0 & 0 & 0 & 0 \\ 0 & -\dot{M}_{\dot{w}} & I_{yy} & 0 & 0 & -I_{xy} & -I_{yz} & 0 & 0 \\ 0 & 0 & 0 & 1 & 0 & 0 & 0 & 0 & 0 \\ 0 & -\dot{Y}_{\dot{w}} & 0 & 0 & m & 0 & 0 & 0 & 0 \\ 0 & -\dot{L}_{\dot{w}} & -I_{xy} & 0 & 0 & I_{xx} & -I_{xz} & 0 & 0 \\ 0 & -\dot{N}_{\dot{w}} & -I_{yz} & 0 & 0 & -I_{xz} & I_{zz} & 0 & 0 \\ 0 & 0 & 0 & 0 & 0 & 0 & 0 & 1 & 0 \\ 0 & 0 & 0 & 0 & 0 & 0 & 0 & 0 & 1 \end{bmatrix} \quad (5.8)$$

$$\dot{\mathbf{x}}(t) = [\dot{u} \quad \dot{w} \quad \dot{q} \quad \dot{\theta} \quad \dot{v} \quad \dot{p} \quad \dot{r} \quad \dot{\phi} \quad \dot{\psi}]^T \quad (5.9)$$

$$\mathbf{A}' = \begin{bmatrix} \dot{X}_u & \dot{X}_w & \dot{X}_q - mW_e & -mg\cos\theta_e & \dot{X}_v & \dot{X}_p & \dot{X}_r & 0 & 0 \\ \dot{Z}_u & \dot{Z}_w & \dot{Z}_q + mU_e & -mg\sin\theta_e & \dot{Z}_v & \dot{Z}_p & \dot{Z}_r & 0 & 0 \\ \dot{M}_u & \dot{M}_w & \dot{M}_q & 0 & \dot{M}_v & \dot{M}_p & \dot{M}_r & 0 & 0 \\ 0 & 0 & 1 & 0 & 0 & 0 & 0 & 0 & 0 \\ \dot{Y}_u & \dot{Y}_w & \dot{Y}_q & 0 & \dot{Y}_v & \dot{Y}_p + mW_e & \dot{Y}_r - mU_e & mg\cos\theta_e & mg\sin\theta_e \\ \dot{L}_u & \dot{L}_w & \dot{L}_q & 0 & \dot{L}_v & \dot{L}_p & \dot{L}_r & 0 & 0 \\ \dot{N}_u & \dot{N}_w & \dot{N}_q & 0 & \dot{N}_v & \dot{N}_p & \dot{N}_r & 0 & 0 \\ 0 & 0 & 0 & 0 & 0 & 1 & 0 & 0 & 0 \\ 0 & 0 & 0 & 0 & 0 & 0 & 1 & 0 & 0 \end{bmatrix} \quad (5.10)$$

$$\mathbf{x}(t) = [u \quad w \quad q \quad \theta \quad v \quad p \quad r \quad \phi \quad \psi]^T. \quad (5.11)$$

Equations (5.7) to (5.11) represent the linearised, 6-DoF form of Newton's second law in matrix form [38] referred to the wing-body coordinate system described in chapter 2 figure 2.6. The mass matrix, \mathbf{M} , contains the mass, m , inertia, I_{xx} , I_{yy} , I_{zz} , I_{xy} , I_{yz} and I_{xz} , and acceleration derivatives (symbols with over-ring). All derivatives in these equations are given the notation of an upper-case letter with subscript denoting the dependent and independent variable respectively. Forces and moments along/about the x , y and z axes are denoted X , Y , Z , L , M and N respectively. The small circular symbols above each derivative indicates that they are dimensional. The acceleration derivatives in the mass matrix were assumed to be zero which is standard practice

for relatively conventional subsonic aircraft configurations⁶. The state matrix, \mathbf{A}' , contains various aerodynamic derivatives, gravitational terms, trim velocity, U_e and W_e , and pitch attitude, θ_e . The subscript, e , denotes equilibrium or trim. The state matrix is multiplied by the state vector, $\mathbf{x}(t)$, containing all the variables that describe the motion from the original derivation of the equations of motion. The variables u , v and w are perturbation velocities along the x , y and z axes, while p , q and r are the corresponding angular velocities. Pitch, roll and yaw attitude perturbations are denoted by θ , ϕ and ψ respectively.

There are two conventions in flight dynamics for the equations of motion, based on British vs. North-American notation, resulting in subtly different definitions for some of the dimensional and dimensionless aerodynamic derivatives. Derivatives based on the North American notation use the prefix ‘C’, such as in table 5.2. The dynamic model used here used British notation, but can be converted to the North-American system if required [38]. This point is made because the vortex lattice method used to obtain the aerodynamic derivatives used the North-American convention, requiring these conversions for solving the dynamic equations in British notation described above.

A commonly used approach for solving equations (5.7) to (5.11) is the state-space method, a widely adopted tool for control system analysis. Introductory flight dynamics texts provide a thorough description of the application of state-space modelling to flight dynamics [38, 96], with the basic principles described here. The general equations of a linear time invariant dynamic system are written

$$\begin{aligned}\dot{\mathbf{x}}(t) &= \mathbf{A}\mathbf{x}(t) + \mathbf{B}\mathbf{u}(t), \\ \mathbf{y}(t) &= \mathbf{C}\mathbf{x}(t) + \mathbf{D}\mathbf{u}(t),\end{aligned}\tag{5.12}$$

where for aircraft, the output matrix, C , is an identity matrix (unless additional ‘augmented’ state variables are required) and the direct matrix, D , is a zero matrix. For a bird or aircraft model with no control surfaces, the control matrix, B , is also zero. Equation (5.7) can be rearranged into state-space or ‘concise’ form by pre-multiplying both sides by the inverse of the mass matrix, M (see Appendix D). The eigenvalues and eigenvectors of the concise form of the state matrix define the ‘poles’ and ‘zeros’ of the characteristic equation describing the stability of the system in terms of the Laplace operator. The zeros and poles refer to real and complex eigenvalues respectively, and

⁶Acceleration derivatives are usually non-zero for craft such as airships or combat aircraft [38]

provide important information about dynamic stability, usually presented graphically using a ‘root-locus plot’. The poles and zeros correspond to oscillatory and non-oscillatory system modes respectively, while the sign of the real part describes either a dynamically stable (negative) or unstable (positive) mode. The eigenvectors provide information about the content of each mode in terms of its state variables. The natural frequencies and damping ratios of the modes were calculated from the eigenvalues using

$$\begin{aligned}\omega_n &= Im(\lambda), \\ \zeta &= \frac{Re(\lambda)}{Im(\lambda)},\end{aligned}\tag{5.13}$$

where ω_n , ζ and λ are the undamped natural frequency, damping ratio and eigenvalue of a given mode. The relative magnitudes of corresponding elements within each eigenvector, provides information about the dominant state variables present within the different modes. For example, the u element within the eigenvectors is usually larger for the phugoid mode than the short period mode in conventional aircraft, due to the relative dominance of this state variable within these modes. Time-histories were obtained using Matlab [139] with each eigenvector used as an initial perturbation to excite the modes. Where the eigenvectors were complex, the magnitude and phase of each eigenvector element, Λ , was evaluated to generate the real-valued perturbation element:

$$\begin{aligned}\Lambda_{in} &= |\Lambda| \cos(\phi) \\ |\Lambda| &= \sqrt{Re(\Lambda)^2 + Im(\Lambda)^2} \\ \phi &= \tan^{-1} \frac{Im(\Lambda)}{Re(\Lambda)}.\end{aligned}\tag{5.14}$$

For each time-history, the state matrix was augmented with angle of attack and angle of sideslip so that these variables were included in the analysis, as described in Cook [38].

5.4.3.3 Aerodynamic modelling in AVL

Computational aerodynamic was carried out using Athena Vortex Lattice (AVL) [206], an open source modelling tool for flight stability analysis developed at Massachusetts Institute of Technology (MIT). AVL was used due to its flexibility, low computation

time and flight stability analysis capability. Vortex lattice methods such as AVL treat lifting surfaces as arrays of horseshoe vortices superimposed with the free stream condition. The distribution of circulation over the lifting surface is solved numerically such that flow tangency is imposed normal to the lifting surface profile. Forces and moments can then be calculated by integration over the entire surface based on the free stream conditions and the circulation distribution. Vortex lattice methods are based on the assumptions of inviscid flow over thin lifting surfaces at low angles of attack. AVL does have the option to include section-wise profile drag polars, but this was not utilised due to time constraints. Therefore, the AVL models used here estimated only induced drag due to vortex shedding from the lifting surfaces, and not profile drag due to skin friction and flow separation from the wings, torso and tail. This would have led to more significant under-predictions of drag for the barn owl, given its very bluff head and body. Furthermore, non-linear aerodynamic effects at high angles of attack (i.e. stall) are not captured by vortex lattice methods. Previous validation of AVL suggests it provides reasonably accurate lift, drag and rolling moment at low angles of attack up to approximately 10° [189, 207]. For the six flights tested, it was clear that the maximum spanwise angle of attack reached approximately 20° (figure 3.14A) and that the tail angle of attack was up to 28.5° (table 3.1) which could adversely affect the AVL analysis. For this reason, wind tunnel testing was also carried out to validate the AVL data (see section 5.4.2).

The AVL model geometry was defined using six distinct ‘surfaces’ (in the sense used in the AVL manual) all treated as the same ‘component’ and joined by matched geometric interfaces (figure 5.16). These surfaces included the left and right definitions of the wing, body and tail and were divided this way to allow flexibility regarding symmetric or asymmetric configurations, should comparisons have been needed. The wing geometry was based on the arm and hand wing mean camber lines described in sections 5.4.1.3 and 5.4.1.4. The tail geometry was based on a thin plate smoothing spline fitted to the dorsal reconstruction of the rectrices using Matlab [139]. The thin plate spline was divided into spanwise sections and extrapolated to the edge spline points to form the complete mean camber line of each tail section. This method allowed the tail to be accurately represented as an individual thin surface, based on the rectrices. The body was represented using straight lines joining the anterior interface between the upper and lower body data described in section 5.4.1.5 and the anterior point on the tail thin plate spline, for each spanwise position. Straight lines were used because the body was generally lacking camber. To represent the thickness of

the body, the AVL option to distribute a chordwise array of doublets in the sagittal plane was utilised. The position and strength of the doublets was based on the profile closest to $y = 0$ (similar to the sections in figure 5.5). The model was run with and without inclusion of the thick central body to evaluate the effect of this setting.

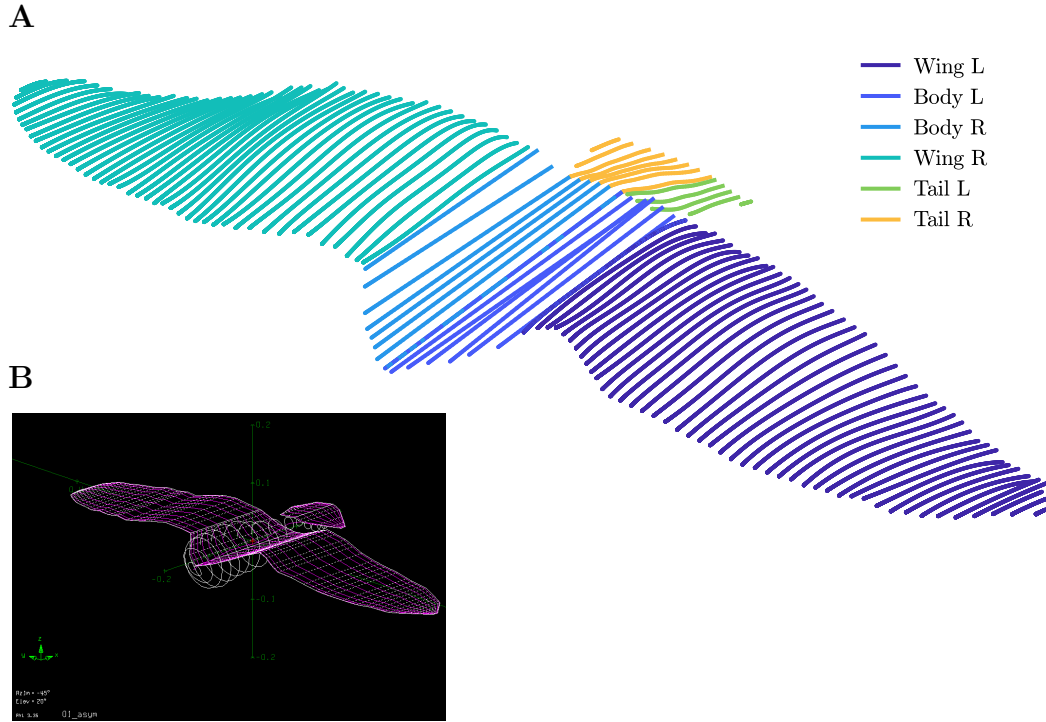


Fig. 5.16 A) Geometric representation of flight O1 as a thin surface. Each AVL model used 15 sections per wing (a subset of the sections shown), and each flight was modelled with and without a thick central torso, represented by a chordwise array of doublets whose strength was set based on the local torso diameter. B) AVL visualisation of flight O1 with a thick central torso.

For flight P2, the lack of dorsal surface reconstruction for the left wing (see chapter 3) meant that it was not possible to estimate mean camber lines for these sections. Instead, the profile of the ventral surface was used to represent the mean camber lines for these sections. This had the effect of slightly over-estimating the camber and under-estimating the twist angle between 39 mm and 204 mm along the left wing. The error due to these effects is difficult to quantify, and therefore the results from P2 should be interpreted in light of this limitation.

To obtain reliable results from AVL, it was important to ensure a relatively even vortex distribution [206]. This was done by measuring the relative proportions between

the length and width of the various surface regions shown in figure 5.16 and then defining the number of vortices in each region accordingly. The spacing distributions of the vortices were also set so that their spatial density was higher in regions of rapidly changing circulation - i.e. wing tips, leading and trailing edges and wing roots. This ensured the more rapid spatial changes in forces and moments were adequately resolved in these regions. It was also important to ensure that the trailing legs of vortices from the wing did not pass too close to control points on the tail [206]. Due to the large number of vortices generated, and the difficulty carrying out a robust visual check, the model was run with and without the same ‘component’ definition for the wing-body and tail surfaces. When different component definitions were used, AVL uses a finite circulation strength for the vortex core to minimise the effects of the interference. If problems were present due to the interaction of trailing legs and control points, these ought to have resulted in significantly different results between the two trial runs. The fact that the results were unchanged by component definition between the wing-body and tail, suggests that interference between trailing legs and control points was not an issue. The total number of vortices was selected based on computation time. Pilot tests showed that beyond a threshold number of vortices, AVL did not function effectively (i.e. crashed, did not converge for 24 hours etc). Furthermore, it was generally necessary to select twice as many vortices as sections to allow effective interpolation of the vortices along the span. A reasonable compromise between computational efficiency and spatial resolution was found to be 15 sections per wing, equivalent to every 3% span for P1 (worst case). To confirm ‘grid’ independence, the model was initially run for coarse, medium and fine lattice resolutions. This enabled use of a Richardson Extrapolation approach to determine the sensitivity of the results to lattice spatial resolution [208]. The Richardson Extrapolation is commonly used within computational aerodynamics to estimate numerical errors and confirm grid independence of results.

For validation against the wind tunnel results, the AVL model of flight O1 was run at angles of attack of (-5° to 7°) to obtain the lift, drag and pitching moment variation with angle of attack that would usually be obtained for conventional rigid aircraft. Obviously, the results for angles of attack significantly outside those of the actual flight conditions do not represent the performance curves of the bird, since it would certainly change its geometry for different flight conditions. Additional validation included comparison between wind tunnel and AVL estimates of the longitudinal derivatives (see section 5.4.3.4), and checks of the AVL conversion to concise deriva-

tives (see Appendix D). The latter revealed significant errors in three of the twenty-four conversions and these were corrected for the flight dynamics analysis.

To estimate the stability of each flight, the AVL models were run at the lift coefficient and pitch attitude estimated in the field (chapter 3 table 3.1). Critical input parameters such as mass, wing area, mean aerodynamic chord and true air speed were also taken from chapter 3 table 3.1. During each simulation, the angle of attack was adjusted to match the lift coefficient required for steady, trimmed flight. Sensitivity studies were carried out for flights O1, P1 and P3 based on uncertainty in the trimmed lift coefficient, anteroposterior centre of mass position and the inertia tensor. Due to the very low air speeds (<15 m/s), a Mach number of zero was assumed for all AVL calculations, as compressibility corrections were negligible. For all flights, the profile drag was estimated by subtracting the AVL far-field estimate of induced drag from the total drag measured in the wind tunnel for flight O1. The additional profile drag significantly improved the estimate of C_{X_u} (North American notation for X_u) for flight O1 in comparison with the wind tunnel estimate (see section 5.4.3.4), but did not affect pitching moment or any other derivatives significantly. When comparing the AVL aerodynamic derivatives with the wind tunnel estimates for validation, they were transformed from body to wind axes using the equations defined in table 5.1.

Wind axes	Body axes
\dot{X}_{u_w}	$\dot{X}_{u_b} \cos^2 \alpha_e + \dot{Z}_{w_b} \sin^2 \alpha_e + (\dot{X}_{w_b} + \dot{Z}_{u_b}) \sin \alpha_e \cos \alpha_e$
\dot{Z}_{u_w}	$\dot{Z}_{u_b} \cos^2 \alpha_e - \dot{X}_{w_b} \sin^2 \alpha_e - (\dot{X}_{u_b} - \dot{Z}_{w_b}) \sin \alpha_e \cos \alpha_e$
\dot{M}_{u_w}	$\dot{M}_{u_b} \cos \alpha_e + \dot{M}_{w_b} \sin \alpha_e$
\dot{X}_{w_w}	$\dot{X}_{w_b} \cos^2 \alpha_e - \dot{Z}_{u_b} \sin^2 \alpha_e - (\dot{X}_{u_b} - \dot{Z}_{w_b}) \sin \alpha_e \cos \alpha_e$
\dot{Z}_{w_w}	$\dot{Z}_{w_b} \cos^2 \alpha_e + \dot{X}_{u_b} \sin^2 \alpha_e - (\dot{X}_{w_b} + \dot{Z}_{u_b}) \sin \alpha_e \cos \alpha_e$
\dot{M}_{w_w}	$\dot{M}_{w_b} \cos \alpha_e - \dot{M}_{u_b} \sin \alpha_e$

Table 5.1 Formulae used for conversion of AVL body axes derivatives to wind axes for table 5.4 [38]. The subscripts ‘w’ and ‘b’ refer to wind and body axes respectively and α_e is angle of attack. These conversions may be applied to dimensional or non-dimensional derivatives of British or North American notation.

To assess the effectiveness of the wings and tail for control, the AVL models were defined such that the tail could be used as an elevator, while the aft 50% of the wing could be used as a hinged flap. Calculations were also run for various degrees of linear sweep and washout applied to the wings, to assess the effectiveness of these movements

for pitch control.

5.4.3.4 Wind tunnel derivative estimation

Longitudinal aerodynamic derivatives (in wind axes) were estimated from the wind tunnel data using table 5.2 which represent the North American conventions for these derivatives (used by AVL) [38]. Mach number, \tilde{M} , was estimated assuming an air temperature of 293 K (speed of sound = 343 m/s). The lift, moment and Mach number derivatives were estimated by linear fitting, while the drag derivatives were obtained based on the gradient of quadratic fits at the lift coefficient of the flight. The static margin, K_n , was dimensionalised by multiplication with the mean aerodynamic chord.

Derivative	Formula
C_{X_u}	$-(\tilde{M}C_{D_{\tilde{M}}} + 2C_D)$
C_{Z_u}	$-(\tilde{M}C_{L_{\tilde{M}}} + 2C_L)$
C_{M_u}	$\tilde{M}C_{M_{\tilde{M}}}$
C_{X_w}	$C_L - \frac{\partial C_D}{\partial \alpha}$
C_{Z_w}	$-(C_D + \frac{\partial C_L}{\partial \alpha})$
C_{M_w}	$\frac{\partial C_M}{\partial \alpha}$
K_n	$-\frac{\partial C_M}{\partial C_L}$

Table 5.2 Formulae used to calculate North American notation longitudinal derivatives from the wind tunnel data in wind axes [38].

Dynamic wind tunnel tests were not carried out, so the derivatives with respect to pitch rate, q , were estimated analytically, based on the assumptions used for conventional aircraft. The derivative C_{Z_q} was calculated using

$$C_{Z_q} = -2\overline{V_T}a_1, \quad (5.15)$$

where $\overline{V_T}$ is the ‘tail volume coefficient’ and a_1 is the lift slope of the tail. The tail volume coefficient was calculated using

$$\overline{V_T} = \frac{S_T l_T}{S \bar{c}}, \quad (5.16)$$

where S_T , l_T and \bar{c} are the tail planform area, the distance between the centre of mass and tail quarter-chord and the wing mean aerodynamic chord respectively. Estimates

of the relevant input values for equations (5.15) to (5.16) are shown in table 5.3.

Flight	O1	O2	O3	P1	P2	P3
S_T (m ²)	6.4×10^{-3}	6.4×10^{-3}	6.4×10^{-3}	2.1×10^{-2}	1.3×10^{-2}	1.4×10^{-2}
l_T (m)	0.150	0.150	0.150	0.145	0.145	0.145
A_T	1.0	1.0	1.0	1.1	0.6	0.6
a_1	1.48	1.48	1.48	1.61	0.92	0.92

Table 5.3 Inputs used to estimate C_{Z_q} and C_{M_q} from equations (5.15) to (5.18)

The variables S_T and l_T were estimated directly from measurements of the point clouds carried out in CloudCompare [143]. The lift slope of the tail was estimated using Helmbold’s equation for low aspect ratio lifting surfaces [3]

$$a_1 = \frac{\pi A_T}{1 + \sqrt{1 + \left(\frac{A_T}{2}\right)^2}}, \quad (5.17)$$

where A_T is the aspect ratio of the tail. There has been much debate, and limited consensus, about how to accurately estimate the lift of avian tails [84, 104–107], although a more recent contribution [107] suggested that this model is not unreasonable for low tail spread angles below 60° and angles of attack below 20°. Until improved aerodynamic models of avian tails are available however, it was felt this approach would provide numbers of at least the right order of magnitude. The derivative C_{M_q} was calculated using

$$C_{M_q} = \frac{l_t}{\bar{c}} C_{Z_q}, \quad (5.18)$$

with C_{Z_q} determined from equation (5.15).

5.5 Results

5.5.1 Validation

Figure 5.17 shows wind tunnel measurements of lift, drag and pitching moment coefficient versus angle of attack for flight O1 based on three repeats of each test point, for Reynolds numbers between approximately 70×10^3 and 170×10^3 . The order of magnitude of the pitching moment coefficients were similar to those from wind tunnel tests of extinct gliding animals and a model gull [80]. The maximum lift-to-drag ratio

derived from these measurements (figure 5.18) was lower than the equilibrium glides of a swift (*Apus apus*) [155], jackdaw (*Corvus monedula*) [152] and laggar flaon (*Falco jugger*) [151] suggesting that the barn owl is not aerodynamically efficient compared with other birds, although not as inefficient as suggested by Kroeger et al [202]. The repeatability of the pitching moment estimates was lower than the lift and drag, probably due to the lower repeatability of the drag-based contribution to pitching moment (equation (5.4) and figure 5.13). Assuming the bird was close to equilibrium resulted in a C_L estimate of $0.6^{+0.09}_{-0.07}$ based on the bird's weight, airspeed, glide angle, measured wing area and estimated air density. Field estimates of the bird's body angle of attack at the assumed close-to-equilibrium condition (see chapter 3 section 3.4.2 for details of method) resulted in an estimate of $5.1^\circ \pm 3.6^\circ$. The wind tunnel data were relatively close to these estimates and showed that the trimmed (i.e. $C_M = 0$) body angle of attack was approximately 6° with a corresponding C_L of 0.73. At an angle of attack of 6° the lift-to-drag ratio was also close to its maximum value (figure 5.18), which interestingly was relatively constant between 3° and 7° . Wind tunnel estimates of angle of attack and lift coefficient were likely to be more accurate than those obtained from video and anemometer data, and confirm video observations that barn owl was close to being trimmed. Given the consistency between flights observed in the video footage, it is reasonable to suggest that all the barn owl flights were close to trim. This assertion could also be made for the peregrine based on the video footage, however further wind tunnel testing would help to strengthen this conclusion.

The lift slope of 4.78 rad^{-1} (table 5.4) was within 3% of the theoretic estimate of 4.65 rad^{-1} for elliptical wings from lifting line theory

$$a = \frac{a_0}{1 + a_0/\pi A}, \quad (5.19)$$

where a_0 was assumed equal to 2π and A is the aspect ratio of the wing from chapter 3 table 3.1. Above 0° a linear least squares fits of pitching moment had positive gradients of between 1.05 rad^{-1} and 1.19 rad^{-1} depending on Reynolds number (table 5.4). Both the lift and pitching moment slopes were relatively insensitive to Reynolds number while drag coefficient gradually increased as Reynolds number decreased, at a given lift coefficient. This was not unexpected, given the increasing influence of viscous forces and skin friction drag at lower Reynolds numbers [3, 209].

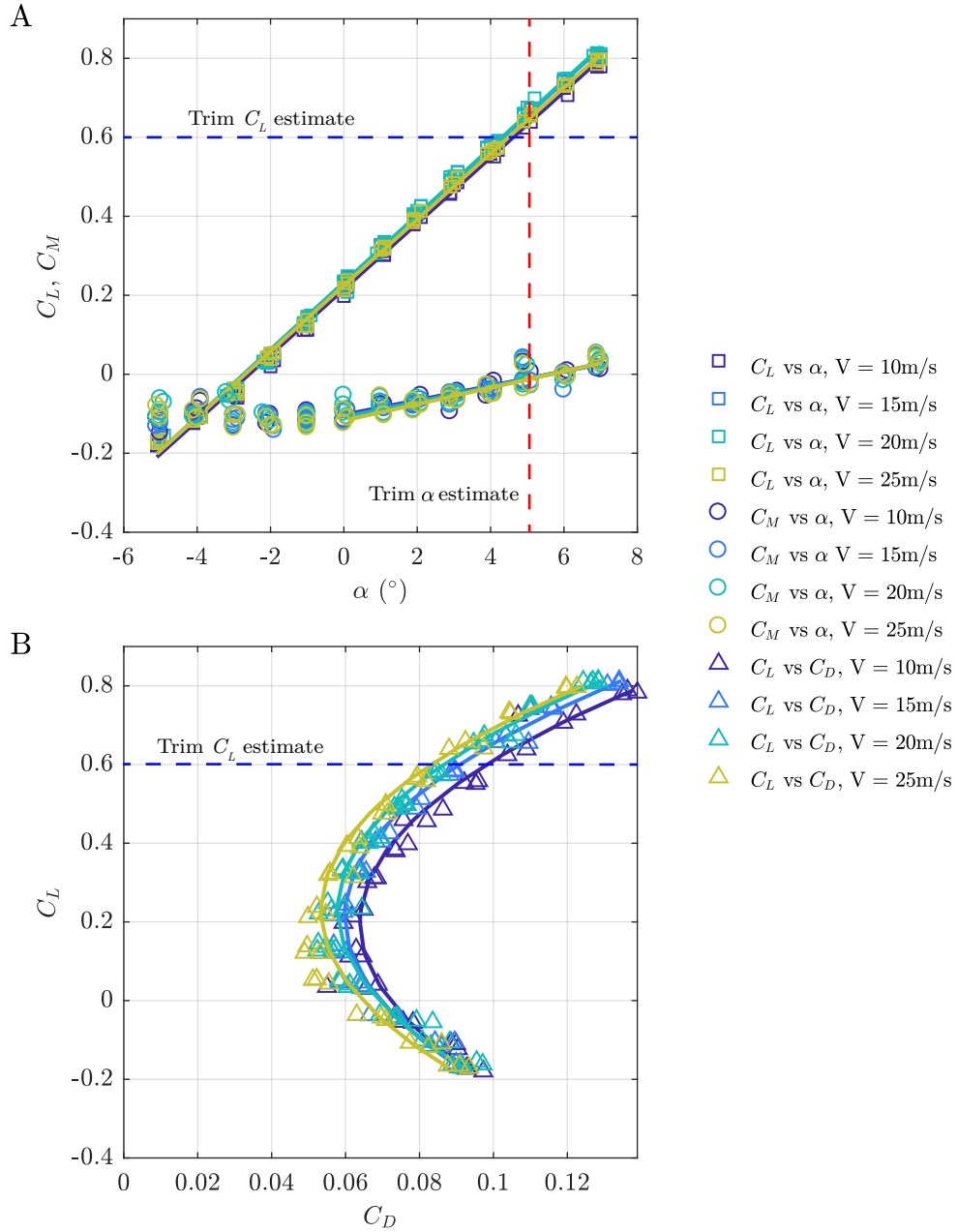


Fig. 5.17 Wind tunnel lift, drag and pitching moment measurements for flight O1 across a range of angles of attack and flow velocities ($\text{Re} = 70 \times 10^3$ to 170×10^3). Linear fits were applied to lift and moment coefficient, while a quadratic fit was applied to the drag polars. For the pitching moment coefficient, the linear fit was only applied to the data between 0° and 7° as some non-linearity is visible below this. All repeated measurements were used for each fit. Values of R^2 for the lift, moment and drag curves were greater than 0.99, 0.81 and 0.95 respectively, with error rms of less than 0.0165, 0.0201 and 0.0048 respectively. The biggest source of error was the repeatability of the drag and pitching moment measurements.

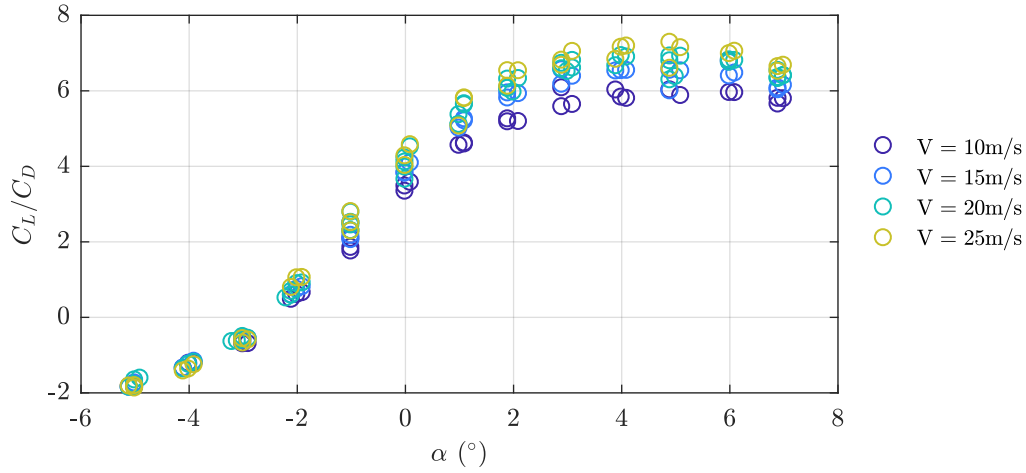


Fig. 5.18 Wind tunnel measurements of lift-to-drag ratio for flight O1 between Reynolds numbers of approximately 70×10^3 (10m/s) and 170×10^3 (25m/s).

Figure 5.19 shows AVL estimates of lift, drag and pitching moment coefficients versus angle of attack for flight O1 based on coarse, medium and fine lattice resolution. The numerical errors were negligible, except for lift coefficient at $\alpha = 5^\circ$ where the increased error was due to almost identical values for the coarse and fine grids, resulting in a low order of convergence for this point. Error bars were not plotted with AVL data for subsequent figures due to the negligible values observed here.

Figure 5.20 compares wind tunnel and AVL estimates of the lift, drag and pitching moment of flight O1 between angles of attack of -5° and 7° . The wind tunnel data were plotted based on the Reynolds number closest to the actual flight of approximately 70×10^3 (10m/s). Table 5.4 provides the actual values of lift and moment slope, trim angle of attack (based on C_L required for steady flight) and the drag and moment coefficients for the trimmed C_L . AVL over-predicted lift coefficient and nose-down pitching moment coefficient compared with the wind tunnel data (figure 5.20A). The AVL model was therefore not trimmed, in contrast with the wind tunnel data which showed that the barn owl was very close to equilibrium during flight O1. The higher accuracy of the wind tunnel data (a real flow) compared with the AVL model (inviscid, thin lifting surfaces, low angles) suggested that the absolute values of AVL lift and pitching moments should be used with caution. In contrast, the lift and pitching moment slopes between AVL and the experimental data were in close agreement (see figure 5.20 and table 5.4).

An interesting feature of figure 5.20, which was observed for all Reynolds num-

bers tested (figure 5.17), was the flattening out of the pitching moment vs. angle of attack below approximately 0° . One of the important assumptions in chapter 3 section 3.6.2 was that the pitching moment slope was linear with angle of attack. In this prior discussion, it was assumed that given a linear moment slope, geometric features contributing towards the zero-lift pitching moment could be used to infer longitudinal static stability without knowing the relative positions of the centre of mass and neutral point. With these assumptions, an unstable configuration required a nose-down zero-lift pitching moment and vice-versa, to be able to trim. From figure 5.17, the zero-lift pitching moment is clearly negative, consistent with the expectation of chapter 3. However, while the non-linearity in the moment slope does not necessarily negate the validity of the discussion in chapter 3, it does lead to the conclusion that any inferences about longitudinal static stability from shape alone should be held tentatively. Inferring longitudinal static stability from geometry is a useful starting point for stability analysis of gliding birds, but cannot replace the more rigorous approach of measuring the relative positions of the centre of mass and neutral point.

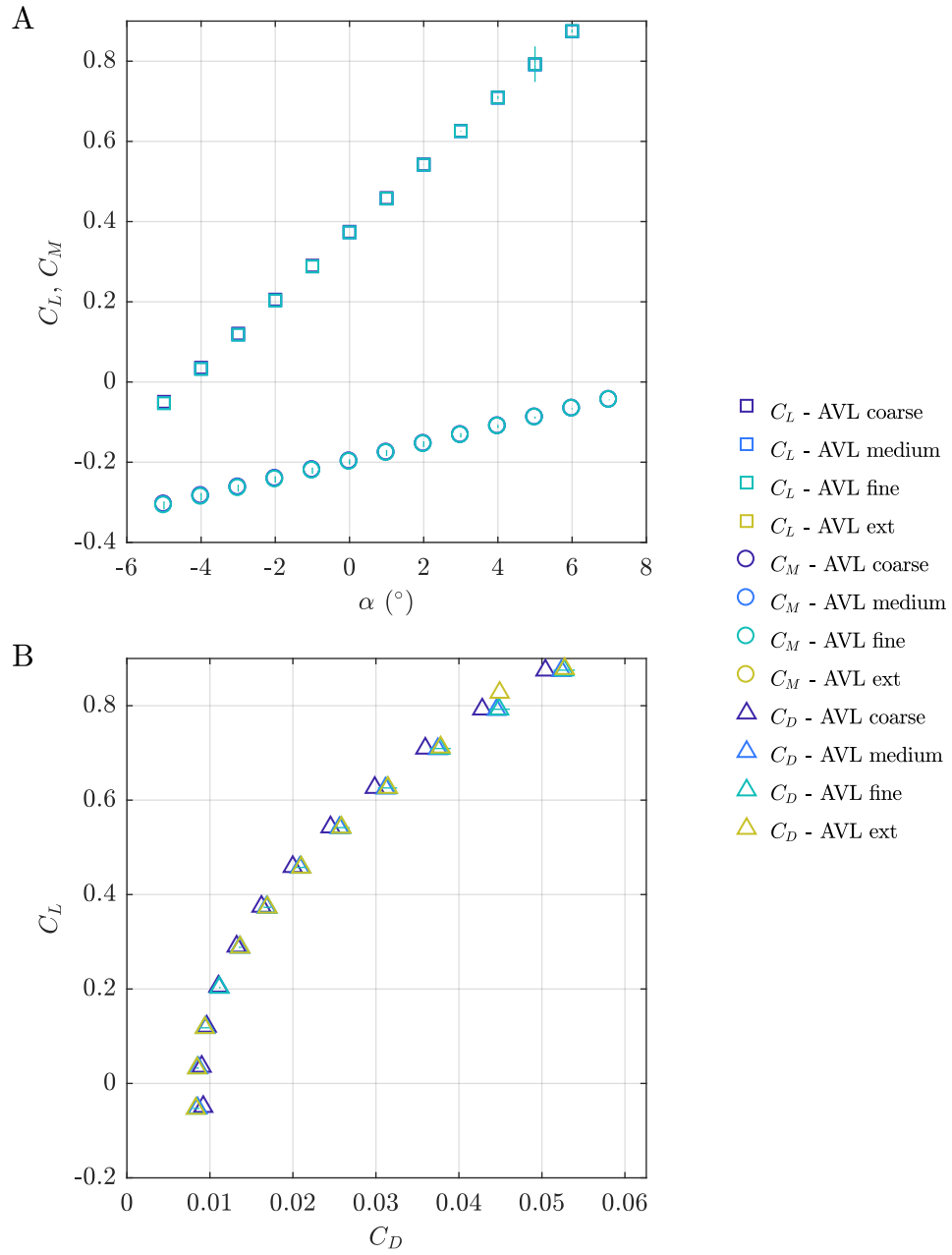


Fig. 5.19 AVL generated lift, drag and pitching moment for flight O1 based on 15 sections per wing showing error bars estimated using the grid convergence index from Richardson's extrapolation for coarse, medium and fine lattice spacing. The estimated discretisation errors were so small in most instances that they are not easily visible. Drag was based on the far-field estimate.

The accuracy of these slopes was important for flight stability analysis, however, an initial trim condition was still required because lateral-directional derivatives are sensitive to lift coefficient. The flight dynamics analysis was therefore carried out using the nominal lift coefficient of each flight, with sensitivity studies undertaken for $C_{Ltrim} \pm 0.1$ (see section 5.5.5). The degree of sensitivity was considered reasonable given the level of agreement between the wind tunnel and field data estimates of lift coefficient (section 5.5.1). The AVL overestimate of lift was similar to a recent study [189], with the lack of viscous effects being the likely cause. In a real flow, the boundary layer thickens in the stream-wise direction, reducing the effective camber experienced by the freestream, thus reducing lift. Lift coefficient increases of similar magnitude were observed through the use of a panel method [210] to compare viscous and inviscid aerofoil lift for a NACA 3403 (somewhat resembling a hand wing section) at $Re = 70 \times 10^3$. Over-estimations of nose-down pitching moment were probably for the same reasons as the over-estimation of lift; increased effective camber would increase the nose-down pitching couple. AVL under predicted drag because, being an inviscid flow model, it does not capture profile or parasite drag. The discrepancy between AVL (induced drag) and the wind tunnel results (total drag) was very similar to those measured for a common swift (*Apus apus*) [155] and jackdaw (*Corvus monedula*) [152]. Estimations of the profile and parasite drag contribution to pitching moment showed that although these were nose-up (the centre of mass was below the neutral point by approximately 13 mm), they were less than $0.01 C_M$.

Although there were discrepancies (approx. $+0.1 C_L$ and $-0.1 C_M$) in the absolute estimates of lift, drag and pitching moment (figure 5.20), the derivatives of most importance to flight dynamics (lift and pitching moment) were in close agreement (table 5.4). In addition to absolute values, Table 5.4 shows the non-dimensional longitudinal derivatives referred to wind axes, calculated using tables 5.1 and 5.2. Table 5.4 also compares AVL results with and without the inclusion of a thick body/torso (these terms are used interchangeably). The lift slope was almost perfectly matched between the wind tunnel and AVL model with a thick body, whereas the thin body model underestimated it by approximately 11%. The AVL estimates of moment slope were also sensitive to the inclusion of the thick body, with both models being approximately 20% from the wind tunnel estimate at 10 m/s (table 5.4). Given the closer agreement in lift slope for the thick torso model, and the obvious fact that the real birds had a thick torso, all subsequent results were based on a thick body.

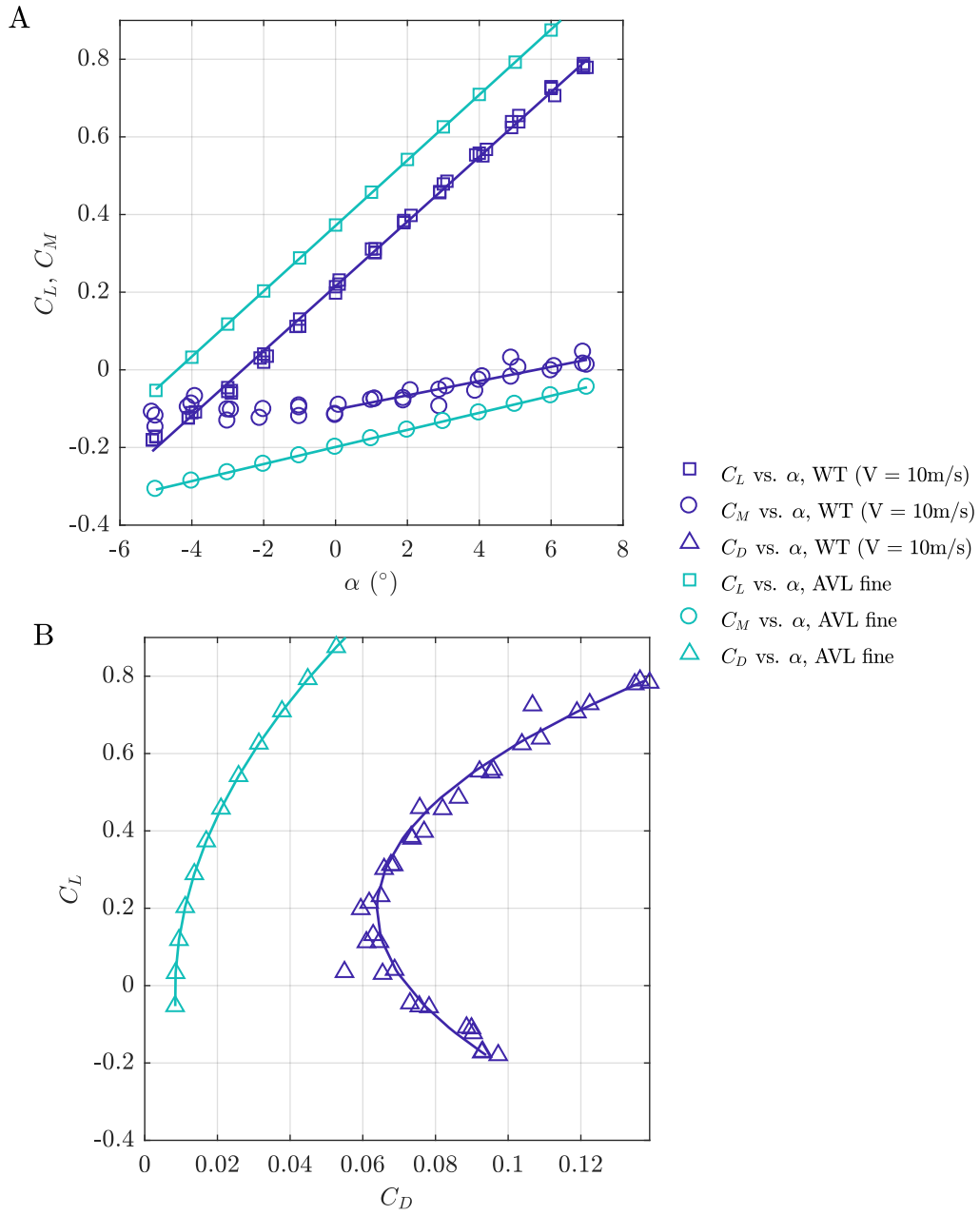


Fig. 5.20 Comparison of wind tunnel measurements and AVL estimates (thick torso/body) of lift, drag and pitching moment coefficient across a range of angles of attack for flight O1. The wind tunnel data shown corresponds to the Reynolds number of the flight. Linear fits are shown for the lift and moment coefficient data (only $\alpha > 0^\circ$ for the C_M) while quadratic fits are shown for the drag polars. Drag was based on the far-field (Trefftz plane) estimate.

	WT ($V = 10$ m/s)	WT ($V = 25$ m/s)	AVL (thick torso)	AVL (thin torso)
$\partial C_L / \partial \alpha$	4.78	4.79	4.79	4.29
$\partial C_M / \partial \alpha$	1.05	1.19	1.26	0.85
$K_n \bar{c}$ (mm)	-27.8	-31.4	-33.1	-25.0
α ($^\circ$)	4.56	4.43	2.63	2.72
C_M	-0.0188	-0.0253	-0.140	-0.121
C_D	0.0973	0.0824	0.0278	0.0285
$\partial C_D / \partial C_L$	0.1679	0.1586	0.0484	-
$\partial C_D / \partial \alpha$	0.8018	0.7592	0.232	-
C_{X_u}	-0.1848	-0.1402	-0.2036	-0.1923
C_{Z_u}	-1.1968	-1.1200	-1.1900	-1.1900
C_{M_u}	-0.0041	-0.0102	-0.2803	-0.2419
C_{X_w}	-0.2068	-0.1642	0.3609	0.3179
C_{Z_w}	-4.8729	-4.8697	-4.9769	-4.4823
C_{M_w}	1.0519	1.1921	1.2574	0.8501

Table 5.4 Comparison between wind tunnel (WT) and Athena Vortex Lattice (AVL) estimated non-dimensional derivatives. Wind tunnel results are shown for the minimum and maximum Reynolds numbers tested for comparison. AVL results are shown for input geometry with and without the incorporation of a thick torso. All data were referred to wind axes using table 5.2 at $C_L = 0.595$ from chapter 3 table 3.1.

The AVL derivatives were of reasonable accuracy with the exception of C_{X_w} , C_{M_u} and the drag derivatives, $\partial C_D / \partial C_L$, $\partial C_M / \partial \alpha$. From figure 5.20 it was clear that under-estimates of the drag derivatives were due to the lack of profile drag in the AVL model. The over-estimation of C_{X_w} was due to the under-estimation of $\partial C_D / \partial \alpha$ (see table 5.2). The non-zero AVL values of C_{M_u} were surprising given that this derivative is concerned with Mach number effects [38], that should be negligible for low-speed avian flight, as shown from the wind tunnel estimates. Although dynamic wind tunnel testing was not carried out, analytical estimates of C_{X_q} , C_{Z_q} and C_{M_q} in wind axes were made using equations (5.15) to (5.18) [38, 96]. For conventional aircraft, C_{X_q} is negligible if the rate of tail drag with angle of attack is very small [38]. There was a significant difference between the AVL and analytical estimates of C_{Z_q} that may have been due to the differences between birds and conventional aircraft, such as the

	Analytical estimate	AVL (thick body)	AVL (thin body)
C_{X_q}	0	-0.0619	-0.0328
C_{Z_q}	-0.1932	-4.0535	-4.0993
C_{M_q}	-0.2300	-0.7658	-0.6534

Table 5.5 Comparison between analytical estimates of C_{X_q} , C_{Z_q} and C_{M_q} with AVL estimates for flight O1.

generally smaller tail area and moment arm in birds. There was better agreement for C_{M_q} (i.e. correct order of magnitude), however, it was still more than three times the analytical estimate.

To check the sensitivity of the longitudinal dynamics to these derivatives, dynamic models were created with analytical and corrected estimates of C_{X_w} , C_{X_q} , C_{Z_q} and C_{M_q} , replacing the AVL estimates. The derivative C_{X_w} was updated using table 5.2, with lift coefficient obtained from chapter 3 table 3.1 and the drag derivative obtained using the wind tunnel data for flight O1 (this was done for all flights). The updated values of C_{M_u} and C_{X_q} were set to zero. These derivative ‘updates’ had a negligible influence on longitudinal stability (see section 5.5.3). In summary, the longitudinal derivatives estimated by AVL were likely to result in accurate descriptions of the system dynamics for small perturbations about trim for flight O1. Assuming this flight is representative of the others, this provides reasonable grounds for trusting the longitudinal dynamics presented in sections 5.5.2 and 5.5.3.

5.5.2 Longitudinal static stability and control effectiveness

Figure 5.21 shows AVL estimates of the neutral point position for all flights with a thick body, along with estimates of the centre of mass position repeated from chapter 4 figure 4.17. The close agreement between the lift and moment slopes for the wind tunnel and AVL data resulted in close agreement regarding the static margin (table 5.4). However, comparison with the Reynolds number of the actual flight shows that AVL underpredicted the static margin by approximately 5 mm or 4% mean aerodynamic chord. This would have the effect of making the birds slightly more unstable compared with the real viscous flow, although this could also be partly due to the lower repeatability of the wind tunnel pitching moment results.

For all flights, the neutral point was forward of the centre of mass, indicating that the configurations were longitudinally statically unstable [38]. Table 5.6 provides

the dimensional and non-dimensional estimates for the values plotted in figure 5.21. The static margin was relatively fixed for the barn owl flights, but became increasingly negative (a change of 16% chord or 16 mm) between peregrine flights P1 and P3, as the wings were retracted and the tail adducted (furled). The change in static margin was similar between P1 and P2 compared with P2 and P3 (8% and 5% chord or 8 mm). These changes are explained by comparing the planforms (figure 5.21) and lift distributions (figure 5.22) across these three flights. As expected from their highly positive angles of attack, the peregrine's tail generated positive lift. The neutral point is defined as the point about which pitching moment remains constant with changes in angle of attack (within the linear region of the lift slope). Therefore, the reduction in tail area and lift in P2 (and P3) compared with P1, and the forward sweep of the wing proximally where loading was highest, required the forward movement of the neutral point. In P3 the tail was slightly less furled, the arm wing was slightly further forward and the primaries were more aft-swept (especially for the left wing) than P2. The continued forward movement of the neutral point between P2 and P3 was due to a reduction in the lift slope caused by the reduced aspect ratio combined with the small continued forward movement of the wing proximally due to the increased retraction.

Table 5.7 shows estimates of the centre of mass and wing aerodynamic centre obtained using a similar approach to Thomas and Taylor [76]. Comparison is made with the AVL and CT estimates to show where the differences exist. The centroid of the full planform gave an inaccurate estimate for centre of mass, with errors of 21 mm, 37 mm and 39 mm for O1, P1 and P3 respectively (17%, 36% and 36% mean aerodynamic chord). Differences between AVL estimates of the neutral point and the planform-based wing aerodynamic centre were 13 mm, 6 mm, 25 mm respectively (10%, 6% and 23% mean aerodynamic chord). These significant differences show that the simplifications made with this approach do not yield accurate estimates of the static margin, however, for these cases they do answer the basic question of whether the birds were longitudinally statically stable or unstable. The reason for the significant error of the planform based approach is likely due to (i) the lack of inclusion of the tail in the estimation of the neutral point (ii) the lack of spanwise loading information (iii) the uniform density assumption inherent in the estimation of the centroid.

Figure 5.22 shows the spanwise loading of the wing and tail for all flights. In general, the barn owl flights (O1-O3) had a relatively even loading distribution across each wing, with a sharp decline at the wing tips. Each distribution emphasises the complex wing geometry described in chapter 3, including asymmetries between the

wings. The peregrine's loading distribution contrasted with the barn owl, exhibiting more symmetric and bell-shaped distributions, with higher loading proximally and reduction distally. All flights had lift generating tails, although for P2 the loading was small. Across the torso the loading generally reduced slightly due to the lack of camber, but this depended on the relative angle between the entire wing and the torso (angle of incidence), and the angle of attack of the body, which was higher in O3. For example, in O1, P1 and P3 the torso incidence was less than the mean wing angle of attack (see chapter 3 table 3.1) so its lack of camber resulted in a reduction in loading. In the remaining flights (O2, O3 and P2) the torso was at a higher angle than the mean wing, helping to maintain loading. The complexity of the loading distributions reflects the complex variations in spanwise camber, twist, thickness and dihedral explored in chapter 3, and further draws attention to the overall angle between the complete wing and the torso. The asymmetries correspond nicely with the nullification of the roll rates observed in the video footage (see chapter 3 sections 3.5.1 and 3.6.3).

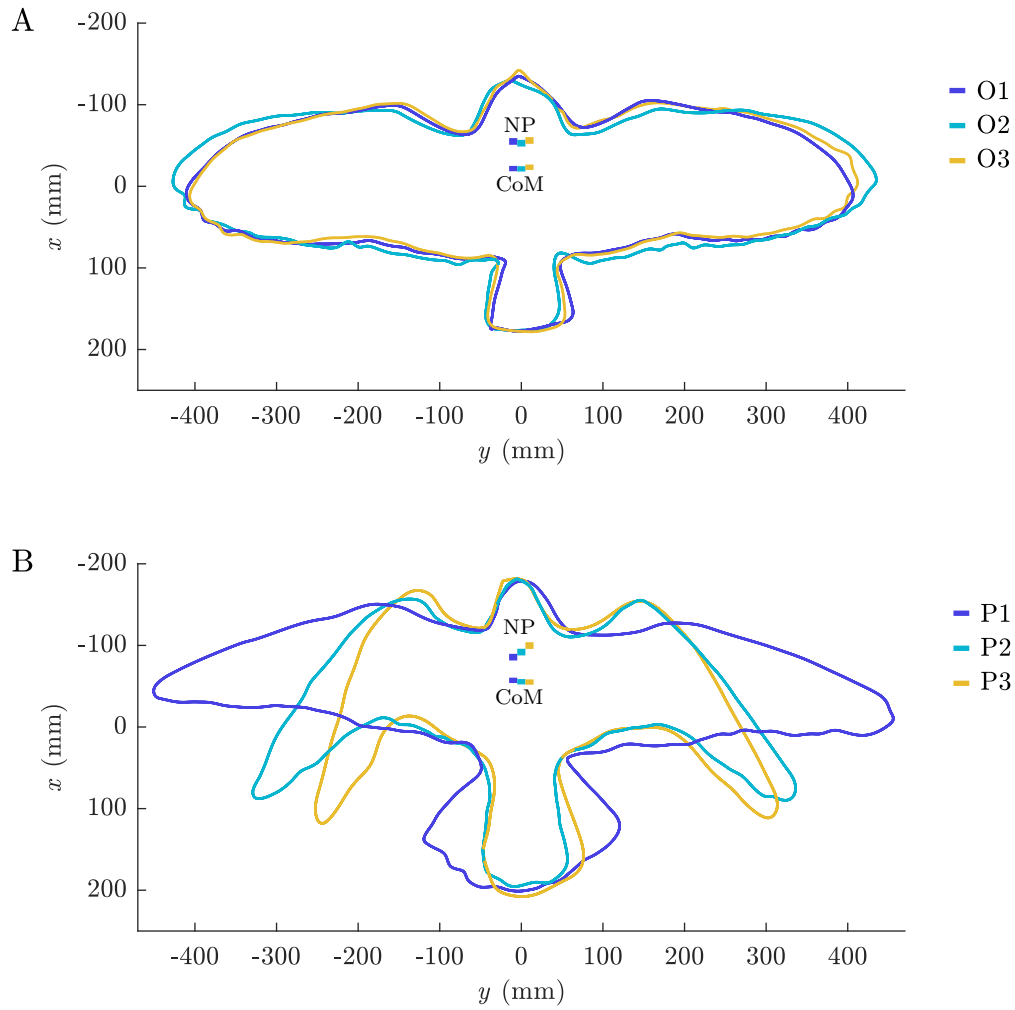


Fig. 5.21 AVL estimates of the static margin for the barn owl (O1-O3) and peregrine (P1-P3) flights, shown as the relative position of the centre of mass (CoM) and neutral point (NP). This plot is equivalent to figure 4.17 in chapter 4 with the neutral point location added. The neutral point and centre of mass spanwise offset in the spanwise direction are to aid visualisation only.

Flight	O1	O2	O3	P1	P2	P3
$K_n \bar{c}$ (mm)	-33.2	-31.4	-32.8	-28.3	-36.0	-44.3
K_n	-0.26	-0.24	-0.26	-0.27	-0.35	-0.40

Table 5.6 AVL estimates of the static margin. The negative values indicate that the centre of mass was aft of the neutral point.

Flight	O1	P1	P3
CoM - planform (mm)	-1	-20	-16
CoM - CT (mm)	-22	-57	-55
Aerodynamic centre - planform (mm)	-42	-80	-75
Neutral point - AVL (mm)	-55	-86	-100
Static margin - planform (mm)	-41	-60	-59
Static margin - AVL and CT (mm)	-33	-29	-45

Table 5.7 Estimates of the centre of mass and neutral point using the planform only, with the wing aerodynamic centre determined as wing area over wing span and centred upon the centre of area of the wing [76]. Centre of mass was estimated as the centroid of the full outline of the bird, including the head, wings and tail. AVL estimates of static margin are shown to the nearest millimetre for comparison.

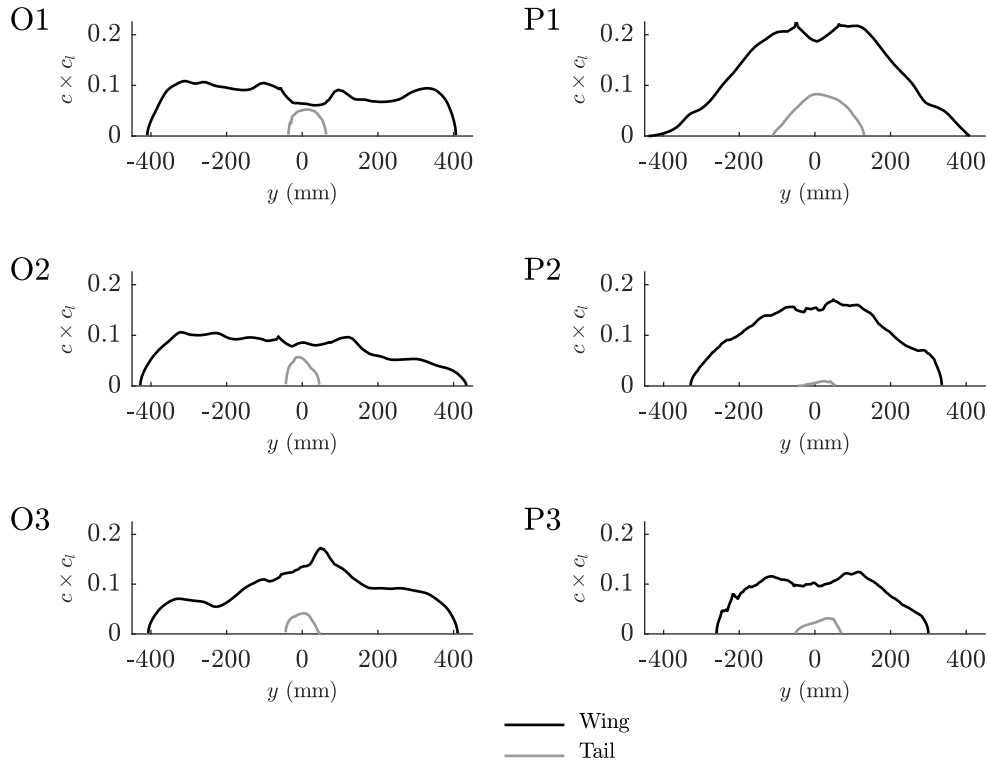


Fig. 5.22 AVL estimated spanwise loading of the wing and tail for the barn owl (O1-O3) and peregrine (P1-P3) flights.

Figure 5.23 shows AVL estimates of pitch control effectiveness, based on the use of the tail as an elevator, a 50% chord trailing edge flap across both wings and linear

spanwise sweep and twist adjustments. The data are shown dimensionally to illustrate differences in control moments between flights and birds. A furled tail (O1-O3, P2, P3) was significantly less effective for pitch control than an unfurled tail (P1). The peregrine’s longer furled tail was more effective than the barn owl’s short furled tail (compare O1-O3 with P2 and P3), in contrast to Hummel [79], who found that tail length made no difference to control effectiveness. Changes in wing camber or sweep were effective for pitch control in the barn owl. For the peregrine, the effectiveness of wing sweep reduced as the wings were retracted and vice versa for the effectiveness of camber. Varying wash-out was generally least effective for pitch control. Comparison between P1, P2 and P3 clearly shows that control effectiveness is dependent on the overall configuration adopted by the bird. The control inputs used for manoeuvring or stabilisation of flight might therefore depend on the configuration adopted by the bird.

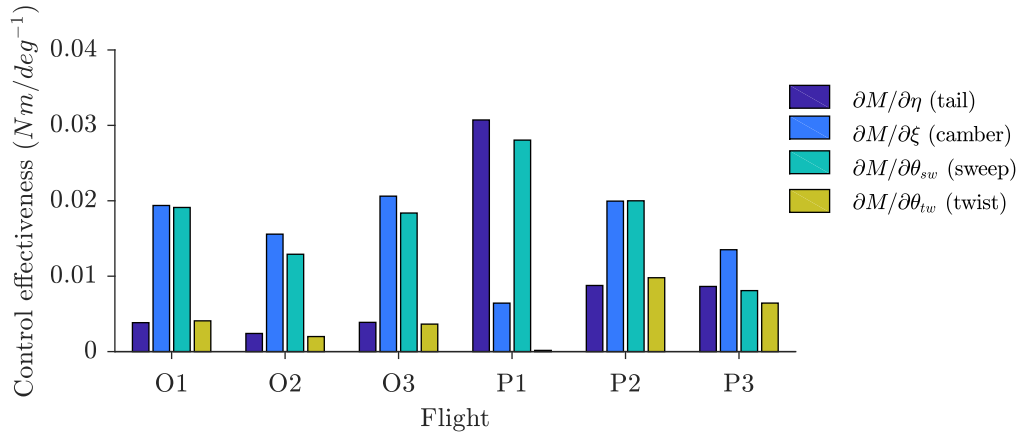


Fig. 5.23 AVL estimates of pitching moment control derivatives based on the tail used as an elevator with rotation angle, η , a trailing edge flap hinged at 50% chord across the full span of each wing with rotation angle, ξ , to simulate camber. Adjustments to sweep angle (root to tip), θ_{sw} , and linearly distributed wash-out, θ_{tw} , are also shown.

5.5.3 Longitudinal dynamic modes

Conventional aircraft usually exhibit two longitudinal modes: the ‘short period’ and ‘phugoid’ [38]. The short period mode is a higher frequency, well damped pitching oscillation, while the phugoid mode is a much lower frequency, lightly damped oscillation. Both may be excited by pitch perturbations or control inputs.

Figure 5.24 shows root-locus plots of the eigenvalues corresponding to the de-coupled longitudinal modes for each flight. For a summary of the interpretation of root locus plots, see section 5.4.3.2. The difference between the coupled and de-coupled estimations of these modes was negligible. Conventional subsonic aircraft typically feature two complex modes with negative real parts corresponding to the stable short-period and phugoid modes respectively; sometimes the phugoid is marginally unstable. However, since both the barn owl and peregrine were longitudinally statically unstable (figure 5.21), the short period pole (complex, oscillatory mode) divided into two zeros (real, non-oscillatory modes), one stable, one unstable. From here on, the unstable mode is referred to as the ‘pitch divergence mode’, while the stable mode is unnamed because it has no practical relevance in terms of the system dynamics during flight. For unstable aircraft, the complex mode is called the ‘third oscillatory mode’ and typically has similar natural frequency to the phugoid, but with damping similar to the short-period mode [71]. For the birds, the third oscillatory mode was very similar to the phugoid mode of conventional configurations, based on comparison with a reduced order model (equation (5.20)) of the phugoid

$$\begin{aligned}\omega_p &= \frac{g\sqrt{2}}{V}, \\ \zeta_p &= \frac{C_D}{\sqrt{2}C_L},\end{aligned}\tag{5.20}$$

where ω_p and ζ_p are the damped natural frequency and damping coefficient of the mode, g is gravitational acceleration, V is airspeed and C_L and C_D are the coefficients of lift and drag respectively. The results of the reduced order model are presented in table 5.8 [38] where they are compared with the third oscillatory mode. The third oscillatory mode was only mildly sensitive to the updated longitudinal derivatives discussed in section 5.5.1.

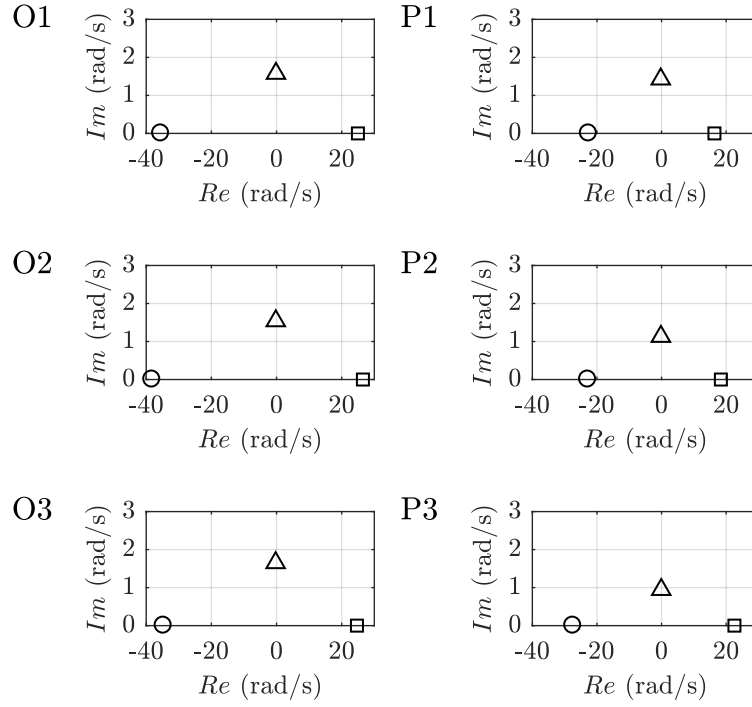


Fig. 5.24 Root-locus plots showing the de-coupled longitudinal modes modelled with a thick body for the barn owl (O1-O3) and peregrine (P1-P3) flights. The triangle corresponds to the third oscillatory mode, while the short-period mode typical of conventional aircraft is split into highly stable (circle) and highly unstable (square) real modes. The unstable mode is referred to here as the ‘pitch divergence mode’.

	O1	O2	O3	P1	P2	P3
$\omega_{original}$ (rad/s)	2.30	2.39	2.27	1.63	1.00	0.95
$\omega_{updated}$ (rad/s)	1.58	1.54	1.65	1.43	1.13	0.95
$\omega_{reduced}$ (rad/s)	1.59	1.56	1.67	1.45	1.16	0.96
$\zeta_{original}$	0.103	0.105	0.101	0.158	0.134	0.073
$\zeta_{updated}$	0.115	0.153	0.171	0.174	0.180	0.102
$\zeta_{reduced}$	0.121	0.133	0.109	0.148	0.117	0.108

Table 5.8 Comparison between a reduced order model of the phugoid mode with the third oscillatory mode, based on updated and original derivative estimates. The closer match between the updated results and the reduced order model is because their assumptions match more closely.

Comparison of the original and updated root locus plots (compare figures E.1 and 5.24) in Appendix E shows that updating the original estimates of the longitudi-

nal derivatives (see section 5.5.1) did not significantly affect the modes. This shows that even if the updates were inappropriate, their effect on the longitudinal modes was small, at most changing the frequency of the third oscillatory mode from 0.36 Hz to 0.25 Hz for flight O1. Figure 5.25 shows the time-history of the pitch divergence mode using flight O1 as a representative example (see Appendix figure E.3 for all flights). The time constant of a non-oscillatory mode is the inverse of its eigenvalue, revealing that the pitch divergence mode diverges rapidly, with the bird approaching stall (assumed to be approximately 10° - 15°) within approximately 100 ms. The exponential time constant, τ , can be converted to ‘time to double’, T_2 , using equation (5.21):

$$T_2 = \tau \ln 2. \quad (5.21)$$

The time history of the stable, non-oscillatory mode was the convergent equivalent of the pitch divergence mode, but with a different time period. As stated previously, this mode has little (if any) practical relevance during flight.

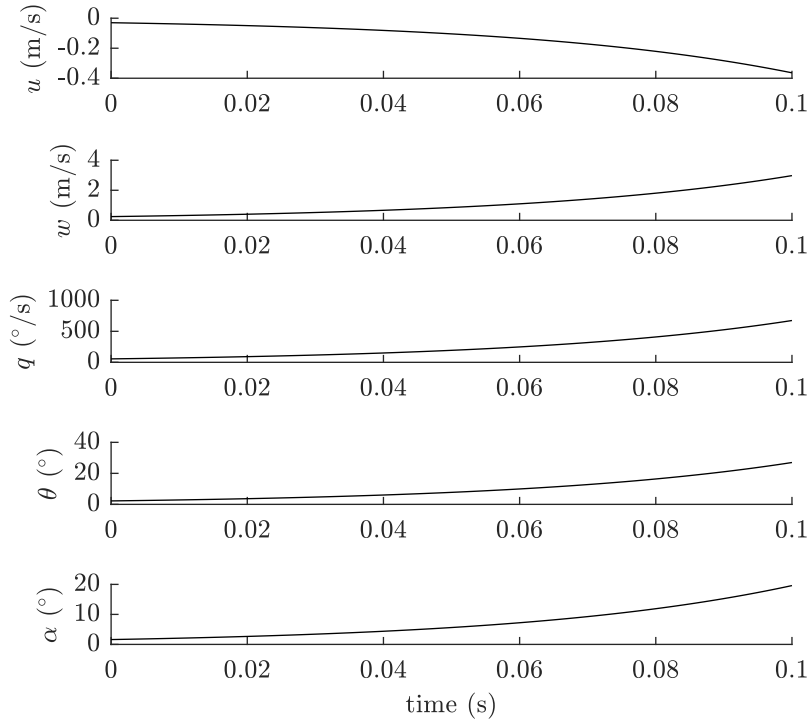


Fig. 5.25 Time-history for the highly unstable pitch divergence mode (see figure 5.24) illustrated using barn owl flight O1 showing perturbations in body axis coordinates of forward velocity, u , vertical velocity, w , pitch rate, q , pitch attitude, θ , and geometric angle of attack, α , from the initial flight condition.

	Pitch divergence mode	Third oscillatory mode
u	0.0640	0.7299
w	-0.4095	0.0509
q	-0.9011	0.1638
θ	-0.0552	-0.0052

Table 5.9 Eigenvectors for the pitch divergence mode and third oscillatory mode for flight P1. Comparing the relative magnitudes of the state variables, u , v , q and θ between and within each mode indicates the relative dominance of the state in the resulting motion.

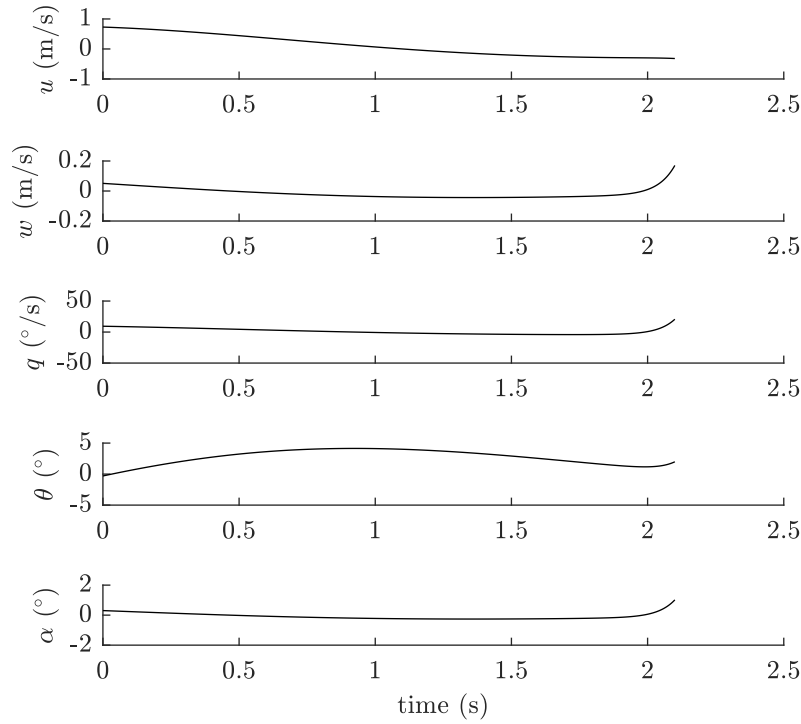


Fig. 5.26 Time-history for the third oscillatory mode illustrated with peregrine flight P1 showing perturbations in body axis coordinates of forward velocity, u , vertical velocity, w , pitch rate, q , pitch attitude, θ , and geometric angle of attack, α , from the initial flight condition. The pitch divergence mode is excited after half a time-period.

The time history of the third oscillatory mode is shown in figure 5.26 for peregrine flight P1, as a representative example (see figures E.4 and E.5 for additional flights). After approximately 2 s (half a time-period) the pitch divergence mode rapidly begins to dominate due to the gradual accumulation of numerical error in the states; this mode is highly sensitive to perturbation and has highly dominant values of q and w

in its eigenvector (see table 5.9).

5.5.4 Lateral-directional stability

Lateral-directional dynamics were more complex than the longitudinal dynamics due to coupling between roll and yaw. Conventional aircraft usually exhibit three lateral-directional modes: roll subsidence, spiral and dutch roll mode [38]. The roll subsidence mode consists of a non-oscillatory rolling motion, and is usually inherently stable through positive dihedral, aft-sweep or a high wing. The spiral mode is a very slow, non-oscillatory mode involving gradually increasing sideslip, roll and yaw (if unstable) which if left unchecked leads to a catastrophic, diverging spiral descent. In conventional aircraft, the spiral mode is influenced by the vertical fin size and wing dihedral. The dutch roll mode is a damped oscillation in yaw, roll and sideslip also influenced by the vertical fin and the shape of wing.

Table 5.10 shows AVL estimates of the lateral-directional derivatives alongside the modes over which they have most influence [38]. The role of these derivatives described by Cook [38] informs the following discussion. The roll subsidence mode is dominated by the ‘roll-damping’ derivative, C_{l_p} . This derivative was negative for all flights (aerodynamic roll moment opposed roll rate), implying a stable roll subsidence mode. This is usually the case, and is caused by restorative lift asymmetry due to roll rate, p . The spiral mode is most affected by C_{l_v} , C_{n_r} , C_{l_r} and C_{n_v} . The first of these, C_{l_v} , represents the roll moment due to sideslip velocity, and is commonly referred to as the ‘dihedral effect’. In positive sideslip, dihedral results in a negative rolling moment that restores the wings to the horizontal position following a roll disturbance. However, C_{l_v} is also influenced by wing sweep and the dorsoventral position of the wing relative to the body. For example, an aft-swept wing generates restorative rolling moments in the presence of sideslip due to the difference in lift between the wings. A high wing experiences asymmetric angle of attack near the root due to the distortion of the lateral component of flow during sideslip from the presence of the body/fuselage. This effect contributes towards a stable C_{l_v} , but was clearly insufficient for O1, O2 and P1 compared with other destabilising features such as wing anhedral. C_{l_v} may have been stable for P2 and P3 due to their high degree of aft sweep distally. Flight O3 had only very slightly negative C_{l_v} , and the change in sign relative to O1 and O2 suggests that this derivative was quite sensitive to subtle changes in wing shape and trim condition. The derivative, C_{n_r} , is the ‘yaw-damping’ derivative and, for all flights, provided a restorative yawing moment due to yaw rate. The roll moment

due to yaw rate, C_{l_r} , was positive for all flights, and results from the differential lift between the wings. Weathercock stability is indicated by C_{n_v} , the yawing moment due to sideslip velocity, and is positive when stable. The barn owl flights showed unstable weathercock stability while the peregrine was stable, confirming the sensitivity of this derivative to changes in distal wing sweep [85–88]. For conventional aircraft, a stable spiral mode is indicated by

$$C_{l_v}C_{n_r} > C_{l_r}C_{n_v}. \quad (5.22)$$

Comparing these derivatives in table 5.10 shows that this condition was only met for O3, leading to the expectation of an unstable spiral mode for most flights. In conventional aircraft, the dutch roll is mainly influenced by C_{n_r} , C_{n_v} and C_{Y_v} . Side-force due to the sideslip, C_{Y_v} , was stabilising because it is mainly influenced by drag acting on the fuselage/torso. Values of the yaw damping derivative and yaw moment due to sideslip, C_{n_r} and C_{n_v} , were likely small compared with conventional aircraft due to the lack of vertical tail, which may have resulted in the lack of dutch roll mode (see figure 5.27 below). For all flights, estimates of C_{n_v} increased in the absence of a thick torso, such that the weathercock stability of the barn owl became stable. This was consistent with the known influence of the fuselage to destabilise yaw in conventional aircraft, and the requirement for a vertical fin for weathercock stability [71].

	C_{l_v}	C_{n_r}	C_{l_r}	C_{n_v}	C_{l_p}	C_{Y_v}
O1	0.0524	-0.0104	0.1470	-0.0113	-0.410	-0.151
O2	0.0436	-0.0034	0.0823	-0.0112	-0.421	-0.131
O3	-0.0051	-0.0028	0.0780	-0.0192	-0.406	-0.128
P1	0.0962	-0.0106	0.0793	0.0143	-0.446	-0.378
P2	-0.0036	-0.0022	0.1300	0.0276	-0.365	-0.297
P3	-0.0159	-0.0047	0.1190	0.0108	-0.332	-0.253
roll subsidence					✓	
spiral	✓	✓	✓	✓		
dutch roll		✓		✓		✓

Table 5.10 AVL estimation of the non-dimensional body axes derivatives most influential to the lateral-direction modes for the barn owl (O1-O3) and peregrine (P1-P3) flights. The derivatives were estimated at the C_L of each flight and are colour based on whether they are stabilising (green) or destabilising (red). The relevance of these derivatives to the lateral-directional modes of conventional aircraft are indicated.

Figure 5.27 shows the root-locus plot for the coupled, lateral-directional modes modelled with a thick central torso in AVL, with corrections applied to the erroneous concise derivative conversions (see Appendix D). All flights showed a strongly negative real mode representing the roll subsidence mode, consistent with the negative values of C_{l_p} (time-histories shown in figure E.6). These estimates for a highly stable roll subsidence mode matched closely those calculated using the reduced order model in Cook [38] (see Appendix E table E.1).

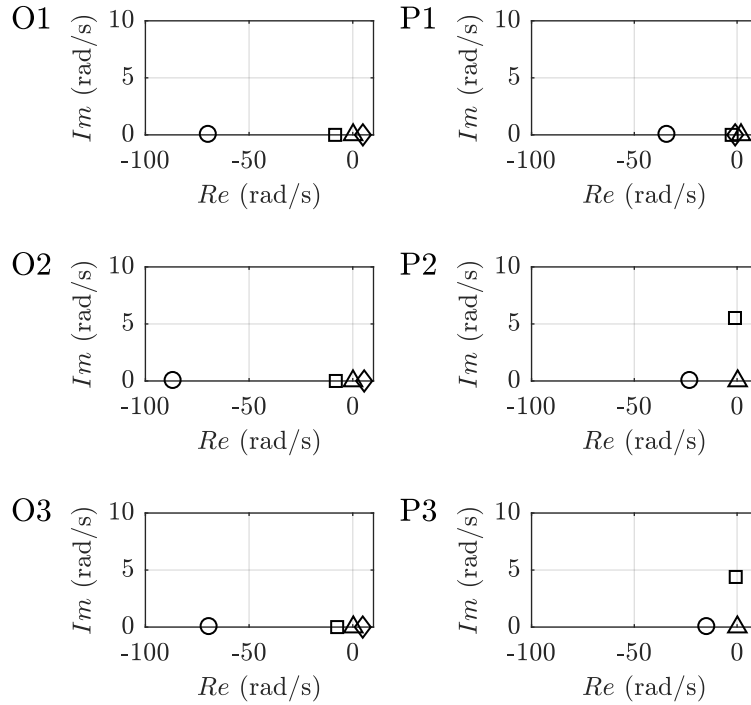


Fig. 5.27 Root-locus plots showing the coupled, lateral-directional, corrected AVL modes modelled with a thick torso for the barn owl (O1-O3) and peregrine (P1-P3) flights. The circle represents the roll-subsidence mode, the triangle represents the spiral mode, and for P2 and P3, the square represents the dutch roll mode. For O1-O3 and P1, the dutch roll mode splits into two real modes shown by the square and diamond.

An unstable spiral mode was also present for all flights, consistent with equation (5.22) with the exception of O3 (equation (5.22) is indicative only). However, the spiral motion of this mode varied between flights, compared with what might be expected for conventional aircraft. For example, the barn owl's spiral mode did not feature sideslip direction of the same sign as roll and yaw, while the time constant of P1's spiral mode was much shorter compared with P2 and P3. Reduced order models for the spiral mode, again from Cook [38], were in close agreement with these results

(see Appendix E table E.2)

The peregrine flights P2 and P3 had a conventional dutch roll mode, unlike the barn owl and P1, whose dutch roll pole divided into two zeros representing various non-oscillatory stable and unstable modes. The full mode breakdown is provided in table 5.11, and provides information on each mode's stability and motion.

	S/U	\mathbb{R}/\mathbb{C}	Motion	O1	O2	O3	P1	P2	P3	Fig.
Roll subsidence 1	S	\mathbb{R}	p	✓	✓	✓	✓	✓	✓	E.6
Spiral 1	U	\mathbb{R}	vpr	✗	✗	✗	✓	✓	✓	5.29, 5.28
Spiral 2	U	\mathbb{R}	$(v)pr$	✓	✓	✓	✗	✗	✗	E.7
Dutch roll	S	\mathbb{C}	$v(p)r$	✗	✗	✗	✗	✓	✓	5.30
Roll yaw sideslip 1	S	\mathbb{R}	vpr	✓	✓	✓	✗	✗	✗	E.8
Roll yaw sideslip 2	U	\mathbb{R}	$vp(r)$	✓	✓	✗	✗	✗	✗	5.31
Roll yaw sideslip 3	U	\mathbb{R}	$(v)pr$	✗	✗	✓	✗	✗	✗	5.31
Roll yaw sideslip 4	S	\mathbb{R}	$vp(r)$	✗	✗	✗	✓	✗	✗	E.9
Roll subsidence 2	S	\mathbb{R}	vpr	✗	✗	✗	✓	✗	✗	E.10

Table 5.11 Lateral-directional mode breakdown for the barn owl (O1-O3) and peregrine (P1-P3) flights/glide configurations. Each mode is named based on a description of the motion, with numbers used where multiple instances of a given mode shape were observed. Column titles indicate whether each mode was stable (S) or unstable (U), real/non-oscillatory (\mathbb{R}) or complex/oscillatory (\mathbb{C}). The sideslip, v , roll rate, p , and yaw rate, r , are indicated, with parentheses used to distinguish the signs of these values: states inside parentheses are of opposite sign to those outside parentheses. Time-histories for each mode are referenced.

Example time-histories for the conventional spiral and dutch roll modes of P2 and P3 are shown in figures 5.28 and 5.30. The faster spiral mode of P1 is shown in figure 5.29, and the slightly unconventional spiral mode of the barn owl is shown in figure E.7. The stable, non-oscillatory modes of the barn owl (roll yaw sideslip 1) and P1 (roll yaw sideslip 4 and roll subsidence 2) are shown in figures E.8 to E.10. The barn owl's unstable, non-oscillatory modes (roll yaw sideslip 2 and 3), are shown in figure 5.31, based on comparison between flights O1 and O3 (O2 was very similar to O1). Both of these two flights showed a spiral-like divergence in roll, yaw and sideslip, but differed in the relative signs of the state variables describing the motion. The divergence in O1 involved sideslip and roll to the right, with yaw to the left, while for O3, the roll and yaw occurred in the opposite sense to sideslip. The differences between O1 and O3 could be due to the opposing signs of C_{l_v} (see table 5.10), since the remaining derivatives all featured similar signs. The divergence involved a rapid departure yaw

(with a small degree of roll) which could be due to the lack of weathercock stability (table 5.10).

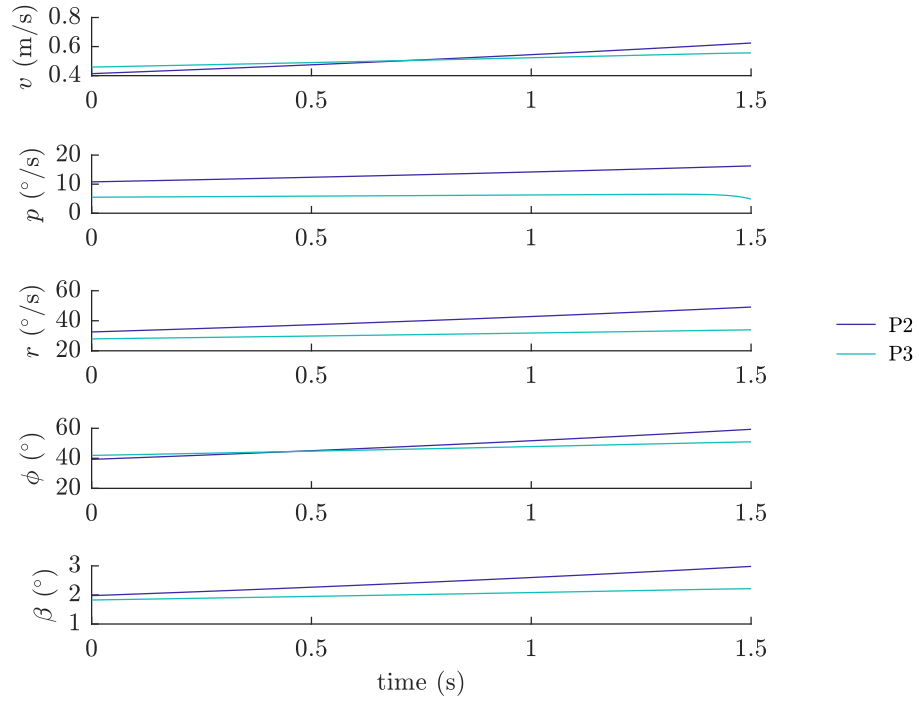


Fig. 5.28 Time-history of the spiral mode of flights P2 and P3.

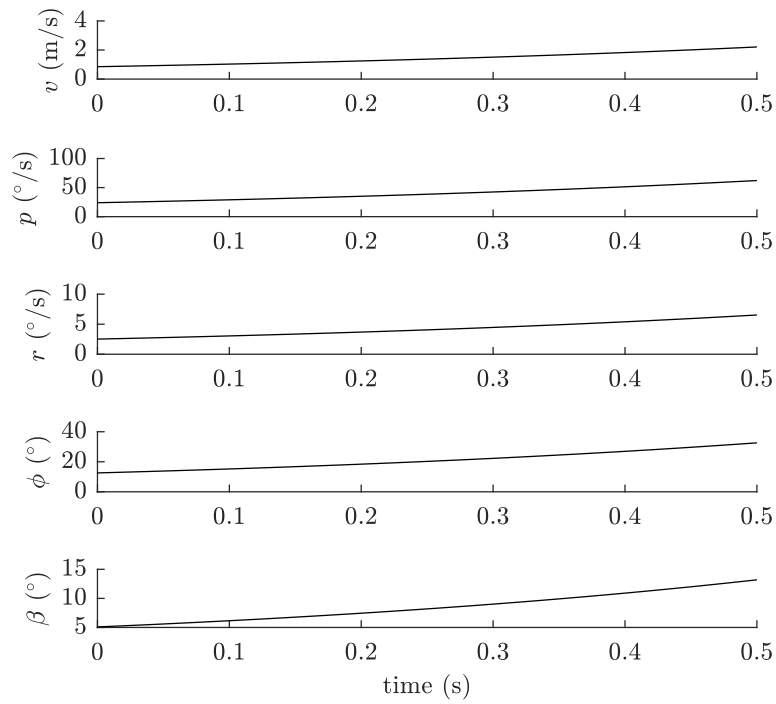


Fig. 5.29 Time-history of the spiral mode of peregrine flight P1, which had a significantly lower time constant compared with the other flights.

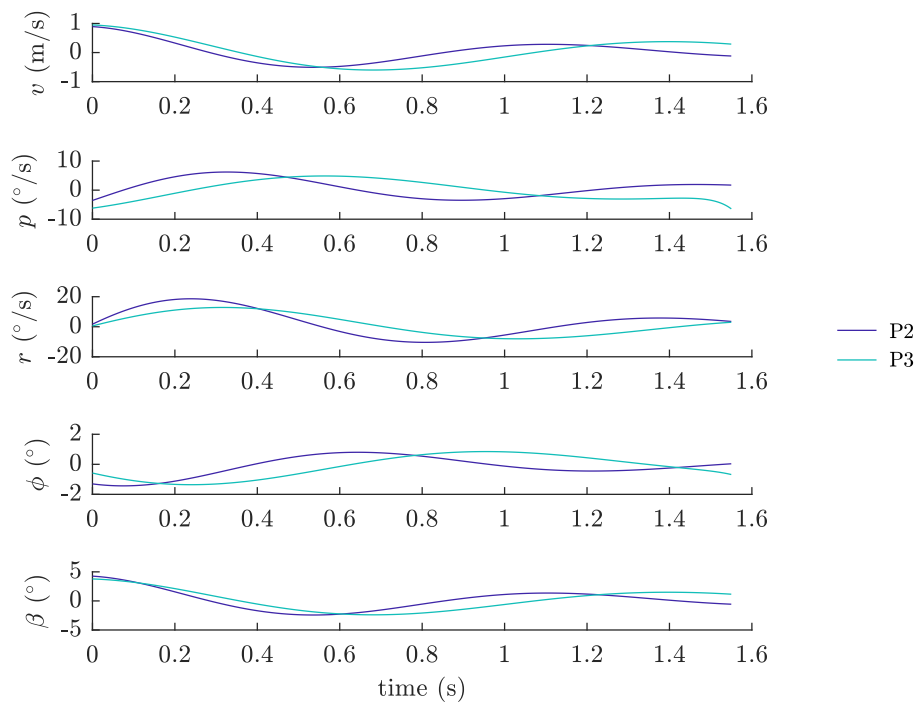


Fig. 5.30 Time-history of the dutch roll mode of P2 and P3.

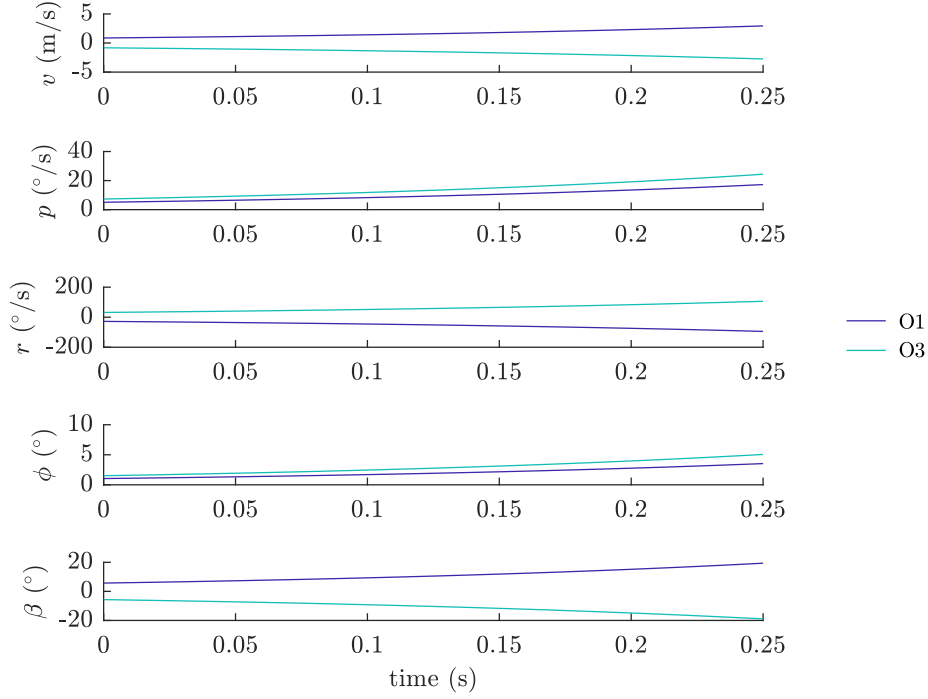


Fig. 5.31 Time-history of the unstable roll yaw sideslip modes 2 and 3 for the barn owl flights. Flight O2 was almost identical to O1 and is therefore not shown.

5.5.5 Sensitivity studies

Sensitivity studies were carried out using flights O1, P1 and P3 to understand how the dynamic modes were affected by uncertainty in trim lift coefficient, centre of mass (CoM) position and the inertia tensor. These three flights were chosen because they were generally representative of all the observed configurations across the six flights. Instances in which variation in these parameters had some effect on the modes were recorded in tables E.4 to E.6 and are summarised below.

Changes in trim lift coefficient resulted in very small changes to the natural frequency and damping of the third oscillatory mode. More significant changes were observed in the dutch roll eigenvalue of P1 and P3. For P1, an increase of 0.1 in C_L changed the two real modes into a complex mode, that had significantly lower frequency and high damping ($\zeta > 1$) compared with the dutch roll mode of P2 and P3 at their nominal lift coefficients. Similar changes were observed for P3, with the complex dutch roll mode dividing into two stable, real modes at the reduced lift coefficient. These changes to the dutch roll mode were probably due to the sensitivity of C_{N_v} , which varied between 34% and 348% of its nominal value, since it is has

primary influence on the natural frequency of the dutch roll mode [38].

Changes to the anteroposterior position of the CoM of ± 15 mm were also investigated based on the expected worst case standard error in the centre of mass position caused by incorrect manual alignment of the CT scan data to the photogrammetric reconstructions (see chapter 4 section 4.6.1). Since the static margin was between approximately 31 mm-44 mm, a 15 mm change was clearly insufficient to make the configuration stable. Forward movement of the CoM position increased the time constant of the pitch divergence mode by 47% - 59% (table E.6). In addition to error in the centre of mass position, the neutral point may have been approximately 5 mm aft based on comparison between the wind tunnel and AVL estimates. This 20 mm reduction in the static margin was still insufficient for a stable configuration. Changes to the pitch divergence mode were also accompanied by changes in its stable counterpart, but the remaining modes did not change significantly.

The pitch divergence mode, roll subsidence, roll/yaw/sideslip and dutch roll modes were all sensitive to changes in the inertia tensor, however the general positioning of these modes on the root locus plot was not fundamentally altered (see section E.5.3). The sensitivity was assessed based on the maximum and minimum values of all principal components of inertia, altered simultaneously, based on error estimates from chapter 4 section 4.6.1. The pitch divergence mode was influenced by I_{yy} (as expected), with a maximum variation in the time constant of 34% from the nominal values of 40 ms, 63 ms and 44 ms for O1, P1 and P3 respectively. Changes in the roll subsidence mode were similar, as a percentage of the nominal values. The roll, yaw, sideslip (RYS) modes 1, 2 and 4 (see table 5.11) also showed subtle variations in their time constants, with a maximum change of 56% for RYS4 between the nominal and minimum inertia tensor. The frequency and damping of P3's dutch roll mode also changed by small amounts. None of the worst case inertia tensor errors resulted in a significant change in 'layout' to the root locus plot.

Finally, the *least unstable* longitudinal case was assessed, with 20 mm forward movement of the CoM and the highest I_{yy} error, resulting in time constants for the pitch divergence mode of 88 ms, 182 ms and 74 ms for O1, P1 and P3 respectively. This represents a significant attempt to make the birds stable, based on potential errors in the critical parameters, given the importance of the static margin to this result.

5.6 Discussion

5.6.1 Summary of results

These results represent the first quantification of the flight dynamics of gliding birds about all axes, based on rigid 6-DoF rigid body, linearised flight dynamics theory for small perturbations about trim. Both the barn owl and peregrine configurations were highly longitudinally unstable for all flights, and exhibited a divergent mode with time constants of less than 100 ms. This is referred to throughout this chapter as the ‘pitch divergence mode’. The different configurations adopted by the peregrine revealed that retracting the wings (proximal forward sweep, distal aft sweep) increased the degree of instability due almost entirely to movement of the neutral point (figure 5.21). The neutral point was sensitive to anteroposterior motion of the arm wing, wing sweep and the spread of the tail (figure 5.22). A mode very similar to the phugoid was also observed, commonly referred to as the ‘third oscillatory mode’ in unstable aircraft [71]. The lateral-directional modes were more complex, due to differences between flights. Peregrine flights P2 and P3 were most similar to conventional aircraft, because they featured the expected trio of roll subsidence, spiral and dutch roll modes. In P1, two stable non-oscillatory modes were present, in place of the dutch roll mode with motion similar to roll subsidence and spiral modes. Similar to the peregrine, the barn owl had a highly stable roll subsidence mode and an unstable spiral mode, however the spiral mode featured sideslip motion of the opposite sign to roll and yaw, probably due to that lack of weathercock stability (table 5.10). The owl’s dutch roll was replaced by non-oscillatory stable and highly unstable modes with motion somewhat similar to the spiral mode. These results quantify the stability of the bird as if it were a rigid body, which is not the case for real birds. In section 5.6.5, the effect of structural compliance (i.e. flexibility) and neural feedback will therefore be discussed in terms of their potential role in stabilisation.

5.6.2 Methods

In contrast to previous work on the flight dynamics of birds [76, 85, 87–89, 95], these results are based on geometric models based on almost complete surface reconstructions of free-gliding birds, rather than dead birds or unverified approximations using ‘bird-like’ shapes. This is important because subtle changes in shape can have a significant impact on the aerodynamic stability derivatives [86, 87, 91]. The surface

reconstructions were compared with a laser-scanned fibreglass model gull and shown to be accurate to within approximately 3 mm for 95% of the points (see chapter 2 section 2.7). The raw points were used to generate watertight surface meshes of the complete bird for 3D-printing and wind tunnel testing, in addition to spanwise mean camber lines for aerodynamic analysis. The mesh of O1 used for wind tunnel testing was shown to be highly representative of the raw points (see section 5.4.1.9). Although the photogrammetric data were lacking close to the leading and trailing edges due to a reduction in the accuracy of the data in these regions, spline fitting to both the laser scanned and photogrammetrically reconstructed model gull showed highly similar spanwise camber, twist, sweep, dihedral and thickness, validating the use of the photogrammetric method for the subsequent stability analysis. Despite the limitations of the surface reconstruction method, it represents a significant improvement over the use of dead birds or unverified approximations to the bird’s shape, which differ markedly from free-flight [21–23, 199].

The inertial properties (centre of mass and inertia tensor) were obtained using a novel, accurate approach (described in chapter 4) that was validated using two independent methods. This too, represented an improvement over the use of bird cadavers and dissection methods for inertia estimation due to its increased utility and accuracy.

Flight stability was quantified using the linearised equations of motion for small perturbations around trim [38]. The static longitudinal stability derivatives were obtained using a vortex lattice method [206], which was shown to provide accurate estimates based on validation against wind tunnel data for flight O1 (section 5.5.1). The wind tunnel and AVL estimates of the lift slope matched precisely for flight O1 when the AVL model included a thick central torso, while the moment slope agreed within approximately 20%. Importantly, the experimental and computational results were in reasonable agreement regarding the magnitude of the static margin (accuracy within approx. 4% mean aerodynamic chord), as this has the most significant impact on stability. Longitudinal derivatives with higher error were updated based on wind tunnel data for flight O1 and analytical estimates used for conventional aircraft, however, this did not have a significant impact on the results. The sensitivity of the results were assessed against the spatial resolution of the vortex lattice, uncertainty in estimates of the trim lift coefficient, centre of mass position and inertia tensor. The dynamic modes were mildly or negligibly sensitive to trim condition, centre of mass position and the inertia tensor (see Appendix E section E.5), but overall these did not

significantly alter the time-constants, natural frequencies or damping of the dynamic modes.

It is possible that the smooth, non-feathered, surface of the wind tunnel model, and the very low freestream turbulence may have led to differences compared with the real bird. However, there was reasonable agreement between the field estimated lift coefficient for O1 and the trim estimate from the wind tunnel data. Furthermore, experiments with bird wings with different degrees of surface roughness have shown that this only has a significant effect on the drag polar at angles of attack near stall [57, 58]. However, future models should seek to assess the influence of feather roughness and porosity on these findings. Furthermore, barn owls have a leading edge comb, whose existence could influence the flow field around the wing tips, though it is unclear how significant this effect would be for the stability derivatives [56, 202, 211]. In summary, the error analyses and sensitivity studies should provide reasonable confidence in the accuracy of the results, assuming that feather roughness and porosity do not have a significant impact on the derivatives.

5.6.3 Longitudinal stability

The dynamic models showed that the barn owl and peregrine were highly longitudinally statically unstable for all flights, corresponding to a rapid pitch divergence mode with a time to double between 22 ms and 69 ms. Previous research on the longitudinal stability of gliding or flapping birds has been almost entirely based on theoretical modelling or observation based inferences. Thomas and Taylor [76] estimated the relative positions of the centre of mass and wing aerodynamic centre using cadavers from 15 bird species. Their results showed that 11 of the 15 species were longitudinally stable fliers, although they did not collect data for a barn owl or peregrine falcon. They did however, collect data for two related species [212], a tawny owl and a sparrow hawk, which suggested these birds were neutrally stable and highly unstable respectively. These results should be held tentatively however, because the wing positions of dead birds may not match those in flight. Moreover, the fully protracted configuration used for these estimates may not have been representative of the least stable configuration. This is supported by figure 5.21 and the observation that wing retraction in a perching Steppe eagle (*Aquila nipalensis*) likely moved its centre of pressure forwards [83]. The conclusion that most modern birds are longitudinally stable [76] was also contrary to the commonly held view that birds progressed from stable to unstable flight morphologies [8, 9, 68, 100, 196, 197], which is supported by the fossil evidence [80].

Observations that birds can fly without a tail [9, 68, 77], and that the tail generates positive lift during gliding [95], are sometimes cited as evidence that birds are longitudinally unstable, however this is inconclusive because balance can also be provided through the wing, as in tailless aircraft [76, 145]. In contrast to prior speculation, the present results empirically demonstrate that the barn owl and peregrine were highly unstable in glide across a range of trim conditions, even taking into account combined uncertainty in the centre of mass, inertia tensor and neutral point estimates. These results do not take into account the effect of feather roughness and freestream turbulence, but at low angles of attack it is unlikely these would have a significant effect on the results. These findings are consistent with the conclusion in chapter 3, that the barn owl was longitudinally statically unstable.

Based on wing planform measurements of a Harris' Hawk (*Parabuteo unicinctus*) gliding in a wind tunnel, it might be assumed that wing protraction always moves the aerodynamic centre forwards [81]. However, this result may not apply to all birds. By retracting its wings, the peregrine was able to increase its degree of instability by moving the neutral point *forwards*. This was due to increased forward sweep in the arm wing, reduced aspect ratio and furling of the tail between P1 and P2/P3. Unlike the hawk, the peregrine furlled its tail causing forward movement of the neutral point, perhaps achieving equilibrium through the lift acting on the wing distally (figure 5.22). This result is consistent with observations of a perching Steppe eagle mentioned previously. The static margin is obtained by dividing the moment slope by the lift slope (table 5.2). Between P1 and P2, the pitching moment slope was very similar, but the lift slope was reduced through lower wing aspect ratio [3]. Between P2 and P3, changes in both the moment and lift slope contributed towards increased static margin, possibly through reduced wing camber (see figure 3.13) and aspect ratio respectively. Clearly, the relationship between geometry and the position of the neutral point is complex, which is why full quantification of the bird's free-gliding shape, combined with aerodynamic modelling, is so crucial for correct understanding. It is interesting to note that when attacking prey, peregrines often retract their wings for increased speed which, based on these results, also increases their instability and manoeuvrability (see section 5.6.6 for further discussion).

5.6.4 Lateral-directional stability

The lateral-directional modes were dissimilar between flights, mainly due to variation in the dutch roll pole, which split into two non-oscillatory modes for all flights except

P2 and P3. Several modes were very mildly sensitive to lift coefficient and inertia; the changes were small in magnitude (see section E.5). The roll subsidence mode was well predicted by the reduced order model, and was highly stable (table E.1). However, this does not mean the birds were stable in roll, due to the presence of more unstable spiral modes. The time constant of the unstable spiral mode was reasonably well predicted by the reduced order model for all flights (table E.2). For the peregrine, this was the least stable mode, and would have dominated the lateral-directional control problem. For the barn owl, the spiral mode was slightly unconventional because sideslip was in the opposite direction to roll and yaw, likely due to the lack of weathercock stability (see table 5.10). Unlike the peregrine however, the barn owl featured a highly unstable non-conventional spiral mode that would have dominated the roll control problem, with time constants of approximately 0.2 s. Most previous research in avian flight has involved speculation about lateral-directional stability based purely on observation. For example, the existence of positive wing dihedral and/or aft sweep has been used to infer roll stability [27, 68, 77, 94], while tail twisting might confer temporary directional stability [63, 79]. Although these inferences are plausible, the complex coupling of lateral-directional dynamics suggests they should be held tentatively in the absence of dynamic models of free-gliding birds [38, 65]. For example, all the barn owl and peregrine flights exhibited significant wing anhedral, which from simple observation might lead to the expectation of roll instability (i.e. positive C_{l_w}). However, table 5.10 shows that this is not the case because the strong aft sweep in P2 and P3 counteracts the anhedral to produce a stable C_{l_w} , while the combination of sweep and dihedral in O3 led to almost neutral roll stability. Clearly the various impacts of glide geometry on lateral-directional stability are difficult to determine from the bird's shape, which is why this was not attempted in chapter 3.

Studies have been conducted in which several important lateral-directional derivatives have been quantified for bird-like geometries to assess directional stability without a vertical tail [85, 88, 89] and with varying wing sweep [86], dihedral [91] and wing tip geometry [87]. Comparison with the present results reveals similar magnitude values for N_β , N_r and L_β , increasing confidence in the AVL estimates. These studies suggested that aft-swept wing tips and a tail are stabilising in yaw, and highlighted the high degree of sensitivity between, for example, N_β , and the sweep angle of the wing tip. Subtle changes in geometry and trim condition can have profound effects on the lateral-directional derivatives, again indicating the importance of accurate free-flight geometry. The shapes used in these studies were based on measurements of

dead birds [90] in which the camber, twist, dihedral, sweep and thickness of the wing were highly simplified. The bird's torso, which has a significant impact on lateral-directional derivatives, was also not included in these models. These studies were informative in terms of highlighting the effect of certain geometry features on several important derivatives, but were not combined into a complete dynamic model. In contrast, the accurate glide geometries and inertial properties obtained in this study were combined into a fully coupled dynamic model of the bird. This revealed the overall lateral directional instability of the barn owl and peregrine, resulting from their conventional and unconventional spiral modes. In particular, the barn owl featured a rapidly diverging spiral mode, although it was still approximately four times slower than the pitch divergence mode, which dominated the flight control problem faced by these birds.

5.6.5 Flight stabilisation

These results show that, treated as a rigid body without feedback control, the barn owl and peregrine are highly unstable gliders that would lose control on the order of 50 ms (the approximate time to double of the pitch divergence mode). However, real birds actively control their flight by morphing their highly flexible wings and tail. Somehow, these birds must stabilise their flight, or they would be unable to survive. Modern combat aircraft are designed to be longitudinally unstable, making them impossible to control even by the best human pilots. These aircraft are stabilised using a 'stability augmentation system' (SAS) which provides corrective control inputs to the elevator and/or canard, typically based on angle of attack or pitch rate feedback [38]. The X-29 demonstrator, for example, had an unstable static margin of 35% mean aerodynamic chord similar to the barn owl and peregrine (table 5.6) and would lose control in 0.17 s without active feedback control [74, 75]. It was stabilised by a highly redundant system with a 40 Hz feedback signal including three digital and three analogue SAS to ensure safety in the event of multiple computer failure [72]. However, the open loop time to double of the X-29 was 150 ms [72], around four-times slower than the barn owl or peregrine. It is therefore interesting to explore whether a hypothetical rigid barn owl or peregrine would have sufficiently fast neural feedback, based on current understanding of avian physiology.

The 40 Hz control system sample rate of the X-29 corresponds to an update time interval of 25 ms which is one-sixth its time to double. This means that every 25 ms the control system was provided with data from the feedback signal (i.e. angle of attack

or pitch rate). Applying this ratio to the birds would require an ‘update rate’ of 6 ms. Although biological systems are not digital, this timescale provides an indication of the high speed at which the efferent neural information and muscle contractions may need to occur. Even accounting for a possible factor of safety on the update rate in the X-29, the feedback signal would still need to be extremely fast, of the order 10 ms. This time-scale would guard against significant changes in angle of attack (see figure 5.25) resulting in the smooth flight observed for these birds.

The reaction times of birds are unlikely to be fast enough to provide the biological equivalent of ‘inner loop’ stability augmentation, based on this crude estimation (see above) of the feedback rate required. For example, the startle reaction time of starlings to both sound and light stimuli was 40 to 125 ms [213]; for humans it is approximately 150 to 250 ms depending on the stimuli. This slow reaction time is consistent with studies which suggest reflexes (rather than reactions) are required for flight control, because they by-pass the brain and are therefore faster [45]. But are they fast enough? In humans, the time-delay for the patellar tendon reflex (i.e. knee-jerk) is approximately 50 ms, which is three times faster than our reaction to touch [214, 215]. Assuming that much of this time is due to the physical lengths of the nerves, it is reasonable to suggest that reflexes in birds are even faster than in humans, though it is not clear by how much. Birds stabilize their vision through their vestibuloocular (ear feedback stabilises eye) and vestibulocollic (ear feedback stabilises head) reflexes [216]. Studies with domestic pigeons revealed ‘state-dependent’ flight control likely based on vestibular feedback, that is activated when the legs are unloaded and air is blown onto the breast feathers [43, 44, 114]. The birds applied combinations of wing sweep and tail elevation that corrected for applied pitch and roll rotations. These rotations were applied relatively slowly (up to 20° per second), with control responses comfortably in-phase with the input motion. Pigeons may also utilise acceleration feedback from stretch receptors in the mesenteries (tissues that attach internal organs to the abdomen wall), because corrective control inputs from the tail continued even when the labyrinths were destroyed and the spinal chord transected [115, 116].

Birds may also use information from different types of mechanoreceptors in the wings for flight control. Herbst corpuscles, most sensitive to vibrations between 100 Hz and 1000 Hz, appear to be concentrated in locations that could be important for flow sensing, such as at the leading edge of the alula [47]. Rapidly and slowly adapting mechanoreceptors have also been identified in association with covert feathers, secondary flight feathers and the alula, and provide neural information that may help

the bird to sense airspeed and stall [49]. However, it is unclear exactly how the bird actually uses this information during flight [46, 48].

The speed of the control system in birds is also dependent on the contraction rate of the wing muscles. Muscle contraction times in chickens between 50 and 500 ms have been measured [109]. Studies have also been carried out using histochemistry to identify ratios of fast and slow twitch (including slow tonic) muscle fibres in the wings of a variety of bird species [110, 112, 113, 113]. It appears that in many volant birds, the pectoralis is comprised of fast twitch fibre types (including owls and falcons), rather than slow tonic fibres, and is most likely due to the need to flap [40, 112]. Similar studies of specialised soaring birds showed that several species have a divided pectoralis with a deep layer that is composed mainly of slow tonic muscle fibres, well suited for the high endurance task of maintaining glide posture [110, 217, 218]. Even these birds need to flap however, and have regions of the pectoralis that contain significant proportions of fast twitch fibres [110]. Surprisingly, some soaring birds do not have significant proportions of slow tonic fibres, which may be consistent with the need for fast correctional control, however it is unclear how the muscles avoid fatigue [113]. Fast twitch fibres would certainly make sense if gulls and kestrels were longitudinally statically unstable, since they contract five times faster than slow twitch fibres [109].

Electromyographic recordings of a Kestrel gliding in a tilting wind tunnel revealed high-frequency activity from the motor neurons that innervate the cranial and deep fascicles of the pectoralis, as well as the supracoracoideus, biceps brachii and triceps humeralis [40]. The recordings from these muscles may imply their use in correctional control during gliding. Similar measurements of the pubocaudalis externis, which is involved in tail control, showed that it was continuously active during slow flapping flight in pigeons [66].

Further research is needed to quantify the speed of the afferent and efferent control signals in birds, and to determine which neural pathways are used for different flight control tasks. Further modelling with the current flights could also be utilised to provide a clear requirement for maximum control system lag allowable, given rigid body assumptions. From this brief exploration, it is possible that the neural time lag and the contraction speeds of avian muscle may be too slow (i.e. combined lag greater than 10 ms) to stabilise the a hypothetical rigid barn owl or peregrine. It is therefore reasonable to explore whether something other than neuromuscular feedback may help to stabilise the gliding flight of these birds. Unlike relatively rigid conventional aircraft, birds have highly flexible (compliant) wings. It is possible that fluid-structure

interaction during a disturbance acts to reduce or eliminate the instability, providing the additional time required for feedback control.

Using similar reasoning to that of chapter 3 section 3.3, Pennycuick [219] suggested that wing surface reconstructions of a gliding bat *Rousettus aegyptiacus* implied that it was longitudinally statically unstable (if treated as a rigid body). However, Pennycuick suggested that while the rigid form would be unstable, membrane compliance during a pitch disturbance could help stabilise the bat. During a reduction in angle of attack, he envisaged a reduction in camber leading to a reduction in nose-down pitching moment and a negative pitching moment slope (figure 5.33 A,C). This explanation only works however, if the reduction in pitching moment due to camber is greater than the increase in pitching moment due to lift, a principle that is sketched conceptually in figure 5.33A and C. With birds, changes in wing camber with angle of attack are likely different to those suggested for bats. For example, a reduction in camber with angle of attack was observed through wind tunnel testing of prepared barn owl wings [54]. This could have the effect of reducing the positive pitching moment slope, if the reduction in pitching moment due to lift is greater than increase in pitching couple due to the reduced camber (figure 5.33B and D). This hypothesis is untested and warrants further experimental testing, but at least provides a conceptual framework for the role of structural compliance in the stabilisation of pitching motions. As mentioned previously in chapter 3 section 3.6.3, the secondary flight feathers on the right wing during flight O1 can be seen deflecting upwards near the centre of the measurement volume, and appeared to be a passive structural response due an atmospheric disturbance. A similar principle with a different mechanism, in which the wing rotates around a torsion spring parallel to the lateral axis, has been demonstrated using both theoretical dynamic modelling and experimental testing of a simple model glider [220]. Application of elastic bands to provide stiffness to the wing hinge resulted in stable flight, even when the centre of mass was behind the neutral point. The advantage of this passive structural feedback mechanism (a concept which has been referred to as ‘preflexive feedback’ [42]) is its extremely fast response time compared with other feedback information [32, 34]. This makes it well placed as a potential stabilisation mechanism of the pitch divergence mode. In light of the present discussion, we agree with Krus [220] that flight stability in birds is probably achieved by the combination of structural compliance and neural feedback. In this scenario, structural compliance reduces the level of instability, increasing the time constant of the pitch divergence mode, providing the additional time necessary for effective neural feedback control.



Fig. 5.32 Compliance in the primary feathers of this bearded vulture (*Gypaetus barbatus*) could reduce roll instability through increases in dihedral. Photograph from Rüppell [94]

Similar stabilising mechanisms are envisaged for the fast, unstable spiral mode of the barn owl configurations. For example, a positive roll rate to the right would increase the dihedral of the right wing due to the compliance of the primaries, introducing dihedral effect and reducing instability (figure 5.32). Subtle changes in dihedral are clearly visible in the video footage of the barn owl flights, providing qualitative support for this suggestion. The barn owl's highly unstable spiral mode was slower than the pitch divergence mode, so the role of compliance in stabilisation would not need to be as significant. All the remaining modes were either highly stable or sufficiently slow that neural feedback would be adequate for control. Testing of this hypothesis represents a potentially fruitful area of future research.

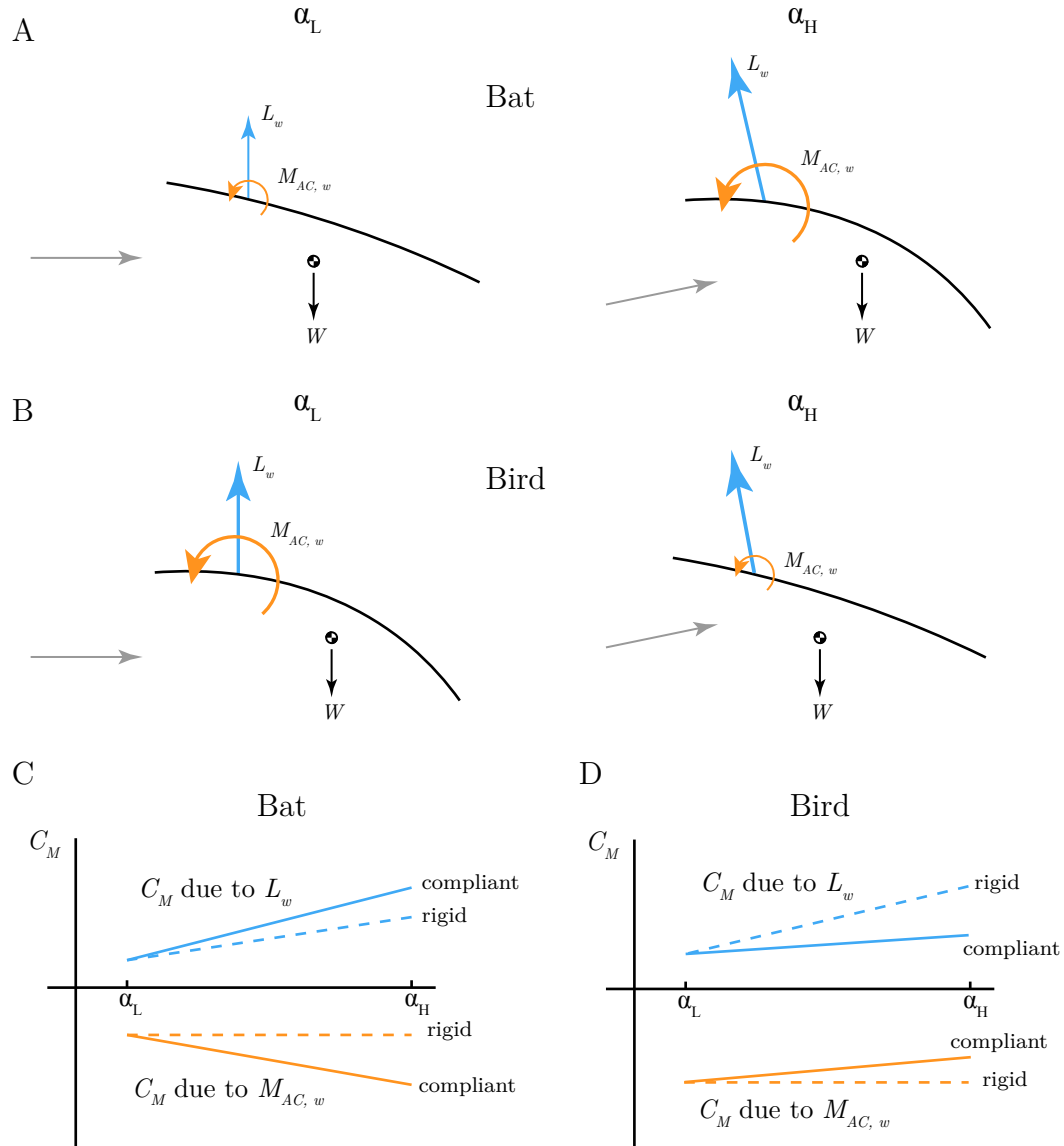


Fig. 5.33 Theoretical scenarios illustrating how trailing edge compliance has the potential to reduce the longitudinal instability of a bat (A,C) or bird (B,D). A) The camber of a bat's wing may increase with increased angle of attack, leading to increased lift and nose-down pitching moment relative to a rigid equivalent [219]. B) The camber of a bird's wing may reduce with increased angle of attack, leading to reduced lift and nose-down pitching moment relative to a rigid equivalent. C) The pitching moment slope contributions due to the lift force (blue) and pitching couple (orange) contributions for the rigid (dashed) and compliant (solid) bat wing. D) The pitching moment slope contributions due to the lift force (blue) and pitching couple (orange) contributions for the rigid (dashed) and compliant (solid) bird wing. Clearly, the sum of the dashed lines (rigid wing) for both the bat and bird leads to an overall positive moment slope (i.e. unstable). However, the sum of the solid lines (compliant wing) may be positive or negative depending on the relative contributions of the lift moment (blue) and couple (orange) - these would need to be quantified. Therefore, compliance *could* stabilise or reduce the instability of a lifting surface that is unstable when rigid.

5.6.6 Ecological implications of instability

The different flight styles of barn owls and peregrines reflect their contrasting foraging tactics. Barn owls are slow fliers with low wing loading that have exploited silent flight and surprise attack to catch their prey on the ground [221]. Peregrines have more than twice the wing loading, relying on high-speed to catch their prey in mid-air and on the ground in open spaces [157, 222, 223]. Alongside the ability to fly efficiently to minimise energy consumption, the ability to effectively catch prey has likely been a significant factor in the evolution of these birds. Research on the predator evasion dynamics of prey in open spaces suggests that both manoeuvrability and speed are crucial for escape [192, 198]. Being small also increases agility due to the relative scaling between aerodynamic moments and mass moments of inertia (see chapter 1 section 1.3) [28]. Since prey are usually smaller than predators it is unsurprising that a common form of escape is through ‘last minute dodge’ [192, 224]. The high degree of instability in the barn owl and peregrine also means a high degree of manoeuvrability. This makes sense in light of the ‘arms race’ between predator and prey, in which the predator is always at a manoeuvrability disadvantage due to scaling effects (see chapter 1 section 1.3). Barn owls attack mice and voles, and can be seen flap-gliding over large open areas within several metres of the ground [221]. When prey are spotted, they suddenly pitch down, a manoeuvre which can be rapidly executed in a longitudinally unstable flier. The speed and surprise of their final attack is important, since they can be heard within 1 m range by their prey [202, 211]. Based on these suggestions, we would expect evolution to drive predators and prey towards highly unstable, highly manoeuvrable configurations [9]. It is interesting that the more retracted configuration (P2,P3) of the peregrine was more unstable (and therefore manoeuvrable) than the fully protracted configuration (P1), given the adoption of the former when attacking prey. However, this may be offset by the reduction in control effectiveness (figure 5.23), and may primarily be for used for increasing speed.

Instability may also reduce power consumption in flight and reduce the risk of control loss during landing due to a reduction in stall speed [9]. Stability always comes at a cost to lift to drag ratio [76] due to the need for a positive zero lift pitching moment for balanced flight. In conventional aircraft, this is achieved through longitudinal dihedral, aft-sweep with washout or reflex camber, all of which reduce lift at a given angle of attack, and limit the maximum lift coefficient. The opposite morphological adaptations apply to unstable configurations, all of which increase lift-

to-drag ratio and reduce stall speed [9]. In addition to enhanced manoeuvrability, the increase in aerodynamic efficiency is one of the reasons why fighter aircraft are designed to be unstable [195]. It may be argued that the correctional control required by unstable configurations means greater energy expenditure. However, being stable could also lead to inefficiencies, for example, having to apply correctional control to avoid weather-cocking into sideslip. This is important for birds because their flight velocities are the same order of magnitude as the wind. Moreover, having a stable configuration does not mean that flight control muscles are inactive or ‘passive’ because the bird must brace its wings in place [39, 41]. Interestingly, skeletal muscle is well suited for unstable control actuation, because its force generating ability reduces with contraction speed [111]. Increased instability means faster muscle contractions but with less force required (due to higher manoeuvrability).

5.7 Conclusions and recommendations

In this chapter, the original aim to quantify the inherent static and dynamic stability of free gliding birds was realised for three flights of an individual barn owl and peregrine falcon. The results showed that both birds were highly longitudinally unstable, with static margins (as % chord) similar to the X-29 highly unstable technology demonstrator aircraft. The barn owl was also highly unstable in roll and yaw, due to a spiral-like non-oscillatory mode that replaced the dutch roll mode of conventional aircraft. Although current knowledge of avian flight control is limited, existing knowledge of muscle contraction speeds, reactions times and reflex-based correctional control was used to explore whether neural feedback might be fast enough to control the pitch divergence mode, with its time constant approximately three times faster than the X-29. Further research is required to answer this question conclusively, but it was suggested that ‘preflexive feedback’ [42] from the compliant structures in the wing (i.e. flexible feathers, muscles acting as springs), could act to reduce the level in instability and provide the additional time required for slower neural feedback to work effectively [220].

These results represent the first complete quantification of the equations of motion for free-gliding birds using a vortex lattice method (inviscid, thin surfaces). The results should therefore be interpreted in light of the assumptions made; rigid 6-DoF structure, linearised equations of motion for small perturbations from trim using smooth aerofoil sections. Real birds are highly compliant, non-linear dynamic sys-

tems with multiple degrees of freedom. Validation of the longitudinal derivatives with wind tunnel data showed that these were relatively accurate. The lateral-directional derivatives were not validated, but were of similar magnitude to those obtained for bird-like shapes using slightly higher-fidelity computational fluid dynamics [88]. The effect of feathered surfaces on the derivatives was not explored, however previous work suggests that this may not have a significant impact below angles approaching stall [57, 58, 209]. Furthermore, the effect of unique adaptations of barn owl wings for silent flight (leading edge comb, trailing edge fringe and velvety surface) on aerodynamic derivatives was not explored [202, 211]. Comparison between wings with and without these features implies they may not have a significant impact of lift and drag derivatives, but do affect aerodynamic efficiency [55, 56].

Future work could include,

1. Further wind tunnel testing to validate the lateral-directional derivatives for O1, and all derivatives for the peregrine flights.
2. Use of higher fidelity computational fluid dynamics models (including viscosity and unsteadiness) to quantify the aerodynamic derivatives.
3. Experimental and/or computational studies of the effect of feather roughness and porosity on the aerodynamic derivatives [60].
4. Experimental and/or computational studies to understand how the compliant features of the avian wing effect stability. This could involve development of the photogrammetry setup for high-speed video, or the application of compliant trailing edges to unstable UAVs. The latter uses the concept of ‘robotics inspired biology’ [225], which refers to the use of biomimicry to better understand biological systems.
5. Quantification of the energy savings of longitudinally unstable configurations on unmanned air vehicles. Does the increased lift-to-drag ratio compensate for potentially increased control system energy consumption? If passive, compliant features are used for reflexive stabilisation, this may reduce control system power compared with active control using electronic feedback.
6. Further use of computational fluid dynamics to further explore control effectiveness between the wings and the tail. How is stability affected by removal of the tail? What effect does tail twisting have on pitch, roll and yawing moments?

Previous research on the aerodynamic function of the avian tail is inconclusive largely due to limitations of the modelling techniques and experimental approaches used [104–107]. This work has produced accurate in-flight geometric models and methods to obtain these that can now be use to explore the function of the tail in more detail.

7. Can recent progress in the flight dynamics of highly flexible aircraft be used to begin exploring non-linear modelling of avian flight dynamics, treating the bird as a compliant, multi-degree-of-freedom dynamic system [226, 227]. A future goal in biomechanics should be the integration of structural dynamics with flight dynamics [39].
8. How does the ‘rigid body’ stability compare between individuals and species? This study was based on only three flights from two individual birds. It would be particularly interesting to compare stability between predator and prey, and to build this into models of their interaction [157, 192, 198, 223].
9. How do birds use neural feedback for flight control? This question is poorly understood currently, with very little known about the involvement of the brain in flight control [45]. Studies of avian neurophysiology should be integrated with research in avian structural and flight dynamics (chapter 1 figure 1.3).

SUMMARY AND CONCLUSIONS

The aim of this work was to quantify, for the first time, the inherent static and dynamic stability of free-gliding birds (chapter 1). This was achieved for a free-gliding barn owl (*Tyto alba*) and peregrine falcon (*Falco peregrinus*), based on three flights per bird. Existing photogrammetric techniques were combined in a novel way to obtain high resolution surface reconstructions of the birds' dorsal and ventral surfaces (chapter 2). The experimental setup was low cost and minimally intrusive to the bird, being usable outdoors with ambient light and the naturally occurring texture patterns of the birds' feathers.

Although the stereo reconstructions lacked data close to the leading and trailing edges and wing tips, post-processing algorithms enabled detailed quantification of the wing and tail geometry in free-flight (chapter 3) that were shown to be representative of the complete geometry. This was based on comparison of camber, twist, sweep, dihedral and thickness between laser-scan and photogrammetric reconstructions of a model gull. The surface reconstructions revealed highly complex variation in camber, twist, sweep, dihedral and thickness along the span. The three barn owl flights were relatively consistent, but featured subtle asymmetries in camber and twist that reflected the complexity of the flow conditions and the need for correctional control. The peregrine adopted three very different wing and tail configurations between flights, varying camber, twist, sweep and dihedral with flight velocity and angle of incidence. This bird also featured some interesting asymmetries, included a significant span asymmetry in P3 that may have been used for roll control. Key geometric features were discussed in terms of their contribution to the zero-lift pitching moment, which was used to indicate longitudinal static stability. Although this was best determined by quantifying the relative position of the centre of mass and neutral point (chapter 5), the requirement for stable and balanced flight can be used to provide geometric indications about longitudinal static stability [76]. A longitudinally stable configuration requires a positive (nose-up) zero-lift pitching moment, and vice versa for an unstable configuration, assuming a linear pitching moment slope [38]. The positive camber and

longitudinal anhedral of the barn owl was indicative of longitudinal static instability, since both of these features would contribute towards a negative zero-lift pitching moment (chapter 3). The peregrine’s longitudinal stability was unclear from its geometry alone, because some features would have contributed towards a nose-up zero-lift pitching moment, while others would have contributed towards a nose-down moment. Video footage of the flights, combined with 3-axis anemometer data obtained 6 m from the flight path, revealed flow conditions with significant temporal variation in velocity, angle of incidence and sideslip. Within the context of these local atmospheric conditions, geometric asymmetry and tail twisting were observed which could have been used for correctional control [39, 63, 77, 79, 228].

In chapter 4, the centre of mass and inertia tensor of the barn owl and peregrine cadavers were estimated using calibrated X-ray computed tomography (CT). This approach represented an improvement over the ‘strip analysis’ technique often used in previous studies for estimating the moment of inertia of individual wings about the humeral head [158, 161, 162, 165], with the main downside being the higher monetary cost of data collection. For example, the method yields more accurate data that is easy to manipulate, such that the mass or inertia of any part of the bird can be quantified about any axis. The results were carefully validated using comparison of ‘virtually’ and ‘physically’ dissected appendage masses and a trifilar pendulum. The latter was itself validated using accurately machined nylon blocks of similar mass to the birds, whose moment of inertia was calculated analytically. The CT approach captured the full inertia tensor, including the cross-coupling terms, though these were small. The principal axes of inertia were similar to the ‘wing-body’ fitted coordinates used for flight dynamics analysis.

To estimate the moments of inertia of the free-gliding birds from chapters 2 and 3, the CT data were manually segmented and aligned to the photogrammetric reconstructions. A carefully conceived approach was used during this process to ensure consistent alignment between multiple cadavers and flights. Subjectivity in the alignment process was reduced because the photogrammetric surface reconstructions were textured. This meant that distinctive features such as the eyes, talons and wing leading edge could be positionally matched between the CT and photogrammetric datasets. However, a sensitivity analysis was also carried out to assess the maximum range of anteroposterior travel of the centre of mass, based on an assessment of the worst-case misalignment of the CT scanned appendages to the photogrammetric surface reconstructions. The sensitivity of the inertia tensor to these worst-case misalignments was also assessed,

with both analyses used in the stability analysis of chapter 5.

Significant changes in wing sweep and dihedral had little influence on the centre of mass and pitch moment of inertia of the peregrine but did have some effect on the roll and yaw moments of inertia. The insensitivity of both the centre of mass and pitch moment of inertia to wing sweep may simplify the problem of longitudinal control, because the bird would only have to respond to changes in the centre of pressure caused by wing morphing. Full retraction of the wings significantly reduced the roll moment of inertia and halved the yaw moment of inertia. The absolute value of the roll moment of inertia was also significantly lower than those of similar sized model aircraft. This is because most of a birds' mass is concentrated in the torso and proximal wing, which has the advantage of minimising inertial power requirements and maximising agility. Although lower inertia results in greater sensitivity to atmospheric turbulence, it is plausible that birds stabilise their flight through passive gust rejection mechanisms (such as feather bending) and high frequency, low amplitude neural feedback control. Despite their low wing inertia, it may still be sufficient to enable inertial manoeuvre control at low speeds, based on comparison with bats [167]. This has not yet been studied in birds and could represent an interesting area for future research.

In chapter 5, the surface reconstructions and inertial data were integrated into linearised flight dynamics models that were used to estimate the inherent static and dynamic stability of the measured glide configurations, based on rigid body assumptions. The raw photogrammetric data were converted into a watertight surface mesh of the barn owl flight O1. This enabled the glide shape to be 3D printed and used to obtain wind tunnel estimates of lift, drag and pitching moment. This data were subsequently used to validate an aerodynamic model of O1, created with the Athena Vortex Lattice (AVL) program. This showed that AVL provided generally accurate predictions of the longitudinal aerodynamic derivatives and, importantly, the static margin. Potentially inaccurate AVL estimates for longitudinal derivatives were identified, and 'updated' with analytic estimates from several flight dynamics textbooks [38, 96]. Comparison between dynamic models with these 'updated' estimates and the original AVL estimates led to only small differences in the dynamic modes. Although the AVL lateral-directional derivatives were not validated, the order of magnitude of their values was similar to inviscid computational fluid dynamics studies with bird-like shapes [85–88, 92]. The sensitivity of the linear flight dynamics models was also assessed against uncertainty in the trimmed lift coefficient, centre of mass position and inertia tensor. Overall, the model was relatively insensitive to these changes, with no

changes to the properties of the dynamic modes that would alter the main findings of the study.

Both the barn owl and peregrine were highly longitudinally unstable and featured the non-oscillatory pitch divergence and ‘third oscillatory’ modes associated with high performance combat aircraft [71]. As a fraction of the mean aerodynamic chord, these birds were similar in their instability to the highly unstable X-29 experimental aircraft [72, 74, 75]. However, their time constant was smaller, being approximately 50 ms, compared with 150 ms for the X-29 [72]. Although both birds had a highly stable roll subsidence mode, their lateral flight dynamics would be dominated by their unstable spiral mode(s), with time constants between approximately 0.2 s - 8 s. The peregrine flights P2 and P3 had a conventional dutch roll mode, but in the other flights for both birds, this mode divided into two non-oscillatory modes. These were stable for P1, but for the barn owl were even more unstable than the conventional spiral mode, with time constants of approximately 0.2 s. Control effectiveness in pitch was also briefly explored using changes in tail elevation, wing camber (modelled as a 50% chord flap across the entire span), twist and sweep. This highlighted that tail spreading can significantly increase control authority [79], and that variation in wing sweep was generally an effective means of pitch control. However, the effectiveness of these different morphological changes was dependent on the baseline configuration, which may have implications for the control motions used during manoeuvring flight. Video footage and surface reconstruction of flight P3 clearly revealed the use of span asymmetry for roll control.

These findings were discussed in terms of the bird as a complete system (figure 6.1), a concept introduced in chapter 1 section 1.4. This was challenging due to limitations in current knowledge of the avian flight control system, especially the neurophysiological aspects. A brief review of avian neurophysiology appeared to suggest that the pitch divergence mode may be too fast for stabilisation with neural feedback control alone, however this conclusion needs further investigation. If this is the case, passive mechanisms such as structural compliance may contribute towards stabilisation, as demonstrated using computational and experimental models of a simple glider [220]. Passive stabilisation mechanisms have also been suggested for bats [219]. A hypothetical scenario for passive pitch stabilisation was described (figure 5.33), and represents a potential area of future research.

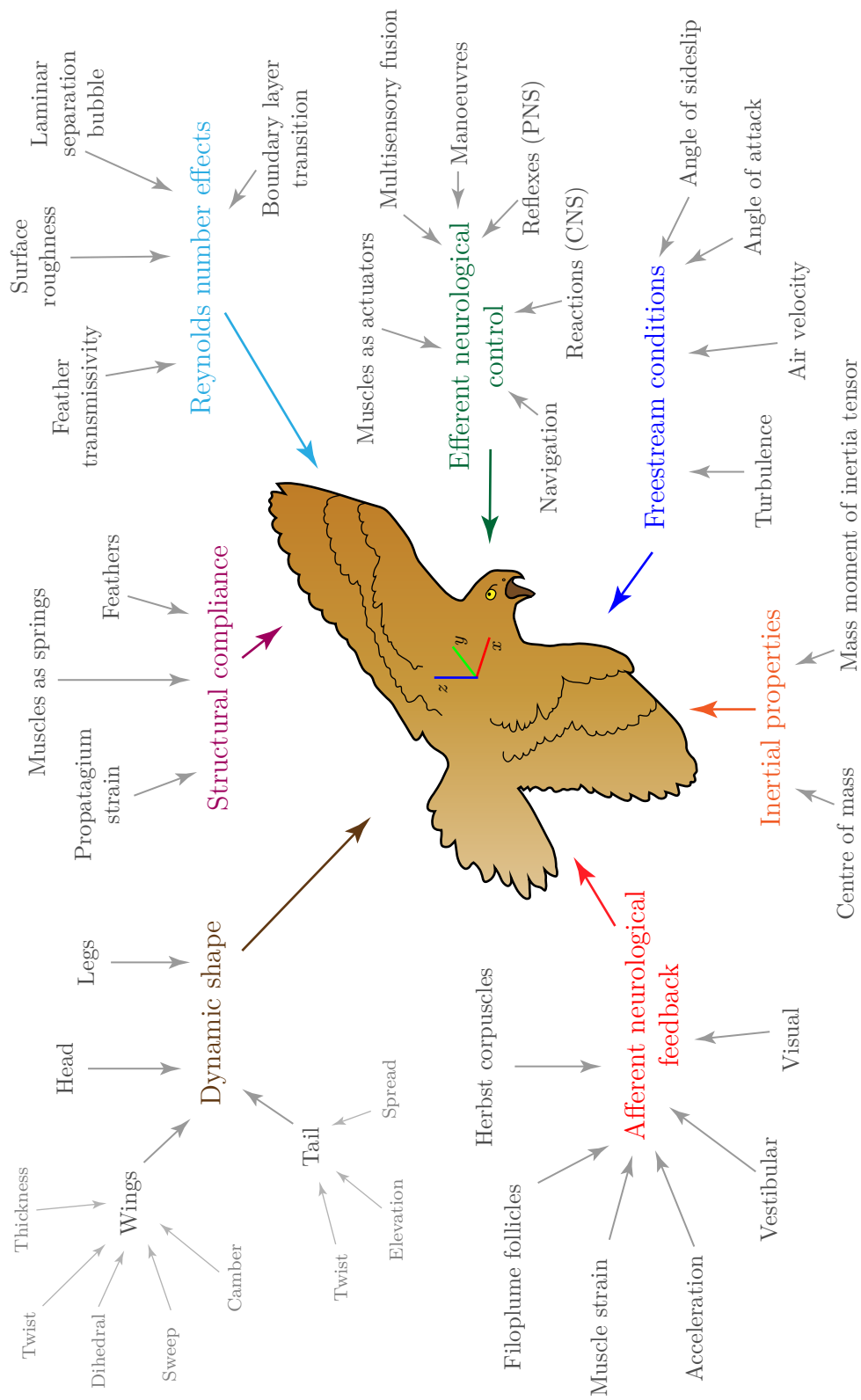


Fig. 6.1 The flight dynamics of birds is the result of numerous, complex interacting phenomena. PNS = peripheral nervous system, CNS = central nervous system.

The significant gap between the current model and the ideal integrated system (figure 6.1) provides a helpful conceptual framework within which to identify future research objectives. The ‘dynamic shape’ aspects could be better captured if the photogrammetry method was developed for use with high-speed video. This would allow dynamic morphing during manoeuvres and perturbations to be analysed in more detail, providing data on time-varying wing and tail geometry¹. These measurements could be coupled to an inertial model, based on the CT data from chapter 4, with time-varying moments of inertia similar to those performed in previous studies [158, 166]. Concepts from the field of ‘highly flexible aircraft’ could then be used to develop non-linear flight dynamics models that would more accurately capture the system behaviour [226]. Due to the sheer complexity of measuring all the elements of figure 6.1, especially structural compliance and the neurological aspects, it may be that some form of ‘robot-inspired biology’ [225] may prove more fruitful for understanding avian flight control than direct measurements of free-gliding birds. This approach utilises bio-mimicry as a means of better understanding biological systems. For example, a future project could include the development of inherently unstable unmanned air vehicles, of similar size and shape to free-gliding birds, capable of trialling different stabilisation mechanisms. It would be interesting to introduce compliant features to the lifting surfaces, capable of passive stabilisation, similar to the very simple model glider created by Krus [220]. These compliant features could be combined with feedback control to understand the extent to which compliance can ‘buy time’ for the control system to work effectively, as hypothesized in chapter 5 for birds. Pressure sensors have already been applied to UAVs to understand whether the reduced lag times associated with these can improve gust rejection capability [34]. This might suggest that birds utilise similar afferent pressure signals to reduce the lag time of their control responses compared with the slower inertial signals.

In summary, this work highlighted the highly unstable gliding flight configurations of a barn owl and peregrine falcon that may indicate a high degree of manoeuvrability in these birds. If more bird species, individuals and flights are analysed in future research, it would build support for the hypothesis of an evolutionary drive towards instability [8, 9, 80], which makes sense given the ‘arms race’ between predator and prey in these birds [155] and the lower energy consumption during flight due to the improved lift-to-drag ratios compared with a stable system [9, 76]. This work provides a potentially important insight for the design and development of ‘agile autonomous’

¹This is what is meant by ‘dynamic shape’

UAVs: instability may be helpful as a means of coping with adverse atmospheric turbulence, given suitably fast stabilisation mechanisms. Furthermore, these mechanisms could represent some combination of passive structural ‘preflexive feedback’ [42] with active feedback control, a strategy that should be further explored for UAVs. The methods and models developed through this project could have a significant long-term impact within the field of bird flight. We hope that their continued development will contribute towards a deeper understanding of these fascinating animals.

FLIGHT VIDEOS

For the purposes of review, the video data can be accessed via the following url:

https://drive.google.com/open?id=1gF_tHuASQ3qojElPqI2oXXPNOINwd4By

Here we describe relevant details for the videos of the barn owl and peregrine flights. In each case, the video is slowed down by a factor of four. The barn owl flights are labelled O1-O3 and peregrine flights are labelled P1-P3.

Tower.MP4

The camera was positioned on the first platform level of the mobile access tower. Cameras 5-8 are visible in the scene, along with the video camera used to obtain Field.MP4 (see below). The white sheet was used to increase the illumination of the ventral surface.

Field.MP4

The camera was positioned approximately 10 m from the centre of the measurement volume and shows the access tower used to support cameras 1-4 and the video camera used to obtain Tower.MP4 (see above).

O1_P1_pointClouds.MP4

This video shows the reconstructed raw points with the edges removed for flights O1 and P1. Each sequence contains complete visualisations of the raw points combined with sections taken at regular intervals along the span.

PRINCIPLE AXES AND COMPONENTS OF INERTIA

B.1 Visualisation of principle axes of inertia

Figure B.1 shows the orientation of the principle axes of inertia of the CT scanned cadavers in their ‘as scanned’ configuration. As expected, the axes are generally similar to the ‘wing-body’ coordinate system (see chapter 2 figure 2.6), although the orientation about the z -axis is usually rotated due to asymmetries. The transformations to the principle axes were checked by calculating the products of inertia and ensuring they were zero. There was a negligible difference between the principle components of inertia and the diagonal components of the inertia tensor when the data was in ‘bird coordinates’ (see chapter 3 section 4.4.2 and section B.2).

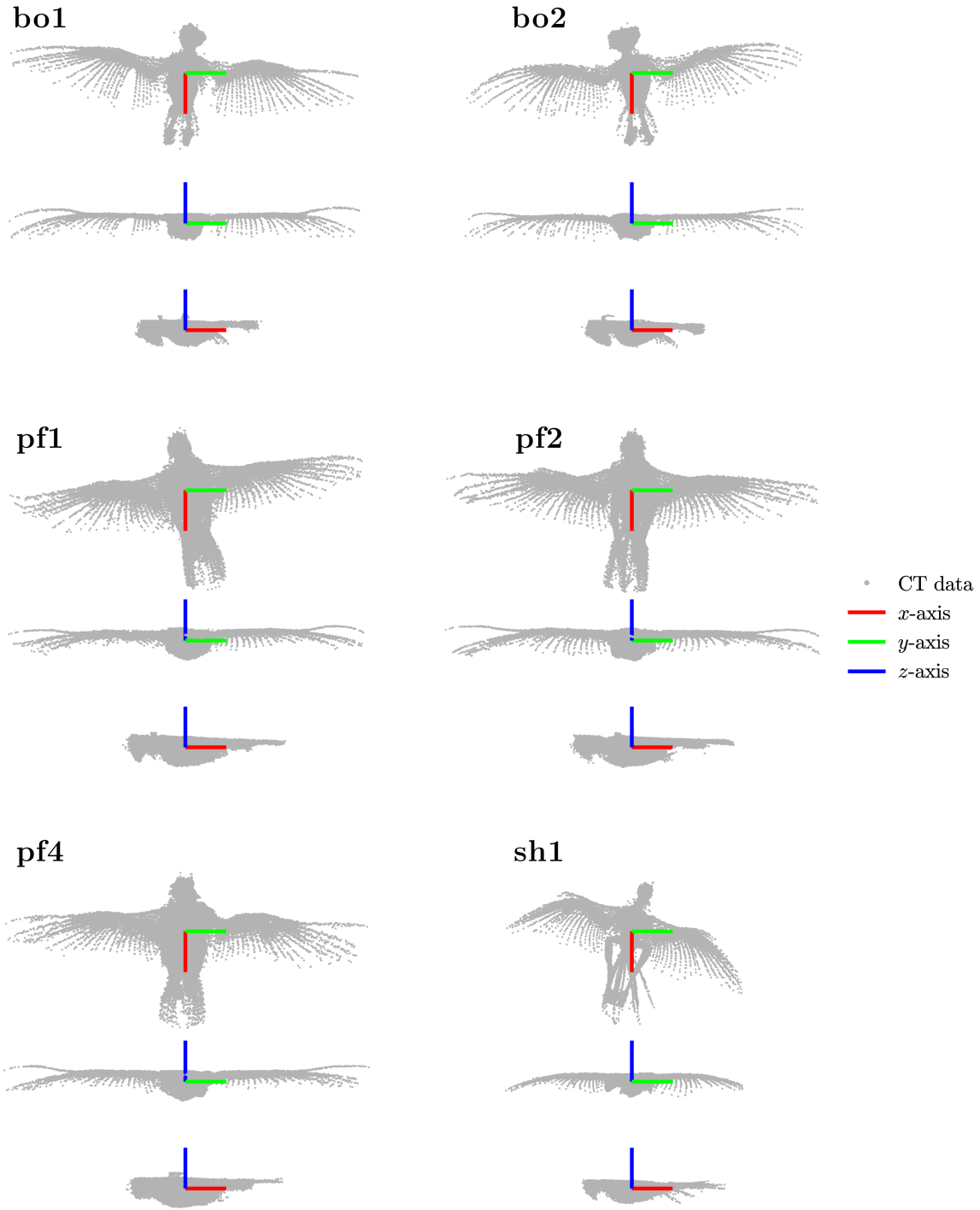


Fig. B.1 Visualisation of the principal axes of inertia relative to the CT scan data for barn owl cadavers bo1 and bo2, peregrine cadavers pf1, pf2 and pf4 and the sparrow hawk cadaver sh1. As shown in section B.2, there is negligible difference between the diagonal elements of the inertia tensor in bird coordinates and the principle components of inertia.

B.2 Inertia tensor data

All inertia data is in kg.m^2

B.2.1 Reference tables

Tensor	bo1	bo2	pf1	pf2	pf4	sh1
Bird coordinates	B.1	B.3	B.5	B.7	B.9	B.11
PCI coordinates	B.2	B.4	B.6	B.8	B.10	B.12

Table B.1 Inertia tensors for the ‘as scanned’ configuration (i.e. not aligned to flight position), where ‘PCI’ refers to principle components of inertia. The coordinate system origin was at the centre of mass.

Tensor	bo1	pf4
O1/P1	B.13	B.17
O2/P2	B.14	B.18
O3/P3	B.15	B.19
OR/PR	B.16	B.20

Table B.2 Principle components of inertia estimation for the free-gliding barn owl (O1-O3) and peregrine (P1-P3) flights based on virtual dissection of cadavers bo1 and pf4. The cadaver CT data was dissected and aligned to the photogrammetric surface data to obtain the estimates. Since care was made to align both photogrammetric surface data and the CT data (see Appendix C), these tensors may be used to isolate the influence of wing morphing on the centre of mass and moments of inertia. Also included are the data for cadavers scanned with wings fully retracted. The coordinate system origin was at the centre of mass.

Tensor	bo1	pf4
O1/P1	B.21	B.24
O2/P2	B.22	B.25
O3/P3	B.23	B.26

Table B.3 Inertia tensor estimation for the free-gliding barn owl (O1-O3) and peregrine (P1-P3) flights based on virtual dissection of cadavers bo1 and pf4. These are the moments of inertia used for the flight dynamics analysis in chapter 5, and were taken about the centre of mass but not transformed to principle axes of inertia. The orientation of the axes was equivalent to ‘wing-body’ coordinates, defined in chapter 2 figure 2.6.

B.2.2 Tensors - table B.1

$$\begin{bmatrix} 1.122 \times 10^{-3} & 3.447 \times 10^{-5} & -7.805 \times 10^{-6} \\ 3.447 \times 10^{-5} & 8.069 \times 10^{-4} & 1.262 \times 10^{-6} \\ -7.805 \times 10^{-6} & 1.262 \times 10^{-6} & 1.815 \times 10^{-3} \end{bmatrix} \quad (\text{B.1})$$

$$\begin{bmatrix} 1.125 \times 10^{-3} & 0 & 0 \\ 0 & 8.0318 \times 10^{-4} & 0 \\ 0 & 0 & 1.815 \times 10^{-3} \end{bmatrix} \quad (\text{B.2})$$

$$\begin{bmatrix} 1.038 \times 10^{-3} & -2.706 \times 10^{-5} & -2.096 \times 10^{-5} \\ -2.706 \times 10^{-5} & 7.120 \times 10^{-4} & 7.729 \times 10^{-6} \\ -2.096 \times 10^{-5} & 7.729 \times 10^{-6} & 1.665 \times 10^{-3} \end{bmatrix} \quad (\text{B.3})$$

$$\begin{bmatrix} 1.039 \times 10^{-3} & 0 & 0 \\ 0 & 7.097 \times 10^{-4} & 0 \\ 0 & 0 & 1.666 \times 10^{-3} \end{bmatrix} \quad (\text{B.4})$$

$$\begin{bmatrix} 2.875 \times 10^{-3} & -1.080 \times 10^{-4} & -6.516 \times 10^{-5} \\ -1.080 \times 10^{-4} & 2.019 \times 10^{-3} & 2.767 \times 10^{-5} \\ -6.516 \times 10^{-5} & 2.767 \times 10^{-5} & 4.611 \times 10^{-3} \end{bmatrix} \quad (\text{B.5})$$

$$\begin{bmatrix} 2.886 \times 10^{-3} & 0 & 0 \\ 0 & 2.006 \times 10^{-3} & 0 \\ 0 & 0 & 4.614 \times 10^{-3} \end{bmatrix} \quad (\text{B.6})$$

$$\begin{bmatrix} 2.654 \times 10^{-3} & 3.049 \times 10^{-5} & -5.496 \times 10^{-5} \\ 3.049 \times 10^{-5} & 2.015 \times 10^{-3} & -2.384 \times 10^{-5} \\ -5.496 \times 10^{-5} & -2.384 \times 10^{-5} & 4.367 \times 10^{-3} \end{bmatrix} \quad (\text{B.7})$$

$$\begin{bmatrix} 2.653 \times 10^{-3} & 0 & 0 \\ 0 & 2.014 \times 10^{-3} & 0 \\ 0 & 0 & 4.369 \times 10^{-3} \end{bmatrix} \quad (\text{B.8})$$

$$\begin{bmatrix} 3.077 \times 10^{-3} & 3.361 \times 10^{-5} & -5.184 \times 10^{-5} \\ 3.360 \times 10^{-5} & 2.150 \times 10^{-3} & -2.756 \times 10^{-6} \\ -5.184 \times 10^{-5} & -2.756 \times 10^{-6} & 4.898 \times 10^{-3} \end{bmatrix} \quad (\text{B.9})$$

$$\begin{bmatrix} 3.077 \times 10^{-3} & 0 & 0 \\ 0 & 2.149 \times 10^{-3} & 0 \\ 0 & 0 & 4.900 \times 10^{-3} \end{bmatrix} \quad (\text{B.10})$$

$$\begin{bmatrix} 5.565 \times 10^{-4} & -7.120 \times 10^{-6} & -1.656 \times 10^{-5} \\ -7.120 \times 10^{-6} & 5.809 \times 10^{-4} & -4.391 \times 10^{-6} \\ -1.656 \times 10^{-5} & -4.391 \times 10^{-6} & 1.094 \times 10^{-3} \end{bmatrix} \quad (\text{B.11})$$

$$\begin{bmatrix} 5.541 \times 10^{-4} & 0 & 0 \\ 0 & 5.829 \times 10^{-4} & 0 \\ 0 & 0 & 1.094 \times 10^{-3} \end{bmatrix} \quad (\text{B.12})$$

B.2.3 Tensors - Table B.2

$$\begin{bmatrix} 1.129 \times 10^{-3} & 0 & 0 \\ 0 & 8.947 \times 10^{-4} & 0 \\ 0 & 0 & 1.914 \times 10^{-3} \end{bmatrix} \quad (\text{B.13})$$

$$\begin{bmatrix} 1.162 \times 10^{-3} & 0 & 0 \\ 0 & 8.462 \times 10^{-4} & 0 \\ 0 & 0 & 1.878 \times 10^{-3} \end{bmatrix} \quad (\text{B.14})$$

$$\begin{bmatrix} 1.108 \times 10^{-3} & 0 & 0 \\ 0 & 8.267 \times 10^{-4} & 0 \\ 0 & 0 & 1.807 \times 10^{-3} \end{bmatrix} \quad (\text{B.15})$$

$$\begin{bmatrix} 1.927 \times 10^{-4} & 0 & 0 \\ 0 & 8.421 \times 10^{-4} & 0 \\ 0 & 0 & 9.222 \times 10^{-4} \end{bmatrix} \quad (\text{B.16})$$

$$\begin{bmatrix} 3.013 \times 10^{-3} & 0 & 0 \\ 0 & 2.189 \times 10^{-3} & 0 \\ 0 & 0 & 4.908 \times 10^{-3} \end{bmatrix} \quad (\text{B.17})$$

$$\begin{bmatrix} 2.433 \times 10^{-3} & 0 & 0 \\ 0 & 2.336 \times 10^{-3} & 0 \\ 0 & 0 & 4.499 \times 10^{-3} \end{bmatrix} \quad (\text{B.18})$$

$$\begin{bmatrix} 2.201 \times 10^{-3} & 0 & 0 \\ 0 & 2.530 \times 10^{-3} & 0 \\ 0 & 0 & 4.460 \times 10^{-3} \end{bmatrix} \quad (\text{B.19})$$

$$\begin{bmatrix} 7.216 \times 10^{-4} & 0 & 0 \\ 0 & 2.189 \times 10^{-3} & 0 \\ 0 & 0 & 2.589 \times 10^{-3} \end{bmatrix} \quad (\text{B.20})$$

B.2.4 Tensors - Table B.3

$$\begin{bmatrix} 1.127 \times 10^{-3} & -3.681 \times 10^{-5} & 5.425 \times 10^{-5} \\ -3.681 \times 10^{-5} & 9.006 \times 10^{-4} & -1.757 \times 10^{-5} \\ 5.425 \times 10^{-5} & -1.757 \times 10^{-5} & 1.910 \times 10^{-3} \end{bmatrix} \quad (\text{B.21})$$

$$\begin{bmatrix} 1.163 \times 10^{-3} & -3.010 \times 10^{-5} & 5.058 \times 10^{-5} \\ -3.010 \times 10^{-5} & 8.495 \times 10^{-4} & 1.425 \times 10^{-5} \\ 5.058 \times 10^{-5} & 1.425 \times 10^{-5} & 1.874 \times 10^{-3} \end{bmatrix} \quad (\text{B.22})$$

$$\begin{bmatrix} 1.103 \times 10^{-3} & -5.519 \times 10^{-5} & 6.460 \times 10^{-5} \\ -5.519 \times 10^{-5} & 8.378 \times 10^{-4} & -8.453 \times 10^{-6} \\ 6.460 \times 10^{-5} & -8.453 \times 10^{-6} & 1.801 \times 10^{-3} \end{bmatrix} \quad (\text{B.23})$$

$$\begin{bmatrix} 3.034 \times 10^{-3} & -7.224 \times 10^{-5} & 2.204 \times 10^{-4} \\ -7.224 \times 10^{-5} & 2.195 \times 10^{-3} & -5.835 \times 10^{-5} \\ 2.204 \times 10^{-4} & -5.835 \times 10^{-5} & 4.880 \times 10^{-3} \end{bmatrix} \quad (\text{B.24})$$

$$\begin{bmatrix} 2.385 \times 10^{-3} & -4.907 \times 10^{-5} & -1.808 \times 10^{-5} \\ -4.907 \times 10^{-5} & 2.383 \times 10^{-3} & -3.454 \times 10^{-5} \\ -1.808 \times 10^{-4} & -3.454 \times 10^{-5} & 4.499 \times 10^{-3} \end{bmatrix} \quad (\text{B.25})$$

$$\begin{bmatrix} 2.203 \times 10^{-3} & 4.666 \times 10^{-6} & -7.844 \times 10^{-5} \\ 4.666 \times 10^{-6} & 2.531 \times 10^{-3} & 3.111 \times 10^{-5} \\ -7.844 \times 10^{-5} & 3.111 \times 10^{-5} & 4.457 \times 10^{-3} \end{bmatrix} \quad (\text{B.26})$$

CONSISTENT CADAVER ALIGNMENT

When assessing the influence of geometric configuration on the position of the centre of mass and the principal components of inertia, it was necessary to ensure consistent alignment of the CT-scanned cadaver data with the photogrammetric surface measurements of the free-gliding birds described in chapter 3. Consistency was achieved when the intra- and inter-flight positions of the head, cervical spine/neck and body were consistent, such that only movement of the wings and legs (tibiotarsae, tarsometatarsae & digits) between flights was captured. ‘Intra-flight’ consistency refers to the consistent alignment of multiple cadavers to a single flight while ‘inter-flight’ consistency refers to consistent alignment between flights across all cadavers. Both types of alignment consistency were required to isolate the effect of wing configuration changes between flights and cadavers on CoM and MoI changes. Figures C.1 to C.2 describe the process of intra-flight alignment while figure C.3 shows the inter-flight alignment process.

To achieve intra-flight alignment, a single cadaver was selected from each species to act as a ‘master’ cadaver, while the remaining cadavers acted as ‘slave’ cadavers (figure C.1). The CT data for both master and slave cadavers was virtually dissected into the various appendages described in chapter 4. A threshold was then applied to the scan data using an absolute density of 1100 kg/m^3 , leaving mainly the skeletal structure (i.e. the bones). The bones from the appendages of the slave cadavers were then aligned to the bones from the master cadaver using iterative-closest-point alignment in CloudCompare [143]. The resulting transformation matrices were then applied to the data without the applied threshold. This process ensured that the positions of the appendages were consistent in their ‘as-scanned’ configurations.

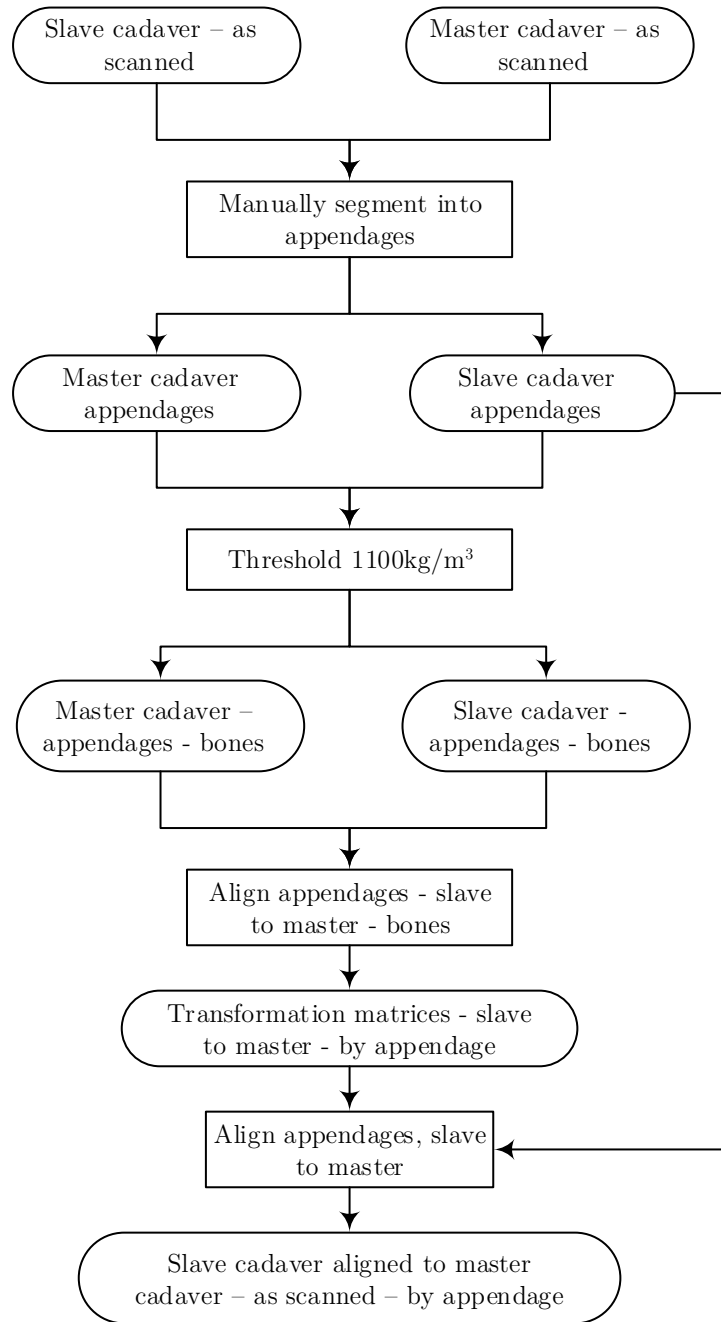


Fig. C.1 The first step towards intra-flight alignment was ensure all cadavers of the same species were aligned in their ‘as scanned’ configuration. This was done by aligning ‘slave’ cadavers to a single ‘master’ cadaver using the skeletal elements of various appendages for the alignment process.

Intra-flight consistency was then achieved by aligning the master cadaver to

the photogrammetric surface data for each flight. During this process, accuracy was achieved by aligning distinctive visual features in both the CT and photogrammetric data, such as the beak, eyes and feet. The alignment of the wings did not require distinctive visual features, since the geometry alone was sufficient to ensure accurate alignment. The transformation matrices for aligning each appendage of the master cadaver were then applied to the slave cadavers, ensuring consistent intra-flight alignment, since the cadavers were already precisely aligned from the previous step (see figure C.1).

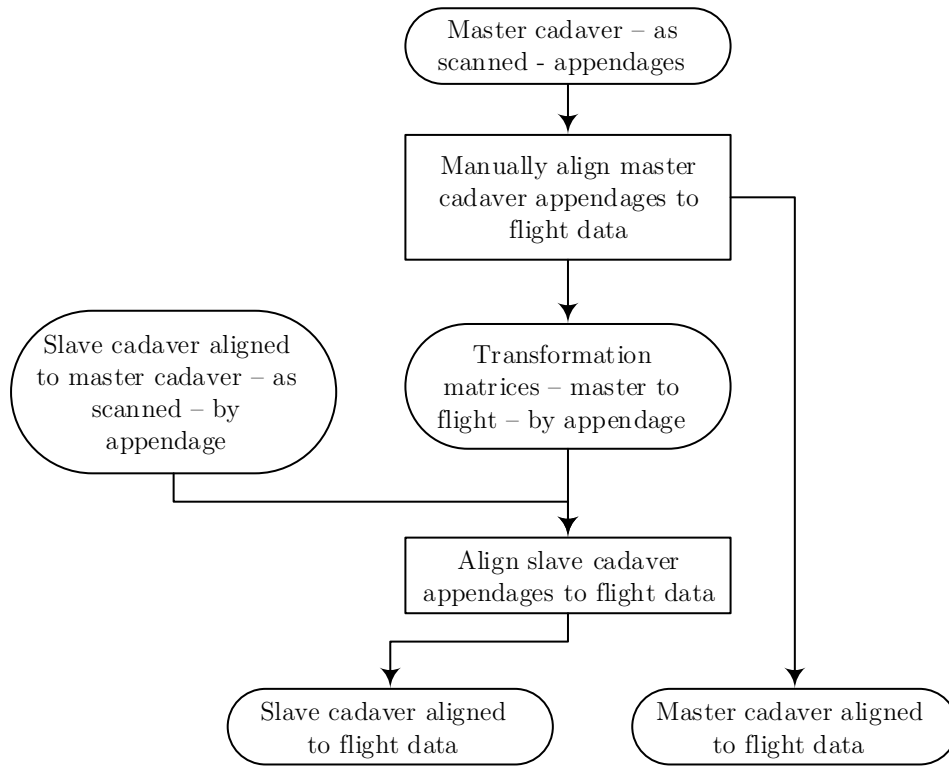


Fig. C.2 Intra-flight alignment of the cadavers was achieved by manually aligning the ‘master’ cadaver appendages to the photogrammetric surface data for each flight, and then by applying the same transformation matrices for each appendage to the slave cadavers which had already been aligned to the master cadaver in the previous step (see figure C.1).

To ensure inter-flight alignment, a ‘master’ flight was selected from the photogrammetric datasets (referred to here as ‘flight data’), with the remaining datasets acting as ‘slave’ flight data. The wings and tail were then manually segmented from the body for the flight data, and iterative-closest-point alignment [143] was used to align

the slave flight data to the master flight data. These transformations were then applied to the master and slave cadaver data, after completion of the intra-flight alignment process. The head, neck and body master cadaver data from the slave flights was then aligned to the master cadaver data from the master flight, again using iterative-closest-point alignment [143]. The transformation matrices obtained were then applied to the slave cadavers aligned to the slave flights to obtain consistent inter-flight alignment of the cadavers. The final results of this process are shown in figure C.4.

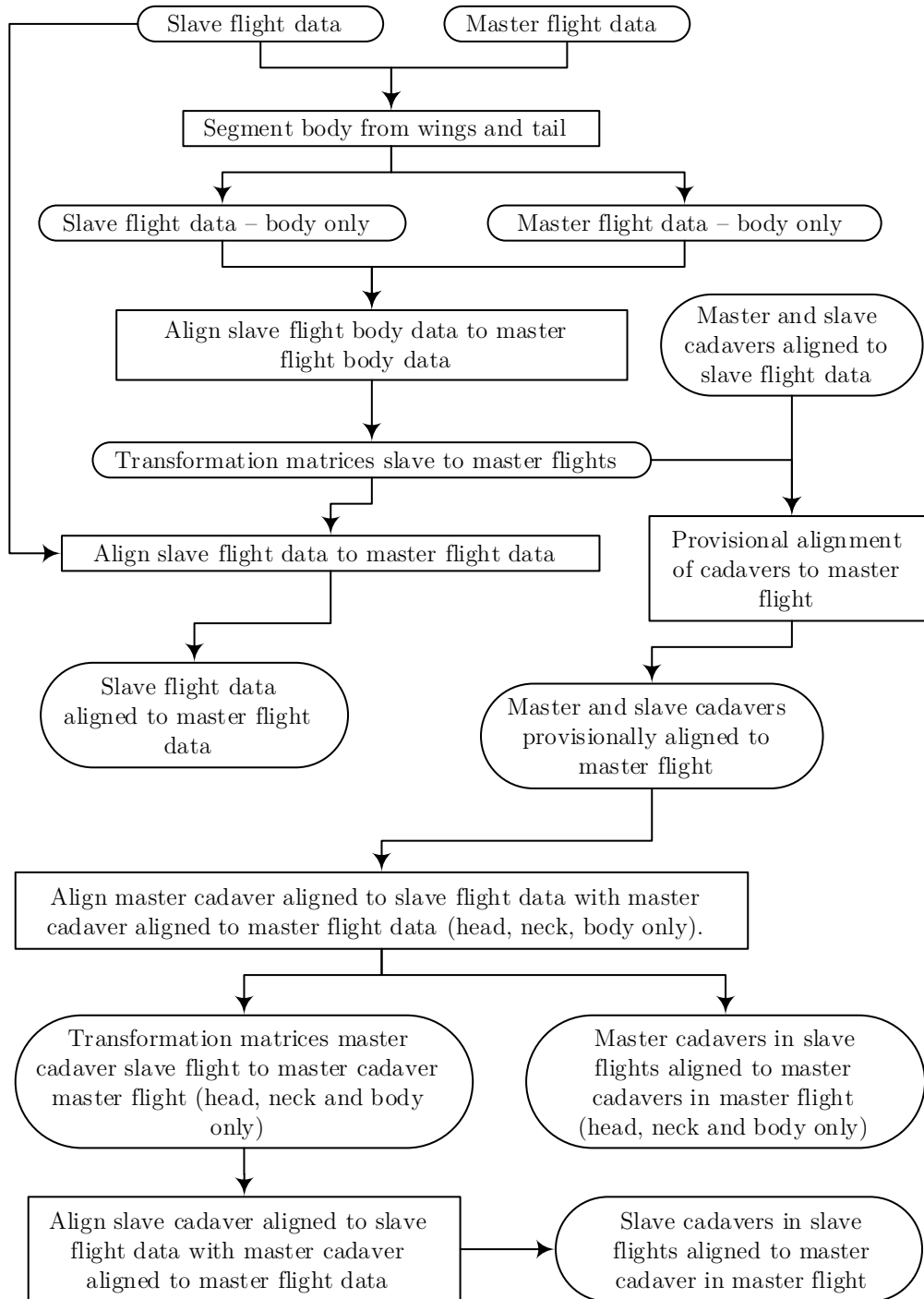


Fig. C.3 Inter-flight alignment process. It is essential here to distinguish ‘flight data’ (photogrammetric surface reconstructions) and ‘cadaver data’ (CT scanned cadaver data). The ‘master’ and ‘slave’ cadavers are defined in the same way as for the intra-flight alignment process. The ‘master’ flight data was used as a fixed reference to which the ‘slave’ flight data was aligned, along with the master and slave cadavers aligned to these slave flights.

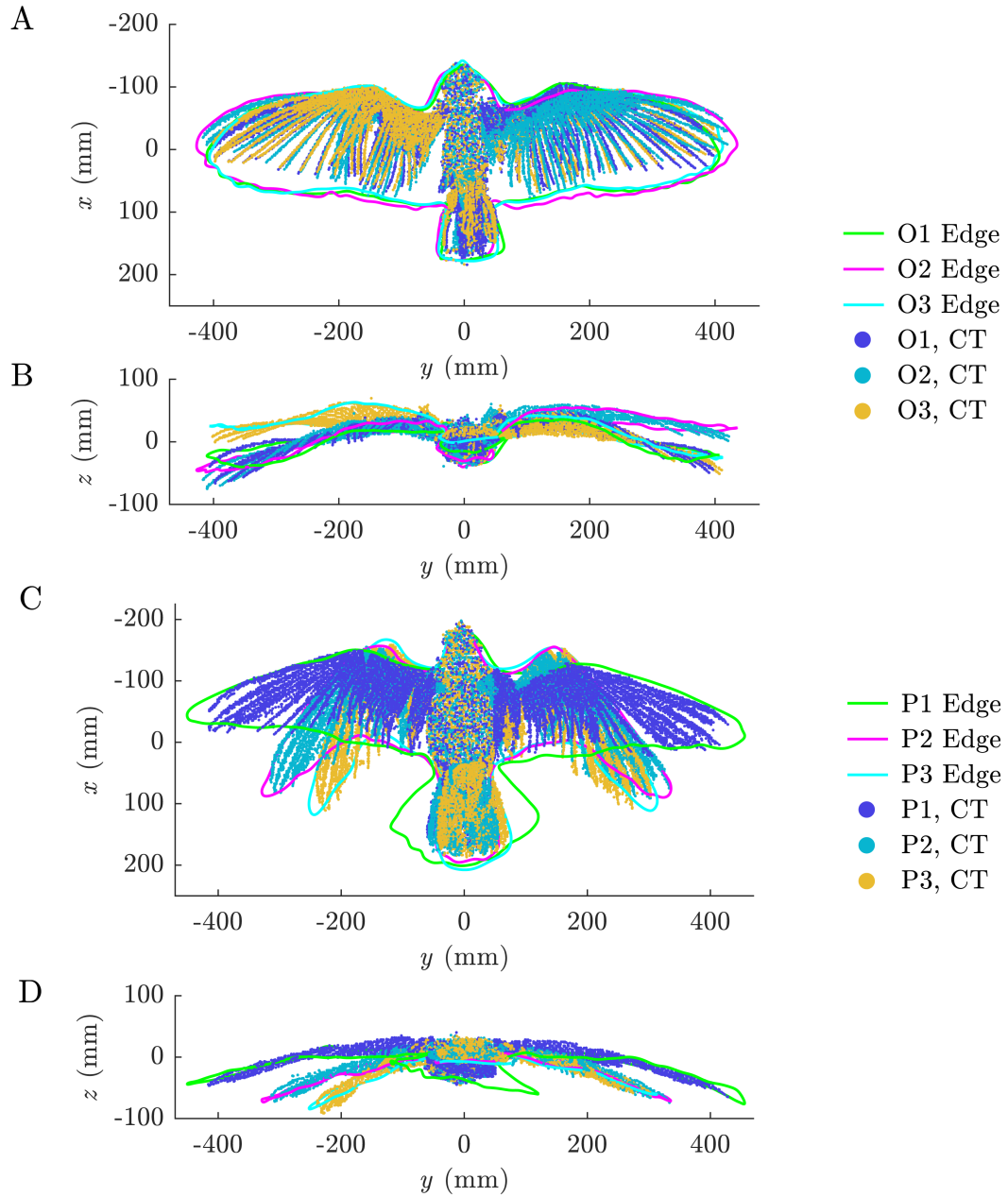


Fig. C.4 CT scan data for all cadavers (bo1, bo2, pf1, pf2 and pf4) aligned to the photogrammetric reconstructions, showing both intra- and inter-flight consistency - i.e. only the wings and legs change position within and between flights. From the photogrammetric reconstructions, only the ‘edge spline’ is shown for clarity. A) Barn owl dorsoventral view B) barn owl posteroanterior view C) peregrine dorsoventral view D) peregrine posteroanterior view.

APPENDIX D

AVL CONCISE DERIVATIVE CHECK

D.1 Summary

The coupled, linearised, rigid-body six-degree-of-freedom equations of motion in matrix form, referred to body axes (equations (D.1) to (D.7)) were converted to concise form by pre-multiplying both sides by the inverse of the mass matrix to obtain equations (D.8) to (D.10). This is an important step in linearised flight dynamics analysis yet prone to error due to the large number of equations and variables involved, the differences between British and North American conventions (see below), and the potential for confusion between wind and body axes. Here, the process behind this conversion is described and comparisons made, based on data for flight O1, between the AVL results and of those based on several widely available textbooks [38, 96]. It was found that although the majority of the AVL conversions were either identical or within 1% of the textbook values, three of the lateral-directional concise derivatives, n_v , n_p and n_r were significantly different, and could represent a calculation error in AVL. The notation used here is identical with [38].

D.2 Calculation procedure

The symbolic concise form the state matrix, \mathbf{A} in equations (D.8) and (D.9), was calculated using Mupad [139]. The equations of motion assume that I_{xy} and I_{yz} were zero. This assumption is not strictly true given the subtle asymmetries of flight O1, however including the terms had negligible influence on the results of the procedure, while significantly increasing the number of terms in the equations. Hence, for simplicity, the assumption was maintained. The results are shown in table D.4 based on the assumption adopted by AVL that the acceleration derivatives are zero. This assumption is typical of subsonic flight dynamics analysis for conventional aircraft configurations, since the acceleration derivatives are usually only significant for craft such as airships and combat aircraft. These equations agreed with both available text-

books, and were subsequently used to check the AVL conversions. Since the control derivative matrix, \mathbf{B}' , and control vector, $\mathbf{u}(t)$, were both zero, conversions to concise form of control derivatives was not required. It is important to note that the equations of motion (equations (D.1) to (D.7)) are referred to body axes, with dimensional derivatives (denoted by the small circle) defined according to British notation. To carry out conversion to concise derivatives defined by (equations (D.1) to (D.10)) and table D.4, it was necessary to convert the North American non-dimensional derivatives in body axes generated by AVL into British dimensional derivatives. This was done by first converting the North American non-dimensional derivatives into British non-dimensional derivatives (table D.2), and then applying British dimensionalisation multipliers (table D.3). North American and British conventions differ for both dimensional and non-dimensional derivatives, and care was taken to ensure the correct calculation procedure was followed.

D.3 Results

Table D.1 shows a comparison between values of the de-coupled concise derivatives calculated by AVL and using table D.4 for flight O1. The tables show that half the conversions are identical with the textbook-based estimates and another nine show negligible differences of approximately 1% or less. However, n_v , n_p and n_r show factors of 1 to 10 times the AVL estimates. If the conversion to dimensional British derivatives described above was somehow in error, it would likely result in significant differences to l_v , l_p and l_r (see table D.4). Since both textbook references agree with the Mupad estimations of table D.4, it seems likely that the AVL estimates were in error.

Concise derivative	AVL conversion	Check	% difference
x_u	-0.2655	-0.2655	0%
z_u	-1.8415	-1.8415	0%
m_u	-24.2399	-24.5261	1.2%
x_w	1.0931	1.0931	0%
z_w	-9.2702	-9.2702	0%
m_w	90.6755	91.3150	0.7%
x_q	-0.3835	-0.3835	0%
z_q	8.2078	8.2078	0%
m_q	-3.4674	-3.5046	1.1%
x_θ	-9.7215	-9.7215	0%
z_θ	-1.3144	-1.3144	0%
m_θ	0	0	0%
y_v	-0.2518	-0.2518	0%
l_v	22.3600	22.6279	1.2%
n_v	-1.9475	-3.3978	74%
y_p	0.5409	0.5409	0%
l_p	-72.0952	-71.5066	0.8%
n_p	-7.0770	-2.4801	285%
y_r	-8.7526	-8.7526	0%
l_r	25.8131	25.9102	0.4%
n_r	-0.1781	-1.8356	1030%
y_ϕ	9.7215	9.7215	0%
l_ϕ	0	0	0%
n_ϕ	0	0	0%

Table D.1 Check results for the AVL conversion to concise derivatives.

D.4 Equations

$$\mathbf{M}\dot{\mathbf{x}}(t) = \mathbf{A}'\mathbf{x}(t) + \mathbf{B}'\mathbf{u}(t) \quad (\text{D.1})$$

$$\mathbf{M} = \begin{bmatrix} m & -\dot{X}_{\dot{w}} & 0 & 0 & 0 & 0 & 0 & 0 & 0 \\ 0 & m - \dot{Z}_{\dot{w}} & 0 & 0 & 0 & 0 & 0 & 0 & 0 \\ 0 & -\dot{M}_{\dot{w}} & I_{yy} & 0 & 0 & -I_{xy} & -I_{yz} & 0 & 0 \\ 0 & 0 & 0 & 1 & 0 & 0 & 0 & 0 & 0 \\ 0 & -\dot{Y}_{\dot{w}} & 0 & 0 & m & 0 & 0 & 0 & 0 \\ 0 & -\dot{L}_{\dot{w}} & -I_{xy} & 0 & 0 & I_{xx} & -I_{xz} & 0 & 0 \\ 0 & -\dot{N}_{\dot{w}} & -I_{yz} & 0 & 0 & -I_{xz} & I_{zz} & 0 & 0 \\ 0 & 0 & 0 & 0 & 0 & 0 & 0 & 1 & 0 \\ 0 & 0 & 0 & 0 & 0 & 0 & 0 & 0 & 1 \end{bmatrix} \quad (\text{D.2})$$

$$\dot{\mathbf{x}}(t) = [\dot{u} \quad \dot{w} \quad \dot{q} \quad \dot{\theta} \quad \dot{v} \quad \dot{p} \quad \dot{r} \quad \dot{\phi} \quad \dot{\psi}]^T \quad (\text{D.3})$$

$$\mathbf{A}' = \begin{bmatrix} \dot{X}_u & \dot{X}_w & \dot{X}_q - mW_e & -mg\cos\theta_e & \dot{X}_v & \dot{X}_p & \dot{X}_r & 0 & 0 \\ \dot{Z}_u & \dot{Z}_w & \dot{Z}_q + mU_e & -mg\sin\theta_e & \dot{Z}_v & \dot{Z}_p & \dot{Z}_r & 0 & 0 \\ \dot{M}_u & \dot{M}_w & \dot{M}_q & 0 & \dot{M}_v & \dot{M}_p & \dot{M}_r & 0 & 0 \\ 0 & 0 & 1 & 0 & 0 & 0 & 0 & 0 & 0 \\ \dot{Y}_u & \dot{Y}_w & \dot{Y}_q & 0 & \dot{Y}_v & \dot{Y}_p + mW & \dot{Y}_r - mU & mg\cos\theta_e & mg\sin\theta_e \\ \dot{L}_u & \dot{L}_w & \dot{L}_q & 0 & \dot{L}_v & \dot{L}_p & \dot{L}_r & 0 & 0 \\ \dot{N}_u & \dot{N}_w & \dot{N}_q & 0 & \dot{N}_v & \dot{N}_p & \dot{N}_r & 0 & 0 \\ 0 & 0 & 0 & 0 & 0 & 1 & 0 & 0 & 0 \\ 0 & 0 & 0 & 0 & 0 & 0 & 1 & 0 & 0 \end{bmatrix} \quad (\text{D.4})$$

$$\mathbf{x}(t) = [u \quad w \quad q \quad \theta \quad v \quad p \quad r \quad \phi \quad \psi]^T \quad (\text{D.5})$$

$$\mathbf{B}' = [0]_{9 \times 9} \quad (\text{D.6})$$

$$\mathbf{u}(t) = [0]_{9 \times 1} \quad (\text{D.7})$$

$$\dot{\mathbf{x}}(t) = \mathbf{A}\mathbf{x}(t) + \mathbf{B}\mathbf{u}(t) \quad (\text{D.8})$$

$$\mathbf{A} = \begin{bmatrix} x_u & x_w & x_q & x_\theta & x_v & x_p & x_r & x_\phi & x_\psi \\ z_u & z_w & z_q & z_\theta & z_v & z_p & z_r & z_\phi & z_\psi \\ m_u & m_w & m_q & m_\theta & m_v & m_p & m_r & m_\phi & m_\psi \\ 0 & 0 & 1 & 0 & 0 & 0 & 0 & 0 & 0 \\ y_u & y_w & y_q & y_\theta & y_v & y_p & y_r & y_\phi & y_\psi \\ l_u & l_w & l_q & l_\theta & l_v & l_p & l_r & l_\phi & l_\psi \\ n_u & n_w & n_q & n_\theta & n_v & n_p & n_r & n_\phi & n_\psi \\ 0 & 0 & 0 & 0 & 0 & 1 & 0 & 0 & 0 \\ 0 & 0 & 0 & 0 & 0 & 0 & 1 & 0 & 0 \end{bmatrix} \quad (\text{D.9})$$

$$\mathbf{y}(t) = \mathbf{C}\mathbf{x}(t) + \mathbf{D}\mathbf{u}(t) \quad (\text{D.10})$$

D.5 Tables

North American	British
C_{X_u}	X_u
C_{X_w}	X_w
C_{X_q}	$2X_q$
C_{Z_u}	Z_u
C_{Z_w}	Z_w
C_{Z_q}	$2Z_q$
C_{M_u}	M_u
C_{M_w}	M_w
C_{M_q}	$2M_q$
C_{Y_v}	Y_v
C_{Y_p}	$2Y_p$
C_{Y_r}	$2Y_r$
C_{L_v}	L_v
C_{L_p}	$2L_p$
C_{L_r}	$2L_r$
C_{N_v}	N_v
C_{N_p}	$2N_p$
C_{N_r}	$2N_r$

Table D.2 Comparison between North American and British non-dimensional derivative notation [38].

Dimensionless	Multiplier	Dimensional
X_u	$\frac{1}{2}\rho V S$	\dot{X}_u
X_w	$\frac{1}{2}\rho V S$	\dot{X}_w
X_q	$\frac{1}{2}\rho V S \bar{c}$	\dot{X}_q
Z_u	$\frac{1}{2}\rho V S$	\dot{Z}_u
Z_w	$\frac{1}{2}\rho V S$	\dot{Z}_w
Z_q	$\frac{1}{2}\rho V S \bar{c}$	\dot{Z}_q
M_u	$\frac{1}{2}\rho V S \bar{c}$	\dot{M}_u
M_w	$\frac{1}{2}\rho V S \bar{c}$	\dot{M}_w
M_q	$\frac{1}{2}\rho V S \bar{c}^2$	\dot{M}_q
Y_v	$\frac{1}{2}\rho V S$	\dot{Y}_v
Y_p	$\frac{1}{2}\rho V S b$	\dot{Y}_p
Y_r	$\frac{1}{2}\rho V S b$	\dot{Y}_r
L_v	$\frac{1}{2}\rho V S b$	\dot{L}_v
L_p	$\frac{1}{2}\rho V S b^2$	\dot{L}_p
L_r	$\frac{1}{2}\rho V S b^2$	\dot{L}_r
N_v	$\frac{1}{2}\rho V S b$	\dot{N}_v
N_p	$\frac{1}{2}\rho V S b^2$	\dot{N}_p
N_r	$\frac{1}{2}\rho V S b^2$	\dot{N}_r

Table D.3 British non-dimensional to dimensional derivative conversion factors used [38]

Concise derivative	Conversion formula
x_u	$\frac{\dot{X}_u}{m}$
z_u	$\frac{\dot{Z}_u}{m}$
m_u	$\frac{\dot{M}_u}{I_{yy}}$
x_w	$\frac{\dot{X}_w}{m}$
z_w	$\frac{\dot{Z}_w}{m}$
m_w	$\frac{\dot{M}_w}{I_{yy}}$
x_q	$\frac{\dot{X}_q - mW_e}{m}$
z_q	$\frac{\dot{Z}_q + mU_e}{m}$
m_q	$\frac{\dot{M}_q}{I_{yy}}$
x_θ	$-g \cos \theta_e$
z_θ	$-g \sin \theta_e$
m_θ	0
y_v	$\frac{\dot{Y}_v}{m}$
y_p	$\frac{\dot{Y}_p + mW_e}{m}$
y_r	$\frac{\dot{Y}_r - mU_e}{m}$
y_ϕ	$g \cos \theta_e$
y_ψ	$g \sin \theta_e$
l_v	$\frac{I_{zz}\dot{L}_v + I_{xz}\dot{N}_v}{I_{xx}I_{zz} - I_{xz}^2}$
l_p	$\frac{I_{zz}\dot{L}_p + I_{xz}\dot{N}_p}{I_{xx}I_{zz} - I_{xz}^2}$
l_r	$\frac{I_{zz}\dot{L}_r + I_{xz}\dot{N}_r}{I_{xx}I_{zz} - I_{xz}^2}$
l_ϕ	0
l_ψ	0
n_v	$\frac{I_{zz}\dot{N}_v + I_{xz}\dot{L}_v}{I_{xx}I_{zz} - I_{xz}^2}$
n_p	$\frac{I_{zz}\dot{N}_p + I_{xz}\dot{L}_p}{I_{xx}I_{zz} - I_{xz}^2}$
n_r	$\frac{I_{zz}\dot{N}_r + I_{xz}\dot{L}_r}{I_{xx}I_{zz} - I_{xz}^2}$
n_ϕ	0
n_ψ	0

Table D.4 Formulae for conversion from British dimensional aerodynamic derivatives in body axes to their concise form [38, 96].

ADDITIONAL FLIGHT DYNAMICS DATA

E.1 Root locus plots

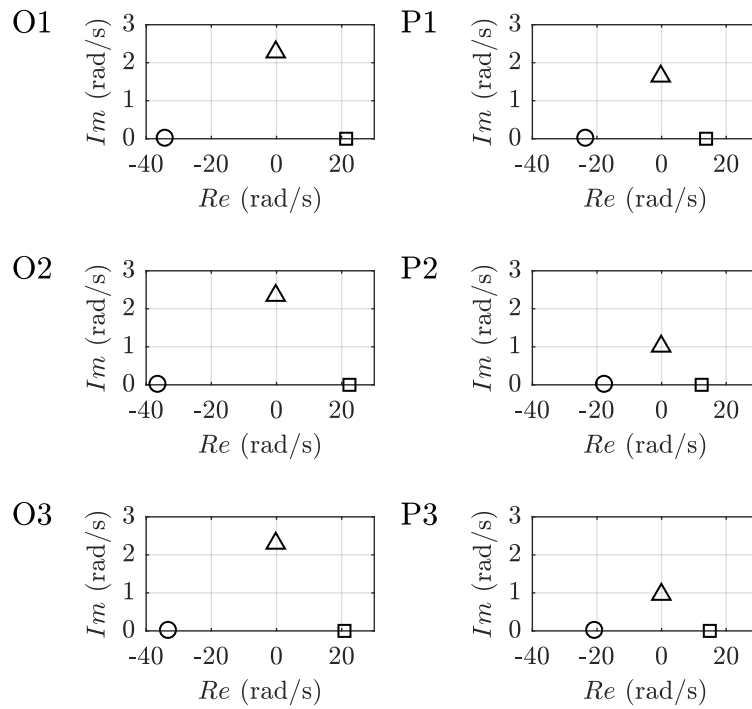


Fig. E.1 Root locus plots showing uncorrected de-coupled longitudinal AVL modes modelled with a thick body for the barn owl (O1-O3) and peregrine (P1-P3) flights. Compare with chapter 5 figure 5.24 where the equivalent plot is provided with corrected AVL derivatives.

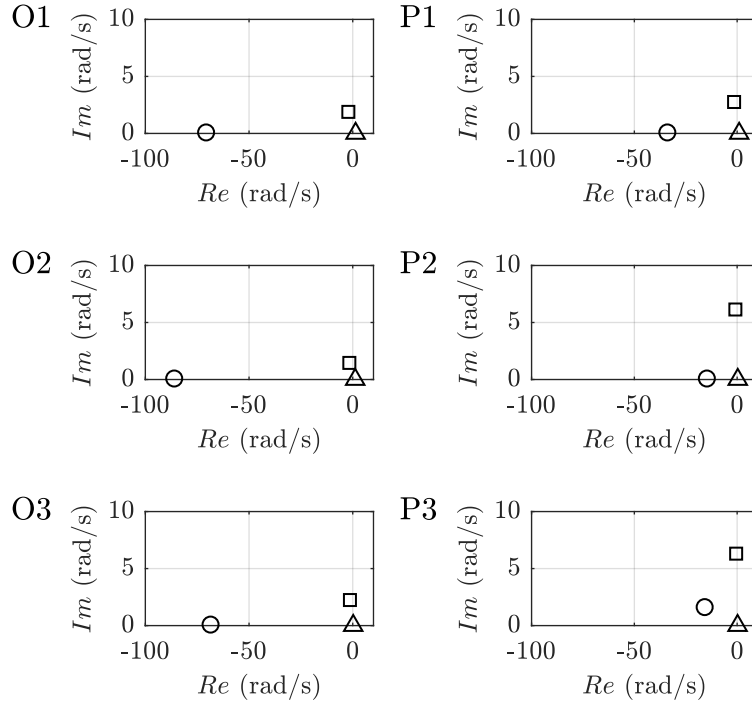


Fig. E.2 Root-locus plots showing the coupled, lateral-directional, corrected AVL modes modelled without a thick torso for the barn owl (O1-O3) and peregrine (P1-P3) flights. Similar to figure 5.27, the circle represents roll-subsidence mode, the triangle represents the spiral mode and the square represents an over-damped dutch roll mode for O1-O3 and P1, and a more conventional dutch roll mode for P2 and P3. Although the roll-subsidence mode for P3 is complex, the damping is so high that it behaves effectively as a non-oscillatory roll-subsidence mode.

E.2 Time histories

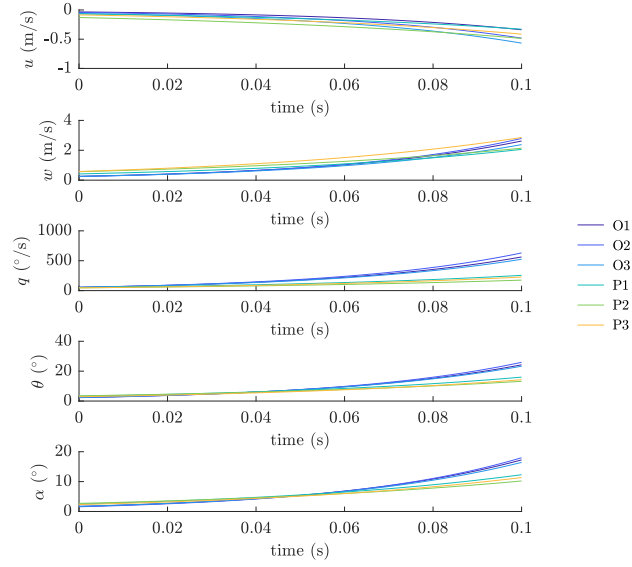


Fig. E.3 Time-history for the highly unstable pitch divergence mode (see figure 5.24) for the barn owl (O1-O3) and peregrine (P1-P3) flights showing perturbations in body axis coordinates of forward velocity, u , vertical velocity, w , pitch rate, q , pitch attitude, θ , and angle of incidence, α , from the initial flight condition.

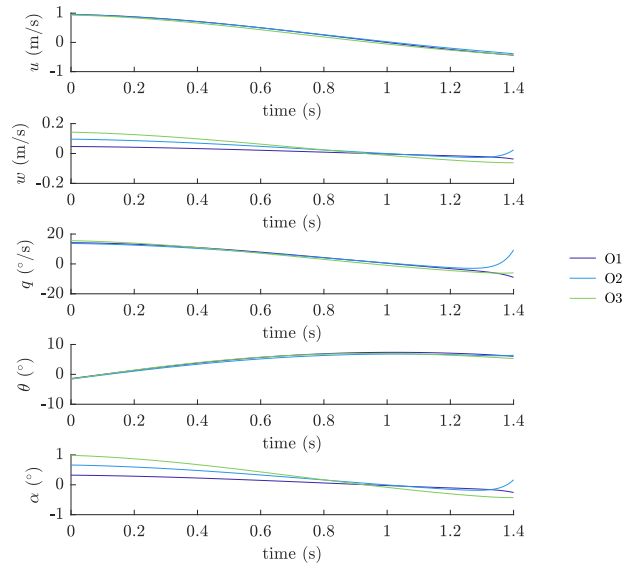


Fig. E.4 Time-history for the third oscillatory mode for the barn owl (O1-O3) flights showing perturbations in body axis coordinates of forward velocity, u , vertical velocity, w , pitch rate, q , pitch attitude, θ , and geometric angle of incidence, α , from the initial flight condition.

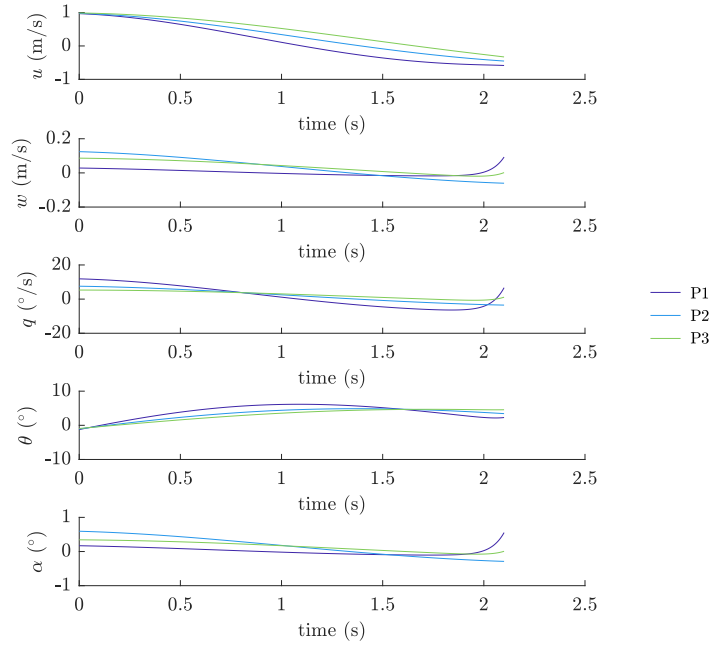


Fig. E.5 Time-history for the third oscillatory mode for the peregrine (P1-P3) flights showing perturbations in body axis coordinates of forward velocity, u , vertical velocity, w , pitch rate, q , pitch attitude, θ , and geometric angle of incidence, α , from the initial flight condition.

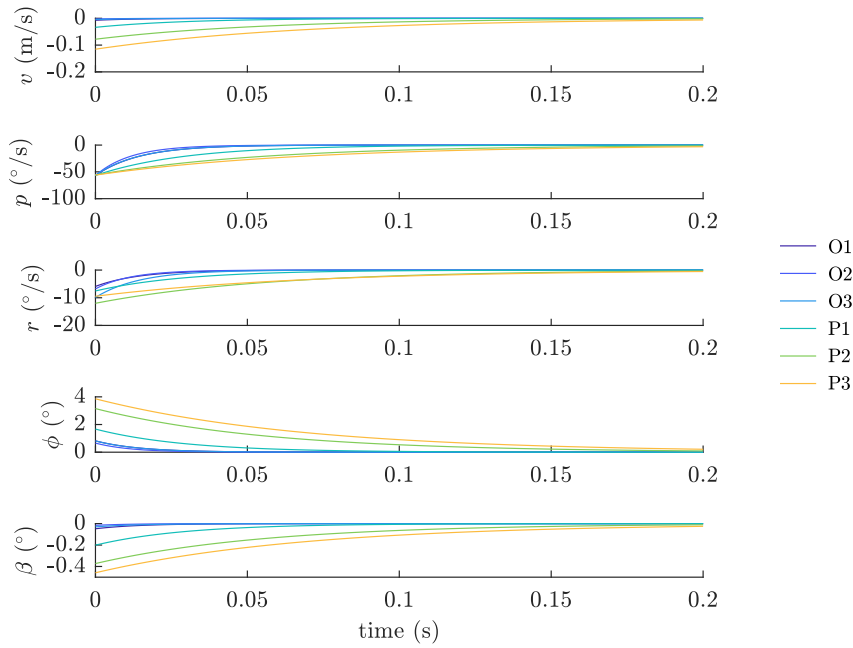


Fig. E.6 Time-history of the roll-subsidence mode for the barn owl (O1-O3) and peregrine (P1-P3) flights.

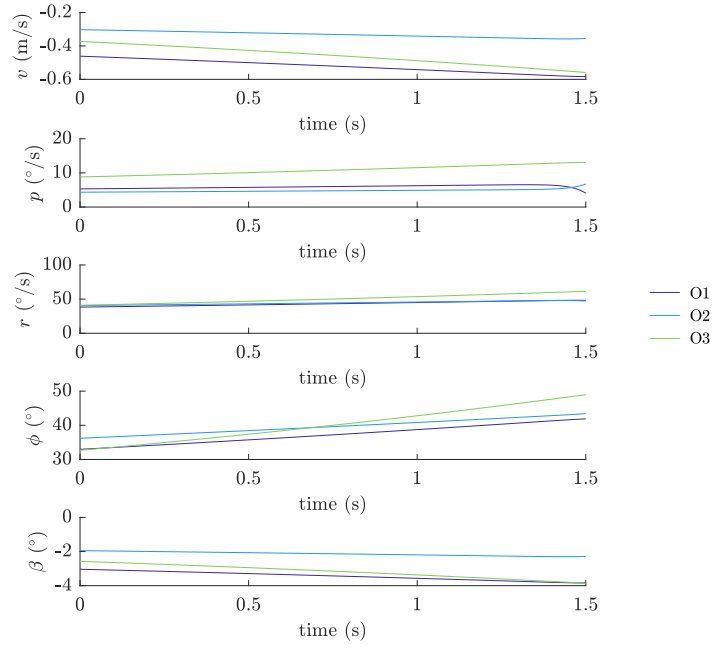


Fig. E.7 Time-history of the spiral mode with opposing sideslip for the barn owl (O1-O3) flights.

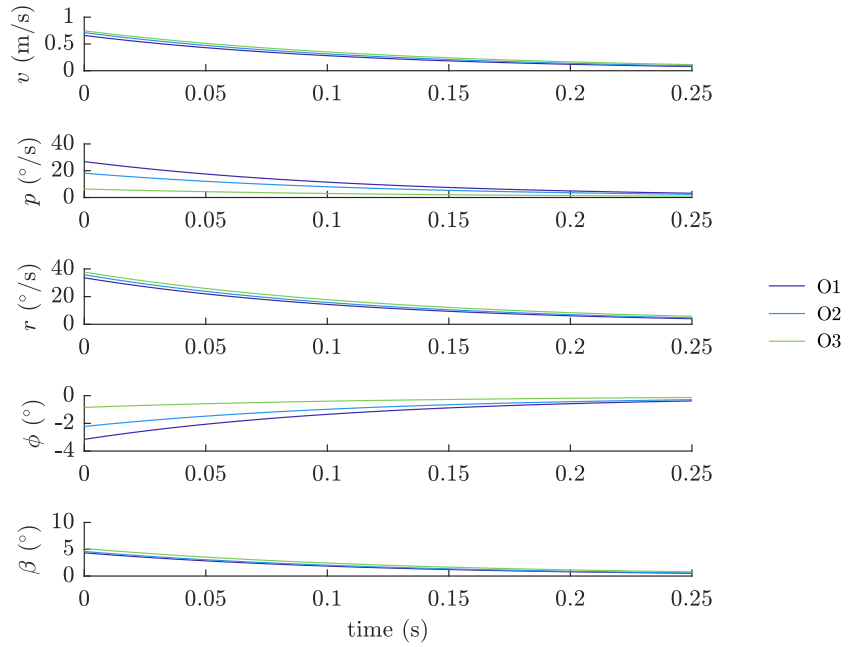


Fig. E.8 Time-history of the roll yaw sideslip 1 mode of the barn owl flights.

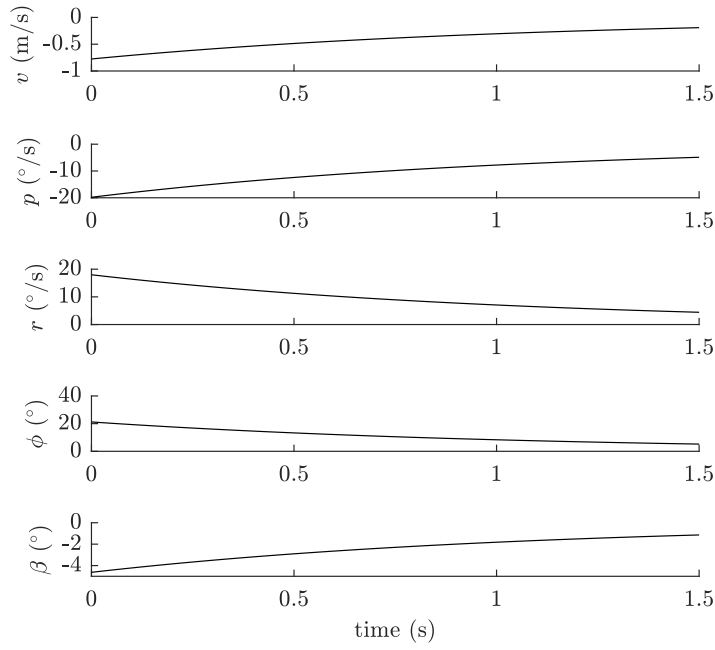


Fig. E.9 Time-history of the roll yaw sideslip 4 mode of flight P1.

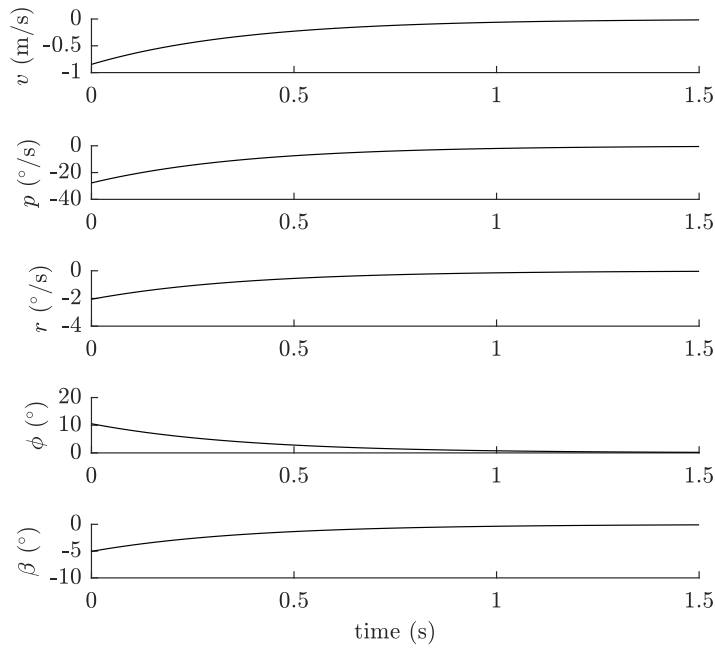


Fig. E.10 Time-history of the roll subsidence 2 mode of flight P1.

E.3 Reduced order model results

	O1	O2	O3	P1	P2	P3
T_{avl} (s)	0.0144	0.0116	0.0145	0.0297	0.0565	0.0694
T_{ro} (s)	0.0138	0.0113	0.0140	0.0285	0.0523	0.0666

Table E.1 Comparison between a reduced order model of the roll subsidence mode and the AVL estimates (with corrected concise derivative conversions).

	O1	O2	O3	P1	P2	P3
T_{avl} (s)	-5.99	-9.01	-3.87	-0.58	-3.65	-7.53
T_{ro} (s)	-5.79	-8.82	-4.15	-0.24	-3.62	-6.86

Table E.2 Comparison between a reduced order model of the spiral mode and the corrected AVL estimates. The negative time periods indicate that the mode is unstable.

	P2	P3
ω_{avl} (rad/s)	5.53	4.68
ω_{ro} (rad/s)	5.25	3.63
ζ_{avl}	0.185	0.127
ζ_{ro}	0.033	0.062

Table E.3 Comparison between a reduced order model of the dutch roll mode and the corrected and uncorrected AVL estimates for the lateral directional pole. Barn owl flights O1-O3 and peregrine flight P1 did not have a dutch roll mode.

E.4 State matrices, eigenvalues and eigenvectors

For all flights in this section, \mathbf{A} is the state matrix in concise form to nine decimal places, λ are the eigenvalues to one decimal place and $\mathbf{\Lambda}$ are the corresponding eigenvectors (by column).

E.4.1 Flight O1

$$\mathbf{A} = \begin{bmatrix} -0.332035000 & 0.015056340 & -0.397229015 & -9.721545189 & 0.004000000 & -0.009000000 & -0.000900000 & 0.000000000 \\ -1.843068530 & -9.303589622 & 8.667873416 & -1.314404479 & -0.017700000 & 0.026500000 & -0.043500000 & -0.000000000 \\ -4.762023128 & 102.849602067 & -1.196726046 & 0.000000000 & 0.378700000 & 3.430100000 & -0.904800000 & 0.000000000 \\ 0.000000000 & 0.000000000 & 1.000000000 & 0.000000000 & 0.000000000 & -0.000000000 & -0.000000000 & 0.000000000 \\ -0.028600000 & -0.158800000 & -0.012100000 & -0.000000000 & -0.285128014 & 0.540932565 & -8.752595644 & 9.721545189 \\ 12.185100000 & 7.025800000 & 1.679200000 & -0.000000000 & 22.394757707 & -72.221478328 & 25.868945005 & 0.000000000 \\ 0.073400000 & -0.719000000 & -0.092600000 & -0.000000000 & -2.205448656 & -7.150625086 & -0.329934198 & 0.000000000 \\ -0.000000000 & -0.000000000 & 0.000000000 & 0.000000000 & 0.000000000 & 1.000000000 & 0.000000000 & 0.000000000 \end{bmatrix} \quad (\text{E.1})$$

$$\lambda = \begin{bmatrix} -69.42 & -35.48 & 25.04 & -8.50 & 4.88 & -0.18 + 1.57i & -0.18 - 1.57i & 0.16 \end{bmatrix} \quad (\text{E.2})$$

$$\mathbf{\Lambda} = \begin{bmatrix} -0.0001 & 0.0035 & -0.0298 & 0.0001 & 0.0087 & -0.9169 & -0.9169 & -0.0265 \\ 0.0085 & -0.3152 & 0.2444 & -0.0130 & -0.0111 & -0.0432 & -0.0432 & 0.0032 \\ -0.0614 & 0.9483 & 0.9679 & 0.0017 & -0.0178 & -0.2353 & -0.2353 & 0.0002 \\ 0.0009 & -0.0267 & 0.0387 & -0.0002 & -0.0036 & 0.0240 & 0.0240 & 0.0010 \\ 0.0073 & -0.0032 & 0.0055 & 0.6587 & 0.8684 & 0.2647 & 0.2647 & -0.4566 \\ 0.9926 & -0.0241 & 0.0269 & 0.4682 & 0.0888 & -0.0816 & -0.0816 & 0.0940 \\ 0.1030 & -0.0091 & -0.0186 & 0.5863 & -0.4870 & 0.0025 & 0.0025 & 0.6701 \\ -0.0143 & 0.0007 & 0.0011 & -0.0551 & 0.0182 & 0.0074 & 0.0074 & 0.5770 \end{bmatrix} \quad (\text{E.3})$$

E.4.2 Flight O2

$$\mathbf{A} = \begin{bmatrix} -0.369782153 & 0.647850716 & -0.848613315 & -9.675461751 & -0.054600000 & -0.013800000 & 0.003700000 & 0.000000000 \\ -1.242090963 & -10.445868963 & 8.835783233 & -1.619117013 & 0.264400000 & -0.028600000 & -0.143100000 & -0.000000000 \\ -11.259991966 & 114.588996632 & -1.297878555 & 0.000000000 & -7.864100000 & 4.258800000 & 0.121000000 & 0.000000000 \\ 0.000000000 & 0.000000000 & 1.000000000 & 0.000000000 & 0.000000000 & -0.000000000 & -0.000000000 & 0.000000000 \\ -0.028300000 & 0.087600000 & 0.007800000 & -0.000000000 & -0.273258511 & 0.960624422 & -8.897756840 & 9.675461751 \\ 30.101800000 & -7.335900000 & 0.435600000 & -0.000000000 & 20.985989530 & -88.404938979 & 17.190685110 & 0.000000000 \\ -1.977200000 & 4.958000000 & -0.609600000 & -0.000000000 & -2.795733331 & -10.418365026 & 0.023699075 & 0.000000000 \\ -0.000000000 & -0.000000000 & 0.000000000 & 0.000000000 & 0.000000000 & 1.000000000 & 0.000000000 & 0.000000000 \end{bmatrix} \quad (\text{E.4})$$

$$\lambda = \begin{bmatrix} -86.39 & -38.00 & 26.50 & -8.17 & 5.51 & -0.16 + 1.37i & -0.16 - 1.37i & 0.11 \end{bmatrix} \quad (\text{E.5})$$

$$\mathbf{\Lambda} = \begin{bmatrix} 0.0004 & 0.0202 & 0.0382 & -0.0022 & -0.0314 & 0.6834 & 0.6834 & 0.0413 \\ -0.0075 & -0.3027 & -0.2316 & -0.0366 & 0.0563 & 0.0179 & 0.0179 & -0.0231 \\ 0.0598 & 0.9432 & -0.9706 & 0.0004 & 0.0661 & 0.1341 & 0.1341 & -0.0002 \\ -0.0007 & -0.0248 & -0.0366 & -0.0001 & 0.0120 & -0.0237 & -0.0237 & -0.0015 \\ -0.0025 & 0.0186 & 0.0105 & -0.7117 & 0.8431 & -0.7031 & -0.7031 & -0.3484 \\ -0.9910 & 0.1008 & 0.0182 & -0.3174 & 0.0784 & 0.0672 & 0.0672 & 0.0688 \\ -0.1187 & 0.0846 & -0.0322 & -0.6244 & -0.5235 & 0.0105 & 0.0105 & 0.6973 \\ 0.0115 & -0.0027 & 0.0007 & 0.0388 & 0.0142 & -0.0031 & -0.0031 & 0.6209 \end{bmatrix} \quad (\text{E.6})$$

E.4.3 Flight O3

$$\mathbf{A} = \begin{bmatrix} -0.340341437 & 0.793431414 & -1.193240685 & -9.657976196 & -0.004500000 & 0.006700000 & -0.001700000 & 0.000000000 \\ -1.109021393 & -8.974280309 & 8.191577949 & -1.720347583 & 0.074600000 & -0.003300000 & 0.048300000 & -0.000000000 \\ -15.427932196 & 102.963694072 & -1.227284275 & 0.000000000 & 1.832000000 & 4.839300000 & -1.159000000 & 0.000000000 \\ 0.000000000 & 0.000000000 & 1.000000000 & 0.000000000 & 0.000000000 & -0.000000000 & -0.000000000 & 0.000000000 \\ -0.037900000 & -0.124600000 & -0.008400000 & -0.000000000 & -0.233351028 & 1.283197712 & -8.244671088 & 9.657976196 \\ -11.665400000 & -2.671100000 & 1.007000000 & -0.000000000 & -2.477112089 & -71.310355074 & 13.554759185 & 0.000000000 \\ 0.807700000 & -2.812600000 & 0.316800000 & -0.000000000 & -5.049710549 & -12.098121482 & 0.197829466 & 0.000000000 \\ -0.000000000 & -0.000000000 & 0.000000000 & 0.000000000 & 0.000000000 & 1.000000000 & 0.000000000 & 0.000000000 \end{bmatrix} \quad (\text{E.7})$$

$$\lambda = \begin{bmatrix} -69.04 & -34.58 & 24.71 & -7.52 & 4.82 & -0.28 + 1.63i & -0.28 - 1.63i & 0.27 \end{bmatrix} \quad (\text{E.8})$$

$$\mathbf{\Lambda} = \begin{bmatrix} -0.0015 & 0.0324 & 0.0538 & 0.0018 & -0.0143 & 0.8221 & 0.8221 & -0.0258 \\ 0.0115 & -0.3046 & -0.2355 & -0.0101 & 0.0144 & 0.1245 & 0.1245 & 0.0038 \\ -0.0850 & 0.9507 & -0.9693 & -0.0118 & 0.0277 & 0.2335 & 0.2335 & 0.0005 \\ 0.0012 & -0.0275 & -0.0392 & 0.0016 & 0.0057 & -0.0240 & -0.0240 & 0.0020 \\ 0.0044 & -0.0077 & -0.0060 & 0.7446 & -0.8214 & 0.4489 & 0.4489 & -0.3808 \\ 0.9811 & 0.0292 & -0.0070 & 0.1108 & 0.1275 & -0.1532 & -0.1532 & 0.1522 \\ 0.1726 & -0.0250 & 0.0210 & 0.6579 & 0.5542 & -0.0068 & -0.0068 & 0.7128 \\ -0.0142 & -0.0008 & -0.0003 & -0.0147 & 0.0264 & 0.0200 & 0.0200 & 0.5684 \end{bmatrix} \quad (\text{E.9})$$

E.4.4 Flight P1

$$\mathbf{A} = \begin{bmatrix} -0.395722206 & -0.777556957 & -0.231911969 & -9.806456691 & 0.014100000 & 0.005300000 & 0.000700000 & 0.000000000 \\ -1.926855183 & -5.008181030 & 9.568275165 & -0.263642125 & 0.149000000 & -0.034500000 & -0.027900000 & -0.000000000 \\ -0.940151494 & 38.709999956 & -1.232005613 & 0.000000000 & 4.534100000 & 1.121600000 & -0.553300000 & 0.000000000 \\ 0.000000000 & 0.000000000 & 1.000000000 & 0.000000000 & 0.000000000 & -0.000000000 & -0.000000000 & 0.000000000 \\ 0.025800000 & 0.016300000 & 0.015900000 & -0.000000000 & -0.335788815 & 0.428280246 & -9.609932333 & 9.806456691 \\ -2.549500000 & -12.124700000 & -1.080700000 & -0.000000000 & 16.698729703 & -35.075270841 & 6.168066054 & 0.000000000 \\ -0.844200000 & -1.584900000 & -0.271200000 & -0.000000000 & 2.292332552 & -4.547957210 & -0.234539097 & 0.000000000 \\ -0.000000000 & -0.000000000 & 0.000000000 & 0.000000000 & 0.000000000 & 1.000000000 & 0.000000000 & 0.000000000 \end{bmatrix} \quad (\text{E.10})$$

$$\lambda = \begin{bmatrix} -33.88 & -22.18 & 16.32 & 1.91 & -2.63 & -0.44 + 1.43i & -0.44 - 1.43i & -0.93 \end{bmatrix} \quad (\text{E.11})$$

$$\mathbf{\Lambda} = \begin{bmatrix} -0.0004 & -0.0235 & 0.0640 & 0.1779 & -0.0115 & 0.7299 & 0.7299 & -0.1789 \\ -0.0218 & -0.4422 & -0.4095 & -0.1117 & 0.1111 & 0.0509 & 0.0509 & 0.1012 \\ 0.0622 & 0.7893 & -0.9011 & -0.0573 & 0.0362 & 0.1638 & 0.1638 & 0.0183 \\ -0.0018 & -0.0356 & -0.0552 & -0.0301 & -0.0138 & -0.0052 & -0.0052 & -0.0196 \\ -0.0337 & 0.0268 & -0.0051 & 0.8524 & -0.8464 & -0.2311 & -0.2311 & -0.7758 \\ -0.9881 & 0.4181 & 0.1130 & 0.4183 & -0.4843 & -0.2222 & -0.2222 & -0.3459 \\ -0.1318 & 0.0608 & 0.0190 & 0.0440 & -0.0359 & -0.1489 & -0.1489 & 0.3139 \\ 0.0292 & -0.0188 & 0.0069 & 0.2195 & 0.1840 & -0.0741 & -0.0741 & 0.3703 \end{bmatrix} \quad (\text{E.12})$$

E.4.5 Flight P2

$$\mathbf{A} = \begin{bmatrix} -0.206358011 & 0.156311680 & -1.520817581 & -9.736877748 & -0.013100000 & 0.005400000 & 0.000300000 & 0.000000000 \\ -1.171135795 & -3.850288510 & 11.884329434 & -1.195538259 & -0.001800000 & -0.009500000 & 0.011100000 & -0.000000000 \\ -4.377920669 & 34.694160977 & -0.736170268 & 0.000000000 & -0.295200000 & -0.075800000 & 0.136900000 & 0.000000000 \\ 0.000000000 & 0.000000000 & 1.000000000 & 0.000000000 & 0.000000000 & -0.000000000 & -0.000000000 & 0.000000000 \\ 0.000400000 & -0.032700000 & -0.000300000 & -0.000000000 & -0.259801585 & 1.722204721 & -11.940483066 & 9.736877748 \\ -3.507700000 & -3.008400000 & -0.522800000 & -0.000000000 & -0.584748094 & -19.113799834 & 6.844258586 & 0.000000000 \\ -0.084500000 & -1.812200000 & -0.057800000 & -0.000000000 & 2.309294801 & -3.969310946 & -0.088266565 & 0.000000000 \\ -0.000000000 & -0.000000000 & 0.000000000 & 0.000000000 & 0.000000000 & 1.000000000 & 0.000000000 & 0.000000000 \end{bmatrix} \quad (\text{E.13})$$

$$\lambda = \begin{bmatrix} 18.37 & -22.75 & -17.69 & -1.02 + 5.52i & -1.02 - 5.52i & -0.20 + 1.13i & -0.20 - 1.13i & 0.27 \end{bmatrix} \quad (\text{E.14})$$

$$\mathbf{\Lambda} = \begin{bmatrix} -0.0926 & 0.0440 & -0.0005 & -0.0002 & -0.0002 & -0.9085 & -0.9085 & -0.0022 \\ 0.4700 & -0.5234 & 0.0038 & 0.0067 & 0.0067 & -0.1140 & -0.1140 & 0.0014 \\ 0.8743 & 0.8331 & -0.0038 & 0.0008 & 0.0008 & -0.1221 & -0.1221 & -0.0001 \\ 0.0476 & -0.0366 & 0.0002 & 0.0007 & 0.0007 & 0.0175 & 0.0175 & -0.0003 \\ 0.0165 & -0.0258 & 0.0781 & 0.8930 & 0.8930 & 0.2228 & 0.2228 & 0.4138 \\ -0.0481 & -0.1544 & 0.9731 & -0.0619 & -0.0619 & 0.1630 & 0.1630 & 0.1882 \\ -0.0361 & -0.0640 & 0.2095 & 0.0296 & 0.0296 & -0.0468 & -0.0468 & 0.5681 \\ -0.0026 & 0.0068 & -0.0550 & -0.0227 & -0.0227 & -0.0721 & -0.0721 & 0.6860 \end{bmatrix} \quad (\text{E.15})$$

E.4.6 Flight P3

$$\mathbf{A} = \begin{bmatrix} -0.161346086 & 0.214439087 & -1.227470672 & -9.629762670 & -0.004000000 & 0.012300000 & 0.000800000 & 0.000000000 \\ -1.042619032 & -3.934768601 & 14.323260056 & -1.871836245 & 0.090200000 & -0.067400000 & -0.007700000 & -0.000000000 \\ -3.680165007 & 42.982777431 & -0.895727896 & 0.000000000 & 2.156900000 & -0.451400000 & -0.136100000 & 0.000000000 \\ 0.000000000 & 0.000000000 & 1.000000000 & 0.000000000 & 0.000000000 & -0.000000000 & -0.000000000 & 0.000000000 \\ 0.005800000 & 0.026800000 & 0.006000000 & -0.000000000 & -0.248810975 & 1.412729631 & -14.385553943 & 9.629762670 \\ -3.520600000 & -22.847900000 & -1.912900000 & -0.000000000 & -2.607690134 & -15.004788787 & 5.402848790 & 0.000000000 \\ -0.438100000 & -1.517300000 & -0.265000000 & -0.000000000 & 0.913873458 & -2.520039303 & -0.200493098 & 0.000000000 \\ -0.000000000 & -0.000000000 & 0.000000000 & 0.000000000 & 0.000000000 & 1.000000000 & 0.000000000 & 0.000000000 \end{bmatrix} \quad (\text{E.16})$$

$$\lambda = \begin{bmatrix} 22.65 & -27.23 & -14.51 & -0.66 + 4.39i & -0.66 - 4.39i & -0.08 + 0.98i & -0.08 - 0.98i & 0.13 \end{bmatrix} \quad (\text{E.17})$$

$$\mathbf{\Lambda} = \begin{bmatrix} -0.0564 & 0.0248 & -0.0009 & -0.0062 & -0.0062 & 0.8021 & 0.8021 & 0.0823 \\ 0.4500 & -0.4088 & 0.0048 & -0.0478 & -0.0478 & 0.0848 & 0.0848 & -0.0134 \\ 0.8346 & 0.6607 & 0.0003 & -0.0171 & -0.0171 & 0.0808 & 0.0808 & -0.0004 \\ 0.0369 & -0.0243 & -0.0000 & -0.0030 & -0.0030 & -0.0151 & -0.0151 & -0.0028 \\ -0.0209 & -0.0146 & 0.1153 & 0.9502 & 0.9502 & -0.3357 & -0.3357 & 0.4589 \\ -0.3095 & -0.6237 & 0.9772 & -0.1081 & -0.1081 & -0.2486 & -0.2486 & 0.0961 \\ -0.0052 & -0.0737 & 0.1652 & 0.0095 & 0.0095 & 0.0502 & 0.0502 & 0.4873 \\ -0.0137 & 0.0229 & -0.0673 & -0.0101 & -0.0101 & 0.0818 & 0.0818 & 0.7320 \end{bmatrix} \quad (\text{E.18})$$

E.5 Sensitivity studies

E.5.1 Lift coefficient

	nominal $C_L - 0.1$	nominal C_L	nominal $C_L + 0.1$
O1	$-0.14 \pm 1.42i$ $\omega = 0.23 \text{ Hz}, \zeta = 0.099$	$-0.18 \pm 1.57i$ $\omega = 0.25 \text{ Hz}, \zeta = 0.12$	$-0.23 \pm 1.70i$ $\omega = 0.27 \text{ Hz}, \zeta = 0.14$
P1	$-0.38 \pm 1.43i$ $\omega = 0.23 \text{ Hz}, \zeta = 0.27$	$-0.44 \pm 1.43i$ $\omega = 0.23 \text{ Hz}, \zeta = 0.31$	$-0.42 \pm 1.37i$ $\omega = 0.22 \text{ Hz}, \zeta = 0.31$
P3	$-0.078 \pm 0.77i$ $\omega = 0.12 \text{ Hz}, \zeta = 0.1$	$-0.08 \pm 0.98i$ $\omega = 0.16 \text{ Hz}, \zeta = 0.09$	$-0.12 \pm 1.03i$ $\omega = 0.16 \text{ Hz}, \zeta = 0.12$

Table E.4 Sensitivity of the third oscillatory mode to lift coefficient showing the eigenvalues with corresponding undamped natural frequencies and damping ratios. Eigenvalue real and complex parts are in radians/second.

	nominal $C_L - 0.1$	nominal C_L	nominal $C_L + 0.1$
P1	-3.39, -0.45 $\tau = 0.295 \text{ s}, 2.2 \text{ s}$	-2.63, -0.93 $\tau = 0.380 \text{ s}, 1.07 \text{ s}$	$-1.72 \pm 1.31i$ $\omega = 0.21 \text{ Hz}, \zeta = 1.31$
P3	-3.00, -0.18 $\tau = 0.33 \text{ s}, 5.7 \text{ s}$	$-0.66 \pm 4.4i$ $\omega = 0.70 \text{ Hz}, \zeta = 0.15$	$-0.51 \pm 6.97i$ $\omega = 1.1 \text{ Hz}, \zeta = 0.073$

Table E.5 Sensitivity of the dutch roll (or equivalent real modes) mode to lift coefficient showing the eigenvalues with corresponding time constant or undamped natural frequencies and damping ratios. Eigenvalue real and complex parts are in radians/second.

E.5.2 Anteroposterior centre of mass position

	nominal $x_{cg} - 15 \text{ mm}$	nominal x_{cg}	nominal $x_{cg} + 15 \text{ mm}$
O1	31 ($\tau = 32 \text{ ms}$)	25 ($\tau = 40 \text{ ms}$)	17 ($\tau = 59 \text{ ms}$)
P1	21 ($\tau = 48 \text{ ms}$)	16 ($\tau = 63 \text{ ms}$)	10 ($\tau = 100 \text{ ms}$)
P3	27 ($\tau = 37 \text{ ms}$)	23 ($\tau = 44 \text{ ms}$)	18 ($\tau = 56 \text{ ms}$)

Table E.6 Sensitivity of the pitch divergence mode to anteroposterior centre of mass position, showing the eigenvalues with corresponding time constant. Eigenvalues are in radians/second and values are more positive cranially.

E.5.3 Inertia tensor

	minimum I_{xx}, I_{yy}, I_{zz}	nominal I_{xx}, I_{yy}, I_{zz}	maximum I_{xx}, I_{yy}, I_{zz}
O1	27 ($\tau = 37$ ms)	25 ($\tau = 40$ ms)	21 ($\tau = 48$ ms)
P1	21 ($\tau = 47$ ms)	16 ($\tau = 63$ ms)	14 ($\tau = 74$ ms)
P3	30 ($\tau = 34$ ms)	23 ($\tau = 44$ ms)	19 ($\tau = 53$ ms)

Table E.7 The sensitivity of the pitch divergence mode of O1, P1 and P3 to worst case inertia tensor errors.

	minimum I_{xx}, I_{yy}, I_{zz}	nominal I_{xx}, I_{yy}, I_{zz}	maximum I_{xx}, I_{yy}, I_{zz}
O1	-77 ($\tau = 13$ ms)	-69 ($\tau = 14$ ms)	-56 ($\tau = 18$ ms)
P1	-45 ($\tau = 22$ ms)	-34 ($\tau = 30$ ms)	-27 ($\tau = 37$ ms)
P3	-34 ($\tau = 29$ ms)	-27 ($\tau = 37$ ms)	-23 ($\tau = 43$ ms)

Table E.8 The sensitivity of the roll subsidence mode of O1, P1 and P3 to worst case inertia tensor errors.

	minimum I_{xx}, I_{yy}, I_{zz}	nominal I_{xx}, I_{yy}, I_{zz}	maximum I_{xx}, I_{yy}, I_{zz}
O1 (RYS 1)	-9.0 ($\tau = 111$ ms)	-8.5 ($\tau = 118$ ms)	-7.2 ($\tau = 139$ ms)
O1 (RYS 2)	5.0 ($\tau = 200$ ms)	4.9 ($\tau = 204$ ms)	4.4 ($\tau = 227$ ms)
P1 (RYS 4)	-1.4 ($\tau = 0.71$ s)	-0.9 ($\tau = 1.11$ s)	-0.7 ($\tau = 1.43$ s)

Table E.9 The sensitivity of the roll yaw sideslip (RYS) 1, 2 and 4 of flights O1 and P1 to the worst case inertia tensor errors.

	minimum I_{xx}, I_{yy}, I_{zz}	nominal I_{xx}, I_{yy}, I_{zz}	maximum I_{xx}, I_{yy}, I_{zz}
Eigenvalue	-1.0 + 5.4i	-0.7 + 4.4i	-0.5 + 3.8i
ω_n (Hz)	0.9	0.7	0.6
ζ	0.18	0.15	0.13

Table E.10 The sensitivity of the dutch roll mode of P3 to worst case inertia tensor errors.

REFERENCES

- [1] Videler JJ. 2005 Avian Flight. New York: Oxford University Press
- [2] Raspet A. 1960 Biophysics of bird flight. *Science* 132:191–200.
- [3] Anderson JD. 2007 Fundamentals of aerodynamics. 4th ed. New York: McGraw-Hill
- [4] Liu T, Kuykendoll K, Rhew R, Jones S. 2006 Avian wing geometry and kinematics. *AIAA J.* 44(5):954–963.
- [5] Hankin EH. 1913 Animal Flight. London: Iliffe & Sons Ltd
- [6] Brown RHJ. 1948 The flight of birds. The flapping cycle of the pigeon. *J Exp Biol* 25:322–333.
- [7] Brown RHJ. 1953 The flight of birds II. Wing function in relation to flight speed. *J Exp Biol* 30:90–103.
- [8] Savile DBO. 1956 Adaptive evolution in the avian wing. *Evolution* 11(2):212–224.
- [9] Smith JM. 1952 The importance of the nervous system in the evolution of animal flight. *Evolution* 6(1):127–129.
- [10] Newman BG. 1958 Soaring and gliding flight of the black vulture. *J. Exp. Biol.* 35(2):280.
- [11] Pennycuik CJ. 1968 A wind tunnel study of the gliding flight in the pigeon, *Columba Livia*. *J. Exp. Biol.* 49:509–526.
- [12] Raspet A. 1950 Performance measurements of a soaring bird. *Aeron. Engin. Rev.* 9(12):14–17.
- [13] Nachtigall W, Wieser J. 1966 Profilmessungen am taubenflügel. *Z. Vergl. Physiol.* 52:333–346.
- [14] Bilo D. 1971 Flugbiophysik von kleinvögeln I. Kinematik und aerodynamik des flügelabschlages beim haussperling (*Passer domesticus l.*). *Z. Vergl. Physiol.* 71:382–454.
- [15] Bilo D. 1971 Flugbiophysik von kleinvögeln II. Kinematik und aerodynamik des flügelauflages beim haussperling (*Passer domesticus l.*). *Z. Vergl. Physiol.* 76:426–437.
- [16] Withers PC. 1981 An aerodynamic analysis of bird wings as fixed aerofoils. *J. Exp. Biol.* 90:143–162.

- [17] Withers PC. 1981 The aerodynamic performance of the wing in red-shouldered hawk *Buteo linearis* and a possible aeroelastic role for wing-tip slots. *Ibis* 123:239–247.
- [18] Bachmann T, Mühlenbruch G, Wagner H. 2011 The barn owl wing: an inspiration for silent flight in the aviation industry? In: *Proc. SPIE 7975* p. 1–14.
- [19] Klaassen van Oorschot B, Mistick EA, Tobalske BW. 2016 Aerodynamic consequences of wing morphing during emulated take-off and gliding in birds. *J. Exp. Biol.* 219(19):3146–3154.
- [20] Elimelech Y, Ellington CP. 2013 Analysis of the transitional flow field over a fixed hummingbird wing. *J. Exp. Biol.* 216:303–318.
- [21] Biesel W, Butz H, Nachtigall W. 1985 Erste messungen der flügelgeometrie bei frei gleitfliegenden haustauben (*Col. liv. var. dom.*) unter benutzung neu ausgearbeiteter verfahren der windkanaltechnik und der stereophotogrammetrie. In: Nachtigall W, editor. *Biona Report 3: Bird Flight - Vogelflug*. Gustav Fischer Verlag p. 139–160.
- [22] Butz H, Biesel W, Nachtigall W. 1985 Einsatz spezieller methoden der photogrammetrie zur untersuchung der flügelgeometrie frei gleitfliegender tauben. In: Nachtigall W, editor. *Biona Report 3: Bird Flight - Vogelflug*. Gustav Fischer Verlag p. 123–138.
- [23] Nachtigall W. 1985 Warum die Vögel fliegen. Hamburg: Rasch und Röhring
- [24] Valasek J. 1. In: Valasek J, editor. *Introduction*. Chichester: John Wiley & Sons 2012. p. 1–10
- [25] Bowman J, Sanders B, Weisshaar T. 2002 Evaluating the impact of morphing aircraft technologies on aircraft performance. In: 43rd AIAA/ASME/ASCE/AHS/ASC Structures, Structural Dynamics, and Materials. vol. 2002-1631. AIAA .
- [26] Teal group predicts worldwide civil drone production will soar over the next decade. Teal Group Corp. 2018. Available from: <http://www.tealgroup.com/index.php/pages/press-releases/54-teal-group-predicts-worldwide-civil-drone-production-will-soar-over-the-next-decade>
- [27] Norberg UM. 1990 Vertebrate flight. Berlin, Germany: Springer-Verlag
- [28] Sachs G. 2007 What can be learned from unique lateral-directional dynamics properties of birds for mini-aircraft. In: *AIAA Atmospheric Flight Mechanics Conference and Exhibit*. AIAA p. 1–16.
- [29] Watkins S, Milbank J, Loxton BJ, Melbourne WH. 2006 Atmospheric winds and their implications for microair vehicles. *AIAA Journal* 44(11):2591–2600.
- [30] Thompson M, Watkins S, White C, Holmes J. 2011 Span-wise wind fluctuations in open terrain as applicable to small flying craft. *Aeronaut. J.* 115(1173):693–701.

- [31] Watkins S, Thompson M, Loxton B, Abdulrahim M. 2010 On low altitude flight through the atmospheric boundary layer. *Int. J. Micro Air Veh.* 2(2):55–68.
- [32] Mohamed A, Massey K, Watkins S, Clothier R. 2014 The attitude control of fixed-wing MAVS in turbulent environments. *Prog. Aerosp. Sci.* 66:37–48.
- [33] Shyy W, Lian Y, Tang J, Viieru D, Liu H. 2008 Aerodynamics of low reynolds number flyers. *Cambridge Aerospace Series*. New York: Cambridge University Press
- [34] Mohamed A, Watkins S, Clothier R, Abdulrahim M. 2014 Influence of turbulence on MAV roll perturbations. *Int. J. Micro Air Veh.* 6(3):175–190.
- [35] Abdulrahim M, Watkins S, Segal R, Marino M, Sheridan J. 2010 Dynamic sensitivity to atmospheric turbulence of unmanned air vehicles with varying configuration. *J. Aircraft* 47(6):1873–1883.
- [36] Tennekes H. 1997 *The Simple Science of Flight from Insects to Jumbo Jets*. 3rd ed. Cambridge, MA: The MIT Press
- [37] Evers JH. 2007 Biological Inspiration for Agile Autonomous Air Vehicles. In: *Platform Innovations and System Integration for Unmanned Air, Land and Sea Vehicles (AVT-SCI Joint Symposium)*. vol. Meeting Proceedings RTO-MP-AVT-146, Paper 15. RTO p. pp. 15–1 – 15–14.
- [38] Cook MV. 1997 *Flight dynamics principles*. 3rd ed. Oxford: Butterworth-Heinemann
- [39] Taylor GK. 2005 Flight muscles and flight dynamics: towards an integrative framework. *Anim. Biol.* 55(1):81–99.
- [40] Meyers RA. 1993 Gliding flight in the American Kestrel (*Falco sparverius*): An electromyographic study. *Journal of Morphology* 215(3):213–224.
- [41] Reynolds KV, Thomas ALR, Taylor GK. 2014 Wing tucks are a response to atmospheric turbulence in the soaring flight of the steppe eagle *Aquila nipalensis*. *J. R. Soc. Interface* 11(101).
- [42] Dickinson MH, Farley CT, Full RJ, Koehl MAR, Kram R, Lehman S. 2000 How animals move: An integrative view. *Science* 288(5463):100.
- [43] Bilo D. 11. In: Davies MNO, Green PR, editors. *Course control during flight*. Berlin: Springer-Verlag 1994. p. 227–247
- [44] McArthur KL, Dickman JD. 2011 State-dependent sensorimotor processing: gaze and posture stability during simulated flight in birds. *J. Neurophysiol.* 105(4):1689–1700.
- [45] Altshuler DL, Bahlman JW, Dakin R, Gaede AH, Goller B, Lentink D, Segre PS, Skandalis DA. 2015 The biophysics of bird flight: functional relationships integrate aerodynamics, morphology, kinematics, muscles, and sensors. *Can. J. Zool.* 93(12):961–975.

- [46] Necker R. 4. In: Whittow GC, editor. The somatosensory system. London: Academic Press 2000. p. 57–67
- [47] Hörster W. 1990 Histological and electrophysiological investigations on the vibration-sensitive receptors (Herbst corpuscles) in the wing of the pigeon (*Columba livia*). J. Comp. Physiol. A 166(5):663–673.
- [48] Necker R. 1985 Receptors in the skin of the wing of the pigeon and their possible role in bird flight. In: Nachtigall W, editor. Biona Report 3: Bird flight - vogelflug. Gustav Fischer Verlag .
- [49] Brown RE, Fedde MR. 1993 Airflow sensors in the avian wing. J. Exp. Biol. 179(1):13.
- [50] Haiden GJ, Awad EA. 1981 The ultrastructure of the avian golgi tendon organ. Anat. Rec. 200:153–161.
- [51] Klän S, Bachmann T, Klaas M, Wagner H, Schröder W. 2009 Experimental analysis of the flow field over a novel owl based aerofoil. Exp Fluids 46:975–989.
- [52] Klän S, Burgmann S, Bachmann T, Klaas M, Schröder W. 2012 Surface structure and dimensional effects on the aerodynamics of an owl-based wing model. Eur. J. Mech. B-Fluid. 33:58–73.
- [53] Winzen A, Roidl B, Klän S, Klaas M, Schröder W. 2014 Particle-image velocimetry and force measurements of leading-edge serrations on owl-based wing models. J. Bionic Eng. 11(3):423–438.
- [54] Winzen A, Roidl B, Schröder W. 2016 Combined particle image velocimetry and force analysis of the three-dimensional fluid-structure interaction of a natural owl wing. Bioinspir. Biomim. 11(2):026005.
- [55] Winzen A, Klaas M, Schröder W. 2015 High-speed particle image velocimetry and force measurements of bio-inspired surfaces. J. Aircraft 52(2):471–485.
- [56] Wagner H, Weger M, Klaas M, Schröder W. 2017 Features of owl wings that promote silent flight. Interface Focus 7(1).
- [57] Nachtigall W. 1998 Starling and Starling Models in Wind Tunnels. Journal of Avian Biology 29(4):478–484.
- [58] Nachtigall W, Wedekind F, Dreher A. 1985 Hinweise auf aerodynamische rauigkeitseffekte an vogel-flügprofilen. In: Nachtigall W, editor. Biona Report 3: Bird Flight - Vogelflug. Gustav Fischer Verlag p. 195–215.
- [59] Lentink D, Kat Rd. 2014 Gliding Swifts Attain Laminar Flow over Rough Wings. Plos One 9(6):1–8.
- [60] Müller W, Patone G. 1998 Air transmissivity of feathers. J Exp Biol 201:2591–2599.
- [61] Wolf T, Konrath R. 2015 Avian wing geometry and kinematics of a freeflying barn owl in flapping flight. Exp. Fluids 56(28).

- [62] Thomas ALR. 1993 On the aerodynamics of birds' tails. *Philos. T. R. Soc. B.* 340(1294):361–380.
- [63] Thomas ALR. 1997 On the tails of birds. *BioScience* 47(4):215–225.
- [64] Taylor GK, Bacic M, Carruthers AC, Gillies J, Ozawa Y, Thomas ALR. Flight control mechanisms in birds of prey 2007
- [65] Gillies JA, Thomas ALR, Taylor GK. 2011 Soaring and manoeuvring flight of a steppe eagle *Aquila nipalensis*. *J. Avian Biol.* 42:377–386.
- [66] Gatesy SM, Dial KP. 1993 Tail muscle activity patterns in walking and flying pigeons (*Columba livia*). *J. Exp. Biol.* 176(1):55.
- [67] Gatesy SM, Dial KP. 1996 From frond to fan: Archaeopteryx and the evolution of short-tailed birds. *Evolution* 50(5):2037–2048.
- [68] Brown RHJ. 1963 The flight of birds. *Biol. Rev.* 38:460–489.
- [69] Sachs G. 2009 Speed stability in birds. *Mathematical Biosciences* 219:1–6.
- [70] Tucker VA. 1988 Gliding Birds: Descending Flight of the White-Backed Vulture, *Gyps Africanus*. *J Exp Biol* 140:325–344.
- [71] Stevens BL, Lewis FL. 2003 Aircraft control and simulation. 2nd ed. Hoboken, New Jersey: John Wiley & Sons
- [72] Wunnenberg H, Bava R, Buchacker E, Choplin J, Fristachi G, Gibson J, Hodgekinson J, Hofinger G, Hoh RH, Huynh HT, et al. AGARD advisory report 279 - Handling qualities of unstable highly augmented aircraft. Advisory group for aerospace research and development (AGARD) 1991.
- [73] Korr AL, Hyer P. A trifilar pendulum for the determination of moments of inertia. Armed services technical information agency 1962.
- [74] Kaplan G. 1985 The X-29: is it coming or going? *IEEE Spectrum* 22(6):54–63.
- [75] Putnam TW. X-29 flight-research program. NASA 1984.
- [76] Thomas ALR, Taylor GK. 2001 Animal flight dynamics I. Stability in gliding flight. *J. Theor. Biol.* 212:399–424.
- [77] Pennycuik CJ. 1. In: Farner DS, King JR, Parkes KC, editors. *Mechanics of flight*. vol. 5. New York: Academic Press 1975. p. 1–73
- [78] Lighthill J. 1. In: Wu TYT, Brokaw CJ, Brennen C, editors. *Aerodynamic aspects of animal flight*. vol. 2. New York: Plenum Press 1974. p. 423–492
- [79] Hummel D. 1992 Aerodynamic investigations on tail effects in birds. *Z. Flugwiss. Weltraumforsch* 16:159–168.

- [80] Evangelista D, Cam S, Huynh T, Kwong A, Mehrabani H, Tse K, Dudley R. 2014 Shifts in stability and control effectiveness during evolution of Paraves support aerial maneuvering hypotheses for flight origins. *PeerJ* 2:e632.
- [81] Tucker VA. 1992 Pitching equilibrium, wing span and tail span in a gliding harris' hawk, *parabuteo uncinctus*. *J. Exp. Biol.* 165:21–41.
- [82] Carruthers AC, Thomas ALR, Taylor GK. 2007 Automatic aeroelastic devices in the wings of a steppe eagle *Aquila nipalensis*. *J. Exp. Biol.* 210:4136–4149.
- [83] Carruthers AC, Thomas ALR, Walker SM, Taylor GK. 2010 Mechanics and aerodynamics of perching manoeuvres in a large bird of prey. *Aeronaut. J.* 114(1161).
- [84] Tobalske BW. 2007 Biomechanics of bird flight. *J. Exp. Biol.* 210(18):3135.
- [85] Sachs G. 2005 Yaw stability in gliding birds. *J. Ornithol.* 146:191–199.
- [86] Sachs G. 2005 Aerodynamic yawing moment characteristics of bird wings. *J. Theor. Biol.* 234:471–478.
- [87] Sachs G, Moelyadi MA. 2006 Effect of slotted wing tips on yawing moment characteristics. *J. theor. Biol.* 239:93–100.
- [88] Sachs G. 2007 Why birds and miniscale airplanes need no vertical tail. *J. Aircraft* 44(4):1159–1167.
- [89] Sachs G. 2007 Tail effects on yaw stability in birds. *J. Theor. Biol.* 249:464–472.
- [90] Herzog K. 1968 Anatomie und flugbiologie der vögel. Stuttgart: Gustav Fischer Verlag
- [91] Sachs G. Flight mechanic and aerodynamic aspects of extremely large dihedral in birds. In: 45th AIAA Aerospace Sciences Meeting and Exhibit. AIAA p. 1–12.
- [92] Sachs G, Moelyadi MA. 2010 CFD based determination of aerodynamic effects on birds with extremely large dihedral. *J. Bionic Eng.* 7:95–101.
- [93] Lawren LG, Daniel JI. 2018 A tale of two tails: developing an avian inspired morphing actuator for yaw control and stability. *Bioinsp. Biomim.* 13(2):026008.
- [94] Rüppell G. 1977 Bird flight. München: Kindler Verlag GmbH
- [95] Hoey RG. 2010 Exploring bird aerodynamics using radio-controlled models. *Bioinsp. Biomim.* 5:045008.
- [96] Etkin B, Reid D. 1996 Dynamics of flight - stability and control. 3rd ed. New York: John Wiley and Sons, Inc.
- [97] Sachs G. 2007 Unique properties of lateral-directional stability and control in birds. In: 45th AIAA Aerospace Sciences Meeting and Exhibit. AIAA p. 1–12.

- [98] Defense Do. Military specification: Flying qualities of piloted airplanes. MIL-F-8785C. Department of Defense 1980
- [99] Douglas RW, Dial KP, Biewener AA. 1998 Asymmetrical force production in the maneuvering flight of pigeons. *The Auk* 115(4):916–928.
- [100] Dudley R. 2002 Mechanisms and implications of animal flight maneuverability. *Integr. Comp. Biol.* 42(1):135–140.
- [101] Tobalske BW. 2016 Evolution of avian flight: muscles and constraints on performance. *Phil. Trans. R. Soc. B.* 371(1704).
- [102] Taylor GK, Carruthers AC, Hubel TY, Walker SM. 1. In: Valasek J, editor. *Wing morphing in insects, birds and bats: mechanism and function*. Chichester: John Wiley & Sons 2011. p. 1–29
- [103] Thomas ALR. 1996 The flight of birds that have wings and a tail: variable geometry expands the envelope of flight performance. *J. theor. Biol.* 183:237–245.
- [104] Maybury WJ, Rayner JMV, Couldrick LB. 2001 Lift generation by the avian tail. *P. Roy. Soc. B-Biol. Sci.* 268:1443–1448.
- [105] Maybury WJ, Rayner JMV. 2001 The avian tail reduces body parasite drag by controlling flow separation and vortex shedding. *P. Roy. Soc. B-Biol. Sci.* 268(1474):1405.
- [106] Evans MR, Rosén M, Park KJ, Hedenström A. 2002 How to birds' tails work? Delta-wing theory fails to predict tail shape during flight. *P. Roy. Soc. B-Biol. Sci.* 269:1053–1057.
- [107] Evans MR. 2003 Birds' tails do act like delta wings but delta-wing theory does not always predict the forces they generate. *P. Roy. Soc. B-Biol. Sci.* 270(1522):1379–1385.
- [108] Biewener AA. 2011 Muscle function in avian flight: achieving power and control. *Phil. Trans. R. Soc. B.* 366(1570):1496.
- [109] Harvey AL, Marshall IG. 8. In: Whittow GC, editor. *Skeletal muscle*. London: Academic Press 2000. p. 123–135
- [110] Meyers RA, Stakebake EF. 2004 Anatomy and histochemistry of spread-wing posture in birds. 3. Immunohistochemistry of flight muscles and the "shoulder lock" in albatrosses. *J. Morphol.* 263(1):12–29.
- [111] Biewener A. 2003 *Animal locomotion*. Oxford: Oxford University Press Inc.
- [112] Rosser BWC, George JC. 1986 The avian pectoralis: histochemical characterization and distribution of muscle fiber types. *Can. J. Zool.* 64(5):1174–1185.
- [113] Meyers RA, Mathias E. 1997 Anatomy and histochemistry of spread-wing posture in birds. 2. Gliding flight in the California Gull, *Larus californicus*: A paradox of fast fibers and posture. *J. Morphol.* 233(3):237–247.

- [114] Bilo D, Bilo A. 1978 Wind stimuli control vestibular and optokinetic reflexes in the pigeon. *Naturwissenschaften* 65:161–162.
- [115] Biederman-Thorson M, Thorson J. 1973 Rotation-compensating reflexes independent of the labyrinth and the eye. *J. Comp. Physiol.* 83:103–122.
- [116] Delius JD, Vollrath FW. 1973 Rotation compensating reflexes independent of the labyrinth. *J. Comp. Physiol.* 83:123–134.
- [117] Ge C, Ren L, Liang P, Zhang C, Zhang Z. 2013 High-lift effect of bionic slat based on owl wing. *J. Bionic Eng.* 10:456–463.
- [118] Nachtigall W, Klimbingat A. 1985 Messung der flügelgeometrie mit der profilkammethode und geometrische flügelkennzeichnung einheimischer eulen. In: Nachtigall W, editor. *Biona Report 3: Bird Flight - Vogelflug*. Gustav Fischer Verlag p. 45–86.
- [119] Carruthers AC, Walker SM, Thomas ALR, Taylor GK. 2010 Aerodynamics of aerofoil sections measured on a free-flying bird. *Proc. IMechE, Part G: J. Aero. Eng.* 224(8):855–864.
- [120] Bilo D, Nachtigall W. 1985 Movements of a sparrow’s wings during free flight in a wind tunnel, demonstrated by stereoscopic anaglyphic prints from high speed rotating-disc camera photographs. In: Nachtigall W, editor. *Biona Report 3: Bird Flight - Vogelflug*. Gustav Fischer Verlag p. 161–169.
- [121] Brill C, Mayer-Kunz DP, Nachtigall W. 1989 Wing profile data of a free-gliding bird. *Naturwissenschaften* 76:39–40.
- [122] Deetjen MR, Biewener AA, Lentink D. 2017 High-speed surface reconstruction of a flying bird using structured light. *J. Exp. Biol.* 220:1956–1961.
- [123] Anderson JD. 1999 *Aircraft performance and design*. Singapore: McGraw-Hill
- [124] Luhmann T, Robson S, Kyle S, Boehm J. 2014 *Close-range photogrammetry and 3D imaging*. Berlin: Walter de Gruyter
- [125] Zitová B, Flusser J. 2003 Image registration methods: a survey. *Image Vision. Comput.* 21:977–1000.
- [126] Hoge WS. 2003 A subspace identification extension to the phase correlation method. *IEEE T. Med. Imaging* 22(2):277–280.
- [127] Alba A, Aguilar-Ponce RM, Vigueras-Gómez J, Arce-Santana E. 2013 Phase correlation based image alignment with subpixel accuracy. In: Batyrshin I, Mendoza MG, editors. *MICAI 2012, Part I, LNAI 7629*. Springer-Verlag p. 171–182.
- [128] Foroosh H, Balci M. 2004 Sub-pixel registration and estimation of local shifts directly in the fourier domain. In: *IEEE Image. Proc.* p. 1915–1918.

- [129] Stone HS, Orchard MT, Chang EC, Martucci SA. 2001 A fast direct fourier-based algorithm for subpixel registration of images. *IEEE T. Geosci. Remote* 39(10):2235–2243.
- [130] Muquit MA, Shibahara T, Aoki T. 2006 A high-accuracy passive 3D measurement system using phase-based image matching. *IEICE T. Fund. Electr.* E89-A(3):686–697.
- [131] Argyriou V, Vlachos T. 2006 A study of sub-pixel motion estimation using phase correlation. *Proc. BMVC* p. 387–396.
- [132] Castro Ed, Morandi C. 1987 Registration of translated and rotated images using finite Fourier transforms. *IEEE T. Pattern Anal.* PAMI-9(5):700–703.
- [133] Reddy BS, Chatterji BN. 1996 An FFT-based technique for translation, rotation, and scale-invariant image registration. *IEEE T. Image. Process.* 5(8):1266–1271.
- [134] Liu JG, Yan H, Morgan G. 2012 PCIAS subpixel technology. *Meas. Control* 45(7):207–211.
- [135] Morgan GLK, Liu JG, Yan H. 2010 Precise subpixel disparity measurement from very narrow baseline stereo. *IEEE T. Geosci. Remote* 48(9):3424–3433.
- [136] Yan H, Liu JG, Morgan G, Liu CC. 2012 High quality DEM generation from PCIAS. In: *IEEE Int. Geosci. Remote. Se. IEEE* .
- [137] Liu JG, Yan H. 2008 Phase correlation pixel-to-pixel image co-registration based on optical flow and median shift propagation. *Int. J. Remote Sens.* 29(20):5943–5956.
- [138] Wu MC, Liu JG, Yan H, Mason PJ. 2012 Three-dimensional surface displacement map of the 2008 Wenchuan earthquake derived from phase correlation (PC) sub-pixel offset method and adaptive local kriging (ALK) DInSAR data. In: *IEEE Int. Geosci. Remote. Se. IEEE* .
- [139] MATLAB 2015a The MathWorks, Inc., Natick, Massachusetts, United States
- [140] Walker SM, Thomas ALR, Taylor GK. 2009 Photogrammetric reconstruction of high-resolution surface topographies and deformable wing kinematics of tethered locusts and free-flying hoverflies. *J. R. Soc. Interface* 6:351–366.
- [141] Theriault DH, Fuller NW, Jackson BE, Bluhm E, Evangelista D, Wu Z, Betke M, Hedrick TL. 2014 A protocol and calibration method for accurate multi-camera field videography. *J. Exp. Biol.* 217:1843–1848.
- [142] Wasmeier P. Geodetic Transformations 2017. Available from: <https://uk.mathworks.com/matlabcentral/fileexchange/9696-geodetic-transformations>
- [143] CloudCompare. CloudCompare GPL software 2017. Available from: <http://www.cloudcompare.org/>
- [144] Walker SM, Thomas ALR, Taylor GK. 2011 Operation of the alula as an indicator of gear change in hoverflies. *J. R. Soc. Interface* 9:1194–1207.

- [145] Nickel K, Wohlfahrt M. 1994 Tailless aircraft in theory and practice. Washington DC: AIAA
- [146] Breaz N. 2004 The cross-validation method in smoothing spline regression. *Acta Universitatis Apulensis* 7:77–84.
- [147] Pennycuick CJ. 1989 Bird Flight Performance: a Practical Calculation Manual. New York: Oxford University Press
- [148] Barlow JB, Rae WH, Pope A. 1999 Low-speed wind tunnel testing. New York: John Wiley and Sons, Inc.
- [149] Warrick DR, Hedrick TL, Biewener AA, Crandell KE, Tobalske BW. 2016 Foraging at the edge of the world: low-altitude, high-speed manoeuvring in barn swallows. *Philos. T. R. Soc. B.* 371(1704).
- [150] Ravi S, Crall JD, McNeilly L, Gagliardi SF, Biewener AA, Combes SA. 2015 Hummingbird flight stability and control in freestream turbulent winds. *J. Exp. Biol.* 218(9):1444.
- [151] Tucker VA, Parrott GC. 1970 Aerodynamics of gliding flight in a falcon and other birds. *J. Exp. Biol.* 52:345–367.
- [152] Rosén M, Hedenström A. 2001 Gliding flight in a Jackdaw: a wind tunnel study. *J. Exp. Biol.* 204:1153–1166.
- [153] Gill F. 1995 Ornithology. 3rd ed. New York: W. H. Freeman
- [154] Warrick DR, Bundle MW, Dial KP. 2002 Bird maneuvering flight: Blurred bodies, clear heads. *Integr. Comp. Biol.* 42(1):141–148.
- [155] Henningsson P, Hedenström A. 2011 Aerodynamics of gliding flight in common swifts. *J. Exp. Biol.* 214:382–393.
- [156] Meriam JL, Kraige LG, Bolton JN. 2015 Engineering mechanics: Dynamics. 8th ed. Hoboken, NJ, USA: John Wiley & Sons
- [157] Mills R, Hildenbrandt H, Taylor GK, Hemelrijk CK. 2018 Physics-based simulations of aerial attacks by peregrine falcons reveal that stooping at high speed maximizes catch success against agile prey. *PLOS Comp. Biol.* 14(4):e1006044.
- [158] Ros IG, Badger MA, Pierson AN, Bassman LC, Biewener AA. 2015 Pigeons produce aerodynamic torques through changes in wing trajectory during low speed aerial turns. *J. Exp. Biol.* 218(3):480–490.
- [159] Sotavalta O. 1954 The effect of wing inertia on the wing-stroke frequency of moths, dragonflies and cockroach. *Ann. Entomol. Fenn.* 20:93–101.
- [160] Thollessen M, Norberg UM. 1991 Moments of inertia of bat wings and body. *J. Exp. Biol.* 158(1):19.
- [161] Kirkpatrick SJ. 1990 The moment of inertia of bird wings. *J. Exp. Biol.* 151:489–494.

- [162] Berg CVD, Rayner JMV. 1995 The moment of inertia of bird wings and the inertial power requirement for flapping flight. *J. Exp. Biol.* 198:1655–1664.
- [163] Hedrick TL, Usherwood JR, Biewener AA. 2004 Wing inertia and whole-body acceleration: an analysis of instantaneous aerodynamic force production in cockatiels (*Nymphicus hollandicus*) flying across a range of speeds. *J. Exp. Biol.* 207(10):1689.
- [164] Ellington CP. 1984 The aerodynamics of hovering insect flight. II. Morphological parameters. *Phil. Trans. R. Soc. B* 305(1122):17.
- [165] Hedrick TL, Biewener AA. 2007 Low speed maneuvering flight of the rose-breasted cockatoo (*Eolophus roseicapillus*). I. Kinematic and neuromuscular control of turning. *J. Exp. Biol.* 210(11):1897.
- [166] Riskin DK, Bergou A, Breuer KS, Swartz SM. 2012 Upstroke wing flexion and the inertial cost of bat flight. *Proc. Roy. Soc. B-Biol. Sci.* 279(1740):2945–2950.
- [167] Bergou AJ, Swartz SM, Vejdani H, Riskin DK, Reimnitz L, Taubin G, Breuer KS. 2015 Falling with Style: Bats Perform Complex Aerial Rotations by Adjusting Wing Inertia. *PLOS Biol.* 13(11):e1002297.
- [168] Hutchinson JR, Ng-Thow-Hing V, Anderson FC. 2007 A 3D interactive method for estimating body segmental parameters in animals: Application to the turning and running performance of *Tyrannosaurus rex*. *J. Theor. Biol.* 246(4):660–680.
- [169] Allen V, Paxton H, Hutchinson JR. 2009 Variation in center of mass estimates for extant sauropsids and its importance for reconstructing inertial properties of extinct archosaurs. *Anat. Rec.* 292:1442–1461.
- [170] Pearsall DJ, Reid JG, Livingston LA. 1996 Segmental inertial parameters of the human trunk as determined from computed tomography. *Annals of Biomedical Engineering* 24(2):198–210.
- [171] Peyer KE, Morris M, Sellers WI. 2015 Subject-specific body segment parameter estimation using 3D photogrammetry with multiple cameras. *PeerJ* 3:e831.
- [172] Goldman LW. 2007 Principles of CT and CT technology. *J. Nucl. Med. Tech.* 35(3):115–128.
- [173] Davis J, Wells P. 1992 Computed tomography measurements on wood. *Industrial Metrology* 2:195–218.
- [174] Lescot T, Degos V, Puybasset L. 2008 Does the brain become heavier or lighter after trauma? *Eur. J. Anaesth.* 25:110–114.
- [175] Malbouisson LM, Préteux F, Puybasset L, Grenier P, Coriat P, Rouby JJ. 2001 Validation of a software designed for computed tomographic (CT) measurement of lung water. *Intensive Care Medicine* 27(3):602–608.
- [176] Levi C, Gray JE, McCullough EC, Hattery RR. 1982 The unreliability of CT numbers as absolute values. *Am. J. Rad.* 139:443.

- [177] Mull RT. 1984 Mass estimates by computed tomography: Physical density from CT numbers. *Am. J. Roentgenol.* 143(5):1101.
- [178] Freyburger C, Longuetaud F, Mothe F, Constant T, Leban JM. 2009 Measuring wood density by means of X-ray computer tomography. *Ann. For. Sci.* 66(8):804–804.
- [179] Wei Q, Leblon B, Rocque AL. 2011 On the use of X-ray computed tomography for determining wood properties: A review. *Can. J. Forest. Res.*
- [180] BirdFacts: profiles of birds occurring in Britain & Ireland (BTO Research Report 407). BTO 2005. Available from: <http://www.bto.org/birdfacts>
- [181] Rao SS. 2004 Mechanical vibrations. New Jersey, USA: Pearson Prentice Hall
- [182] du Bois JL, Lieven NAJ, Adhikari S. 2009 Error Analysis in Trifilar Inertia Measurements. *Exp. Mech.* 49(4):533–540.
- [183] Greenewalt CH. 1962 Dimensional relationships for flying animals. *Smithsonian Misc. Collections* 144(2).
- [184] Madan Mohan B, Vijayakumar N, Chari N. 1982 Flight parameters and energetics of house sparrow *Passer domesticus*. *Comp. Phys. Ecol.* 7(1):8–10.
- [185] Chari N, Janaki Rama Rao N, Ravindar Reddy T, Venkateshwerlu P. 1983 Flight characteristics, moment of inertia of the wing and flight behaviour of house swift *Apus affinis*. *Comp. Phys. Ecol.* 8(1):22–25.
- [186] Baumel JJ, Witmer LM. Handbook of avian anatomy: Nomina Anatomica Avium. Nuttall Ornithological Club 1993.
- [187] Inflammation. Encyclopaedia Britannica 2018. Available from: <https://www.britannica.com/science/inflammation>
- [188] Campos MJdS, de Souza TS, Mota Júnior SL, Fraga MR, Vitral RWF. 2014 Bone mineral density in cone beam computed tomography: Only a few shades of gray. *World J. Rad.* 6(8):607–612.
- [189] Di Luca M, Mintchev S, Heitz G, Noca F, Floreano D. 2017 Bioinspired morphing wings for extended flight envelope and roll control of small drones. *Int. Foc.* 7(1).
- [190] Bribiesca-Contreras F, Sellers WI. 2017 Three-dimensional visualisation of the internal anatomy of the sparrowhawk (*Accipiter nisus*) forelimb using contrast-enhanced micro-computed tomography. *PeerJ* 5:e3039.
- [191] Pennycuik CJ. 1968 Power requirements for horizontal flight in the pigeon *Columba livia*. *J. Exp. Biol.* 49(3):527.
- [192] Hedenström A, Rosén M. 2001 Predator versus prey: on aerial hunting and escape strategies in birds. *Behav. Ecol.* 12(2):150–156.
- [193] Edwards MH. 1986 Zero angular momentum turns. *American Journal of Physics* 54(9):846–847.

- [194] Jusufi A, Kawano DT, Libby T, Full RJ. 2010 Righting and turning in mid-air using appendage inertia: reptile tails, analytical models and bio-inspired robots. *Bioinsp. Biomim.* 5(4):045001.
- [195] Cook MV. 1999 On the design of command and stability augmentation systems for advanced technology aeroplanes. *Trans. Inst. Meas. Control.* 21(2-3):85–98.
- [196] Norberg UM. 1985 Evolution of vertebrate flight: An aerodynamic model for the transition from gliding to active flight. *Am. Nat.* 126(3):303–327.
- [197] Bramwell CD, Whitfield GR. 1974 Biomechanics of *Pteranodon*. *Phil. Trans. R. Soc. B.* 267:503–581.
- [198] Howland HC. 1974 Optimal strategies for predator avoidance: The relative importance of speed and manoeuvrability. *J. Theor. Biol.* 47(2):333–350.
- [199] Wolf T, Konrath R, Erlinghagen T, Wagner H. 2012 Shape deformation measurement of free flying birds in flapping flight. In: Tropea C, Bleckmann H, editors. *Nature-inspired fluid mechanics. Notes on Numerical Fluid Mechanics and Multidisciplinary Design*. Springer-Verlag p. 135–148.
- [200] Riegels FW. 1961 *Aerofoil sections: Results from wind-tunnel investigations, theoretical foundations*. London: Butterworths
- [201] Stack J, Doenhoff AEv. Tests of 16 related airfoils at high speeds. NACA 1934.
- [202] Kroeger RA, Gruschka HD, Helvey TC. Low speed aerodynamics for ultra-quiet flight. Air Force Flight Dynamics Laboratory 1972.
- [203] Barrett RV. 1984 Design and performance of a new low turbulence wind tunnel at Bristol University. *Aeronaut. J.* 88:86–90.
- [204] Mueller TJ, Pohlen LJ, Conigliaro PE, Jansen BJ. 1983 The influence of free-stream disturbances on low Reynolds number airfoil experiments. *Exp. Fluids* 1(1):3–14.
- [205] Mueller TJ. 1985 The influence of laminar separation and transition on low Reynolds number airfoil hysteresis. *Journal of Aircraft* 22(9):763–770.
- [206] Drela M, Youngren H. *Athena Vortex Lattice* 2017
- [207] Lee D, Van Nguyen N, Tyan M, Chun HG, Kim S, Lee JW. 2016 Enhanced multi-fidelity model for flight simulation using global exploration and the Kriging method. *P. I. Mech. Eng. G: J. Aero. Eng.* 231(4):606–620.
- [208] Roache PJ, Ghia KN, White FM. 1986 Editorial Policy Statement on the Control of Numerical Accuracy. *J. Fluids Eng.* 108(1):2.
- [209] Nachtigall W. 2001 Some aspects of Reynolds number effects in animals. *Math. Meth. Appl. Sci.* 24:1401–1408.
- [210] Drela M. *XFOIL: An analysis and design system for low Reynolds number airfoils*. Massachusetts Institute of Technology 1989.

- [211] Lilley G. 1998 A study of the silent flight of the owl. In: 4th AIAA/CEAS Aeroacoustics Conference. Aeroacoustics Conferences. American Institute of Aeronautics and Astronautics .
- [212] Cracraft J, Barker FK, Braun M, Harshman J, Dyke GJ, Feinstein J, Stanley S, Cibois A, Schikler P, Beresford P, et al. 27. In: Cracraft J, Donoghue MJ, editors. Phylogenetic relationships among modern birds (Neornithes): Toward an avian tree of life. New York: Oxford University Press Inc. 2004. p. 468–489
- [213] Pomeroy H, Heppner F. 1977 Laboratory determination of startle reaction time of the starling (*Sturnus vulgaris*). Anim. Behav. 25:720–725.
- [214] Mamizuka N, Sakane M, Kaneoka K, Hori N, Ochiai N. 2007 Kinematic quantitation of the patellar tendon reflex using a tri-axial accelerometer. J. Biomech. 40(9):2107–2111.
- [215] Ohtaki Y, Mamizuka N, Fard M, Harada Y, Minakuchi Y, Ochiai N. 2009 Identification of patellar tendon reflex based on simple kinematic measurement. J. Biomech. Sci. Eng. 4(2):265–273.
- [216] Dubbeldam JL. 6. In: Whittow GC, editor. Motor control system. London: Academic Press 2000. p. 83–98
- [217] Kuroda N. 1961 A note on the pectoral muscles of birds. Auk 78:261–263.
- [218] Goldspink G, Mills C, Schmidt-Nielsen K. 1978 Electrical activity of the pectoral muscles during gliding and flapping flight in the herring gull (*Larus argentatus*). Experientia 34(7):862–865.
- [219] Pennycuik CJ. 1971 Gliding flight of the dog-faced bat *Rousettus aegyptiacus* observed in a wind tunnel. J Exp Biol 55:833–845.
- [220] Krus P. 1997 Natural methods for flight stability in birds. AIAA Journal 97:9653.
- [221] Read M, Allsop J. 1994 The barn owl. London: Cassell Plc
- [222] Ratcliffe D. 1980 The peregrine falcon. Vermillion, South Dakota: Buteo Books
- [223] Brighton CH, Thomas ALR, Taylor GK. 2017 Terminal attack trajectories of peregrine falcons are described by the proportional navigation guidance law of missiles. Proc. Nat. Acad. Sci. 114(51):13495.
- [224] Lima SL. 1993 Ecological and evolutionary perspectives on escape from predatory attack: A survey of north american birds. The Wilson Bulletin 105(1):1–47.
- [225] Gravish N, Lauder GV. 2018 Robotics-inspired biology. J. Exp. Biol. 221(7).
- [226] Tuzcu I. 2008 On the stability of flexible aircraft. Aerospace Science and Technology 12(5):376–384.
- [227] Leylek EA, Costello M. 2015 Use of Compliant Hinges to Tailor Flight Dynamics of Unmanned Aircraft. Journal of Aircraft 52(5):1692–1706.
- [228] Norberg UM. 1995 How a long tail and changes in mass and wing shape affect the cost of flight in animals. Funct. Ecol. 9:48–54.